



UNIVERSITY OF CRETE

DEPARTMENT OF MATERIALS SCIENCE AND
TECHNOLOGY

A Point-of-Care, Microfluidic-based Microscanner for the Identification and Counting of Single Cells

by

Georgia Korompili

June 2019

Supervising committee:

Prof. Nikos Chronis

Prof. Leonidas Alexopoulos

Prof. Maria Chatzinikolaidou

Dissertation committee:

Prof. Nikos Chronis

Prof. Leonidas Alexopoulos

Prof. Maria Chatzinikolaidou

Prof. George Kioseoglou

Prof. Stelios Tzortzakis

Prof. Ilektra Gkizeli

Dr. Kostas Misiakos



ΠΑΝΕΠΙΣΤΗΜΙΟ ΚΡΗΤΗΣ
ΣΧΟΛΗ ΘΕΤΙΚΩΝ ΚΑΙ ΤΕΧΝΟΛΟΓΙΚΩΝ ΕΠΙΣΤΗΜΩΝ
ΤΜΗΜΑ ΕΠΙΣΤΗΜΗΣ ΚΑΙ ΤΕΧΝΟΛΟΓΙΑΣ ΥΛΙΚΩΝ

ΠΡΑΚΤΙΚΟ ΔΗΜΟΣΙΑΣ ΠΑΡΟΥΣΙΑΣΗΣ ΚΑΙ ΕΞΕΤΑΣΗΣ
ΤΗΣ ΔΙΔΑΚΤΟΡΙΚΗΣ ΔΙΑΤΡΙΒΗΣ ΤΗΣ
κ. Γεωργίας Κορομπίλη
ΥΠΟΨΗΦΙΑ ΔΙΔΑΚΤΟΡΑ ΤΟΥ ΤΜΗΜΑΤΟΣ
ΕΠΙΣΤΗΜΗΣ ΚΑΙ ΤΕΧΝΟΛΟΓΙΑΣ ΥΛΙΚΩΝ

Η Επταμελής Επιτροπή της Διδακτορικής Διατριβής της κ. Γεωργίας Κορομπίλη η οποία ορίσθηκε στην 130η Σ.Τ. στις 15/02/2019, εκλήθη την Πέμπτη 20 Ιουνίου 2019 να εξετάσει την σύμφωνα με το Νόμο υποστήριξη της διατριβής του υποψήφιου με τίτλο:

«A Point-of-Care, Microfluidic-Based Microscanner for the Identification and Counting of Single Cells»

Τα παρόντα μέλη της επταμελούς Επιτροπής εκφράζουν ομόφωνα την πλήρη ικανοποίησή τους για την υψηλή ποιότητα του περιεχομένου και της υποστήριξης της διατριβής.

Τα ερευνητικά αποτελέσματα της εργασίας της κ. Γεωργίας Κορομπίλη είναι σημαντικά, πρωτότυπα και διευρύνουν το πεδίο της έρευνας στην Επιστήμη και Τεχνολογία Υλικών.

Ως εκ τούτου, η Εξεταστική Επιτροπή προτείνει ομόφωνα την απονομή του Διδακτορικού Διπλώματος στην κ. Γεωργία Κορομπίλη.

Η Επταμελής Επιτροπή:

Νικόλαος Χρόνης (Επιβλέπων),

Αναπληρωτής καθηγητής, Τμήμα Επιστήμης και Τεχνολογίας Υλικών, Πανεπιστήμιο Κρήτης

Μαρία Χατζηνικολαΐδου,

Αναπληρώτρια καθηγήτρια, Τμήμα Επιστήμης και Τεχνολογίας Υλικών, Πανεπιστήμιο Κρήτης

Αλεξόπουλος Λεωνίδας,

Αναπληρωτής καθηγητής, Σχολή Μηχανολόγων Μηχανικών, Εθνικό Μετσόβιο Πολυτεχνείο

Στέλιος Τζωρτζάκης,

Αναπληρωτής καθηγητής, Τμήμα Επιστήμης και Τεχνολογίας Υλικών, Πανεπιστήμιο Κρήτης

Γεώργιος Κιοσέογλου,

Αναπληρωτής καθηγητής, Τμήμα Επιστήμης και Τεχνολογίας Υλικών, Πανεπιστήμιο Κρήτης

Κωνσταντίνος Μισιάκος,

Ερευνητής Α', Ινστιτούτο Νανοεπιστήμης Νανοτεχνολογίας, Δημόκριτος

Ηλέκτρα Γκιζελή,

Καθηγήτρια, Τμήματος Βιολογίας, Πανεπιστημίου Κρήτης

ΠΕΡΙΛΗΨΗ

Η συνεχής παρακολούθηση της συγκέντρωσης των κυτταρικών πληθυσμών στο αίμα συνδέεται άρρηκτα με τη διάγνωση και την προσαρμογή της θεραπείας σε ένα ευρύ φάσμα ασθενειών. Το φάσμα αυτό περιλαμβάνει απλές λοιμώξεις του ανοσοποιητικού, χρόνιες παθήσεις του αίματος ως και επιπλοκές κατά τη διάρκεια λήψης αντικαρκινικής θεραπείας. Η πλήρης καταμέτρηση των κυτταρικών πληθυσμών του αίματος συνιστά πάγια ιατρική εξέταση, με τη διεξαγωγή της να συνιστάται σε τακτική βάση ως ενδεικτική της ολικής κατάστασης της υγείας του οργανισμού. Ωστόσο, οι χρονοβόρες διαδικασίες ανάλυσης του αίματος στα νοσοκομειακά κέντρα και τα ειδικά εξοπλισμένα εργαστήρια καθώς και το αυξημένο κόστος του ιατρικού εξοπλισμού αποτελούν σοβαρή τροχοπέδη στη έγκαιρη διάγνωση μιας νόσου. Στις αναπτυσσόμενες χώρες όπου οι δαπάνες για την υγεία παραμένουν σε χαμηλά επίπεδα, το αυξημένο κόστος αγοράς και συντήρησης του ιατρικού εξοπλισμού, αλλά και η απουσία κατάλληλα διαμορφωμένου εργαστηριακού περιβάλλοντος με εξειδικευμένο προσωπικό, καθιστούν την απλή εξέταση αίματος μη προσβάσιμη από το μεγαλύτερο τμήμα του πληθυσμού. Εν αντιθέσει με τις χώρες του τρίτου κόσμου, οι αναπτυγμένες χώρες απολαμβάνουν την ύπαρξη προηγμένων υποδομών και καλά εκπαιδευμένου ιατρικού προσωπικού. Μολαταύτα, το κόστος των εξετάσεων αίματος παραμένει αυξημένο και δύσκολο να καλυφθεί από μεγάλο μέρος του κοινωνικού συνόλου. Η διεξαγωγή των εξετάσεων αίματος στα μεγάλα νοσοκομειακά κέντρα, λειτουργεί συχνά αποτρεπτικά προς τους ασθενείς στη διαδικασία αναζήτησης διάγνωσης. Πράγματι, οι χρονοβόρες ιατρικές επισκέψεις αλλά και η έκθεση στους αυξημένους λοιμογόνους παράγοντες του νοσοκομειακού περιβάλλοντος δυσχεραίνουν τη διαδικασία διεξαγωγής απλών ιατρικών τεστ όπως η πλήρης αιματολογική εξέταση, ιδιαίτερα στο γηραιότερο πληθυσμό και τους ασθενείς με ευάλωτο ανοσοποιητικό. Προς αντιμετώπιση των ζητημάτων αυτών αναδύεται μία νέα τάση δόμησης της ιατρικής περίθαλψης η οποία θέτει ως επίκεντρο τον ασθενή, στοχεύοντας στην διεξαγωγή των ιατρικών εξετάσεων, την εξαγωγή της διάγνωσης και την παρακολούθηση και αναδιαμόρφωση της θεραπείας αυτού, «παρά τη κλίνη», ήτοι στο σημείο περίθαλψης του ασθενούς.

Επωφελούμενη από τις πρόσφατες εξελίξεις στα μικρο-ηλεκτρομηχανολογικά συστήματα, τη μικροοπτική και τη μικρο-ρευστονική επιστήμη, η παρούσα εργασία στοχεύει στην ανάπτυξη ενός νέου, φορητού μικρο-συστήματος, για την μικροσκοπική απεικόνιση δείγματος αίματος και την ανίχνευση και καταμέτρηση των κυτταρικών πληθυσμών, στο σημείο περίθαλψης. Η λειτουργία της συσκευής εστιάζεται στην οπτική απεικόνιση υψηλής ευκρίνειας και ευρέως οπτικού πεδίου, επιχρισμάτων αίματος ή μικρο-ρευστονικών καναλιών με αίμα από το δάκτυλο του ασθενούς. Η υψηλής ανάλυσης απεικόνιση επιτυγχάνεται με την χρήση μίας συστοιχίας μικρο-φακών, που κατασκευάστηκε σε υπόστρωμα πυριτίου και ενός χαμηλού κόστους αισθητήρα CMOS. Η διάταξη ακολουθεί την τεχνική μικροσκοπίας διερχόμενου φωτός, με τη διακριτική ικανότητα να προσεγγίζει το 1 μm σε μεγέθυνση 4X. Χάρη στην ιδιαίτερη γεωμετρία της συστοιχίας των μικρο-φακών επιτυγχάνεται η πλήρης απεικόνιση ενός δείγματος με έκταση επιφάνειας περί τα 2.4 cm^2 και ο σχηματισμός μίας δυσδιάστατης εικόνας αυτού, μέσω σάρωσης του δείγματος προς μία μόνο κατεύθυνση. Η σάρωση πραγματοποιείται με τη μετακίνηση τόσο της συστοιχίας των φακών όσο και του αισθητήρα CMOS ως προς το δείγμα. Ο συνδυασμός απεικόνισης ολόκληρου του δείγματος με την αυξημένη διακριτική ικανότητα που παρέχει το σύστημα, αποτελεί μια από τις κρίσιμότερες προκλήσεις στον τομέα των οπτικών συστημάτων μικροσκοπίας, ενώ το ιδιαίτερα μικρό εστιακό μήκος της διάταξης την καθιστά ιδανική για τα φορητά μικρο-συστήματα οπτικής μικροσκοπίας.

Προς την κατεύθυνση περιορισμού του όγκου των συστημάτων μικροσκοπίας, προτείνεται, επιπρόσθετα, μια καινοτόμος σχεδίαση που ενσωματώνει τα στοιχεία οπτικής διέγερσης / φωτισμού του δείγματος με τα στοιχεία συλλογής φωτός (φακοί) στο ίδιο τσιπ. Στόχος είναι η επίτευξη απεικόνισης με την τεχνική μικροσκοπίας ανακλώμενου φωτός σε πολύ μικρού όγκου συσκευές μικροσκοπίας. Ιδιαίτερη

απαιτήση στον τομέα αυτό είναι η μείωση της πολυπλοκότητας της οπτικής διάταξης, που μπορεί επιτυχώς να οδηγήσει στον περιορισμό του όγκου και του κόστους αυτών. Στην προτεινόμενη σχεδίαση, μια διάταξη/συστοιχία δακτυλιοειδών μικρο-LED αναπτύσσεται στη μία πλευρά του τσιπ πυριτίου, το οποίο φιλοξενεί στην αντίθετη πλευρά μια συστοιχία μικρο-φακών, έγκιεντρα τοποθετημένων με τους δακτυλίους φωτισμού. Στα πλεονεκτήματα της διάταξης συγκαταλέγονται το ιδιαίτερα μικρό μήκος οπτικής διαδρομής και ο χωρικός διαχωρισμός της δέσμης οπτικής διέγερσης από τη διαδρομή που ακολουθεί η ανακλώμενη από το δείγμα δέσμη. Το γεγονός αυτό διασφαλίζει την ελαχιστοποίηση του επιπέδου του θορύβου στην παρεχόμενη εικόνα. Το προτεινόμενο ολοκληρωμένο τσιπ επιτυγχάνει ανάλυση εικόνας 8,8 μm . Η αυξημένη απλότητα, το χαμηλό κόστος κατασκευής, η ευκολία ενσωμάτωσης σε ένα ευρύ φάσμα διατάξεων απεικόνισης και η δυνατότητα μεταβολής του μήκους κύματος του εκπεμπόμενου φωτός, καθιστούν την προτεινόμενη τεχνολογία ιδιαίτερα επωφελή στο τομέα μικροσκοπικών συστημάτων ανακλώμενου φωτισμού.

Η προτεινόμενη τεχνολογία απεικόνισης κυττάρων ολοκληρώνεται με την ανάπτυξη ενός μικρο-ρευστονικού τσιπ για την απομόνωση συγκεκριμένων κυτταρικών πληθυσμών, με αυξημένη απόδοση δέσμησης κυττάρων. Η λειτουργία του τσιπ αυτού στηρίζεται στην ενεργοποίηση των εσωτερικών τοιχωμάτων του θαλάμου του τσιπ με αντισώματα κατάλληλα για ειδική δέσμηση σε πρωτεϊνικούς υποδοχείς της κυτταρικής επιφάνειας. Συγκεκριμένα, πραγματοποιήθηκε απομόνωση των λευκών αιμοσφαιρίων μέσω ειδικής σύνδεσης με το αντίσωμα αντι-CD45, ενώ τα CD3⁺ T και CD8⁺ T λεμφοκύτταρα απομονώθηκαν με τη χρήση των αντίστοιχων αντισωμάτων. Κατά τη διαδικασία διαχωρισμού των συγκεκριμένων κυτταρικών πληθυσμών πραγματοποιείται έκπλυση των μη επιθυμητών κύτταρων του αίματος, ήτοι των κυττάρων που δεν προσδέονται στην επιφάνεια του τσιπ. Η διεξαχθείσα έρευνα επικεντρώνεται στην αύξηση της απόδοσης δέσμησης των κυττάρων μέσω εναλλακτικής σχεδίασης της γεωμετρίας του ρευστονικού καναλιού και του πρωτοκόλλου ενεργοποίησης της επιφάνειας. Στόχος είναι ο προσδιορισμός των παραγόντων εκείνων που επηρεάζουν τη πρόσδεση των κυττάρων στα τοιχώματα του θαλάμου ή που οδηγούν στην αποκόλληση των ακινητοποιημένων κυττάρων κατά την έκπλυση των ανεπιθύμητων στοιχείων του αίματος. Εξετάστηκαν αναλυτικά το ύψος του θαλάμου, ο ρόλος των ερυθρών αιμοσφαιρίων, που εμφανίζουν αυξημένη συγκέντρωση στα δείγματα ολικού, μη επεξεργασμένου, αδιάλυτου αίματος και οι συνθήκες ροής κατά την εισαγωγή του αίματος στο θάλαμο αλλά και κατά την έκπλυση. Η μελέτη των παραμέτρων αυτών οδήγησε στην εξαγωγή των βέλτιστων γεωμετρικών χαρακτηριστικών του καναλιού συλλογής του αίματος και στη βελτιστοποίηση του πρωτοκόλλου ενεργοποίησης αυτού. Προτείνεται, ως εκ τούτου ένα νέο πρωτόκολλο επώασης του αίματος, με το οποίο επιτυγχάνεται αύξηση του αριθμού των προσδεμένων κυττάρων από δείγματα ολικού, μη επεξεργασμένου αίματος. Επιπρόσθετα, προσδιορίζεται με ακρίβεια μέσω μοντελοποίησης του ρευστονικού καναλιού το κατώφλι της εφαρμοζόμενης ταχύτητας ροής για την αποτελεσματική απομάκρυνση των ανεπιθύμητων κυττάρων χωρίς αποκόλληση των προσδεμένων κυττάρων. Το σφάλμα δέσμησης που παρουσιάζει η προτεινόμενη τεχνολογία μειώθηκε στο 3,8%, μία τιμή κλινικά αμελητέα, για την περίπτωση των λευκών αιμοσφαιρίων, αναφορικά με μετρήσεις που προέρχονται από την τεχνική της κυτταρομετρίας ροής – το «χρυσό κανόνα» στην ταυτοποίηση και καταμέτρηση κυττάρων. Η παρεχόμενη ακρίβεια και η ομοιόμορφη κατανομή των κυττάρων σε ολόκληρη την επιφάνεια του μικρορευστονικού τσιπ αποδεικνύει την αποτελεσματικότητα της τεχνικής κατά την οποία εξαλείφεται η ανάγκη προεπεξεργασίας του δείγματος. Καθίσταται επομένως ιδανική για μία πληθώρα μικρο-συστημάτων που χρησιμοποιούνται στο σημείο περίθαλψης.

Συνολικά, το προτεινόμενο σύστημα απεικόνισης μαζί με την ανεπτυγμένη μικρο-ρευστονική διάταξη, όπως αυτά περιγράφονται και αναλύονται στην παρούσα διδακτορική διατριβή, αποτελούν μια γενικού τύπου τεχνολογία, υπό την έννοια ότι δύνανται να εφαρμοστούν σε ένα ιδιαίτερα ευρύ φάσμα ασθενειών και διαταραχών που σχετίζονται με το αίμα. Με την προσφερόμενη ακρίβεια στην παρακολούθηση των διακυμάνσεων των κυτταρικών πληθυσμών του αίματος, τον ιδιαίτερα μικρό όγκο της συσκευής και με

την απουσία του σταδίου προεπεξεργασίας ή αραιώσης του δείγματος, η προτεινόμενη τεχνολογία υπόσχεται να αποτελέσει αναπόσπαστο τμήμα στις διαδικασίες ιατρικών εξετάσεων που πραγματοποιούνται «παρά τη κλίνη» του ασθενούς, ως μετρητής αίματος γενικής χρήσης. Για την αποτελεσματική εξαγωγή ιατρικών αποφάσεων, κατά τη διάγνωση ή / και την προσαρμογή της θεραπείας, στο σπίτι ή σε χώρους πρωτοβάθμιας περίθαλψης, οι μελλοντικές έρευνες επιβάλλεται να στραφούν στην καταμέτρηση της προσφερόμενης ακρίβειας, αναφορικά με διαφορετικούς πληθυσμούς κυττάρων. Παράλληλα, η πλήρης αυτοματοποίηση του συστήματος με βάση την προτεινόμενη τεχνολογία είναι από τα κρίσιμα βήματα που πρέπει να ακολουθήσουν τα επόμενα χρόνια. Η ανάπτυξη της προτεινόμενης τεχνολογίας και η επικύρωση της λειτουργίας της, που υλοποιήθηκε στο πλαίσιο του παρόντος έργου, αποδεικνύει τη δυνατότητα ανίχνευσης και καταμέτρησης κυττάρων με μεγάλη ακρίβεια, σε εκτεταμένη επιφάνεια δείγματος και σε πλήρη συμμόρφωση με τις απαιτήσεις του Παγκόσμιου Οργανισμού Υγείας σχετικά με τις κατ' οίκον ιατρικές συσκευές: το χαμηλό κόστος, την ευχρηστικότητα, την απουσία εξωτερικής τροφοδοσίας ή εργαστηριακού εξοπλισμού και τη δυνατότητα να παρέχονται άνευ όρων σε όλους.

ΛΕΞΕΙΣ ΚΛΕΙΔΙΑ

σχεδιασμός μικροσυστημάτων, συστοιχία μικρο-φακών, μικρο-LED σε πυρίτιο, μικροσυστήματα μικροσκοπίας, απεικόνιση ανακλώμενου φωτός, μικρορευστονικές διατάξεις, απομόνωση κυτταρικών πληθυσμών, δέσμευση κυττάρων με ενεργοποίηση επιφάνειας

ABSTRACT

Blood cell population monitoring is related to the diagnosis or therapy adjustment of a wide range of diseases, from infections to blood disorders and cancer treatment. This routinely performed medical examination is indicative of the individual's health status; therefore, it is frequently advised to be conducted at a regular basis. However, the time consuming procedures and the increased cost of standard medical equipment for blood cell identification and counting act both as serious obstacles in the early screening of a disease. In poor-income countries, the increased equipment expenses and the lack of laboratory environment and expert personnel to conduct the examination, render the access of population to routine blood tests unavailable. Though in the developed world, advanced infrastructure and well-trained medical personnel are available, the increased cost of blood tests and the necessity for frequent hospital visits can still be prohibitive for patients to seek diagnosis. To address these issues there is an emerging trend towards a patient-centered healthcare, that can provide medical examination, diagnosis and treatment management, at the point of care.

Profiting from the recent advances in micro-electromechanical systems, micro-optics and micro-fluidics for minute blood sample volume processing on-chip, the present thesis attempts to present a novel device for blood cell identification and counting at the point of care. The operation of the developed prototype device focuses on high-resolution and wide field of view, trans-illuminated, optical imaging of blood smears or microfluidic chips filled with blood retrieved from patients' finger. High quality imaging is achieved with the employment of a mini-lens array fabricated on silicon substrate and a low cost CMOS sensor; the optical system provides approximately 1 μm resolving power at 4X magnification. The special geometry of this lens array design enables the formation of a large 2D image of the entire sample, through 1 direction scanning only, that is accomplished by the translation movement of both the lens array and the CMOS camera employed. The combination of whole slide imaging with increased resolving power, successfully accomplished by the proposed imaging platform, responds to one of the most crucial challenges in the field of miniaturized optical microscopy systems.

Towards the same direction, a novel design integrating the excitation/illuminating and collecting/optical elements on the same chip is suggested for efficient reflection based imaging. Great challenge in the field of epi-illumination miniaturized imaging systems is the decrease of complexity, which has evidently led to increased volume and cost of the recently developed portable optical devices. In the suggested design, a ring-shaped micro-LED array is patterned at the one side of a silicon chip that hosts on the opposite side a mini-lens array. Such integration achieves radical reduction of the volume of the optical system – the optical path length does not exceed 2.5 mm – while it separates the optical path of the excitation and reflection beams, assuring minimized noise level in the provided image. Through the validation process, it is proven that the proposed integrated chip achieves 8.8 μm resolution. Increased simplicity, low manufacturing cost, suitability for a wide range of imaging setups and the possibility to control wavelength range illumination render this technology promising for miniature, reflection-based, imaging systems and for use at the point of care.

The proposed cell imaging/counting technology is completed with the development of a microfluidic chip for specific cell identification and isolation, that enables increased cell capture yield. The operation of this chip relies on the functionalization of the internal walls of the chamber with antibodies for specific binding on cell surface receptors. White blood cells are specifically captured with the use of anti-CD45 antibody, while CD3+ T lymphocytes and CD8+ T lymphocytes capturing has also been examined with the use of the corresponding antibodies. The conducted research focuses on achieving increased capturing yield; therefore it is oriented towards the factors that can affect target cells binding on the chamber's walls or that can result in the detachment of immobilized cells during washing removal of unwanted cell populations. Among these factors, the height of the developed chamber, the role of red blood cells, exhibiting increased concentration in whole unprocessed, undiluted blood, and the flow conditions in both introduction of blood and washing removal of unbound cells have all been examined. This profound investigation led to the extraction of the optimum geometrical properties of the developed microfluidic chamber and the optimization of the functionalization protocol. A novel blood incubation scheme, enabling high cell capturing rate in whole unprocessed blood samples, is proposed. Finally the threshold of the applied flow rate for efficient removal of undesired cells without affecting captured cells is precisely determined through finite element analysis modeling. The capturing error of device has been reduced to a clinically negligible value of 3.8 % for white blood cells fractionation, compared to the corresponding counts derived from the gold standard, flow cytometry based, medical test. The provided accuracy and the uniform distribution of cells over the entire microfluidic chip surface proves the efficient performance of the proposed microfluidic device that eliminates the sample preprocessing step; it is, therefore, suitable for use at the point of care.

The suggested imaging system together with the developed microfluidic device, described and analyzed in this thesis, constitute a platform technology, in the sense that it can be applied in a wide range of diseases and blood related disorders. Achieving high quality monitoring of blood cell populations, operating with whole unprocessed/undiluted blood, retrieved by patient's finger with standard finger pricking method and exhibiting increased purity and capture yield in blood cell fractionation, it promises to be part of the point-of-care testing procedures as a general purpose blood cell counter. Towards effective medical decision extraction for diagnosis and/or therapy adjustment, at home or at primary healthcare settings, future investigation is needed on the provided accuracy in different cell populations. Additionally, full automation of the system based on the proposed platform technology is among the crucial steps to follow. The development of the suggested technology proves the feasibility of performing single cell identification and counting, with high accuracy, over an extended sample and in full compliance with the requirements of World Health Organization for point-of-care devices: they need to be affordable, easy-to-use, battery operated and delivered unconditionally to all.

KEYWORDS

microsystem design, mini-lens array, micro-LED on Si, miniaturized microscopes, reflection-based imaging, microfluidic design, cell fractionation, cell surface binding

Contents

| | |
|-----------------------------------------------------------------------------------------------------------------------------------------------------------------|-----|
| ΠΕΡΙΛΗΨΗ | 5 |
| ABSTRACT | 9 |
| Αντί προλόγου | 13 |
| List of abbreviations | 17 |
| Chapter 1..... | 19 |
| Introduction to blood cells monitoring and counting for diagnosis and therapy at the point of care .19 | |
| 1. Blood cell counting for the diagnosis and treatment adjustment of diseases and blood disorders | 19 |
| 2. The need for cell identification and counting at the point of care..... | 25 |
| 3. Requirements for the accurate and efficient blood count monitoring at the point of care..... | 27 |
| 4. Aim – scope of this study..... | 29 |
| 5. Thesis overview..... | 30 |
| Chapter 2..... | 31 |
| Single cell optical imaging and microfluidic cell fractionation technologies – A critical review of the state-of-the art..... | 31 |
| 1. Portable bright field microscopy imaging platforms | 31 |
| 2. Reflection mode optical imaging – integration of off-axis illumination scheme | 35 |
| 3. Microfluidic chips for cell capturing and identification, for use in optical cell imaging and counting devices | 41 |
| Chapter 3..... | 49 |
| A portable, optical scanning microsystem for large field of view, high resolution imaging of biological specimens..... | 49 |
| 1. Architecture and operating principle of the micro-scanner | 49 |
| 2. The mini-lens array..... | 52 |
| 3. The scanning head and the mechanical components of the micro-scanner | 77 |
| 4. The illumination scheme – transmission mode imaging | 83 |
| 5. Electronic parts of the scanning system and computer-assisted control..... | 84 |
| 6. Image processing algorithms for image mosaicking, cell detection and counting..... | 91 |
| 7. Discussion – Advantages, trade-offs and future perspectives | 99 |
| Chapter 4..... | 103 |
| Integration of an LED structure in a mini-lens array for the implementation of reflection mode illumination scheme in miniaturized optical devices..... | 103 |
| 1. Integration of an LED structure on a ball mini-lens array – design and operating principle of the compound chip. | 104 |
| 2. Fabrication of the proposed illumination/ imaging compound chip. | 113 |
| 3. Characterization of the fabricated illumination/imaging chip. | 116 |
| 4. Discussion – Advantages and tradeoffs, improvements and future perspectives. | 129 |
| Chapter 5..... | 133 |
| A microfluidic bio-chip for enhanced surface capturing of white blood cells or a sub-population: extensive study of factors affecting capturing efficiency..... | 133 |
| 1. Design of the microfluidic dual channel bio-chip for surface capturing of specific cell types | |

| | |
|----------------------------------------------------------------------------------------------------------------------------------------------------|-----|
| 2. Functionalization protocol for WBC and subpopulations surface capturing..... | 140 |
| 3. Characterization of capturing performance based on factors affecting cell surface adhesion. 151 | |
| 4. Discussion – Advantages and tradeoffs, improvements and future perspectives. | 162 |
| Discussion..... | 165 |
| Overall valuation of the suggested system for efficient blood cell identification and counting at the point of care | 165 |
| 1. Innovative aspects and contribution to the corresponding research fields..... | 165 |
| 2. Compliance with generic specifications for point-of-care testing. | 167 |
| 3. Towards a medical tool for point-of-care blood cell analysis: future investigation and validation requirements | 169 |
| 4. Social impact and future perspectives: current fields of application and the potential of a general purpose blood cell analysis device | 169 |
| APPEENDIX 1 | 171 |
| DESIGN DOCUMENTS | 171 |
| APPEENDIX 2..... | 180 |
| SOFTWARE CODE | 180 |
| APPEENDIX 3..... | 199 |
| SURFACE FUNCTIONALIZATION PROTOCOL..... | 199 |
| Bibliography | 201 |
| Publications | 221 |

Αντί προλόγου

Κάθε τι που φτάνει σε επιτυχές τέλος μοιάζει ονειρικό· σβήνουν εύκολα οι δυσκολίες του παρελθόντος τόσο που φτάνει κανείς να ομολογήσει μια νοσταλγία ακόμη και για τις πιο άσχημες στιγμές. Αυτό το διδακτορικό ξεκίνησε χωρίς επαγγελματικές φιλοδοξίες, παρά μόνο με τη χαρά της ενασχόλησης με έναν από τους πιο ενδιαφέροντες τομείς της σύγχρονης επιστήμης, δίπλα σε ανθρώπους με βαθειά γνώση, εμπειρία και καταξίωση, αλλά κυρίως με το όνειρο ότι μπορούσε να προσφέρει έστω και λίγο στην ανθρώπινη ύπαρξη, στην ποιότητα ζωής και σε μία χώρα που βρισκόταν – και βρίσκεται ακόμη – υπό το καθεστώς γενικευμένης οικονομικής κρίσης, με όλα όσα αυτή συνεπάγεται.

Από το πρώτο αυτό όνειρο, το 2012, που συνοδεύτηκε από τη χαρά επιστροφής στην Ελλάδα, ως σήμερα, οι αντικειμενικοί στόχοι αυτής της έρευνας δεν μεταβλήθηκαν καθόλου. Η αξιοποίηση της τεχνολογίας μικροκατασκευής για τη δόμηση ενός ολοκληρωμένου συστήματος ανίχνευσης κυττάρων του αίματος από πολύ μικρό ανεπεξέργαστο δείγμα, αποδείχθηκε, όχι απλά ένα ενδιαφέρον επιστημονικό πεδίο, αλλά και μία άρτια εφαρμοσμένη επιστήμη με στόχο την επίλυση ουσιαστικών προβλημάτων της ζωής του ανθρώπου. Τα αποτελέσματα της ερευνητικής διαδικασίας μπορούν να χαρακτηριστούν ιδιαίτερα ελπιδοφόρα για την υλοποίηση τέτοιων συστημάτων και την πεποίθηση ότι οι επόμενες γενιές θα μπορούσαν να γνωρίσουν μια εντελώς διαφορετική δομή του εθνικού συστήματος υγείας. Ο όρος ‘θα μπορούσαν’ αναφέρεται στις τεχνολογικές δυνατότητες, ενώ περιορίζεται ταυτόχρονα από την προϋπόθεση ύπαρξης της πολιτικής βούλησης για την αξιοποίηση αυτών προς την βελτίωση της ζωής των πολιτών.

Στα χρόνια της κρίσης, ο όρος ‘ανάπτυξη’ χρησιμοποιήθηκε ως η κύρια αιτία για τη συνεχή φτωχοποίηση του πληθυσμού και την επιβολή αβάσταχτων μέτρων λιτότητας. Η ‘ανάπτυξη’, μετρούμενη με οικονομικούς παράγοντες, μπήκε στον καθημερινό λόγο των απλών πολιτών και συνδέθηκε με τα οικονομικά στοιχεία της χώρας που ελάχιστα γίνονται κατανοητά από τους μη οικονομολόγους. Αυτού του τύπου η ‘ανάπτυξη’ δεν συνδέθηκε καθόλου με εγχειρήματα που σχετίζονται με τη βελτίωση των παροχών στην υγεία ή στην παιδεία, εφόσον αυτά προϋποθέτουν μεγάλης κλίμακας δαπάνες του κράτους. Έτσι τέτοιου είδους εγχειρήματα δεν πραγματοποιούνται ή όταν πραγματοποιούνται γίνονται ελάχιστα γνωστά καθώς παρουσιάζουν πλέον μειωμένο ενδιαφέρον, μη συνδεδεμένα με την ‘ανάπτυξη’ της χώρας.

Στον αντίποδα του περιορισμού των δαπανών και σε πλήρη σύνδεση με τα τεχνολογικά επιτεύγματα στον τομέα των μικροσυστημάτων ιατρικής διάγνωσης, η ελληνική αστυνομία είναι σήμερα εξοπλισμένη με φορητά συστήματα ανίχνευσης του HIV ιού, με τη δυνατότητα να πραγματοποιεί δια της βίας ιατρικές εξετάσεις και με στόχο την περιθωριοποίηση ή και την ποινική δίωξη πολιτών αυτής της χώρας¹. Με τα ιατρεία της πρωτοβάθμιας υγείας να παραμένουν ελλιπώς εξοπλισμένα, η αξιοποίηση τέτοιων συστημάτων από την ελληνική αστυνομία γεννά εύλογα το ερώτημα του σκοπού που μπορεί να εξυπηρετήσει σήμερα η ανάπτυξη τέτοιων συστημάτων από νέες ερευνητικές ομάδες, υπό το παράλληλο πρίσμα ύπαρξης χιλιάδων, δημόσια διαθέσιμων, ερευνών και έργων διδακτορικών διατριβών, που παραμένουν αναξιοποίητα από το κράτος που τις χρηματοδότησε, στις βιβλιοθήκες των πανεπιστημίων.

Τα τελευταία χρόνια σημειώθηκε μικρή αύξηση των οικονομικών πόρων για την έρευνα, μετά τη ισχυρή συρρίκνωση που υπέστησαν κατά τα πρώτα χρόνια της κρίσης. Παρόλα αυτά, οι δαπάνες προσφέρονται σήμερα πάντα με γνώμονα τα οικονομικά κέρδη των επιχειρήσεων, ενώ ελάχιστοι πόροι διατίθενται για την βασική έρευνα, παραγνωρίζοντας το γεγονός ότι τα ερευνητικά κέντρα της χώρας αναπτύχθηκαν και

¹ Η υπόθεση διαπόμπευσης οροθετικών γυναικών το 2012 περιγράφεται στο ντοκιμαντέρ Ruins <https://ruins-documentary.com/>, με την υπόθεση να ειδικάζεται το 2016 και να οδηγεί στην αθώωση των γυναικών που αρχικά είχαν κατηγορηθεί. Η υγειονομική διάταξη που εισήγαγαν οι υπουργοί υγείας Ανδρέας Λοβέρδος και Άδωνις Γεωργιάδης, βάσει της οποίας επιβαλλόταν η υποχρεωτική εξέταση, νοσηλεία και υποχρεωτική θεραπεία για ασφώς ορισμένα λοιμώδη νοσήματα (<http://www.avgi.gr/article/573269/ugeionomiki-diataxi-%C2%ABloberdou-adoni%C2%BB>) καταργήθηκε οριστικά το έτος 2015.

εξοπλίστηκαν με κύριο σκοπό της εκπόνηση επιστημονικής έρευνας και όχι την παραγωγή εμπορικά εμπορεύσιμων προϊόντων ή τη δημιουργία επιχειρήσεων. Άμεση συνέπεια του καθεστώτος αυτού είναι η υιοθέτηση πρακτικών επιχειρήσεων στα ερευνητικά εργαστήρια, με ιδιαίτερα μειωμένες αμοιβές ή και πλήρη απουσία αυτών προς τους εκπονούντες το ερευνητικό έργο. Σύμφωνα με το Εθνικό Κέντρο Τεκμηρίωσης, κατά το έτος 2015, σε ένα ποσοστό 23,6%, οι διδάκτορες χρηματοδότησαν οι ίδιοι από "προσωπικές αποταμιεύσεις και υποστήριξη από την οικογένεια" τις διδακτορικές τους σπουδές, ενώ "υποτροφία στην Ελλάδα" είχε το 23,1%, "αμοιβή από άλλη εργασία" το 21,5% και "αμοιβή από απασχόληση ως βοηθός διδακτικού ή ερευνητικού προσωπικού" το 17,4%.² Δυστυχώς το παρόν καθεστώς υποχρηματοδότησης της ερευνητικής εργασίας των υποψήφιων διδακτόρων υιοθετείται χωρίς πλέον αμφισβήτηση και από μεγάλη μερίδα της μόνιμης ερευνητικής κοινότητας.

Απόρροια των προβλημάτων και των προβληματισμών αυτών, τα χρόνια εκπόνησης της διατριβής ήταν χρόνια έντονων δυσκολιών. Για μεγάλες χρονικές περιόδους η εκπόνηση αυτής της διδακτορικής διατριβής φάνταζε η πλέον λανθασμένη επιλογή καθώς πέρα από τα οικονομικά ζητήματα, αποκαλυπτόταν μια σταδιακή κατάρρευση του αρχικού εκείνου ονείρου, του Οκτωβρίου του 2012. Όμως 'τη ζωή οφείλεις να την ονειρεύεσαι ενώ συνάμα τη ζεις'³, όχι με την έννοια του να προσβλέπεις ανυπόμονα σε ένα ωραίο μέλλον αλλά με την έννοια της ονειρικής διάστασης του παρόντος. Σε οποιοδήποτε συμβάν της περιόδου αυτής, σε οποιαδήποτε δύσκολη ή εύκολη χρονική στιγμή, μου είχε χαριστεί η ευκαιρία να ασχοληθώ με κάτι εντυπωσιακά όμορφο, με κάτι που ήταν αληθινά χρήσιμο, αντανακλώντας μια κάποια χρησιμότητα και στη δική μου δουλειά. Δεν ξέρω να πω ακριβώς ποια διάσταση των ανθρώπων που συνάντησα σε αυτή την πορεία είναι η εντελώς αληθινή τους ή αν κάπως την ονειρεύτηκα. Με τον κ. Χρόνη περάσαμε από ισχυρές και ηχηρές διαφωνίες μέχρι συζητήσεις απεριγράπτα ονειρικές και δημιουργικές· το μόνο σίγουρο είναι ότι διδάχτηκα και από τα δύο και τον ευχαριστώ για όλες τις ημέρες που μοιραστήσαμε τα τελευταία επτά σχεδόν χρόνια. Με την ελπίδα ότι όλοι όσοι συνέβαλλαν στο ερευνητικό αυτό έργο – η Κατερίνα, ο Χρήστος, ο Γιώργος – μοιράζονται την ίδια σκέψη, μέσα από αυτά τα χρόνια γνωριστήκαμε ως άνθρωποι περισσότερο από όσο ως συνεργάτες και πάντα θα υπάρχει η νοσταλγία για τα χρόνια που υπήρξαμε μαζί στο εργαστήριο.

Φυσικά, το μεγαλύτερο βάρος των δυσκολιών το φέρουν εκείνοι που από αγάπη στέκονται – σιωπηλοί ή φωναχτάδες – πλάι σου όταν θυμώνεις ή απελπίζεσαι ή εμμονικά θυσιάζεις τα πλέον απαραίτητα για μια ακατανόητη ομορφιά του επιστημονικού αντικειμένου. Ποια ουσία θα είχε άλλωστε αυτή η διατριβή χωρίς αυτούς; Ελπίζω ότι σε αυτές τις γραμμές οι φίλοι μου θα ανακαλύψουν ο καθένας ξεχωριστά τον εαυτό του, αλλά και εκείνοι που από αγάπη άνευ όρων υπέμειναν τις πιο δύσκολες ώρες. Το βιβλίο αυτό χαρίζεται σε όλους αυτούς και ξεχωριστά στον άνθρωπο που κάθε μέρα μου θυμίζει πως ζωντανός είναι αυτός που μπορεί να αγαπά.

² <https://www.ekt.gr/el/magazines/features/19878>

³ Χρήστος Βακαλόπουλος

Στην Ιφιγένεια
και τους μελλοντικούς της φίλους
- μάθημα πρώτο: το χρώμα 'κόκκινο'

List of abbreviations

| | |
|-------|----------------------------------------------|
| WHO | World Health Organization |
| RDTs | Rapid Diagnostic Tests |
| MEMS | Micro- Electro-Mechanical Systems |
| FOV | Field of View |
| AIDS | Acquired ImmunoDeficiency Syndrome |
| HIV | Human Immunodeficiency Virus |
| ART | Anti-Retroviral Therapy |
| HAART | Highly Acute Anti-Retroviral Therapy |
| RNA | RiboNucleic Acid |
| CD4 | Cluster of Differentiation 4 |
| FC | Flow Cytometry |
| POC | Point of Care |
| WBC | White Blood Cell |
| RBC | Red Blood Cell |
| SCA | Sickle Cell Anemia |
| OFM | Optofluidic Microscope Implementation Method |
| HM | Holographic Microscopy |
| BSDK | BackScattering Dark Field |
| EF | Epi-Fluorescence |
| IRF | Interferometer Reflection Contrast |
| DRS | Darkfield Reflected Surface |
| TIR | Total Internal Reflection |
| LED | Light Emitting Diode |
| GREEN | Gradient Index lenses |
| SDFI | SideStream Dark Field Imaging |
| PDMS | Polydimethylsiloxane |
| CTCs | Circulating Tumor Cells |
| EpCAM | Epithelial Cell Adhesion Molecule |
| CMOS | Complementary Metal Oxide Semiconductor |
| DRIE | Deep reactive Ion Etching |
| EFL | Effective Focal Length |
| NA | Numerical Aperture |
| rms | root mean square |
| TTV | Total Thickness Variation |
| PVC | Polyvinyl Chloride |
| PMMA | Poly(methyl methacrylate) |
| CNC | Computer Numerical Control |
| GUI | Graphical User Interface |
| PID | Proportional Integral Derivative |

BHF (BOE)

IR

PTPRC

LCA

Buffered Oxide Etching

InfraRed

Protein tyrosine phosphatase, receptor type, C

Leukocyte Common Antigen

Chapter 1

Introduction to blood cells monitoring and counting for diagnosis and therapy at the point of care

Counting blood cells is an important aspect of diagnostic hematology. It is a routinely performed medical examination for the diagnosis and monitoring of a wide range of diseases or blood disorders. It requires blood collection either by vein puncturing or finger pricking method, specialized blood analysis equipment and health-care professionals. However, time consuming procedures and the increased cost of equipment related to standard blood cell population monitoring, act as serious obstacles in the early screening of a disease. Though in the developed world advanced infrastructure and well-trained medical personnel are available, the cost of healthcare can still be prohibitive for patients to seek diagnosis. In low-resources settings, access to medical equipment may not even be available (L.Frost & M. Reich, 2008). To address these issues, there is an emerging trend to adapt a patient-centered healthcare (Davis, Schoenbaum and Audet, 2005). In this context, the development and use of point-of-care devices for blood cell monitoring and counting is an excellent field of application of recent advances in portable microscopy. Despite the numerous research studies that it has already attracted, this field still presents a great challenge: to overcome technical limitations and provide a general purpose platform for highly specific and accurate monitoring of blood cell populations. Recent technological advances in micro-optics, micro-electronics and micro-electromechanical systems (MEMS) have the potential to improve screening and detection of a wide range of diseases at the point of care or in primary health care settings, in both low- and high-income countries.

1. Blood cell counting for the diagnosis and treatment adjustment of diseases and blood disorders

A blood cell count is a routine medical examination required to diagnose or monitor a variety of blood related disorders or infections and diseases that affect blood. It is also performed at regular intervals to determine general health status, to adjust received treatment known to affect specific cells concentration or to indicate virus infection progress. In many cases, a specific population of main group components of blood may be required. In the following sections, a report of some of the most ‘important’ cases of diseases whose diagnosis or progression is determined by specific blood cell identification and counting, is performed. The criteria for the selected cases to report are mainly based on the magnitude of disease burden worldwide as well as the necessity for accurate, timely blood cell monitoring tests for the diagnosis and therapy or treatment management.

1.1. Malaria epidemic and the diagnostic procedures

Malaria, an infection illness often referred to as the ‘king of diseases’, presents a global health threat (Arrow, KJ.; Panosian, C.; Gelband, 2004) with nearly half of the world’s population being at risk of infection. Despite being preventable and treatable, malaria continues to have a devastating impact on people’s health and livelihoods around the world. In 2016, an estimation of 216 000 incidences of

malaria occurred worldwide, while approximately half a million of malaria deaths were reported. Young children, pregnant women and non-immune travelers from malaria-free areas are among the most vulnerable groups to be infected by the disease (WHO Global Malaria Programme, 2017). The largest burden of the disease rests in Africa with the access to diagnostic tools and skilled personnel being one of the most important factors preventing transmission elimination. According to the annual report of 2017 of the World Health Organization (WHO) on Malaria, new threats to respond are the false-negative diagnosis and the parasite resistance to antimalarial drugs (WHO Global Malaria Programme, 2017).

The conventional diagnostic process of Malaria infection is based on a microscopic examination of stained peripheral blood smears. The gold standard diagnosis requires examination of the entire smear slide under light microscope to detect infected cells identified by Giemsa staining protocol (Tangpukdee *et al.*, 2009), as it is the only providing accurate results of infection. However, this technique is time consuming and requires bulk complex equipment, laboratory environment and personnel expertise that are unavailable, in most cases of countries with high transmission rate. Thus, the WHO global technical strategy for 2015-2030 encourages for research investment on the development of alternative portable and easy to use diagnostic tools that could provide accurate, fast results of diagnosis (WHO, 2015a). In fact, within the past decades an important research in the proposal of rapid diagnostic tests (RDTs) for malaria took place. The vast majority of the designed tools employ lateral-flow immunochromatography to detect specific antigens in a finger-prick sample of blood. Major advantages they present over the gold standard of optical microscopy imaging of thick or thin blood films are rapidity and simplicity of use. It is though questionable whether they can safely replace microscopy imaging of blood sample, mainly due to the limitations they present in false-negative results (Moody, 2002). It is reported that substantial misdiagnosis for malaria is currently present in parts of Asia using RDTs and misdiagnosis may lead to mistreatment or over-treatment and consequently to potential immunity to antimalarial drugs (Ashraf *et al.*, 2012; Leslie *et al.*, 2012). In the WHO guidelines for Malaria prevention it is stipulated that, prior to any anti-malarial treatment initiation, a prompt infection confirmation must be taken through microscopy or alternative RDTs. However, it is also declared that RDTs already developed should not be regarded as substitute of microscopy, but they may be used alongside blood films for diagnostic purposes (WHO, 2012; Co-operative and Oxford, 2015).

The advances in micro-optics and micro-electronics led to a recently emerging trend towards portable microscopy imaging systems that could provide a promising alternative to the gold standard for Malaria diagnosis (Sousa-Figueiredo *et al.*, 2010; Pirnstill and Coté, 2015; Yang *et al.*, 2017). Fully compliant with routine laboratory method of white light or fluorescent microscopy, such approaches promise to provide high specificity and sensitivity of diagnosis making also profit of automation in imaging and scanning of large sample slides (Pollak, Hourri-Yafin and Salpeter, 2017). The field of portable microscopy imaging to diagnose Malaria remains open to new research studies that could effectively overcome technical limitations as these are in detail described in the following chapter.

1.2. Human immunodeficiency virus infection and antiretroviral therapy adjustment

Acquired immunodeficiency syndrome (AIDS) is a spectrum of conditions present in the progression of Human Immunodeficiency Virus (HIV) infection when interfering with the individual's immune system. HIV/AIDS is considered a pandemic (Kallings, 2008) claiming approximately 36.9 million people living worldwide with HIV in 2017 (UNAIDS, 2018) and a 70% of them being in middle-income countries (WHO, 2016). Though there has been a great decrease (43%) of HIV/AIDS related deaths since 2003 – the year when global treatment strategy was first set – in 2014, 17 million infected individuals were not aware of their HIV status, resulting in mistreatment or total absence of antiretroviral therapy (ART) (WHO, 2016).

ART initiation is strongly recommended when virus load exceeds a value of approximately 10^6 HIV RNA copies/ml. Following virus progression in interfering with the immune system, there is a radical decrease in the number of $CD4^+$ T cells (Figure 1) (Kallings, 2008) and an increasing susceptibility at opportunistic infections (Okoye and Picker, 2013). Initiation time of HAART ('highly active antiretroviral therapy') can be determined by the population of $CD4^+$ T cells, when this drops below the threshold of 500 cells/ μ l (WHO, 2015b). Both viral load and $CD4^+$ T lymphocytes count should be tested in regular intervals to determine the efficiency of received HAART and possible need for adjustment (O'Brien *et al.*, 1997; Usdin, Guillermin and Calmy, 2010; Therapy and Infection, 2013; WHO, 2015b). These regular blood test counts can prevent inadequate medication or overtreatment and consequently development of virus resistance to specific drugs (Kallings, 2008). Research studies have indicated the importance of timely adjustment of HAART to enhanced $CD4^+$ T cells recovery and immune system recovery rate, independently of the absolute viral load at the time of initiation (Le *et al.*, 2013; Therapy and Infection, 2013). Thus, frequent and accurate blood cell counts are a prerequisite for treatment optimization and prolongation of life expectancy of the patient.

The gold standard for $CD4^+$ T cells counting and HIV progression monitoring is flow cytometry (FC), mainly because of the accuracy of provided results, in terms of specificity and sensitivity (Wu and Zaman, 2012). The increased cost of a single test, the requirement for well-trained healthcare professionals and dedicated laboratory spaces, as well as the low throughput and the high cost of maintenance of the available bulk flow cytometers all affect HIV monitoring in low or middle income countries, where the above requirements cannot be met. Additionally, provided the high expenses for a single test and the necessity for frequent hospital visits, it can still be prohibitive for HIV infected patients in developed countries to seek their status monitoring at a regular basis. The need for point-of-care devices that could meet all criteria for efficiency and accuracy is obvious. Despite, large investments in this research field the last decades and the numerous proposed devices (B.L., 2002; Wu and Zaman, 2012), there is still plenty of room for new platforms for single cell identification and counting at the point of care, that could prove promising to provide optimized performance (Diagnostics, Reliability and Results, 2015).

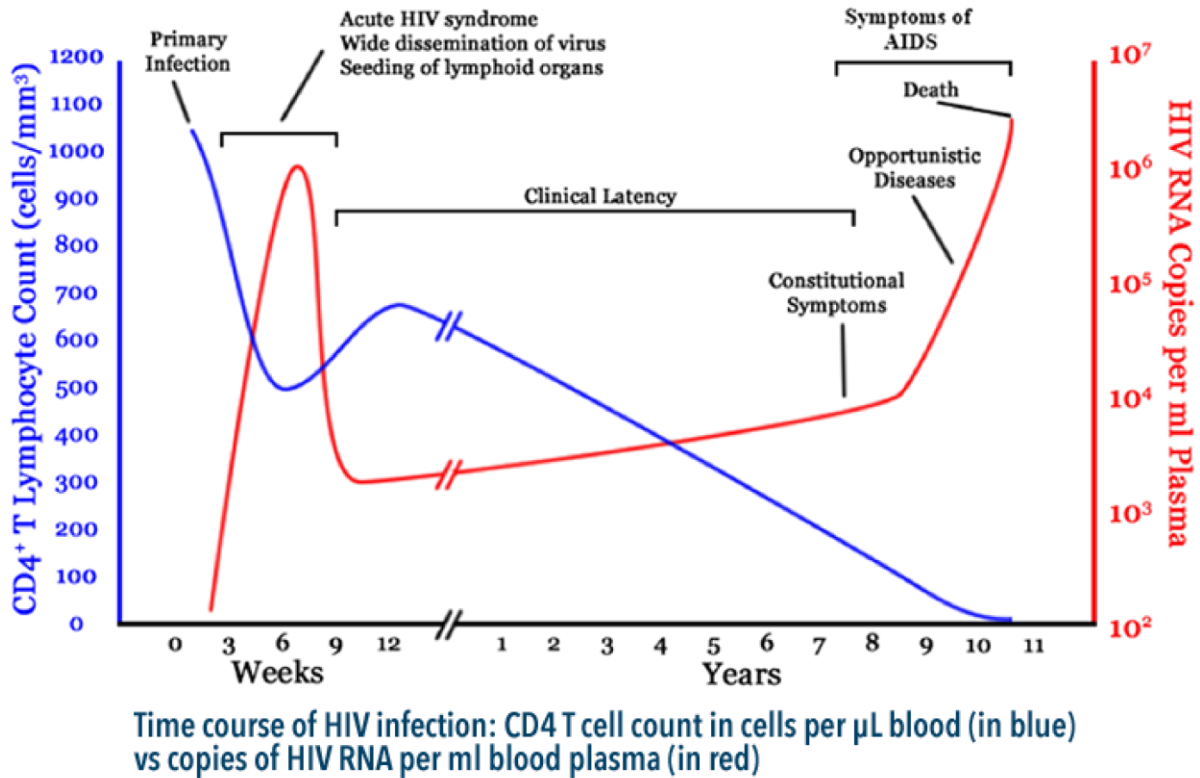


Figure 1.1. Typical course of HIV infection: the rapid drop of CD4⁺ T lymphocytes below 500 cells/ μ l indicates the initiation of the destruction of the lymphoid system, while below 200 cells/ μ l more severe symptoms usually appear.

1.3. Cancer treatment and white blood cell count

Cancer is a generic term referring to a wide range of diseases, all arising from the transformation of normal cells into abnormal tumors. Generally, the disease progresses from a pre-cancer lesion to a malignant tumor. In this multistage process the abnormal cells invade adjoining body parts and spread to other organs (Siegel, Miller and Ahmedin, 2017). Accounting for over 8 million deaths in 2015 cancer remains the second leading cause of death globally (WHO, 2018). Apart from some specific cancer diseases related to blood, it is well-known that patients undergoing chemotherapy often suffer from neutropenia and/or leukopenia, which are among the most frequent side effects for cancer treatment (Kim and Demetri, 1996; Crawford, Dale and Lyman, 2004; Iwamoto, 2013). Consequently, patients are suffering from fatigue and are susceptible to opportunistic infections, during cancer treatment period.

As white blood cells (WBCs) drop during chemotherapy, the patient should perform frequent blood count examinations to assure that absolute number of leukocytes is not below a threshold of 1000 cells/ μ l. While in the developing world, patients usually have access to the necessary medical laboratories and trained technicians, the high cost and time consuming process is always an obstacle to overcome. Additionally, frequent hospital visits may present a high risk of exposure of patients, with vulnerable immune system, to infections. In the case of low resources settings, patients may not even have access to white blood cell monitoring tools, due to the lack of facilities and personnel.

Only 26% of low-income countries reported having pathology services generally available in the public sector in 2017 and less than 30% reported treatment services availability (WHO, 2018). With opportunistic infections being among the causes of highest mortality rates during cancer treatment (Zaorsky *et al.*, 2016), the need to solve the aforementioned aspects of mistreatment is of vital importance. A patient-centered healthcare system providing portable, easy-to-use, accurate and rapidly responsive WBC monitoring tools seems to be the most promising solution.

1.4. Sickle cell disease diagnosis and monitoring

Sickle cell anemia is a hemoglobin disorder that affects the shape and stiffness of red blood cells (RBCs). Normal erythrocytes are discs-shaped and flexible enough to travel through the smallest blood vessels. In the case of sickle cell anemia, RBCs have an abnormal crescent shape resembling a sickle (Figure 2) (Wheless *et al.*, 1994; Frenette and Atweh, 2007). They become sticky and rigid, thus, prone to getting trapped in small vessels. Consequently, blood is blocked from reaching different parts of the body, which can cause pain and tissue damage.

According to WHO research publications, in 2008, hemoglobin disorders present a significant health problem for over 165 countries. Approximately 270 000 infants affected by the disease are born annually, while about 3.4% of deaths in early life – less than 5 years of age – are attributed to hemoglobin disorders (both sickle cell anemia and thalassemia) (Modell and Darlison, 2008). The geographical distribution of the disease has spread worldwide due to migration, being most prevalent in regions of Sub-Saharan Africa, the Americas, Saudi Arabia, India, and Mediterranean countries such as Turkey, Greece, Italy and South East Asia (Piel *et al.*, 2013; Society, 2016).

Proper sickle cell anemia management recommendations include early in life accurate diagnosis, ideally during the newborn period. Timely identification of affected infants by neonatal screening is critical to prevent early mortality due to infections or stroke and allows for proper treatment and prolongation of life expectancy up to the third decade (Powars *et al.*, 2005). However, this early diagnosis as well as continuous monitoring of the disease still remains a challenge for resource-limited settings and developing regions of the world, requiring well-trained technicians and complex instrumentation such as microscopes, to accomplish tests of the conventional approaches (Alapan *et al.*, 2016). Portable platform technologies for blood film imaging promise to provide a critical part of the diagnostic tools for sickle cell diseases' early detection and continuous screening. Technical challenges to be met in the field of point-of-care microscopy imaging inevitably open the field to new approaches to be proposed (Alapan *et al.*, 2016).

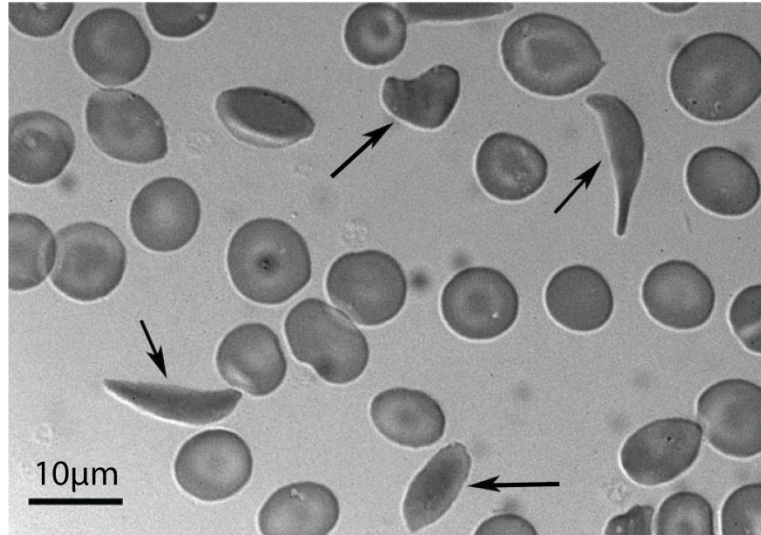


Figure 1.2. Sickle erythrocytes. Peripheral blood smear from a patient with Sickle Cell Anemia obtained during a routine clinical visit. The smear shows classical sickle-shaped and various other misshaped erythrocytes (Frenette and Atweh, 2007).

1.5. Other diseases and blood disorders – the necessity for blood counts at regular basis

Blood cells screening and counting is related to a wide range of diseases in the sense that it can safely lead or be part of the diagnostic process and in many cases it is an integral part of the disease progress monitoring after detection. Various infections and inflammatory diseases can be diagnosed by the WBC count in a periodic health care examination independently of the presence of symptoms. WBCs should also be tested in a regular basis for myeloid neoplasms and leukemia (Cheson *et al.*, 2003; Hallek *et al.*, 2008; Vardiman *et al.*, 2009), related to lymphocytosis. Additionally, WBC population monitoring is reported to be a potent factor indicating possible future coronary heart disease, with regular counting medical tests proving to be a significant part of risk management and mortality prevention (Grimm, Neaton and Ludwig, 1985).

Following the correlation of blood cell counts with the aforementioned acute or chronic health conditions, identification and counting of cells of the peripheral blood of human body is not only advised in cases of detected illness, but it is highly recommended as part of the periodic health examinations in adults (Virgini *et al.*, 2015) and preventive medical examinations in neonates (Manroe *et al.*, 1979). Depiction of general health status, prognosis of severe health risks and prevention of mortality are the main reasons for peripheral blood count tests performed at a regular basis.

In the following table a sort summary of the requirements of an ideal optical cell detection system is presented for each of the diseases or blood conditions described above. The required resolution is estimated to be less than one half of the target cells size. The imaging technique and cell sorting method is extracted based on well-established techniques for each particular case.

| Disease or blood related condition | Target cell population | Optical resolution required | Minimum amount of blood to be observed | Ideal detection range | Gold standard technique |
|-------------------------------------------------------|--------------------------------|-----------------------------|----------------------------------------|-------------------------------------------------------------------------------------------------|--------------------------------------------------------|
| Virus prolongation in HIV infected individuals | CD4 ⁺ T lymphocytes | <3 μm | 2-3 μl | 0 – 500 cells/μl for HIV infected individuals 500 – 1500 cells/μl for HIV-negative adults | Flow cytometry |
| Malaria | Whole blood samples | <3 μm | 2-4 μl | Detection limit: 1 Parasite/μl of blood (Gascoyne, Satayavivad and Ruchirawat, 2004) | Microscopic observation of Giemsa stained blood smears |
| Cancer related white blood cells drop | White blood cells | <3 μm | 2-3 μl | 0 – 10000 cells/μl | Flow cytometry |
| Sickle cell anemia | Red blood cells | <2 μm | 5 μl | Within the range of red blood cells: 4-5.5 million cells/μl | Microscopic observation of whole blood samples |
| General health status monitoring | Whole blood samples | <1 μm | 2-3 μl | WBCs: 3400 -9600 cells/μl RBCs: 4-5.5 million cells/μl Platelets:135000 – 371000 cells/μl | Flow cytometry |

Table 1.1. Disease related requirements of an ideal optical system

2. The need for cell identification and counting at the point of care

Point-of-care testing is a term used to distinguish diagnostic or health screening medical examinations performed near or at the location of patient from traditional practice of medical tests accomplished in central laboratories or health care facilities (Willmott, 2010). In the past, the establishment and use of central laboratories was the only option for medical care to be available, due to the complexity and volume of medical equipment, the necessity for a laboratory environment for clinicians to perform tests and the relevant need for power supply. Compared with conventional

laboratory examinations, point-of-care testing is able to radically improve throughput – defined as the number of tests accomplished in the time unit – thus, expedite diagnosis and medical decision making (Larsson, Greig-Pylypczuk and Huisman, 2015). Though the advent of technological advances is frequently considered as the main cause for an alteration of healthcare system towards point-of-care diagnosis and treatment, it was indeed the necessary step that urged many countries to adapt a more patient-centered healthcare that is up to now proven to be highly advantageous for both patients and clinical care institution.

Particularly in the case of low-resources settings, point of care testing and treatment was the only feasible solution against augmented percentage of inaccessibility to conventional medical facilities. The increased cost and demands of healthcare professionals, power supply, clean laboratory environment of the traditional diagnostic instrumentation presented an imperceptible barrier towards accessibility of all populations in medical care, with the economic burden cumbering both poorer population groups and national medical institutions. Point-of-care devices are portable, low-cost, usually battery-operated medical tools that can be handled easily by non-trained people or even patients themselves (Haney *et al.*, 2017). Though still applied at a limited extend, point-of-care devices allow for immediate diagnosis and continuous monitoring of diseases of high risk for people in low or middle income settings (S. Satyanarayana, K. Sagili, S. S. Chadha, 2014) and have been proven, in specific cases of diseases, to contribute to the reduction of mortality rates (Rossi and Khan, 2004).

In the case of the developed world, despite the available resources of medical institutions in order to provide dedicated medical equipment and expert personnel, there is still a large part of the society that cannot afford the expenses of specific medical examinations (The World Bank, 2017). Point-of-care medical tools could provide a solution to this economic suffering. Additionally, the transmission of health care away from hospital facilities and bringing it to patients' bedside is of vital importance for many cases. Frequent hospital visits for routine medical tests, may present a high risk of opportunistic infections for patients with severe illness or vulnerable immunity system. Fatigue, weakness of the elderly and inability to be physically present in large medical centers are among the main worries of a patient-centered health care structure, to which the implementation of a point-of-care testing program can provide the ideal solution.

In this context, blood cell point-of-care counters are particularly important in primary health care and for continuous health status monitoring when necessary (Giuliano and Grant, 2002). With the blood analysis tests comprising almost 43 % of the data used for clinical decision making, the use of portable automatic blood cell counters could be beneficial for both patients and medical institutions (Giuliano and Grant, 2002). Especially, optical, imaging, point-of-care medical tools present a highly advantageous technique for blood cell identification and counting. They can provide real-time and high-resolution microscopic or macroscopic information of blood specimen, by making profit of the latest advances in micro-optics and micro-electromechanical systems. Furthermore, their combination with microfluidics and computer vision can lead to specific or general purpose platforms towards accurate and immediate automatic diagnosis. Last but not least, miniaturization and cost reduction seem to be almost limitless for the years to come, as a result of the rapid growth

of consumer electronics market and more specifically of the ubiquity of high resolution phone cameras (Zhu, Isikman, *et al.*, 2013).

In contrast to their numerous advantages and despite the great research interest that the field has attracted leading to many promising approaches, the application of them in both restricted resources setting and high-income countries remains limited. Research studies conducted up to now have not yet succeeded in providing high accuracy together with meeting the general and technical requirements as these are defined clearly by the WHO and are presented in the following. The need for new approaches for improvement and optimization of the provided performance of portable blood cell counters inevitably emerges.

3. Requirements for the accurate and efficient blood count monitoring at the point of care.

3.1. General requirements for point-of-care testing

The generic requirements to fulfill, concerning a point-of-care device, are described, by the WHO, with the term ‘ASSURED’ (Kosack, Page and Klatser, 2017). According to this set of criteria, a point-of-care device should be Affordable, Sensitive, Specific, User-friendly, Rapid and Robust, Equipment-free and Deliverable to end-users - ASSURED. All these criteria, regarded as equivalently necessary, impose specific requirements for the development of a novel point-of-care device: (a) Affordability indicates decreased cost for both the production of the device and the cost of a single test to perform, which is crucial for frequently repeated medical examinations. (b) Sensitivity refers to high resolving power provided by the device while (c) Specificity clearly imposes the requirement for accuracy of the provided result so that decision-making can be accomplished in a deterministic manner. (d) User-friendliness illustrates the necessary ease of use, so that the end-users could be non-trained persons, ideally the patients themselves, and no expert healthcare professionals or technicians are needed. (e) Rapidness and robustness refer to the high throughput of the device and the repeatability of the performed medical tests, respectively. (f) The demand for absence of equipment refers to the need to operate in non-laboratory environments, without any requirement for external power supply or other facilities. (g) Deliverability clearly defines the requirement for portability and compactness of the proposed medical tool. Some examples for the target specifications referring to each criterion separately are presented in the table 1, where HIV diagnostic tests are used as an application example (Wu and Zaman, 2012).

| CRITERION | EXAMPLES OF TARGET SPECIFICATIONS |
|-------------------------------|---------------------------------------------------------------------------------------------------------------------------------|
| AFFORDABLE | Less than US\$ 500 per machine, less than US\$ 10 per test |
| SENSITIVE and SPECIFIC | Lower limit of detection: 500 HIV RNA copies per mL, 350 CD4 ⁺ T-cells per μ L |
| USER-FRIENDLY | 1–2 days of training, easy to use |
| RAPID and ROBUST | < 30 minutes for diagnosis, < 1.5 hours for HIV load monitoring, minimal consumables (i.e. pipettes), shelf life >1year at room |

| | |
|-----------------------|-------------------------------------------------------------------------------------------------------------------------------------|
| EQUIPMENT-FREE | temperature, high throughput Compact, battery powered, on-site data analysis, easy disposal, easy sample handling, no cold chain |
| DELIVERABLE | Portable, hand-held |

Table 1.2. Examples for the target specifications of the ‘ASSURED’ criteria described by WHO (Wu and Zaman, 2012).

3.2. Technical requirements and challenges for blood cell imaging devices at the point of care.

Particularly for blood cell imaging and counting devices, in addition to generic requirements as these were described previously, there are always great challenges to overcome. Combination of high resolution imaging with wide field of view (FOV) is crucial for the diagnostic process, as the accuracy of the extracted result is proportional to the amount of blood tested. Such a requirement is particularly difficult to fulfill in the case of imaging platforms at the point-of-care where the amount of blood used should be restricted at a volume of a few μl . This has been the intension of many research studies, where sophisticated scanning systems were employed resulting inevitably in increased cost of manufacturing and bulk complex devices. In order to compensate complexity and high cost with the provided resolving power, in several approaches dilution of blood was employed as a means to provide rather sparse samples and reach higher resolution. However, accuracy has been consequently affected by the total number of blood cells examined in low volume, diluted blood samples.

Blood composition and density of cells in unprocessed, undiluted blood samples can easily affect sensitivity and specificity in cell imaging. The increased number of RBCs – 2-4 million cells/ μl – prevents efficient capturing or sorting of specific WBC populations in microfluidic devices and decreases contrast in the imaging process. With the demand for minimized use of reagents and the elimination of blood preprocessing procedure, there is a great challenge for microfluidic technology to produce a platform device, suitable for a wide range of diseases that can provide accurate cell capturing from whole blood samples.

In the case of reflection mode fluorescent imaging systems, the compactness and miniaturization is frequently affected by the need to integrate off-axis optical components and illumination sources. In general, the trend towards complexity gives space to simplicity (Boppart and Richards-Kortum, 2014) because of the wide range of factors to control and errors induced, affecting additionally, cost of production, preservation needs, operation requirements and ease of use. Though still controversial if the point-of-care devices need to be of equal accuracy as the gold standard laboratory medical examination, the great challenge to fulfill is the production of a highly sensitive and specific optical device that is based on a simple, clever, well established technology, to render it available unconditionally to all.

4. Aim – scope of this study

The ultimate purpose of the present thesis is to describe the design and development of a portable optical micro-scanning device for imaging at the point of care. This micro-scanning system comprises of a micro-positioning stage that is able to perform one direction scanning combined with a micro-fabricated, Si-based, mini-lens array of a special design. The combination of these key elements can provide a 2D image of a blood sample with high resolution – less than 1 μm – over a large FOV area – approximately 2 cm^2 . Manufacturing process of the mini-lens array is based on well-established microfabrication techniques to assure optimal quality of the array, in terms of uniformity, resolution and contrast. The device is validated by imaging typical unstained smear blood films on standard glass microscope slides and a microfluidic chip with functionalized walls containing surface immobilized white blood cells. The feasibility of automatic cell detection in both cases and the automation of the scanning/imaging procedures prove the possibility of the device to operate in full portability at the point of care, as a diagnostic and blood cell monitoring tool for a broad range of diseases and blood related disorders.

The proposed device operates in transmission mode illumination scheme; however, the integration of reflection illumination in portable optical microscopes has proven to be of crucial importance to achieve imaging techniques that can be accomplished only with this illuminating structure such as Backscattering Darkfield (BSDK), epi-fluorescence (EF), Interferometer Reflection Contrast (IRC) and Darkfield Reflected Surface (DRC). The challenge that inevitably emerges is the integration of off-axis components in highly compact microscopy devices without increasing the cost of fabrication or the complexity of the optical system. To meet this challenge, in the present study, a novel design integrating a ring-shaped LED array on the mini-lens array of the imaging platform is proposed and developed. This hybrid lens/LED array chip is a successful solution for reflection based imaging for all compact portable microscopy devices, combining the excitation source and the collection elements on the same silicon chip. Main advantages of this design are (a) the separation of the excitation and reflection beams – they do not share the same optical components as in conventional epi-illumination scheme of bulk microscopes – and (b) the radical reduction of the total optical path length down to less than 2.5 mm. Validated by bright field reflection imaging of a resolution chart, this lens/LED array achieves 8.8 μm maximum resolution and sufficient uniformity of illumination of the imaged sample.

In the context of the development of a portable compact imaging device for single cell detection, a microfluidic chip has been developed for passive capturing of a specific population of WBCs. The two chamber glass microfluidic chip that can be filled with a total blood volume of 3 μl contains specially functionalized surfaces to perform capturing of WBCs. To fabricate a highly sensitive and specific microfluidic chip for cell capturing and imaging, in this work, an extended study is conducted on the factors that affect the efficiency of cell immobilization with respect to the geometrical characteristics of the chip, the lyophilization protocol employed and the washing flow rate for non-captured cells removal. The dual chamber design can provide with the optimized blood incubation protocol, the optimum concentration of antibodies solution used in functionalization process and the decreased chamber height assures minimized error in capturing efficiency while it can be used for differential capturing of WBC populations, provided the two chambers are

accordingly functionalized with different anti-bodies. The designed chip, validated with CD45, CD3 and CD8 antibodies is intended for use with the developed imaging scanning platform with total capturing/imaging surface that matches the total FOV of the aforementioned device.

5. Thesis overview

The detailed presentation of this research work is based on an extended study of the advances in the fields of single cell optical imaging miniaturized systems and microfluidic cell fractionation techniques, critically reviewed at the starting chapter of the thesis. In accordance with the presented challenges in the field of trans-illumination imaging devices, a complete design of the proposed imaging/scanning platform is presented in chapter 2. In this chapter, the theoretically studied optical system is confirmed by extended characterization process of the optical performance, combined with scanning characterization experiments conducted. The device is validated with specific blood cell population tests and automatic detection of single cells. In the chapter to follow, the design of a hybrid lens/LED array chip is analyzed on a theoretical and experimental basis. The proof of concept for this novel design, intended for use in epi-illumination portable microscopy platforms of biological specimen imaging, is provided by illuminating, thermal and imaging performance analysis. The last part of this work concerns the design and development a dual chamber microfluidic chip. The optimization of the capturing efficiency is analyzed by indicating the factors severely affecting the surface immobilization of cells on chambers' walls. This novel differential cell population fractionation device is validated by WBCs, CD3 and CD8 lymphocytes specific capturing. The entire study is concluded by an extended discussion on optimization steps and future perspectives and a detailed explanation of the field of applications, at which this research approach can be useful.

Chapter 2

Single cell optical imaging and microfluidic cell fractionation technologies – A critical review of the state-of-the art.

The implementation of cell identification and optical imaging techniques for miniaturized systems is a rather new field of research, triggered a few decades ago, in the sense that new approaches had to be employed compared to laboratory observation and inspection of cell samples. The development of platforms, aiming mainly at miniaturized trans- and epi-illumination imaging schemes, mimicking the conventional bulk laboratory microscopes, are always a field open in research, as only a few devices have managed to fulfill the requirements imposed by the WHO for effective point-of-care testing. On the other hand, passive cell fractionation techniques present the great challenges of high specificity and sensitivity with elimination of sample preprocessing steps. The advances in these two different research fields have to be extendedly and in parallel studied to provide new clever approaches towards a patient-centered, general purpose, blood cell monitoring device of increased efficiency.

1. Portable bright field microscopy imaging platforms

Bright field microscopy remains the gold standard for the identification and counting of single cells. Observation of cells under a conventional bright field microscope with high resolving power can provide information on the cells' size, their shape as well as their intracellular structure with nucleus imaging. Cells identification and the feasibility to distinguish a specific cell type from other cell populations, present in the same sample, can be accomplished either based on the inspected characteristics (size, shape, nucleus morphology) or by employing a specific staining, added in preprocessing step of the sample. Both identification and counting were, initially, steps of the observation process, accomplished by the researcher or healthcare professional, manually. The emerging need to develop portable, compact and automated devices for cells fractionation and counting, therefore deterministic and accurate diagnosis and clinical decision making, triggered a global endeavor towards the development of miniaturized bright field microscopy imaging systems for the automated screening of single cells.

In this direction, numerous approaches focused on the integration of conventional bulk microscopy to a compact and miniaturized inverted-light setup in order to reduce the total volume ($7.5 \times 13 \times 18$ cm) and weight (less than 1 kg) of the device (Breslauer et al., 2009; Miller et al., 2010; Baek et al., 2014; Skandarajah et al., 2014). Though the achieved spatial resolution ($0.8 \mu\text{m}$) promises efficient performance for blood cell imaging, the restricted field of view (FOV) is prohibitive for observing sufficient volume of blood samples, so as to allow for accurate diagnostic results. To easily address this FOV limitation, full frame camera sensors may be employed (Ozcan and Demirci, 2007; Moon and Keles, 2009; McCall et al., 2011), resulting, however, in lower resolution – camera pixel limited; with pixel size of full-frame sensors being approximately $10 \mu\text{m}$ – and inevitably increased cost of production. This challenge in optical imaging: combining large FOV observation with increased resolving power, led with the years in novel imaging techniques as described in the following.

1.1. Cell-phone based applications for improved mobile optical imaging

The advent of mobile phones, the pioneer advances in computational power of mobile microprocessors and the radical decrease of the cellphone costs followed by their ubiquitous intrusion in everyday life were key elements for a wide and rapidly spreading effort to make use of these tools for portable microscopy systems. Cellphone based bio-imaging devices usually employ a miniaturized sample holder setup placed at close proximity to the phone camera (Breslauer et al., 2009; Navruz et al., 2013; Baek et al., 2014; Lee and Yang, 2014; Skandarajah et al., 2014; Orth et al., 2018). To increase resolving power of the imaging system, an optical setup of bulk optics is utilized (Breslauer et al., 2009; Baek et al., 2014; Skandarajah et al., 2014; Orth et al., 2018). The optical part comprises of an objective lens and/or an eyepiece to achieve high magnification and push resolution to submicron level. In most cases it also includes an illumination part referring to the optical components for uniform and coherent illumination of the sample (Figure 1). With the entire optical scheme resembling to that of a conventional microscope, the aforementioned setups present efficient imaging techniques, providing promising resolution for blood cell samples observation – though still of a restricted FOV. However, they remain rather experimental setups, whose entire structure is bulk or difficult to use and to preserve under non-laboratory conditions; the presence of dust and mechanical stress of everyday usage is believed to affect their optical performance.

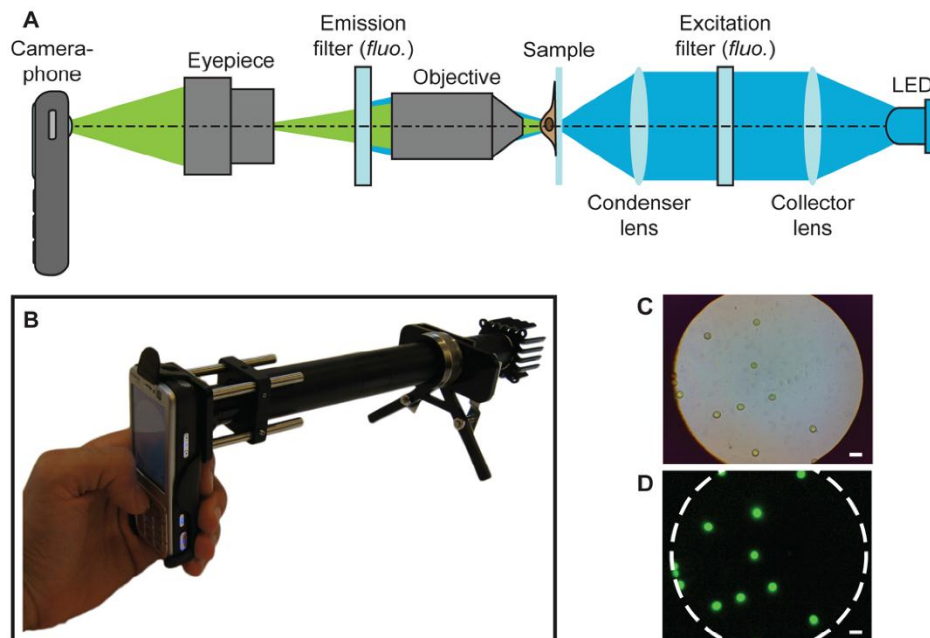


Figure 2.1. (A) Schematic of the optical setup for illumination and imaging in transmission mode, mobile phone-based bio-imaging system. (B) Figure of the provided portable microscopy imaging device. (C) and (D) Figures of the samples in bright field and transmission fluorescent modalities (Breslauer et al., 2009).

To overcome difficulties from the use of bulk optics and leveraging the technological advances in the field of mobile microprocessors, several groups focused on the use of image processing techniques to increase the achieved resolution, in some cases combined with sophisticated opto-mechanical parts and the acquisition of multiple images of the same sample (Navruz et al., 2013; Lee

and Yang, 2014). In this context, super-resolution image reconstruction from multiple low-resolution images has been proposed by Yang group. In this technique, the samples are placed in contact with the phone camera and shadow images of pixel-limited resolution are obtained by sub-pixel angular movement of the illumination source. The reconstruction of the final image, claiming to provide less than 1 μm resolving power, is based on the additional combination of multiple images (Lee et al., 2014). A similar image processing method is equivalently used with manual tilt of the phone camera when ambient light is used for illumination. Robustness of the system is subjected to mechanical damage, in the case of high precision movement requirement, while, in the much simpler case of manual movement of the cellphone, the error induced by tilt calculation can highly affect final image quality.

The implementation of a fiber-optic array manually rotated with discrete angular increments of 1-2 degrees was used with a cell phone camera based setup by Navruz et al. (Navruz et al., 2013). Again, a reconstruction algorithm profits from augmented computational power of mobile processors. However, it is clearly depicted that the increased number of transmission images/frames used for shift-and-add based reconstructions that is required to achieve a higher-resolution, will act at the cost of increased computation time.

1.2. Lens-free imaging techniques for high resolution and large field of view optical imaging

The restriction of the FOV to the effective sensing area of the CMOS or CCD sensor employed and the effort to prevent further diminishment of the observation area induced by large magnification optical components, led to the rapidly accelerated research field of lens-free imaging. In a few approaches, the total absence of lenses was not replaced by any specific image processing algorithm to improve image quality (Ozcan and Demirci, 2007; Moon and Keles, 2009). The system's optical performance is restricted by sensor pixel size (9 μm), while the detected cells are imaged larger by their shadow projection on the active area of the detector. In this approach, the research team claimed to detect features smaller than the pixel size when the sample is located at longer distances from the detector, however, it remains questionable if this approach can accurately identify cells – of 8-10 μm size – and distinguish them from blood residues and cells clusters within the observed microfluidic chamber.

In most cases of lens-less microscopic observation a series of images of the same sample are acquired and processed to improve quality of monitoring in terms of resolution and contrast. Two dominant imaging techniques are used for this implementation, Optofluidic Microscope Implementation method (OFM) (Heng et al., 2007; G. Zheng et al., 2011; Guoan Zheng et al., 2011) and Holographic Microscopy (Isikman et al., 2010, 2011; Su et al., 2010; Bishara et al., 2011; Mudanyali, Bishara and Ozcan, 2011; Sanz et al., 2017). The optofluidic microscopy is regarded as a contact-mode shadow imaging technique, that is based on diffraction elimination due to the minimum selected distance between the observed features and the imaging sensor (Greenbaum et al., 2012). To mitigate low spatial resolution – limited by the camera pixel size – a time sequence of images is acquired, in which motion of the specimen within a microfluidic chamber is performed (Heng et al., 2007; Guoan Zheng et al., 2011). Algorithmic synthesis is claimed to result in sub-pixel

resolution. In the technique of in-line holography, implemented approaches are based on computational correction of artifacts produced by diffraction that occurs between the observed features and the detector surface. In this case, the scattered light from each object interferes with itself and an interference pattern is extracted, allowing for final image reconstruction after processing (Greenbaum et al., 2012). Recently, Im et al. designed and developed a point-of-care device for aggressive lymphoma diagnosis based on micro-holographic imaging principle (Im et al., 2018).

Lens-free imaging has the potential of inexpensive high quality imaging, achieving in many cases sub-micron resolution. It is affected however by three major defects, the restriction of the FOV to the sensor's active area borders, the computational requirements in both time and power and the decreased image quality in case of dense samples. Increased computational time demand precludes the integration of such techniques in scanning systems to allow for extended sample imaging, or equivalently the use of full frame detectors with this imaging technique affected by both time and computational power needs. Additionally, it is rather doubtful whether connected or overlapping features, as cells in whole blood samples, could be distinguishable through this type of microscopy observation due to overlapping shadows projected on the sensor surface.

1.3. Integration of scanning systems to achieve extended biological sample imaging at the point of care.

Aiming at extended observation area of the sample, many of the evolved systems include scanning components (Weinstein et al., 2004; Huang et al., 2013; Walzik et al., 2014), to compensate large pixel size and increased cost of medium or large format detectors. In such systems, the critically important factors that hinder implementation are defocusing or decrease in image quality due to movement induced errors and time or computational power needs for the construction of the entire image, frequently referred to as the 'virtual slide' (Ghaznavi et al., 2013). To compensate possible defocusing during scanning, many approaches resulted in employing sophisticated 3-direction scanning components, increasing the cost of manufacturing and processing time for optimal image plane adjustment in each scanning step (Weinstein et al., 2004; Huang et al., 2013). Additionally to the use of bulk optical elements (Huang et al., 2013), such approaches increase the volume and weight of the final setup, controverting their compliance with compactness and portability criteria, thus, rendering them suitable for educational or research applications (Walzik et al., 2014), rather than diagnosis and clinical decision making in primary healthcare. However, the field remains promising for future approaches (Weinstein et al., 2009). The advances in image mosaicking computational algorithms, the advent of 3D printing technology and the remarkable achievements in microfabrication processes can all contribute to the deployment of highly accurate, compact and cost-effective scanning imaging platforms.

1.4. Integration of micro-lens array technology as a means of miniaturization and high quality imaging.

Micro-optics are optical elements that are between a few micrometers and a millimeter in size, including small lenses and lens arrays and are proven to be of critical importance in the field of

integrated optics and imaging platforms. The technological progress in the field of micro-optics, believed to be initiated by the observation of natural compound eyes in insects, has enabled the evolution of highly precise and uniform micro-lens arrays (Eisner and Weible, 2003). Micro-lens arrays, when accurately aligned with subsequent optics and optoelectronic structures can give very thin, simple and monolithic imaging platforms, ideal for miniaturized microscopy imaging medical devices (Duparre and Reinhard, 2007).

With the bloom of microfabrication processes (Gale and Knop, 1983; Popovic, Sprague and Neville Connell, 1988; Wu, Whitesides and Quality, 1997; Tripathi and Chronis, 2011) and soft lithography techniques (Chronis et al., 2003) and the recent progress of three-dimensional printing in the micron-sized optical elements (Thiele et al., 2016, 2017; Vaidya and Solgaard, 2018), the production of adequately uniform micro-lens arrays with nanoscale surface roughness and excellent imaging performance are already available. However, only a few approaches in the field of microscopy imaging systems have already attempted micro-lens arrays integration to improve compactness and image quality (Weinstein et al., 2004; Barretto, Messerschmidt and Schnitzer, 2009; Orth and Crozier, 2012; Varjo, Hannuksela and Silven, 2012). Particularly for imaging extended surface samples, Weinstein et al. integrated a multi-level micro-lens array-based optical setup to enhance resolution. The system includes a three dimensional scanning to cover large surface areas and correct defocusing artifacts attributed to imperfections in lens arrays uniformity (Weinstein et al., 2004). Thus, increased complexity of the final device, as well as the large volume and high cost remain important tradeoffs of this approach rendering it unsuitable for use at the point of care.

The field of micro-lens array imaging for biological sample screening at the micro-scale requires further investigation. Main drawbacks to circumvent are the existence of blind regions between the lenses in the array and the difficulty to align all lenses in the array to focus on the same plane. It is a challenge to profit from the compactness of such optical elements without at the same time increasing the complexity of the imaging setup.

2. Reflection mode optical imaging – integration of off-axis illumination scheme

Reflection mode optical imaging refers to a wide class of illumination schemes that present a common feature: the separation in the direction of the excitation and reflection/emission beams. In transmission mode imaging, the illumination source, the imaged sample and the detector are placed in collinear positions with their axis concurring with the optical axis of lenses and optical elements placed between them. In contrast to trans-illumination, reflection mode or epi-illumination refers to all schemes where the illuminating source and the imaging camera are placed on the same side with respect to the sample. The main reasons leading to the implementation of a certain type of reflection based imaging are found among the restrictions or purposes of the application itself. Thus, epi-illumination is imperative when the sample is not optically accessible by both sides, either due to its own characteristics – optically dense or thick tissue – or due to the setup employed – opaque microfluidic chips, lab-on-a-chip on Silicon, non-transparent sample holders etc. However, epi-illumination is also preferred than transmission scheme in a wide range of imaging techniques – Backscattering Darkfield (BSDK), epi-fluorescence (EF), Interferometer Reflection Contrast (IRC), Darkfield Reflected Surface (DRC). All these sophisticated, reflection based imaging techniques are

widely used in biological sample microscopy applications satisfying the needs for isolation and identification of specific structures in the sample – cell/protein/bacteria labelling – and meeting the requirements for enhanced specificity and sensitivity due to higher signal to background noise ratio images, that they can provide. Particularly concerning the most known and applied scheme of fluorescence, though recent advances in filter technology may promise equally high quality in trans-illumination images, epi-illumination still dominates this field of microscopy (Tran and Chang, 2001), rendering reflection mode scheme an irreplaceable part of all microscopy platforms. Recent technological achievements in microelectromechanical systems (MEMS), accompanied by the increasing need to develop highly specific and sensitive microscopy tools for biological specimen observation at the point of care, have given the motivation to numerous research groups to propose various approaches towards this direction that include both transmission and reflection mode imaging systems (Lee, Yaglidere and Ozcan, 2011; Zhu *et al.*, 2011, 2012; Schaefer, Boehm and Chau, 2012; Zhu, Sencan, *et al.*, 2013). Common aspect of the conducted research and the developed modules is the decreased size scale and short optical path that present the main challenge of the integration of epi-illumination scheme. As the distances between lens components, signal detectors and the biological sample shorten, it becomes harder to include off-optical axis components for the epi-mode illumination, such as laser or LED-based light sources and condensers or collimators, needed in most cases.

2.1. Miniaturized reflection mode imaging systems based on standard optical microscopy configuration.

The first approaches for portable, low-cost and compact epi-illumination optical systems are inspired by the dominant configuration in standard bulk optical laboratory microscopes. In this scheme a dichroic mirror is always employed to separate the excitation from the emitted light. Among these approaches, Schaefer *et al.* as well as Lee *et al.* proposed a dual mode compact imaging setup, capable of both trans-illumination and epi-illumination imaging that chose a Light Emitting Diode (LED) source as the excitation source of reflection imaging scheme, placed perpendicular to the optical axis (Ghosh *et al.*, 2011; Schaefer, Boehm and Chau, 2012). Following a similar idea, other groups developed portable miniaturized reflection based systems that make use of mercury arc lamps (Flusberg *et al.*, 2008) or laser diodes as excitation sources (Jiang *et al.*, 2000; Elson *et al.*, 2002; Engelbrecht, Voigt and Helmchen, 2010). Concerning the use of laser diodes, one of the crucial problems to overcome is the photobleaching effect, especially in cases where beam expanders are used to perform wide field of view imaging. Unless implementing additional beam expanders and collimators, this configuration is subjected to limited field of view - a disc of approximately 50 μm radius (Schaefer, Boehm and Chau, 2012). The use of additional optical elements – condensers, collimators, beam expanders and microscope objectives – increasing consequently the complexity, cost and volume of the entire system, is a strong demand in these applications. Indeed, more sophisticated setups have been developed by several research groups (Engelbrecht, Voigt and Helmchen, 2010; Ishmukhametov *et al.*, 2016) aiming at higher resolution and signal-to-noise ratio imaging, suffering, however, from complexity and increased production and maintenance expenses

that render it suitable for use as part of the laboratory equipment rather than as individually operating devices.

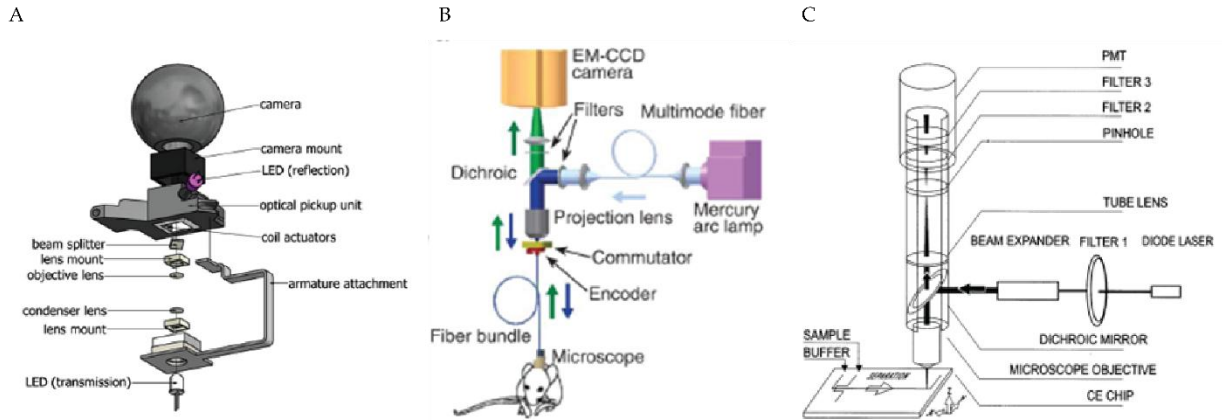


Figure 2.2. Miniaturized setups for reflection mode imaging based on the standard scheme employed in bulk laboratory optical microscopes where LED (A) (Schaefer, Boehm and Chau, 2012), a mercury arc lamp (B) (Flusberg et al., 2008), or a laser diode (C) (Jiang et al., 2000) is used as the excitation source. Common feature of these epi-illumination schemes is the main structure that makes use of a dichroic mirror as a splitter of the excitation and emission beams.

2.2. Cell phone based approaches for epi-illumination optical imaging

Often reviewed as a separate category of miniature epi-illumination microscopy devices, smartphone based applications benefit from the low cost and ubiquitous presence of cell phones in everyday life, as well as of the advances in integrated microprocessors for the development of point-of-care devices. Transmission mode imaging, previously reported, even in the simplest setup of ambient light and lens-free imaging, requires minimum hardware addition to the cell phone. On the other hand, reflection mode imaging, in any way of implementation, is eventually based on the demand for a compact hardware setup permanently attached or attachable/detachable at any time on the smartphone for the integration of off-axis optical elements. Thus, Maamari et al. developed a rather simple setup, that relies on the general idea of beam splitting of conventional epi-illumination microscopes to produce an Ocular CellScope (Maamari et al., 2014). Numerous approaches by the group of Aydogan Ozcan, referring to a cell phone, make use of an LED based Total Internal Reflection (TIR) that produces an evanescent field of illumination to perform epi-fluorescent imaging (Zhu *et al.*, 2011, 2012; Zhu, Sencan, *et al.*, 2013).

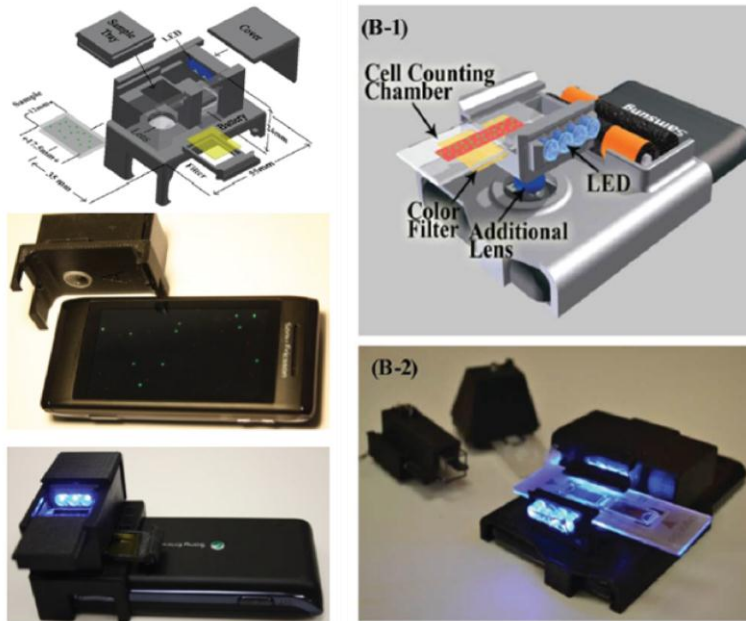


Figure 2.3. Housing of optical elements for evanescent field based epi-illumination setups attachable to smartphones developed by the group of Aydogan Ozcan (Zhu *et al.*, 2011; Zhu, Sencan, *et al.*, 2013).

Though profiting from the undoubted advantages of cell-phones, these approaches lack of the capability of wide field of view specimen investigation, unless combined with a scanning setup. Most of them are restricted to the use of fluorescence, excluding bright field illumination schemes; therefore sample processing with corresponding agents is a prerequisite. Inevitably, these systems have not been adapted to the point-of-care testing, where laboratory facilities and trained personnel are not available.

2.3.Total Internal Reflection – an alternative off-axis illumination scheme in miniature imaging systems

A widely used illumination scheme integrating a light source –LED or laser diode – placed vertically to the imaging axis, is the evanescent field created by total internal reflection (TIR). TIR occurs when light rays striking an interface between two materials under an angle wider than a critical value, travelling from the optically dense material to the one with lower optical density – therefore, with lower index of refraction. The internally reflected light beams create an evanescent field on the borders of the two materials that is capable of penetrating within the second material. This evanescent field is able to illuminate a sample seated on the interface between the two materials.

Evanescent field excitation, achieved through TIR scheme, is the most promising way to perform fluorescent sample observation with minimal background noise and reduced optical path (Lochhead *et al.*, 2010; Zhu *et al.*, 2011, 2012; Zhu, Sencan, *et al.*, 2013; Guo *et al.*, 2018). This method can be combined with all types of optical systems – lens-less to micro-lens arrays – and promises to maximize the resolution beyond the diffraction threshold due to the use of fluorescence, to minimize background noise due to the short depth of penetration of the evanescent field and to be accomplished with a compact setup with minimum requirements; a single LED source in contact

with the vertical face of the sample holder – typical microscopy glass slide – is sufficient (Zhu et al., 2012). However, this type of alternative epi-mode illumination is limited to applications of rather sparse or film like biological samples while optically dense tissue and opaque substrate chips are eventually excluded. It cannot be used with opaque plastic sample holders, while it is strictly applied in cases that fluorescent staining is used, thus bright or dark field applications cannot be included.

2.4. Micro-lens arrays as part of reflection mode imaging setup in compact systems

The possibilities of micro-lens fabrication have eventually motivated the evolvement of reflection mode imaging setups based of complex micro-lenses systems. Towards this direction Barretto et al. produced micro-fabricated GRIN lenses combined with a plano-convex micro-lens to image neurons in an aberrations corrected setup (Barretto, Messerschmidt and Schnitzer, 2009). The idea of minimizing the size of optical elements and combine them in well-established imaging systems is beneficial in terms of resolution and volume with respect to the conventional bulky optics. However, the complexity of the system is not sufficiently decreased to reduce the production cost, while the system has restricted field of view, therefore, limited application range.

The integration of micro-lens arrays in reflection mode setups benefits from high compactness compared to conventional bulky optical components, providing at the same time high resolution and wide field of view imaging based on simultaneous observation of multiple regions of the sample (Orth and Crozier, 2012, 2013, 2014; Lim et al., 2013). In systems developed by the group of Orth et al. the lens array is always part of a larger complex system and the structure follows the conventional epi-illumination scheme of standard laboratory microscopes. The wide area that the lenses intend to cover induces the need to expand the illuminating beam to provide homogeneous and uniform light to all lenses in the array simultaneously. Beam expanders and collimators are therefore a necessity, while the system may suffer from photo-bleaching effect, in case a laser diode is used.

In other approaches, micro-lens arrays are employed with the intention to reach higher resolution (Levoy et al., 2006; Douglass et al., 2016) or achieve stereoscopic view (Levoy, Zhang and McDowall, 2009) of the sample, in complex optical setups, with a restricted application field in research and in laboratory environments. Only in few approaches of epi-illuminating systems, micro-fabricated optical elements – either refractive or diffractive – are integrated in the chip hosting the sample (Schonbrun, Steinvurzel and Crozier, 2011; Lim et al., 2013).

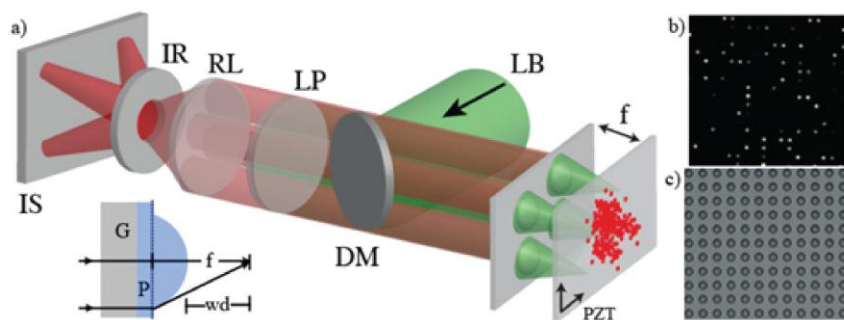


Figure 2.4. Integration of micro-lens arrays as part of reflection mode imaging setup for epi-fluorescent observation (Orth and Crozier, 2012).

2.5. Integrated LEDs in the optical system for epi-illuminated samples observation

Though the integration of lenses on illumination source has been a common practice for enhanced illumination or increased spatial uniformity of light (Ding et al., 2008; Casutt, 2012), only a few researchers have opted for an integration of the illumination source onto the main imaging element. Particularly, Goedhart et al. proposed a novel, illuminating, hand-held system for monitoring tissue-buried microcirculation, termed Sidestream Dark Field Imaging. In this setup, a central light guide is surrounded by concentrically placed, ring-shaped LEDs, that illuminate the tissue with a 530 nm wavelength emitted light, corresponding with the application's requirements. The central core lens, responsible for imaging, is optically isolated by the LEDs to assure no contamination of the image by the reflections of the LED light, due to the tissue surface reflections (Goedhart et al., 2007).

A similar idea was developed by Murari et al. for a different kind of application: an epi-illumination imaging platform for monitoring the brain activity of awake, behaving animals. In this design, the idea of replacing the conventional epi-illumination scheme with off-the-optical-axis components led to the integration of 3 or 6 LEDs, placed on the outer ring of the compound lens system. The optical system comprises of an aspherical lens that is able to move perpendicularly to the optical axis to focus on different planes. The LEDs are mounted permanently on the bottom of the circular tube hosting the lens.

These ideas have not yet been widely studied, though they present clever architectures that can prove beneficial towards further compactness and miniaturization. The use of LEDs in these approaches is of crucial importance due to their minimized volume and the emission of light over a wide angle. The main problems that need to be overcome concern the spatial uniformity of provided illumination over the observation area and the possible increase of temperature beyond the acceptable limit when imaging biological specimens. In fact, in this configuration the LEDs are placed in close proximity to the sample and the temperature increase may affect the viability of imaged cells.

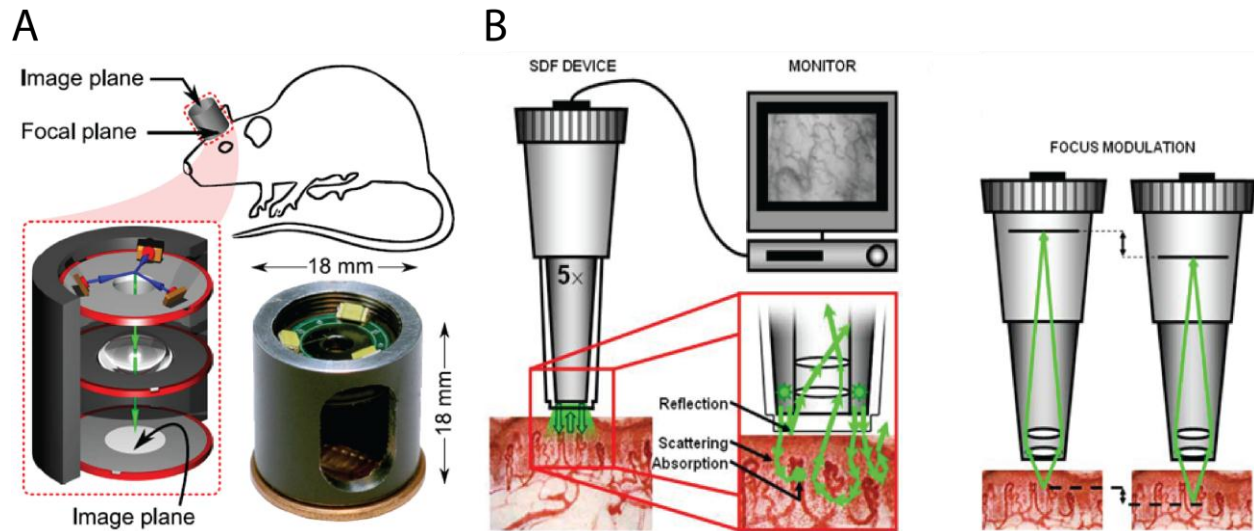


Figure 2.5. Integration of illuminating source (LED based) on the optical component of the imaging system. (A) Compound lens/ LED on the same structure for imaging brain activity of awake, behaving mice. (B)

Optical system with a ring-shaped LED placed concentrically to the optical axis for tissue-buried microcirculation monitoring.

3. Microfluidic chips for cell capturing and identification, for use in optical cell imaging and counting devices

Blood cell fractionation on microfluidic chips is a broad field of research motivated by the need to reduce the scale, the cost and the time to process blood samples. Targeting specific applications in diagnostic and therapeutic procedures, to be accomplished at the point of care, as well as in biological and biomedical experimental research, microfluidics profit from physical phenomena that are prominently manifested at the micro-scale (Squires and Quake, 2005). The main characteristics of fluidic manipulation at this scale: low Reynolds number, highly controllable laminal flow, low throughput due to increased speed of fluid handling, radically decreased sample volume and possibility of fabrication from poly-dimethyl-siloxane (PDMS), enable the development of devices simple, cheap and amendable to imaging (Jackson and Lu, 2014).

The isolation of cellular subtypes is based on their intrinsic properties – mainly electrical or magnetic and compressibility behavior of cells – or the extrinsic ones – such as their size or shape, the morphology they present under specific conditions and the biomarker they present on their surfaces (Yousuff et al., 2017). These cellular properties combined with the specific laws dominating low volume fluid behavior have led to the development of numerous miniaturized devices offering similar capabilities that exploit a variety of physical principles. Depending on the operating principle employed, a classification of the proposed cell sorting microfluidic approaches can be made, distinguishing active systems from the passively operating ones. Particularly, active systems make use of an externally applied field – acoustic (Laurell, Petersson and Nilsson, 2007), electric (Voldman, 2006), magnetic (Furlani, 2007) or optical (Wu et al., 2012) to impose forces on the targeted cell population and displace them to accomplish sorting. In contrary, passively enabled systems use inertial forces, filters or adhesion mechanisms to purify cell populations (Wyatt Shields Iv, Reyes and López, 2015). The actively enabled techniques, though providing high efficiency in terms of specificity – pure cell population – and sensitivity, require higher power consumption and in most cases a system of increased complexity, failing, therefore, to comply with the most crucial requirements of point-of-care testing. Moreover, they are most frequently used as stand-alone applications where imaging is not the dominant sensing principle, thus, they present low correlation with the purposes of this study. In the sections to follow, an emphasis on the state-of-the-art passive cell sorting microfluidic chips is given, for devices capable of being integrated in portable imaging/scanning micro-systems. Though in many cases a combination of different mechanisms is employed to reach high levels of efficiency, a classification is attempted based on the dominant mechanism.

| | METHOD | MECHANISM | SEPARATION MARKERS | FLOW RATE/ THROUGHPUT |
|----------------|----------------------------------|-------------------------------------------------|----------------------------------------|------------------------------------|
| ACTIVE | Flow cytometry (FACS) | Fluorescence | Fluorescent labels | 100 s ⁻¹ |
| | Magnetic | Homogeneous/ inhomogeneous magnetic field | Size, magnetic susceptibility | 10,000 s ⁻¹ |
| | Dielectrophoresis | Inhomogeneous electric field | Size, polarizability | 10,000 s ⁻¹ |
| | Electrophoresis | Homogeneous electric field | Size, charge density | 0.1–0.2 mm s ⁻¹ |
| | Optical | Optical force | Size, refractive index, polarizability | 1,500 min ⁻¹ |
| | Acoustic | Ultrasonic standing waves | Size, density, compressibility | 0.1–0.4 ml min ⁻¹ |
| PASSIVE | Pillar and weir structures | Laminar flow | Size, deformability | 1,000 μm s ⁻¹ |
| | Pinched flow fractionation (PFF) | Hydrodynamic force (parabolic velocity profile) | Size | ~ 4000 min ⁻¹ |
| | Hydrodynamic filtration | Hydrodynamic force | Size | 20 μl min ⁻¹ |
| | Inertial | Shear-induced and wall-induced lift | Size, shape | ~10 ⁶ min ⁻¹ |
| | Surface affinity | Specific binding to surface markers | Surface biomarkers | 1–2 ml h ⁻¹ |
| | Biomimetic | Hydrodynamic force/ Fahraeus effect | Size, deformability | 10 μl h ⁻¹ |
| | Hydrophoretic filtration | Pressure field gradient | Size | 4000 s ⁻¹ |

Table 2.1. List of cell separation methods classified according to the operating principle and the employed mechanism in two main categories, active systems and passively enabled systems (Bhagat et al., 2010). Specific examples are given in each category, along with the markers used for cell sorting in each case and the estimated throughput of the developed systems.

In the following critical review, the use of reagents and the requirement of sample preprocessing are both considered major tradeoffs of the proposed approaches. Aiming to be used at the point of care, in absence of laboratory clean environment and of expert personnel to handle sample preparation, the developed devices should be able to perform label-free imaging or automated on-chip labelling and washing. However, in cases where reported research studies do not include automated fluid handling, the potential use with an integrated automatic flow controller render these approaches promising to comply with prerequisites for point-of-care tools.

3.1. Micromachined surfaces for cell sorting and membrane filtration based on size, shape and deformability of target population.

Cell separation based on different physical properties that blood cells exhibit such as their size, shape and deformability has been widely studied and numerous approaches have been developed, implementing promising avenues for cell capturing applications. In this technique of cell isolation, the operating principle makes use of thin membrane layers with micro-pores of predefined size, geometry and spatial distribution. The membrane filters profit from material micromachining advances and can be made of various polymer materials, like thermoplastic materials (Didar et al., 2013), parylene material (Zheng et al., 2007), photo definable materials (Adams et al., 2014), and PDMS (Fan et al., 2015). These membranes contain openings – pores – of predefined size to prevent passage of target large size cells – usually White Blood Cells (WBCs) (Li et al., 2014) or Circulating Tumor Cells (CTCs) (Hosokawa *et al.*, 2010; S. Zheng *et al.*, 2011; Tang *et al.*, 2014) – and permit to the smaller particles suspended in blood to pass through the membrane towards the waste container. Captured cells can then be counted under microscope imaging platforms either by florescent illumination (Lim et al., 2012) or in high resolution bright field imaging schemes (Gogoi et al., 2016). In these devices, the trapping pores fabricated in the membranes are smaller in diameter (down to 8 μm) than target cells (WBCs diameter is 8 – 10 μm and CTC 10 -12 μm) while Red Blood Cells (RBCs) normally expressing a donut shape of 6 – 8 μm diameter and platelets are much smaller in size. RBCs exhibit a highly compressible behavior, thus they can be suppressed and easily pass through these holes.

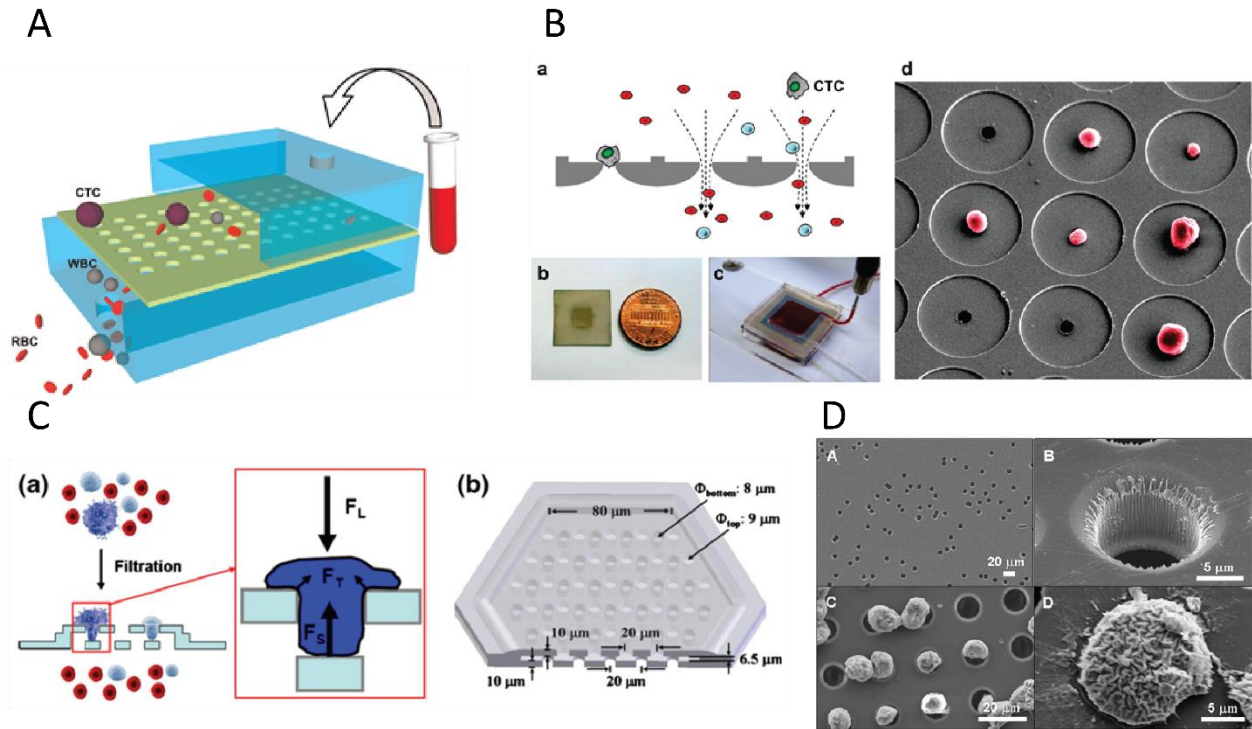


Figure 2.6. (A) A microfluidic chip integrated with a high – density, PDMS – based, micro-filtration membrane for rapid isolation and detection of circulating tumor cells (Fan et al., 2015). (B) CTC recovery device equipped with the size-selective micro-cavity array with the figure illustrating the schematic of the operating principle (a), photographs of the membrane and the device (b, c) and a picture captured in scanning electron microscopy where the micro-cavity and the MCF-7 trapped cells can be observed (d) (Hosokawa et al., 2010). (C) Operating principle and design of a 3D micro-filter device for viable circulating tumor cell (CTC) enrichment from blood comprising of 2 levels of membranes (S. Zheng *et al.*, 2011). (D) Commercially available and micro-machined membranes containing pores of predefined size for CTC trapping (Zheng et al., 2007).

Though, size is an accurately defined property of different cell types suspended in blood, the filtration mechanism suffers frequently from clogging problem, appearing very early in the flowing procedure. The rapidly increasing number of pores of the membrane that are gradually clogged, increases the resistivity to blood flow affecting the flow rate, while the regions that surround the pores contain decreased density of openings. Therefore, they act as trapping regions for all types of cells that create clusters superimposed on trapped cells and prevent effective imaging and cell detection. To enhance specificity, these devices need to integrate fluorescent labelling of target cells in addition to micro-filtration (Lim et al., 2012; W. Chen et al., 2013). Moreover, as RBCs exhibit a highly deformable behavior, while their concentration in unprocessed whole blood samples is increased, they can form clusters blocking the pores, affecting evidently the sensitivity of micro-filtering devices. To overcome this obstacle lysis is frequently an option, that consequently increases complexity and reagents usage (J. Chen et al., 2013). To meet the aforementioned clogging-related challenges, alternative approaches attempted to use filtering structures placed perpendicular to the flow axis (Li et al., 2014; Yousang Yoon et al., 2014) – profiting from gravity – or micro-machined

structures of oblique walls (Sarioglu et al., 2015) to enhance displacement of undesired small particles. Different micro-machined designs towards the same direction try to spatially separate captured cell types by gradual decreasing the height of the microfluidic chamber (Xu et al., 2015; Hvichia et al., 2016).

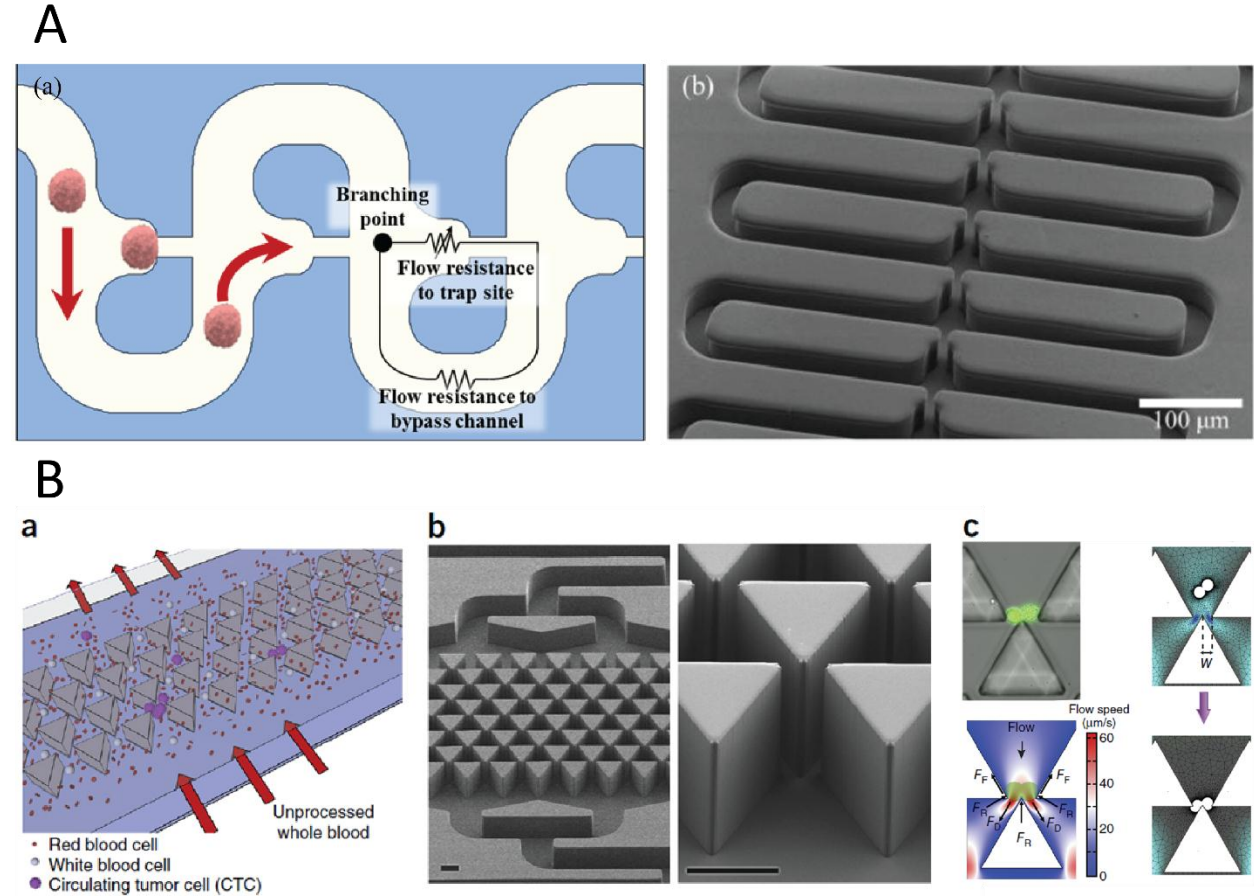


Figure 2.7. (A) Trapping pores placed vertically to flow direction (Yousang Yoon et al., 2014). Micro-machined surface of the entire microfluidic chamber, enhancing the displacement of decreased size particles, reducing clustering of RBCs (Sarioglu et al., 2015).

3.2. Surface functionalization for specific cell capturing

Separation of a specific cell type by the use of microfluidic chambers with functionalized walls has been the most frequently employed technique, profiting from fabrication easiness, compared to special structure micro-machining, and relatively low cost of production. In this technique, target cells flow through the chambers, along with all undesired cell types, they are captured and tightly bound on the chambers walls by cell surface receptors coupling with antibodies immobilized on the functionalized walls (Wang et al., 2011). To improve purity yield and capture rate, microfluidic implementations use specific antibodies for walls modification to achieve highly specific binding of cell types expressing the corresponding biomarker on their surfaces. Particularly, CTCs are captured by surfaces functionalized with antigen Epithelial cell adhesion molecule (anti-EpCAM) antibodies (Didar and Tabrizian, 2010; Gaskill, Launier and Eddington, 2012). Suffering from low sensitivity

due to the rarity of targeted cells, novel design employing micro-posts – also activated – have been developed to increase surface-to-volume ratio (Kurkuri et al., 2011; Mitchell, Castellanos, and King, 2012; Gupta, Baker and Tang, 2013). Consequently, lower volumes need to be processed to achieve adequate cell capturing efficiency.

Anti-CD3, anti-CD8 and anti-CD4 (Watkins et al., 2013; Asghar et al., 2016) antibodies were used for the selective trapping of lymphocytes expressing the corresponding biomarker on their surfaces. Based on the selected substrate, surface preparation with O₂ plasma treatment is performed for hydroxyl groups to appear (Zhang et al., 2005; Watkins et al., 2013) and a lyophilization protocol based on the use of proteomic solutions follows to perform bio-activation of the internal surfaces of the chip.

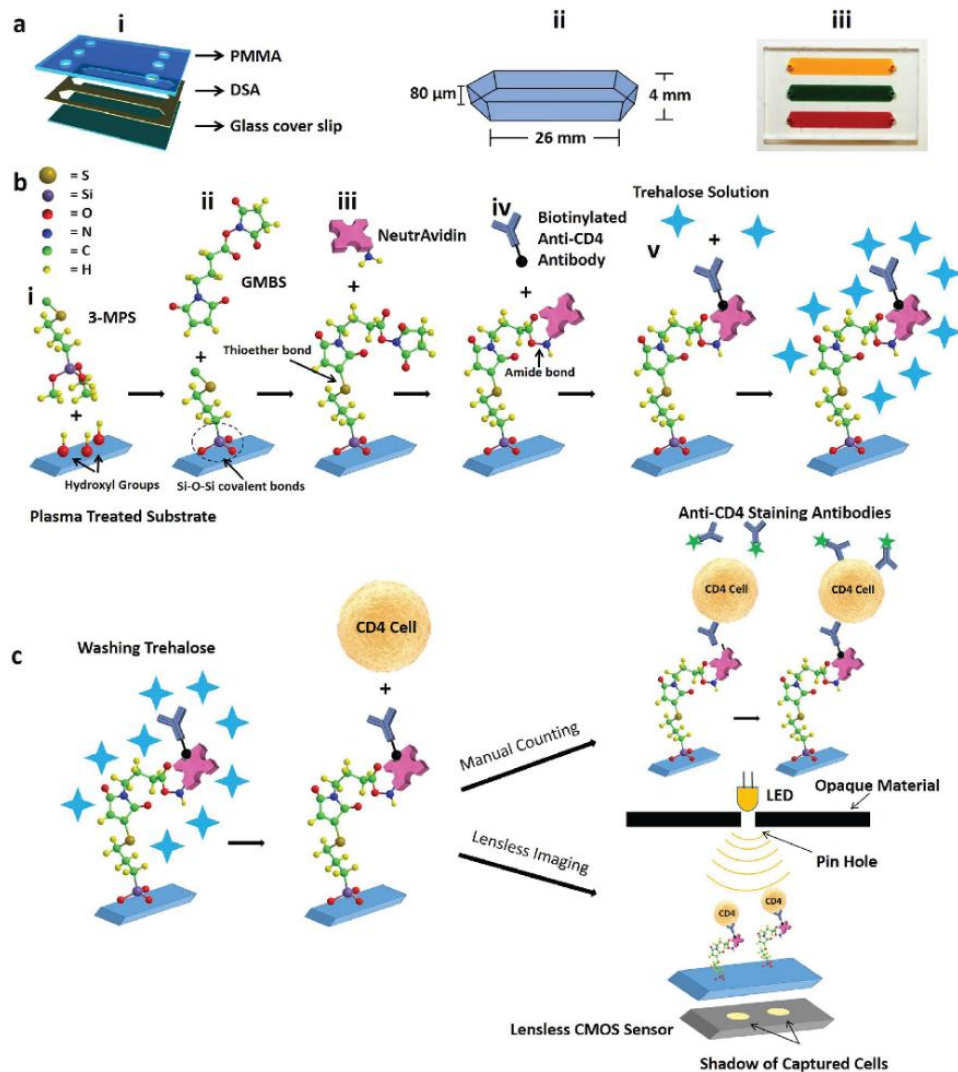


Figure 3. Surface functionalization protocol for CD4⁺ T lymphocytes capturing used in HIV diagnostic tool employing lens-less fluorescent imaging of immobilized cells (Watkins et al., 2013).

3.3.Enhanced surface capturing specificity and sensitivity based on special structures and flow control

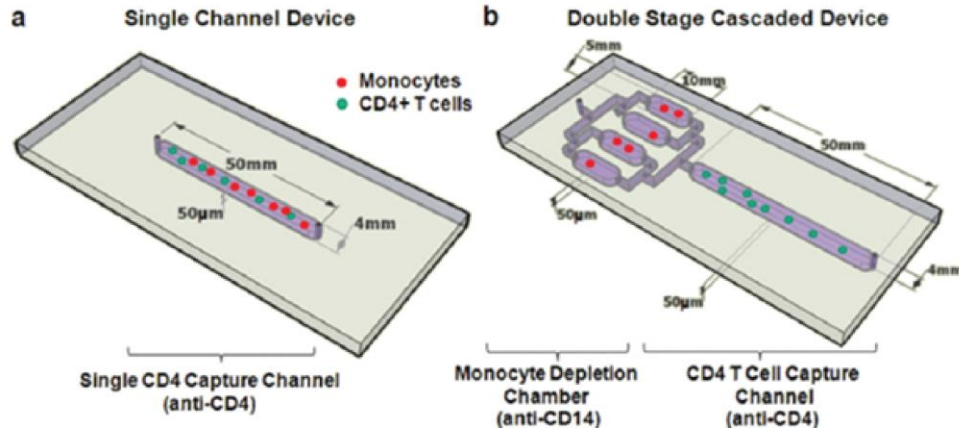


Figure 2.9. Microfluidic designs of (a) single channel and (d) dual channels for separation of monocytes from targeted CD4⁺ T lymphocytes (Cheng, Irimia, Dixon, Ziperstein, et al., 2007).

Separation by surface marker properties, though being popular in cases of heterogeneous mixtures of whole blood, suffers from low specificity since the selected biomarkers are rarely uniquely expressed on the surface of one specific cell type. To improve specificity, researchers usually employ additional fluorescent staining to distinguish between the different captured cell populations, during the imaging process (Watkins et al., 2013). Particularly concerning CD4⁺ T lymphocytes, required to be counted in high accuracy for the determination of HIV virus progress in HIV infected patients, the cells expressing CD4 surface marker are CD4⁺ T lymphocytes and monocytes. Towards increased purity of this specific blood cell subpopulation Cheng et al. proposed a sequential chamber structure functionalized with different antibodies – CD14 for monocytes capturing and CD4 for CD4⁺ T lymphocytes and monocytes surface binding (Cheng, Irimia, Dixon, Ziperstein, et al., 2007). The exact count of CD4⁺ T lymphocytes is extracted by the subtraction of these two populations, provided equal concentration in both chambers. In other approaches, researchers claimed to achieve relatively high purity of the trapped CD4⁺ T lymphocytes by controllable flow within the chamber, preventing monocytes from binding onto the functionalized surfaces (Cheng, Irimia, Dixon, Sekine, et al., 2007).

Flow rate of inserted whole blood samples has been extensively studied as a factor affecting sensitivity of the proposed microfluidic devices (Murthy et al., 2004; Sin et al., 2005). Increased flow rates induce relatively high velocities to the cells, preventing them from binding on the activated surfaces. A decrease in the microfluidic chamber's height is related to the velocity of cells for a fixed value of pressure applied, while at the same time increased chamber height prevents cells from reaching the surfaces of the bottom and top walls, therefore bind to them. In most cases, the increased chamber height, allowing for smooth flow of low rate, is considered to be the most crucial factor affecting sensitivity of the device. However, this factor remains poorly studied in literature. In the same direction, the presence of highly concentrated RBCs in whole blood sample, prevent contact between the targeted WBCs, CD4⁺ T lymphocytes, CTCs or other subpopulation with the

anti-body coated surface. Despite the numerous promising approaches, the field is open to investigation towards enhancement of the specificity and sensitivity of surface cell capturing.

Chapter 3

A portable, optical scanning microsystem for large field of view, high resolution imaging of biological specimens

Despite the numerous approaches that already exist, the field of point-of-care cell optical imaging and counting still presents a challenge, as there has been no approach that, in full compliance with the criteria imposed by the WHO, could overcome the technical limitations and provide a general purpose, portable, low-cost device for high resolution and wide FOV imaging. To be effective at the point of care, evolved technologies need to be simple (Boppart and Richards-Kortum, 2014). In the analysis to follow, a novel approach is presented, making use of a specially patterned mini-lens array combined with a simple, one direction (1D) scanning system for whole slide, high resolution imaging of a biological specimen. The technical characteristics of the employed sapphire ball lenses of high numerical aperture ($NA \sim 0.7$) and large FOV ($290 \mu\text{m}$) contribute to both increased image quality, in terms of resolution and contrast, and reduced number of required images in order to cover an extended surface of the specimen; approximately 400 scanning steps are adequate to screen a 4 cm long sample surface in 1X magnification. The simplicity of the proposed portable setup relies on the one-direction scanning and the incorporation of only one layer of mini-lenses (1 mm in diameter), the combination of whom succeeds in providing perfectly focused images of the sample and high resolution observation of it; the systems provides a resolving power of up to $1 \mu\text{m}$ feature size. It is this simple and clever operating principle that renders it compact, inexpensive in production and with reduced power or computational requirements. It is, therefore, ideal for use as a point-of-care device in poor resources areas or in primary health care in the developed world.

1. Architecture and operating principle of the micro-scanner

The operation principle of the presented imaging, scanning platform relies on the step movement of an optical head across one direction, in order to scan and image an extended surface of the selected biological sample. The specimen – typically blood sample inserted in a microfluidic chamber or sitting on a glass slide or coverslip – is placed at a short distance ($\sim 0\text{--}500 \mu\text{m}$) from the optical head, on top of the setup and held in place with the use of two laminated springs. An optical window formed at the bottom side of the sample holder allows for optical access to the specimen from the back side, where the optical head, attached to the translation stage, performs the stepping and imaging procedure. The optical/scanning head is an assembly of the optical components responsible for imaging the specimen: a mini-lens array, of one layer, aligned and permanently mounted on top of a 10.7 Mpixel monochrome complementary metal-oxide semiconductor (CMOS) detector sensor (Imaging Source, DMM 27UJ003-ML). This optical head is equipped with two micro-positioners allowing for accurate movement of the lens array and the CMOS detector with respect to the sample. These two stepper motors are responsible for providing sharp, in-focus imaging of the specimen at different magnification scale, from 1X to 4X. The system operates in transmission mode with the illumination to the specimen being provided by an external homogeneous white light emitting diodes (LED) square array (EdmundOptics, #66-830) placed on

top of the entire device at a working distance from the sample of approximately 20 cm. This square LED array has a side length of 5 cm and is capable of providing homogeneous illumination to the entire sample surface during the scanning procedure, without the need to follow the translation movement. The system includes a board of electronic components to control the movement of the motorized stage and the focusing micro-positioners and adjust the parameters for image acquisition, such as the exposure time of the detector, the gain and contrast of the acquired image and the scanning step and total length. The electronics board includes an Arduino Uno microprocessor board, externally controlled by the user, through a LabVIEW platform, that is also responsible for automatic scanning/imaging the sample and data storage, according to the selected specifications.

Prior to every scan, the user can manually select and adjust the distances between the sample, the lens-array and the CMOS camera. These distances determine the magnification preferred and the optimal focused plane. During scanning there is no perpendicular movement and the micro-positioners for magnification and focusing maintain their initial state. In each step of the scanning process, light rays coming from the illumination source are scattered by the sample and collected by the mini-lens array, so that the image of the specimen is projected on the effective area of the detector. After image acquisition and storage, the translation stage moves the optical head to the next step until the length of the entire sample is covered. Only one direction scanning is allowed and the maximum travelling distance across this direction is 40 mm. This configuration, combined with the specific geometric design of the mini-lens array, can create a complete image of the biological specimen with a maximal surface of 6 mm x 40 mm. After the accomplishment of the entire scanning and imaging process, the pictures stored are subjected to image processing to enhance signal-to-noise ratio, to detect the illustrated cells of the blood sample and perform picture stitching/mosaicking to provide the final 'virtual slide' of the observed sample. The aforementioned procedures are performed in MATLAB environment.

The operation of the developed micro-system relies on the use of five separated elements: (a) the mini-lens array, whose optical and geometrical characteristics allow for high resolution and wide FOV imaging of the sample, (b) the mechanical components, including the sample holder, the translation stage and the stepper motors of the optical head, whose micro-positioning accuracy provides sharp screening across the entire surface of the sample, (c) the illumination scheme, responsible for transmission mode observation of the specimen, (d) the electronics parts and the Graphical User Interface (GUI) capable of controlling the imaging and scanning parameters and (e) the post-processing of stored images to provide enhanced quality of the 'virtual slide'. These key elements and their performance are separately discussed in the sections to follow.

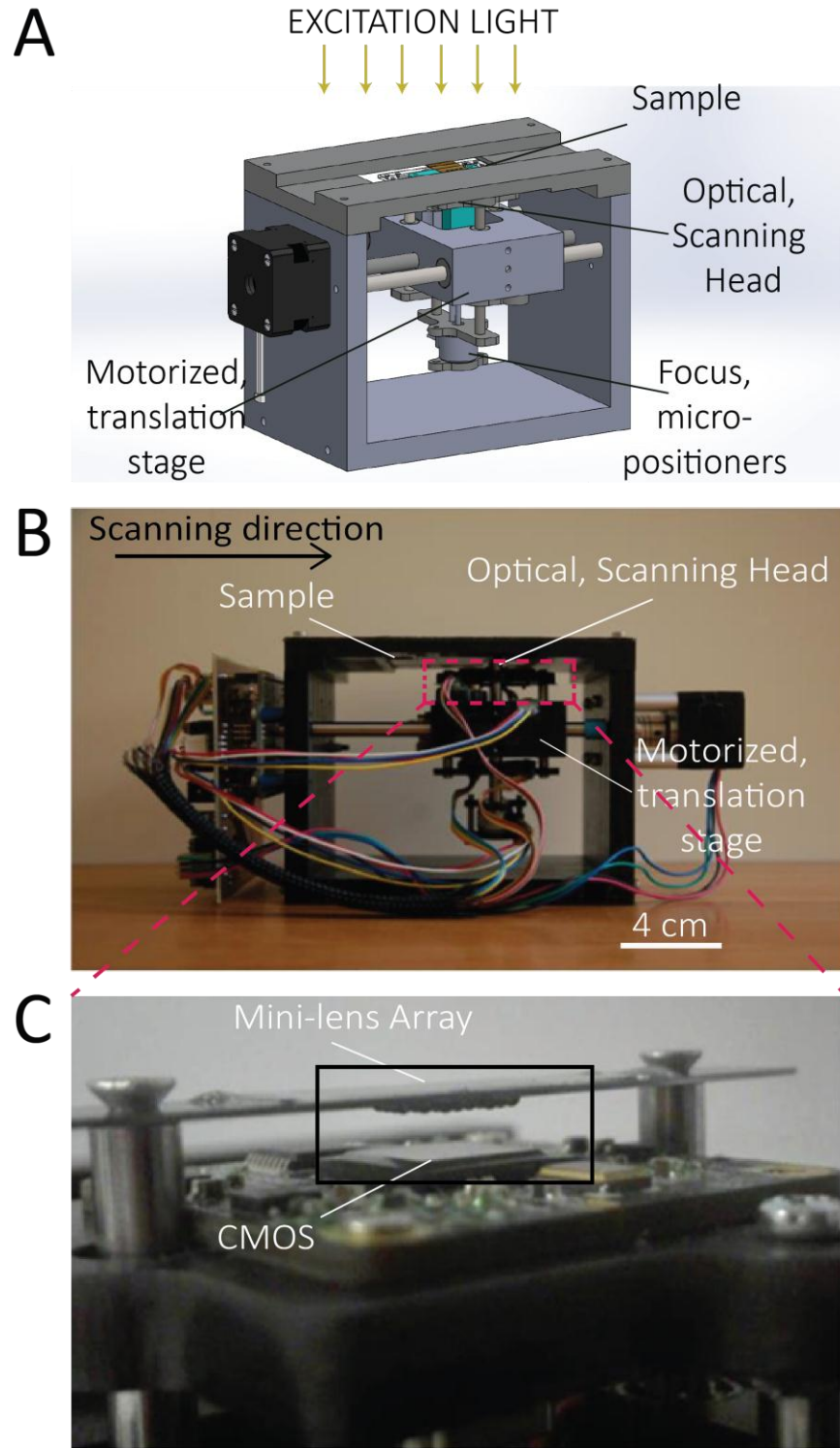


Figure 3.14. (A) Schematic of the architecture of the portable scanning microsystem, (B) Picture of the prototype and (C) close-up view of the optical head. The total size of the prototype is $21\text{ cm} \times 8\text{ cm} \times 11\text{ cm}$ and it weighs $\sim 1\text{ kg}$. The main optical components of the optical head, illustrated in (C), are: the mini-lens array and the CMOS detector.

2. The mini-lens array

The mini-lens array participates in the system as the unique optical component for the collection of light that is scattered from the imaged cell sample and the projection of their image on the detector surface. This mini-lens array comprises of 36 sapphire ball mini-lenses of 1 mm in diameter (EDMUND OPTICS #43-638) and a refractive index of 1.768. These sapphire ball lenses are placed on top of a Silicon die specially patterned with Deep Reactive Ion Etching process (DRIE) that contains through holes/wells upon which the lenses are seated. The wells are sealed from the backside of the silicon die with a glass slide piece of standard thickness No. 1 (borosilicate glass, thickness: 130-170 μm) in order to form the wells. The gap between the ball lens and the bottom side of the well – the thin glass slide – is filled with a UV curable optical adhesive (NORLAND 60) of a refractive index close to that of sapphire, 1.62. Prior to a detailed description of the geometrical design and fabrication process of this mini-lens array, it is crucial to present the theoretical principle of imaging with these mini-lenses to inspect all theoretical expectations relevant to the geometric optics and any expected artifacts on image formation.

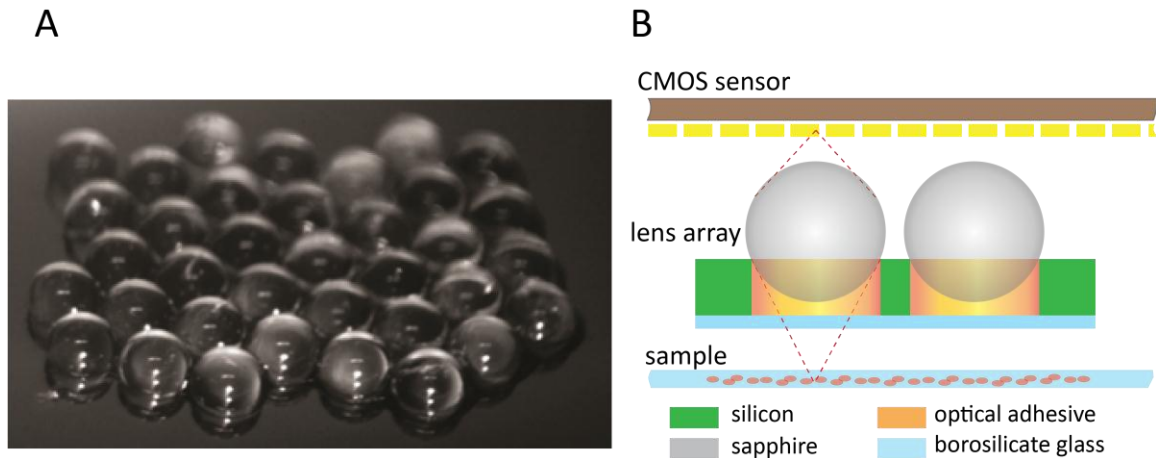


Figure 3.2. (A) Picture of the mini-lens array where all lenses are seated on top of the silicon chip. (B) Schematic of the imaging principle, where the image from the sample is acquired by each lens in the array and projected on the surface of the CMOS sensor.

2.1. Geometrical design of the mini-lens array – the scanning principle

The mini-lens array comprises of 36 sapphire ball lenses of 1 mm in diameter that are placed on top of a silicon chip, with a thickness of 400 μm . The silicon chip is patterned in a way that through holes of 960 μm in diameter are created. The lenses are seated on these holes, therefore, there is a gap of 140 μm between the bottom surface of each spherical lens and the bottom flat surface of the silicon die. This gap is filled with an optical adhesive (Norland 60) cured with UV and a glass cover slip of standard thickness No. 1 (130 - 170 μm) is used to seal these silicon wells from the bottom side of the silicon die. The silicon wells are patterned in a hexapolar array (60°) instead of a rectangular one (90°) so that the lenses are equidistant with each other (Figure 3). The edge-to-edge distance between the lenses is selected to be 50 μm , therefore the center-to center distance between

neighboring lenses is $1050\ \mu\text{m}$ and the distance between adjacent wells in the silicon die is $90\ \mu\text{m}$, edge-to-edge. The number of lenses (36) is selected such that they can adequately cover the entire active area of the detector surface ($4.28\ \text{mm} \times 5.7\ \text{mm}$). With such a design of the lens array the blind areas lying underneath the region between the lenses is reduced to the strict minimum and the total surface of the sample that the CMOS camera can observe in a single shot is maximized.

Top View

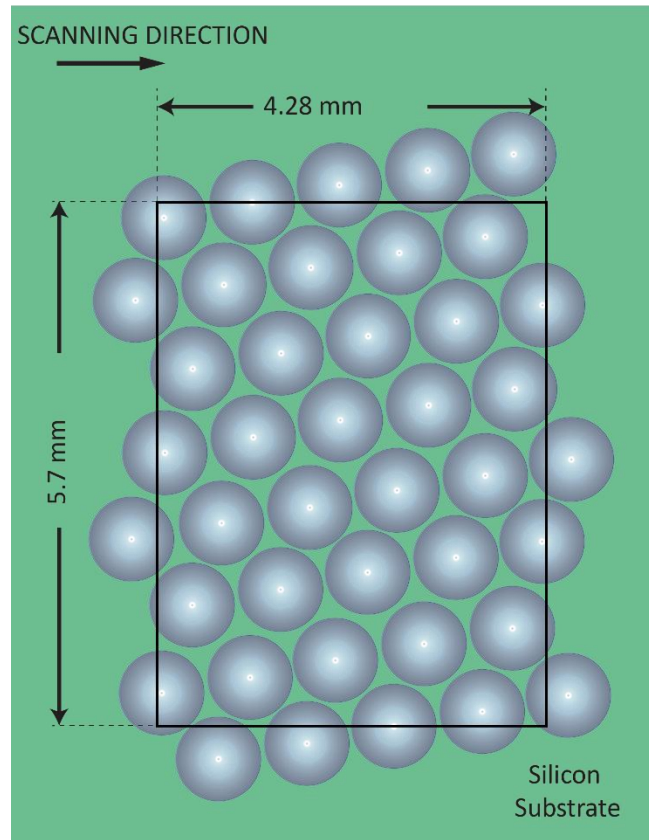


Figure 3.3. Schematic presenting the geometrical design of the lens array (top view). The active area of the CMOS sensor employed is marked with the black square. The lenses placed in a tilted hexapolar array cover the entire effective area of the detector.

The geometrical design of the lens array is the key element for the operation of the entire system and particularly for the successful imaging of the entire surface of the sample by only one direction scanning of it. More precisely, the entire array of lenses is placed with a tilt of approximately 17° with respect to the scanning direction. Based on this tilted design, neighboring lenses have an overlap in their FOV so that undetected regions of the sample in one shot can be effectively imaged in the next scanning steps. With the diameter of the FOV of each lens in the array being estimated approximately equal to $290\ \mu\text{m}$ –see sections 2.2.1 and 2.4.1 – the image produced by each lens, during scanning, overlaps by a factor of 20 % with the image produced by the adjacent lenses in a direction vertical to the scanning direction (Figure 4). Thus, by performing one direction scanning,

there are no undetected areas of the sample. The calculation of the tilt angle φ was based on the geometry of the array:

$$\varphi = \frac{80\% \text{ of lens FOV diameter}}{\text{Lens diameter} + \text{lenses distance}}$$

where the FOV diameter is selected to be equal to 290 μm , the lens diameter is 1000 μm and the lenses distance refers to the edge-to-edge distance between them, equal to 50 μm . The measurement of the FOV was performed with the use of a lines grid projection over the CMOS surface. The estimated 290 μm FOV is the diameter of the disc surface where light intensity is not lower than 90 % of its maximum value – located at the center of the lens.

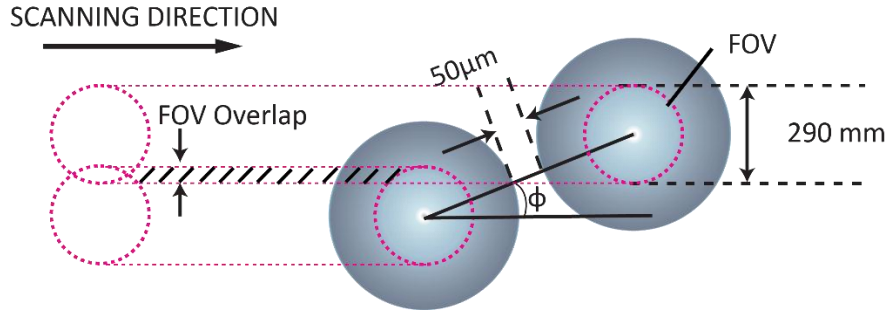


Figure 3.4. Scanning principle of the system based on the tilted design of the lens array. In the schematic two adjacent lenses are illustrated with their FOV surface overlapping during scanning by a factor of 20 %, in a direction vertical to the scanning one.

2.2. Imaging principle – theoretical background on imaging with the mini-lens array.

The analysis of imaging with spherical micro-lenses, as those employed in this particular design, relies on thick lens optics of complex systems. The compound optical element comprises of the sapphire ball lens, a cured optical adhesive part with a concave plano shape and index of refraction of 1.62 and, at the end, a glass slide sealing the lens chip that is a flat optical element with approximately 150 μm thickness and 1.52 refractive index. To analyze this multiple thick lenses optical component, the matrix system is used, in which the entire system is represented by a matrix extracted by the multiplication of the refraction and translation matrices in all surfaces and bulk components respectively (Pedrotti and Pedrotti, 1993).

The refraction matrix at the spherical surface of the ball lens in air is:

$$R_1 = \begin{bmatrix} 1 & \Phi_{1S} \\ 0 & 1 \end{bmatrix}, \quad (3.1)$$

Where:

$$\Phi_{1S} = \frac{n_{\text{air}} - n_L}{R} \quad (3.2)$$

is the power of this spherical surface, with $n_{\text{air}} = 1$ being the refractive index of air, $n_L = 1.768$ the refractive index of the sapphire ball lens and $R = 500 \mu\text{m}$ the radius of spherical curvature of the lens.

The translation matrix within the body of the ball lens is extracted as:

$$T_1 = \begin{bmatrix} 1 & 0 \\ \frac{d_L}{n_L} & 1 \end{bmatrix}, \quad (3.3)$$

where d_L is the center thickness of the lens, thus

$$d_L = 2R. \quad (3.4)$$

The refraction matrix at the spherical interface between the ball lens and the optical adhesive is represented as:

$$R_2 = \begin{bmatrix} 1 & \Phi_{OS} \\ 0 & 1 \end{bmatrix} \quad (3.5)$$

where:

$$\Phi_{OS} = -\frac{n_L - n_{OA}}{R} \quad (3.6)$$

is the power of this second spherical surface and $n_{OA} = 1.62$ is the refractive index of the optical adhesive. In this case the concave surface is translated with a negative radius expression.

The translation within the body of the optical adhesive is given by the matrix:

$$T_2 = \begin{bmatrix} 1 & 0 \\ \frac{d_{OA}}{n_{OA}} & 1 \end{bmatrix}, \quad (3.7)$$

where d_{OA} is the center thickness of the gap between the ball lens and the glass cover slip at the bottom of the silicon chip which is filled with the selected optical adhesive. Calculated by the geometry of the fabrication, and particularly on the diameter of wells patterned on silicon chip – $960 \mu\text{m}$ – the center thickness of this concave plano lens is equal to $d_{OA} = 140 \mu\text{m}$.

The matrix representing the refraction on a plane surface is:

$$R_3 = R_4 = \begin{bmatrix} 1 & 0 \\ 0 & 1 \end{bmatrix}, \quad (3.8)$$

since the radius of curvature of a flat surface is ∞ , therefore the power $\Phi = 0$. The same matrix presents the refraction on the last surface between the glass cover slip and the air, R_4 . Consequently, these matrices do not contribute to the entire system.

Last matrix is the one representing the translation of the incident ray within the glass slide:

$$T_3 = \begin{bmatrix} 1 & 0 \\ \frac{d_G}{n_G} & 1 \end{bmatrix}, \quad (3.9)$$

where d_G refers to the used glass slide of standard thickness No.1 (130-170 μm according to manufacturer specifications) and $n_G = 1.52$ is the refractive index of borosilicate glass.

The final matrix representation of this compound optical element is derived by the multiplication of the aforementioned matrices:

$$\begin{aligned} M &= R_1 \cdot T_1 \cdot R_2 \cdot T_2 \cdot R_3 \cdot T_3 \cdot R_4 \\ &= \begin{bmatrix} 1 & \Phi_{IS} \\ 0 & 1 \end{bmatrix} \cdot \begin{bmatrix} 1 & 0 \\ \frac{d_L}{n_L} & 1 \end{bmatrix} \cdot \begin{bmatrix} 1 & \Phi_{OS} \\ 0 & 1 \end{bmatrix} \cdot \begin{bmatrix} 1 & 0 \\ \frac{d_{OA}}{n_{OA}} & 1 \end{bmatrix} \cdot \begin{bmatrix} 1 & 0 \\ 0 & 1 \end{bmatrix} \cdot \begin{bmatrix} 1 & 0 \\ \frac{d_G}{n_G} & 1 \end{bmatrix} \\ &\cdot \begin{bmatrix} 1 & 0 \\ 0 & 1 \end{bmatrix} = \begin{bmatrix} A & B \\ C & D \end{bmatrix} \end{aligned} \quad (3.10)$$

Where the elements of the array A, B, C, D , after substituting the equations (3.1) - (3.9) to the matrix expression given by (3.10), are given by the equations (3.11) - (3.14) below:

$$\begin{aligned} A &= \left(1 + \frac{d_L}{n_L} \cdot \Phi_{IS}\right) \cdot \left(1 + \frac{d_{OA}}{n_{OA}} \cdot \Phi_{OS}\right) + \frac{d_{OA}}{n_{OA}} \cdot \Phi_{IS} + \left(\left(1 + \frac{d_L}{n_L} \cdot \Phi_{IS}\right) \cdot \Phi_{OS} + \Phi_{IS}\right) \\ &\quad \cdot \frac{d_G}{n_G} \\ &= \left(1 + \frac{2 \cdot (n_{air} - n_L)}{n_L}\right) \cdot \left(1 + \frac{d_{OA} \cdot (n_{OA} - n_L)}{n_{OA} \cdot R}\right) + \frac{d_{OA}}{n_{OA}} \cdot \frac{n_{air} - n_L}{R} \\ &\quad + \left(\left(1 + \frac{2 \cdot (n_{air} - n_L)}{n_L}\right) \cdot \left(-\frac{n_L - n_{OA}}{R}\right) + \frac{n_{air} - n_L}{R}\right) \cdot \frac{d_G}{n_G} \end{aligned} \quad (3.11)$$

$$B = \left(1 + \frac{d_L}{n_L} \cdot \Phi_{IS}\right) \cdot \Phi_{OS} + \Phi_{IS} = \left(1 + \frac{2 \cdot (n_{air} - n_L)}{n_L}\right) \cdot \left(-\frac{n_L - n_{OA}}{R}\right) + \frac{n_{air} - n_L}{R} \quad (3.12)$$

$$\begin{aligned} C &= \frac{d_L}{n_L} \cdot \left(1 + \frac{d_{OA}}{n_{OA}} \cdot \Phi_{OS}\right) + \frac{d_{OA}}{n_{OA}} + \left(\frac{d_L}{n_L} \cdot \Phi_{OS} + 1\right) \cdot \frac{d_G}{n_G} \\ &= \frac{2 \cdot R}{n_L} \cdot \left(1 + \frac{d_{OA} \cdot (n_{OA} - n_L)}{n_{OA} \cdot R}\right) + \frac{d_{OA}}{n_{OA}} + \left(\frac{2 \cdot (n_{OA} - n_L)}{n_L} + 1\right) \cdot \frac{d_G}{n_G} \end{aligned} \quad (3.13)$$

$$D = \frac{d_L}{n_L} \cdot \Phi_{OS} + 1 = \frac{2(n_{OA} - n_L)}{n_L} + 1 \quad (3.14)$$

Each lens in the array is described by this matrix M , which has a determinant equal to $\frac{n_{\text{material before the lens}}}{n_{\text{material after the lens}}}$. Since this compound lens is placed on air the representative matrix should have a determinant equal to 1, due to the rays travelling from air, through the lens's different refractive indices, to the air again. Indeed, the determinant in this system is equal to 1, proving the integrity of the aforementioned analysis.

After substituting the corresponding numerical values of the variables, the final matrix of the optical component is given as:

$$M = \begin{bmatrix} -29.0197 & -1.5748e + 05 \\ 1.5977e - 04 & 0.8326 \end{bmatrix}, \quad (3.15)$$

This matrix involving 2x2 refraction and transfer matrices enables the determination of the fundamental optical system parameters such as the system's equivalent power Φ , the effective focal length EFL, the system's focal lengths f_1, f_2 and the position of both principal planes relative to the lens vertices, $\overline{V_1H_1}$ and $\overline{V_2H_2}$, respectively.

Particularly:

$$\Phi = -B = 15.748 \mu\text{m}^{-1} \quad (3.16)$$

$$\text{EFL} = \frac{1}{\Phi} = 6.3498 \mu\text{m} \quad (3.17)$$

$$f = -\frac{n_{\text{air}}}{B} = 6.3498 \mu\text{m} \quad (3.18)$$

$$\overline{V_1H_1} = -\frac{n_{\text{air}} \cdot (1 - A)}{B} = 190.62 \mu\text{m} \quad (3.19)$$

$$\overline{V_2H_2} = -\frac{n_{\text{air}} \cdot (D - 1)}{B} = -1.0631 \mu\text{m} \quad (3.20)$$

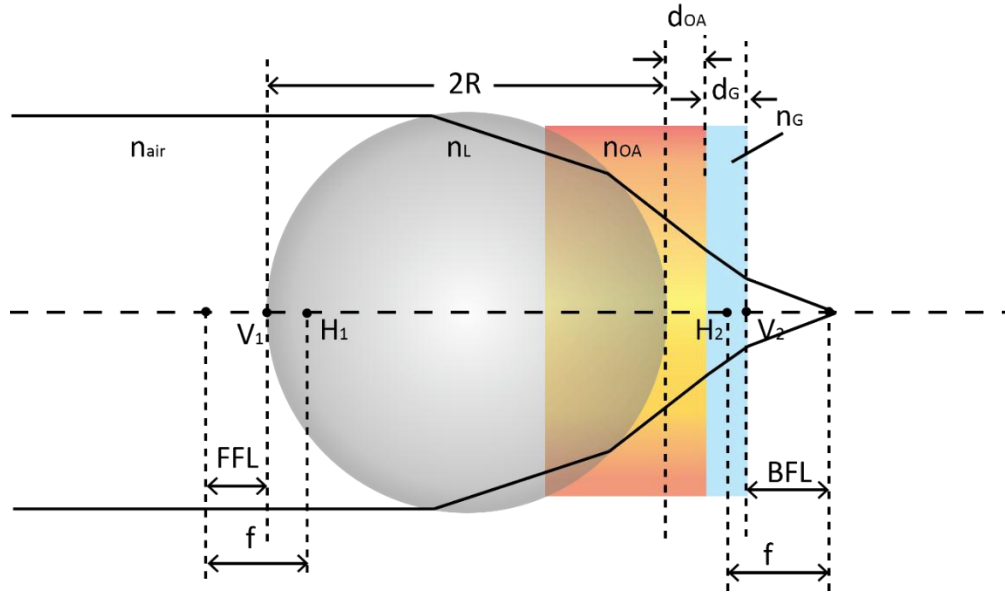


Figure 3.5. Schematic indicating the fundamental optical properties of the used compound mini-lens, being the unit element of the array.

The optical parameters were confirmed by the simulation of the compound mini-lens performed in COMSOL 5.3 (Ray Optics module). Back focal point was indicated by tracing a set of rays released by a line of equidistant spots placed on a plane perpendicular to the lens axis. The set of rays covers a length of $300\ \mu\text{m}$ with a distance of $20\ \mu\text{m}$ between neighboring spots. The back focus point was indicated $9.4\ \mu\text{m}$ away from the back surface of the lens – the outer surface of the glass cover slip at the bottom of the compound lens (Figure 6). The same simulation was performed to determine the front focal plane where parallel rays are travelling to the opposite direction (Figure 7). The rays converged on a plane $690.17\ \mu\text{m}$ away from the outer spherical surface of the lens, creating a spot smaller than $0.08\ \mu\text{m}$.

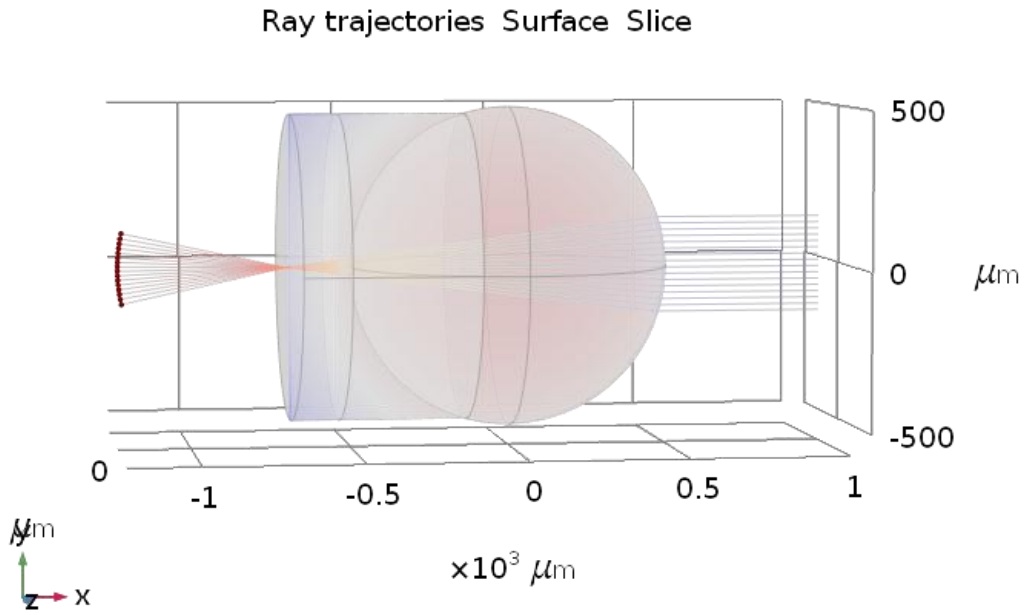


Figure 3.6. Back focal point based on COMSOL Ray Optics simulation. The focal plane is a few micrometer away from the back surface of the glass cover slip.

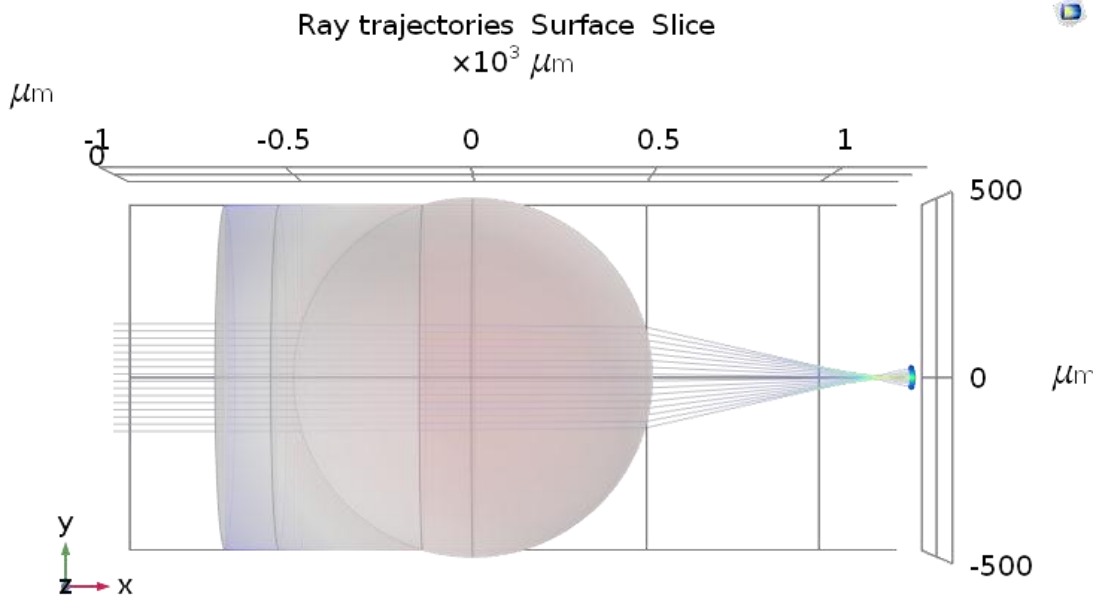


Figure 3.7. A set of parallel rays released from the backside of the lens (side of imaging plane) are converged on a spot $690.17 \mu\text{m}$ away from the spherical surface of the lens.

2.2.1. Expected artifacts in image, produced by a spherical compound mini-lens

Though spherical lenses present high Numerical Aperture (N.A.), the image quality is relatively poor due to the presence of aberrations that reduce resolution of the image (Tsai, Chen and Yang, 2008). In the case of the used spherical mini-lens, the N.A. was previously reported to be approximately 0.7 (Gulari et al., 2014). In this optical system spherical aberrations and defocus are dominant and can be observed even by the convergence point of rays travelling through the lens in the simulations explained before. Paraxial focus can be clearly observed in Figure 8 where rays travelling in parallel converge in a different point when coming from the outer ring surface with respect to the lens axis.

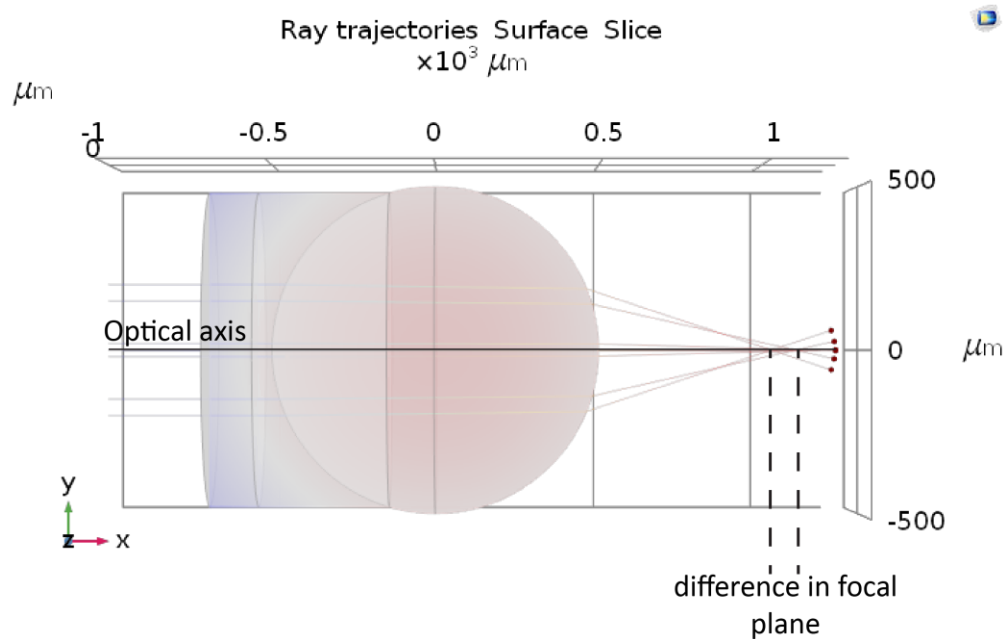


Figure 3.8. The indicated difference in the focal plane results in defocused rays on the image plane and artifacts in the produced image. In the selected compound lens, the expected aberrations are mainly due to the spherical surface of the sapphire ball lens and the paraxial focus of the rays.

Transverse aberrations can be studied by the observation of the spot diagram of a rectangular array of rays on the focal plane. Thus, a dense rectangular grid of rays, with a side length of 150 μm and a distance of 5 μm separating release spots (Figure 9.A)– was selected to travel through the lens and the spot created by their convergence on a sequence of flat surfaces parallel to the image plane was plotted (Figure 9). To plot the position of rays in each plane a Poincaré map was selected. In the presentation of rays, a color expression was used to indicate the initial distance of each point on the release grid from the center of the lens – optical axis. By comparing the plotted distribution of rays on each surface with the corresponding spot diagrams from literature (Gross et al., 2005), defocus and spherical aberrations dominate as expected due to the spherical surface of the ball sapphire lens.

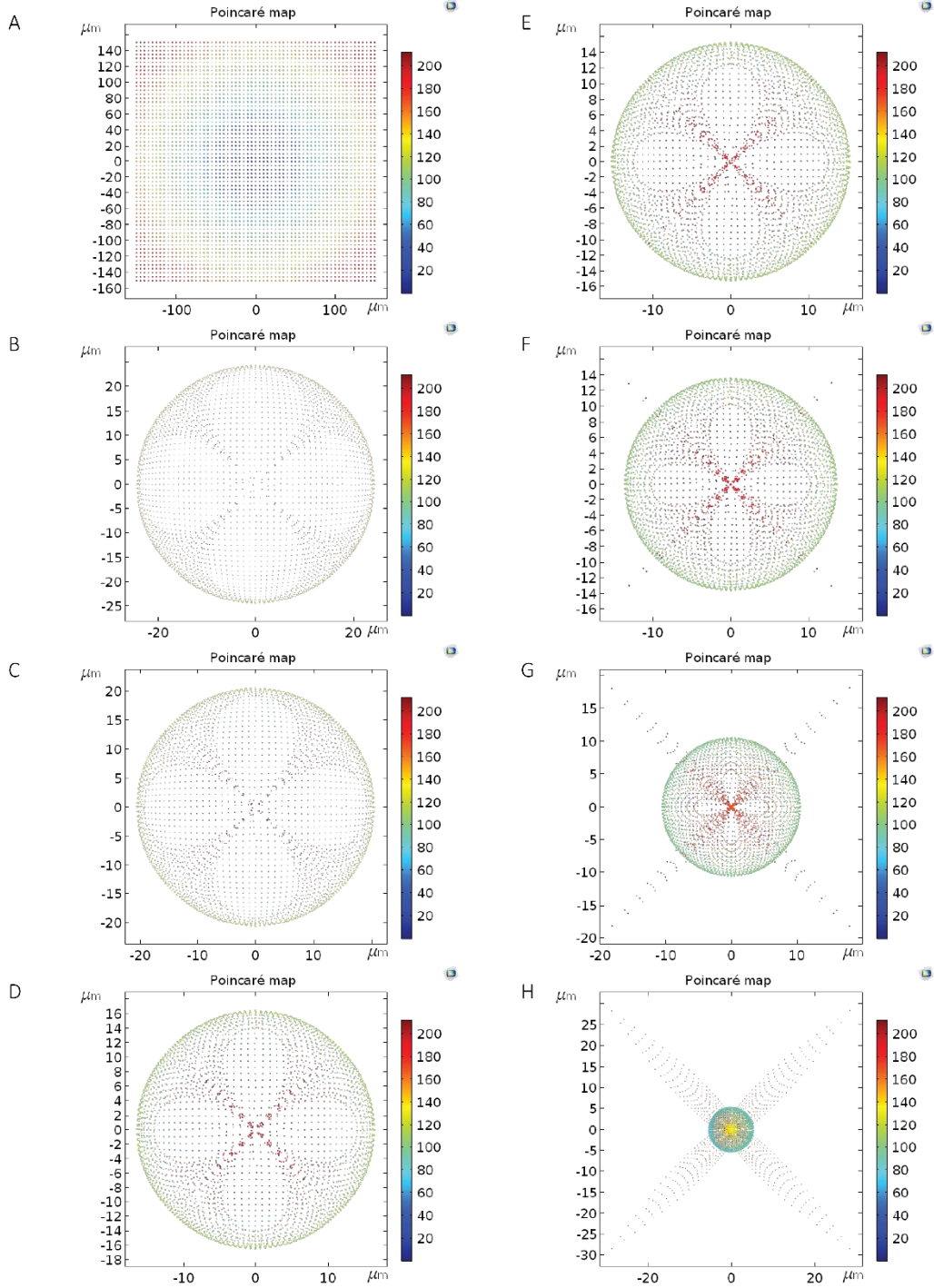


Figure 3.9. (A) Diagram of the array of rays release spots with a direction parallel to the optical axis. (B)-(H) Spot diagrams of the convergence of the rays on surfaces parallel to the image plane close to focal point. Paraxial focus is apparent, as rays travelling away from the optical center of the lens converge earlier in the sequence of planes – red spots in (B) and (C) – while rays released close to the optical axis – distance up to 150 μm corresponding to yellowish spots based on color expression – converge later in the sequence creating a smaller spot with a radius less than 5 μm (H).

To further examine field curvature due to optical aberrations, Zernike polynomials were extracted for different entrance pupil sizes. Zernike polynomials are a sequence of polynomials that are continuous and orthogonal over the unit circle and are often used to express aberration of the wavefront in the case of optical elements with a circular pupil. The main advantage of the normalized Zernike expansion, as a means of aberration representation, is the orthogonality of these polynomials (Lakshminarayanan and Fleck, 2011), meaning that they are linearly independent, therefore, each coefficient or value represents the root mean square wavefront error that is attributed to the corresponding mode – described by a specific polynomial in the set of them. Even further, this independence induced by the orthogonality allows the inclusion of any additional mode/term without affecting the coefficients of the modes already computed. The modes with the higher coefficients indicate the dominant modes in the wavefront aberrations, thus those modes having the greatest impact on image quality.

For optical systems that use a flat detector surface, field curvature induced by the spherical surface of the lens can be partially corrected by balancing positive and negative power surfaces (Gross et al., 2005). Thus, conventional microscopy systems employ complex objective lenses. In this study, the concave plano lens of the optical adhesive can act towards this direction to compensate large spherical aberrations by the ball sapphire lens. However, this study of aberrations does not aim at defining possible ways to correct the wavefront error, but to estimate the dependence of the wavefront error on the size of the entrance pupil and further more to define an approximation of the aberrations-free disc space centered at the optical axis. That aberrations-free disc would represent the effective field of view (FOV) of each lens. This parameter is crucial for the geometrical design of the array of lenses and the performance of scanning principle (see section 2.2). Given the linear scaling relationship between the influence of aberrations and the imaging FOV (Lohmann, 1989), we exported the wavefront curvature expressed by Zernike coefficients up to the 5th order through COMSOL ray optics simulation of the optical system in use, for three different circular pupil sizes: 200 μm radius (Figure 10.A), 150 μm radius (Figure 10.B) and 100 μm radius (Figure 10.C). Observation of the resulting wavefront curvature error maps clearly determines the reduction of impact of aberrations with the restriction of the FOV. Apart from graphical plotting, we derive the wavefront variance from the vector of Zernike amplitudes as:

$$\sigma = \left(\sum_{j=3}^5 C_j^2 \right)^{\frac{1}{2}} \quad (3.21)$$

where the first terms, representing the pseudo-aberrations of piston, tip and tilt, are ignored.

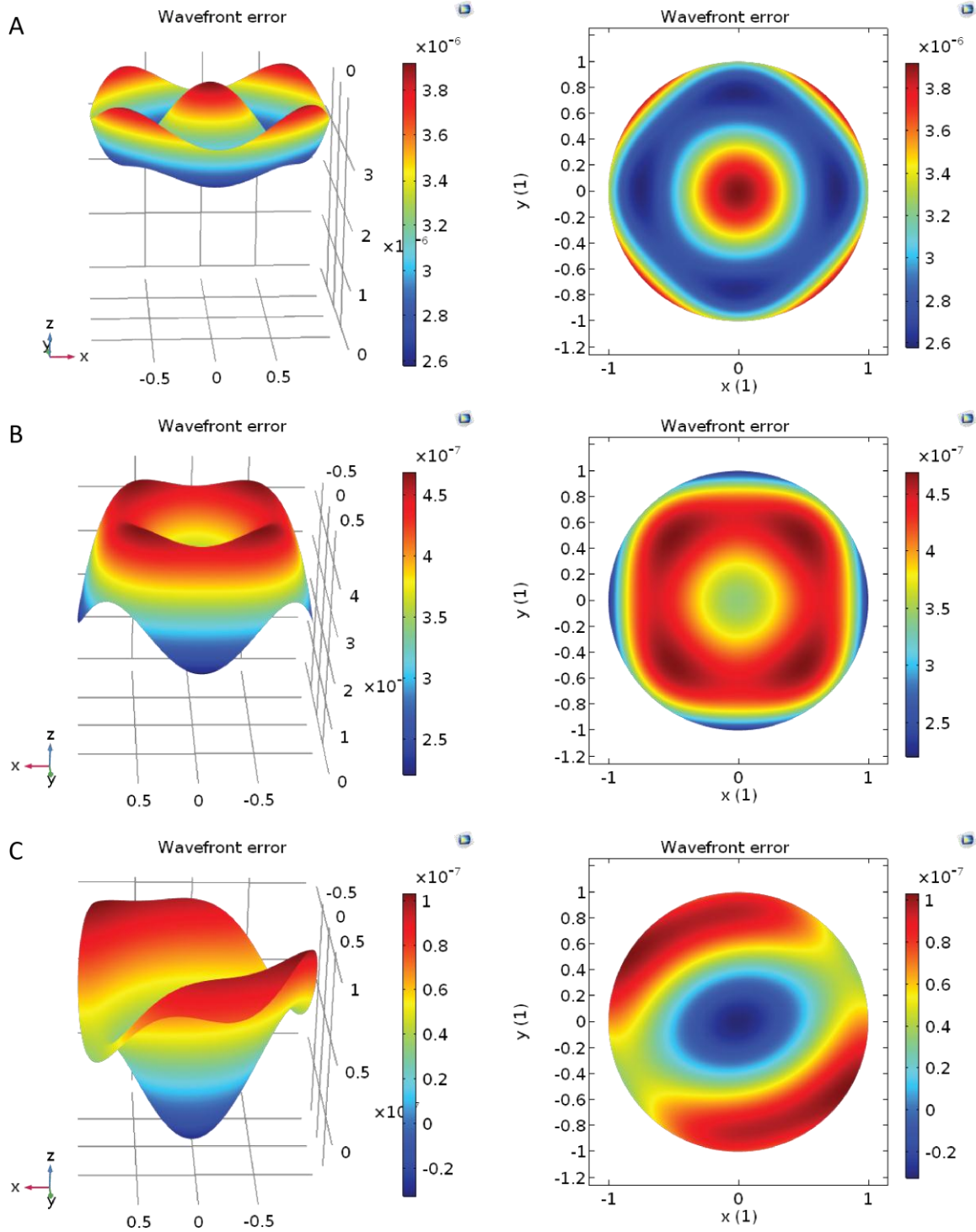


Figure 3.10. 3D and flat surface maps of the optical aberrations based on Zernike polynomials representation of the wavefront curvature. From (A) to (C) different sizes of entrance pupils were examined from a circular pupil of 200 μm radius (A), 150 μm (B) and 100 μm (C) to observe the response of the optical elements.

The corresponding values of wavefront variance for each case are 3.469 e-07 m, 5.0 e-08 m and 3.9 e-08 m for 400 μm , 300 μm and 200 μm entrance pupil diameters. Taking into account the

dominance of spherical aberrations on the above values (see Appendix) and based on Marechal criterion for an aberration-free system over the entire surface of the entrance pupil the rms value of wavefront error should not exceed $\lambda/2.22$. This threshold is extracted by the equation (Gross et al., 2005):

$$W_{rms} \leq \frac{2 \cdot \pi \cdot \lambda}{14} \quad (3.22)$$

Thus, assuming a wavelength equal to 550 nm, we can extract a first estimation of the effective FOV for adequate image quality close to an upper limit of 300 μm in diameter. This simulation based conclusion is confirmed by the observation of the image produced by each lens in the array as reported in the following, where contrast and light intensity reduction are used as the criteria to precisely determine the disc of a blurring-free FOV.

2.2.2. Expected artifacts in image, produced by an array of mini-lenses

Despite optical aberrations induced by the spherical surface of the employed mini-optics, the use of an array of optical lenses is a source of artifacts due to the possible imperfections in the fabrication and assembly process of the lens array or its alignment procedure with respect to the object plane and the detector surface. In figure 11, a set of simple schematics presents these misalignments that could result in a blurred, defocused image. Any minor tilt in the surface of the object plane or the detector plane will result in gradually increased defocus error across one direction of the image. Perfect parallelism is therefore a demand to avoid vertical scanning for a single picture acquisition with sharp, in-focus imaging from all lenses in the array. Equivalently, the fabrication and assembly process of the array of lenses must be accomplished with great accuracy to obtain a uniform set of identical optical elements. Any difference in the height of lenses will result in spatially random defocused spots on the acquired image.

Nevertheless, even in a perfectly fabricated and aligned optical system, the use of an array of lenses is subjected to an effect of ‘ghost image’ that are superimposed and may lead to severe blurring of the image. Ghost images derive from adjacent lenses when light rays – from the illuminated sample - travelling at a wide angle with respect to the optical axis of each lens, are allowed to pass through neighboring lenses and reach the detector surface. Even if the produced ghost image is not in-focus on the detector, light rays coming from all neighboring lenses in the array are superimposed and lead to severe decrease of the contrast in the acquired image; therefore the effect results in a radical decrease of resolving power of the optical system. The phenomenon is well known as ‘crosstalk’ and it is previously reported in expected artifacts when imaging with a lens array (Davies, McCormick and Brewin, 1994; Daily, 2000; Sinzinger, 2003). Among the ways to eliminate crosstalk small apertures can be added to reduce the size of the entrance pupil. This technique blocks the light rays of a wide angle to pass through the lenses.

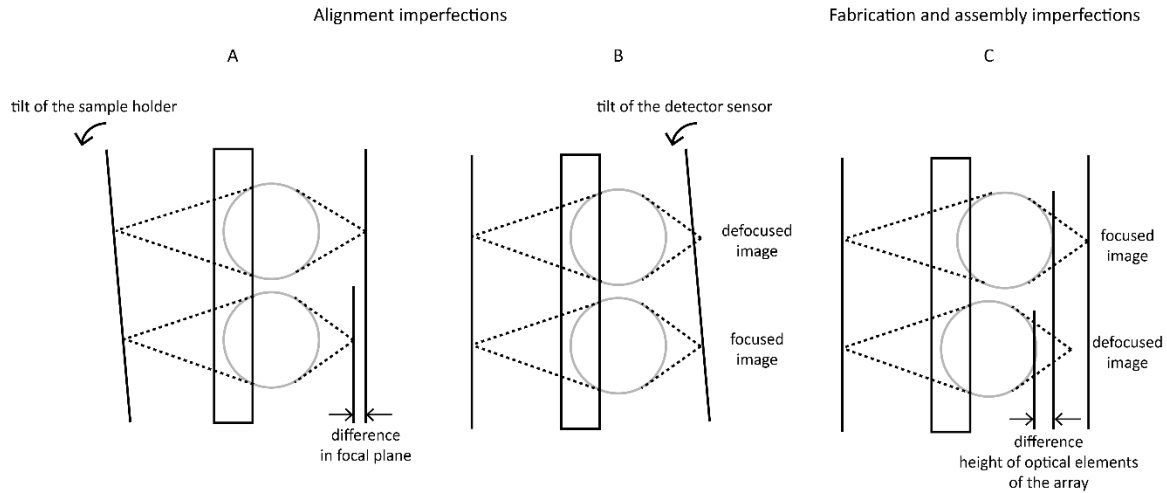


Figure 3.11. Alignment and fabrication imperfections that may lead to non-focused imaged provided by several lenses of the array. Such artifacts, when present in an image imply the use of scanning to the direction that is perpendicular to the imaging surface to acquire sharp in-focus images from all lenses of the array.

Aiming at an estimation of the angle of rays, needing to be blocked, a simulation in COMSOL Ray Optics module was used (Figure 12). Only two among the lenses of the array participate in this simulation and the two different sets of rays derive from the same object plane with an angle of 0° and 63.435° ($\tan(63.435^\circ) = 2$) respectively, in a conical shape. The image plane is selected at a distance where rays travelling in parallel with the optical axis converge to a point to create the image of the illuminated object. Observation of the resulting Poincaré map illustrating the points from rays hitting the detector surface proves the superposition of rays travelling through the adjacent lens. Taking into account that for a lens in the array the crosstalk is six times more intense than that illustrated in the simulation – since each lens is surrounded by six identical lenses placed at equivalent distances – the image contrast will be eventually affected. The angle of approximately 60° is estimated to be a threshold that can adequately reduce crosstalk phenomenon at all magnification cases. Indeed, a much higher value is required for crosstalk to be present when the image plane is closer to the lens array – higher magnification – or for rays coming from the outer ring of lenses – second and third ring of lenses around each lens.

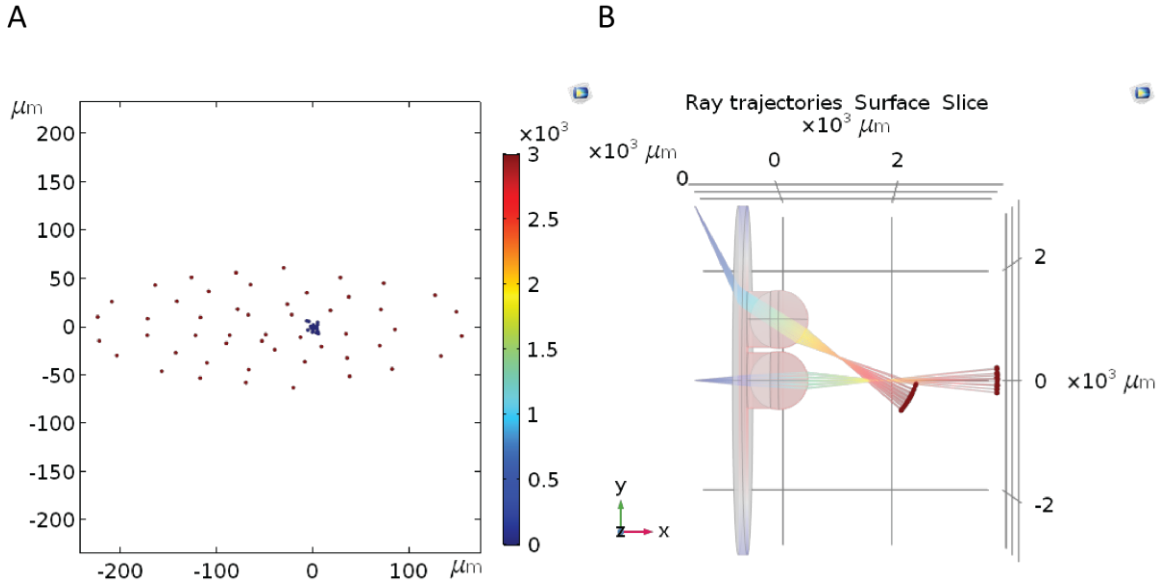


Figure 3.12. The Poincaré map (A) and ray tracing trajectories illustration (B) for crosstalk phenomenon in the case of the analyzed mini-lens array using COMSOL Ray Optics module simulations. In (A) blue spots represent rays coming from the region underneath the lens, while red spots represent rays coming from a region 3 mm away from this lens after passing through the adjacent lens.

2.3. Fabrication and assembly process of the mini-lens array

The fabrication of the lens array is based on single mask standard micromachining processes. A 400 μm thick silicon wafer is thermally oxidized to form a 200 nm thick silicon dioxide layer (SiO_2). A photoresist is spin coated on this SiO_2 layer and exposed based on standard photolithography process. SiO_2 is HF-etched to the regions that are unprotected by the photoresist to create circular openings in the oxidation layer. The SiO_2 layer serves as the mask for Deep Reactive Ion Etching process performed on silicon. Standard DRIE Bosch process was used to etch through the silicon wafer and create circular holes with vertical walls. The Bosch process was used for DRIE etching, which is a time-multiplexed process where two different modes are repeatedly alternated. Sulfur hexafluoride (SF_6) was used in the first step to isotropically etch silicon, followed by the deposition of Octafluorocyclobutane (C_4F_8) to protect all etched regions and prevent further etching of them. The resulting wafer with through holes is divided in smaller pieces by saw dicing and serves as the substrate for assembling the lens array. The fabrication process (steps 1-3 in Figure 13) results in submicron error in the silicon wafer features, since photolithography does not induce any remarkable error in the size of the circular patterns and DRIE process achieves a side wall roughness in the nanometer scale.

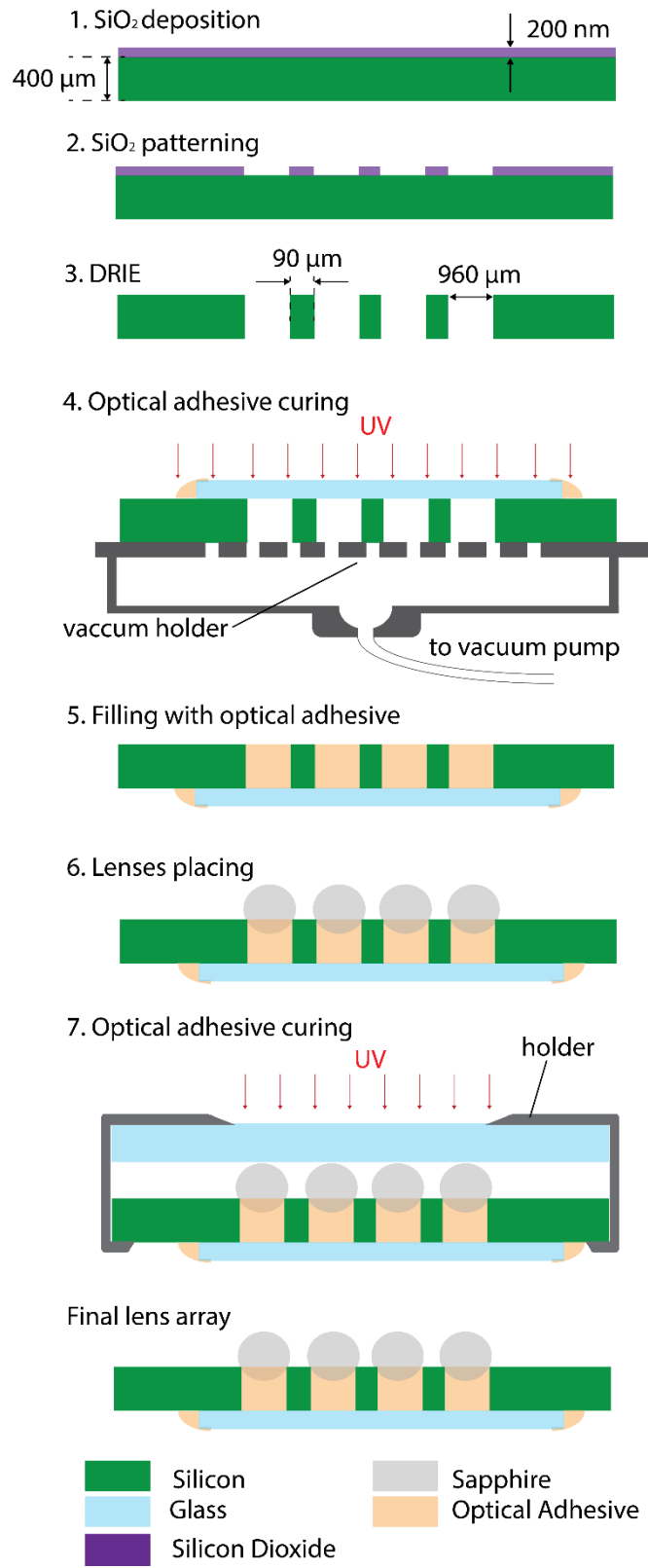


Figure 3.13. Fabrication and assembly process of the silicon based mini-lens array.

The assembly process (steps 4-7 in Figure 13) is crucial to achieve identical lenses, mainly affected by the differences in lenses' height. In the assembly procedure, a glass cover slip is placed at the bottom side of the silicon die and held in place with the use of vacuum. While being vacuum immobilized a small portion of UV curable optical adhesive is added on its borders and cured under UV exposure. This thin glass slide is used to seal the bottom side of silicon through holes to turn them into wells. The wells are filled with uncured optical adhesive and the silicon chip is inserted into a dessicator to remove any air bubbles trapped in the wells while viscous optical adhesive is poured into them. Placement of the lenses on top of each lens is performed one by one starting from the center of the array towards the edges of it. Thus, any excess of liquid adhesive is not trapped in the center of the array and gradually moves away from it. After completing assembly and prior to UV exposure and optical adhesive curing, the entire chip is placed on a custom made holder where a thick glass slide is placed on top of the lenses. Stresses that may be induced during the cure process might push higher some of the ball lenses resulting in a non-uniform array. Thus, the used thick glass slide serves at keeping all lenses in tight contact with the silicon die during curing. UV exposure and curing process is feasible due to an optical window formed on the top of the holder and the use of the transparent glass slide. A 2 min exposure to UV light (# ASN 36W 2) was adequate to assure complete curing of the optical adhesive.

2.4. Characterization of the optical performance

2.4.1. Image based FOV measurement

The importance of the accurate determination of the FOV of each lens relies on the necessity for an overlap between neighboring lenses' FOV so that there are no undetected areas of the specimen during scanning. An accurate measurement of the FOV is not only crucial for the design and scanning principle of the entire device but also for the definition of the maximum scanning step for each configuration. For 1X magnification where the image is an 'one-to-one' projection of the sample on the detector, the maximum scanning step to prevent loss of information due to blind areas in the sample is:

$$scanning\ step_{max} = R_{FOV} \cdot \sqrt{\left(1 - \frac{overlapping\ factor}{100}\right)^2} \quad (3.23)$$

where R_{FOV} is the radius of the disc of FOV for each lens and *overlapping factor* is the percentage of overlap between neighboring lenses during scanning in a direction perpendicular to the scanning direction. Consequently, reduction in the FOV of the lenses, or equivalently operation in higher magnification results in the reduction of scanning step threshold and an increase in the scanning time to complete imaging of the same specimen.

The determination of the FOV was performed by the image produced by the lenses when the selected object for observation is a grid of lines of known gradually decreasing width. The lines pattern was produced by the deposition of a 100 nm thick Cr film on a 1 mm thick glass slide. To accurately measure the FOV by the projected image, without taking into account the magnification induced by the relative position of the lens with respect to the sample, the measurement was based

on the pitch of the pixel array on the CMOS detector employed (DMM 72BUCO2-ML – Imaging Source, with pitch of 2.2 μm and square pixels).

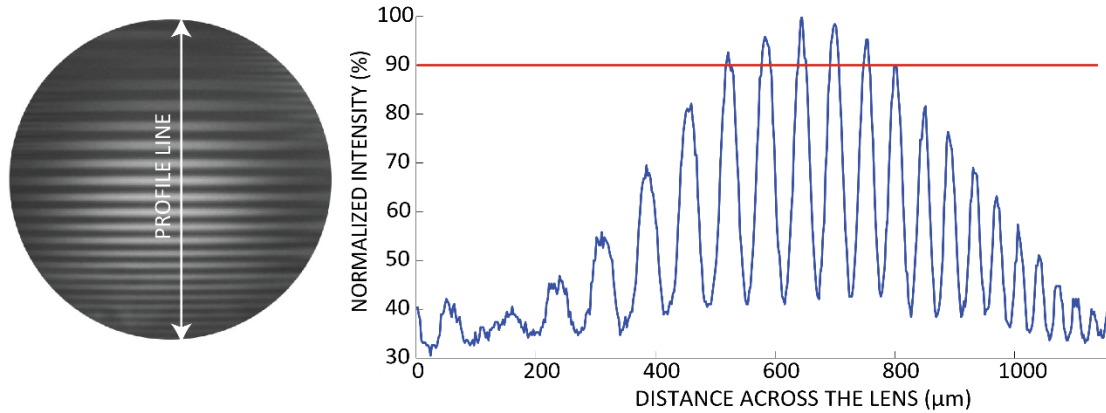


Figure 3.14. Estimation of the FOV of a lens based on the image of a grid of Cr lines on glass projected on a CMOS sensor with 2.2 μm pixel size.

The profile of a line passing through the lens center and vertically to the imaged grid was measured as the intensity of the pixels participating in the line. The light intensity presents a Gaussian shape of gradual decrease when moving away from the lens center as expected (Figure 14). The criterion to determine the radius of the effective FOV disc was selected as the maximum distance from the center of the lens, in which light intensity is not reduced below a threshold of 90% of its maximum value located at the center of the bell shaped distribution. The resulting estimation of the FOV diameter was approximately 290 μm , confirming the simulation results of defocus aberrations simulation.

2.4.2. Image based aberrations estimation

To verify the results of COMSOL simulations three different parallel line patterns of know width were fabricated and imaged with the use of the lens array. These patterns consist of an Aluminum film, of 150 nm thickness, deposited on a standard glass microscope and etched to create parallel lines of 10 μm , 15 μm and 20 μm width and separating distance. The pattern of perfectly parallel lines – appearing black and white – enables the estimation of the aberrations induced by the lenses, due to their spherical phase, by the way they are deformed at the borders of the image. Expected changes in the width of the lines and the spaces separating are combined with a radical blurring of the image in the borders, an effect know as vignetting aberrations also attributed to the spherical phase of the lens. The images acquired are illustrated in figure 15 proving negligible spherical aberrations in the FOV of the lens identified by the red circle (Hadjiński et al., 1996).

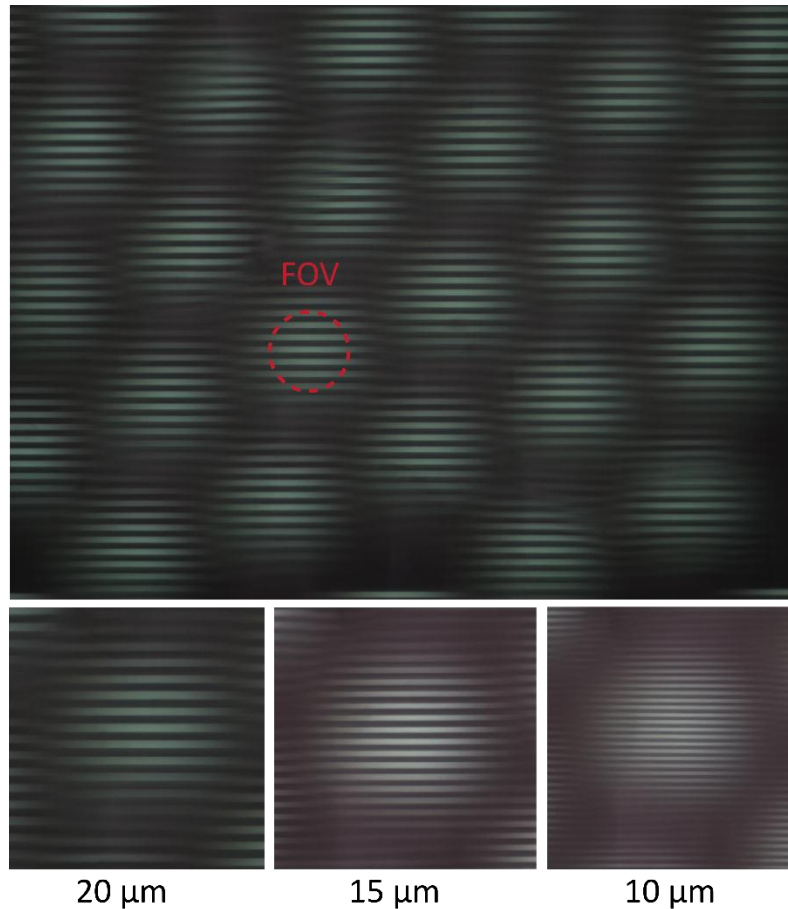


Figure 3.15. Imaging of a lines pattern of different width and separating distances for the estimation of lens aberrations. Blurring due to defocusing (vignetting) dominates in the borders of the lens image while changes in the width of the lines due to barrel distortion are negligible.

2.4.3. Magnification range and focal plane distances for each configuration

In order to define the magnification of the optical system, images were acquired from a blood smear test at different distances between the sample and the lens array. The range of distances was selected from $0\ \mu\text{m}$ – closest position of the lens array with respect to the imaged sample – until $420\ \mu\text{m}$ with a step of $20\ \mu\text{m}$. For each position, a series of images was acquired with the CMOS camera stepping away from the lens array from the closest distance – $0\ \mu\text{m}$ – until a $2000\ \mu\text{m}$ distance. This vertical scanning process – with a scanning step of $20\ \mu\text{m}$ – provides a series of images – 101 images for each position of the sample with respect to the lens array – that are subjected to an algorithmic function in order to define the best sharp and in focus plane for each configuration. Though a large number of algorithms are developed to automatically define focal plane in cytogenetic microscope images (Santos and Solorzano, 1997; Sun, Duthaler and Nelson, 2004), in the conducted experiment the algorithm selected is based on image curvature. As sharpness of an image increases, the variance of the grey values increases. Thus, on a 3D surface plot of the grey values $g(x,y)$ of an image with respect to their pixel coordinates $(x, y) - (x,y,g(x,y))$ – the sharpest image is expected to present higher curvature than the images that are out-of-focus (Helmlí and Scherer, 2001). The calculation

of the focus metric in this algorithm, selected because it provided more consistent results in the specific case of imaging with these mini-lenses, is derived as:

$$FM = |p_1| + |p_2| + |p_3| + |p_4| \quad (3.24)$$

where p_1 , p_2 , p_3 and p_4 are the coefficients used to represent the surface $f(x, y) = p_1 \cdot x + p_2 \cdot y + p_3 \cdot x^2 + p_4 \cdot y^2$ and their values is calculated from the convolution of the image with the arrays g_0 and g_2 as in the following:

$$g_0 = \begin{bmatrix} -1 & 0 & 1 \\ -1 & 0 & 1 \\ -1 & 0 & 1 \end{bmatrix} \text{ and } g_2 = \begin{bmatrix} 1 & 0 & 1 \\ 1 & 0 & 1 \\ 1 & 0 & 1 \end{bmatrix} \quad (3.25)$$

$$p_1 = \frac{g_0 * I}{6}$$

$$p_2 = \frac{g_0^T * I}{6}$$

$$p_3 = \frac{3 \cdot g_2 * I}{10} - \frac{g_2^T * I}{5} \quad (3.26)$$

$$p_4 = -\frac{g_2 * I}{5} + \frac{3 \cdot g_2^T * I}{10}$$

The calculations were performed in MATLAB environment for a specific cropped image of a lens to avoid misleading calculations from defocused regions between adjacent lenses. The derived focal plane position of the CMOS camera with respect to the lens array is presented in Figure 15 for the corresponding distance between the sample and the lens array. The value of the magnification was extracted from the number of pixels used in each configuration across a red blood cell diameter with its nominal value being 8 μm . The extracted working range of magnification is from 1X up to 4X approximately.

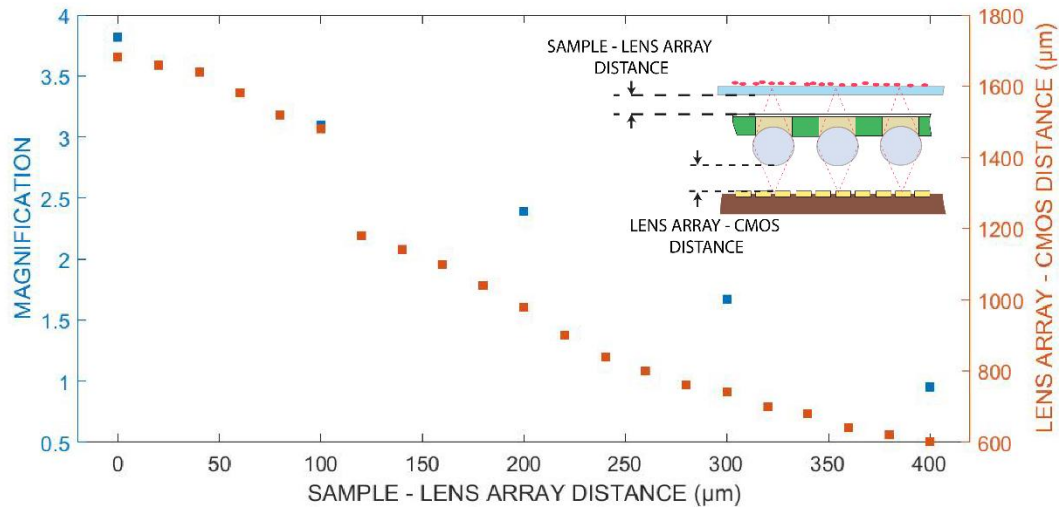


Figure 3.16. Magnification range estimation and automatic focal plane detection for a series of different imaging distances between the sample and the lens array – selected range 0 – 400 μm.

2.4.4. Resolution at minimum and maximum magnification

To extract resolving power of the optical system a custom made grid of 100 nm thick lines were deposited on glass. The grid is based on standard USAF 1951 resolution pattern with the width of line pairs and the separating space between them gradually decreasing from a maximum value of 500 μm – group 0, element 1 in USAF 1951 resolving power test chart, equal to 1 line pairs / mm – until a minimum value of 0.55 μm – group 9, element 6 in USAF 1951 resolving power test chart, equal to 912.3 line pairs / mm. This resolution pattern was observed through the lens element of the array and a profile line was extracted from the acquired image presenting the pixel intensity of the pixels across the line. Local maxima and minima were automatically detected in the profile line plot. The criterion to determine resolution, as the minimum line width visible in each configuration (1X magnification and 4X magnification), was the detection of the line pairs producing a change in pixel intensity – normalized with respect to the maximum value - greater than 0.05 a.u. in both transmissions from local maximum to local minimum and vice versa. The extracted values were 1.95 μm and 0.98 μm for a configuration close to 1X and 4X magnification, respectively. The conducted experiment intended to define the resolution provided by the optical system rather than the resolving power of the lens unit element in the array. The pixel size of CMOS sensor employed for this experiment being 1.67 μm, the resolution of optical system is still camera limited at maximum magnification.

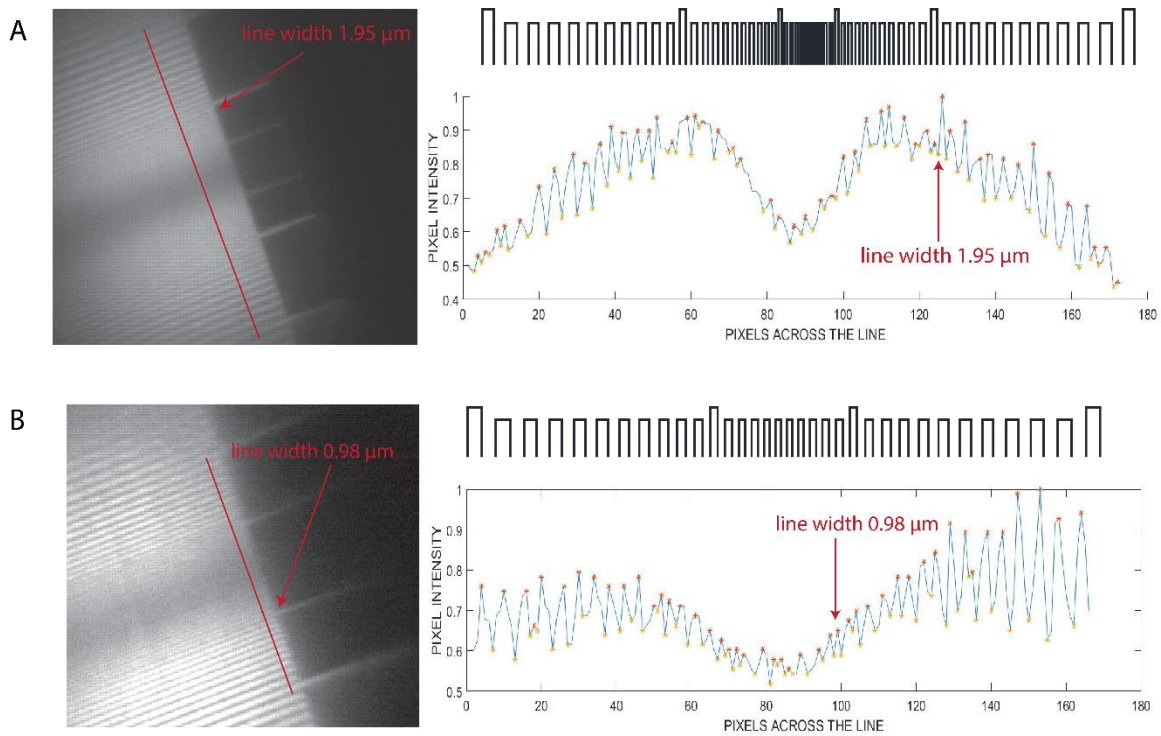


Figure 3.17. A photograph of the resolution line pattern as imaged through a single lens at 1X (A) and 4X (B) magnification and their corresponding light intensity profiles. The red line in the images indicates the profile line in which pixel intensity was measured. A minimum line width of 1.95 μm and 0.98 μm was successfully detected at a configuration close to 1X and 4X magnification respectively.

2.4.5. Uniformity of the lens array

Taking into account the exclusion of vertical focus scanning during specimen observation, the uniformity of the lens array is a critical factor of the optical performance of the device. To characterize uniformity a series of experiments was conducted starting from the observation of the lens array itself and measuring critical feature sizes until the key aspects of imaging with all lenses such as the determination of the focal plane and the out-of-focus error induced by each lens in the array for the common optimal focal plane. These factors resulted in the uniformity estimation in terms of resolution and contrast.

2.4.5.1. Fabrication and assembly process characterization

The factors in fabrication that affect the lens array uniformity are the lens diameter tolerance, the error in the wells diameter and wells edge-to-edge distance resulting from the DRIE process and the thickness tolerance of the Si wafer and the glass cover slip at the bottom of the chip. Referring to sapphire ball lenses, according to manufacturer specifications these present a sphericity $\Psi=0.64 \mu\text{m}$ and a diameter tolerance of $\pm 2.54 \mu\text{m}$. The DRIE process did not result any significant error in the diameter of wells, therefore the error can be estimated less than 0.5 % mainly based on the pixel of the sensor employed to image the wells (Figure 17). The Si wafer thickness variation is claimed by the manufacturer to be less than 5 μm . However, the total thickness variation (TTV) refers to the

entire wafer (4inch wafer diameter) and this value is much smaller for a silicon die of the size of the lens array (approximately 6 mm x 6 mm). Equivalently, the bow defined as the maximum deviation of the median surface to a reference plane and the warp, defined as the deviation of the median surface of the wafer from a reference plane which is already corrected by the bow of the entire wafer, are values describing thickness inhomogeneity to the entire wafer and are expected to be in the submicron scale in the case of the used silicon die. Surface roughness of the polished wafer is held below 1 nm and does not affect the uniformity of lenses' height. Finally, for the case of the used piece of thin glass of standard thickness No. 1, while the nominal thickness could vary from 130 μm to 170 μm , the variation of the thickness in the same cover slip is less than 5 μm and it is expected to be much less than 1 μm for a glass die of the aforementioned size.

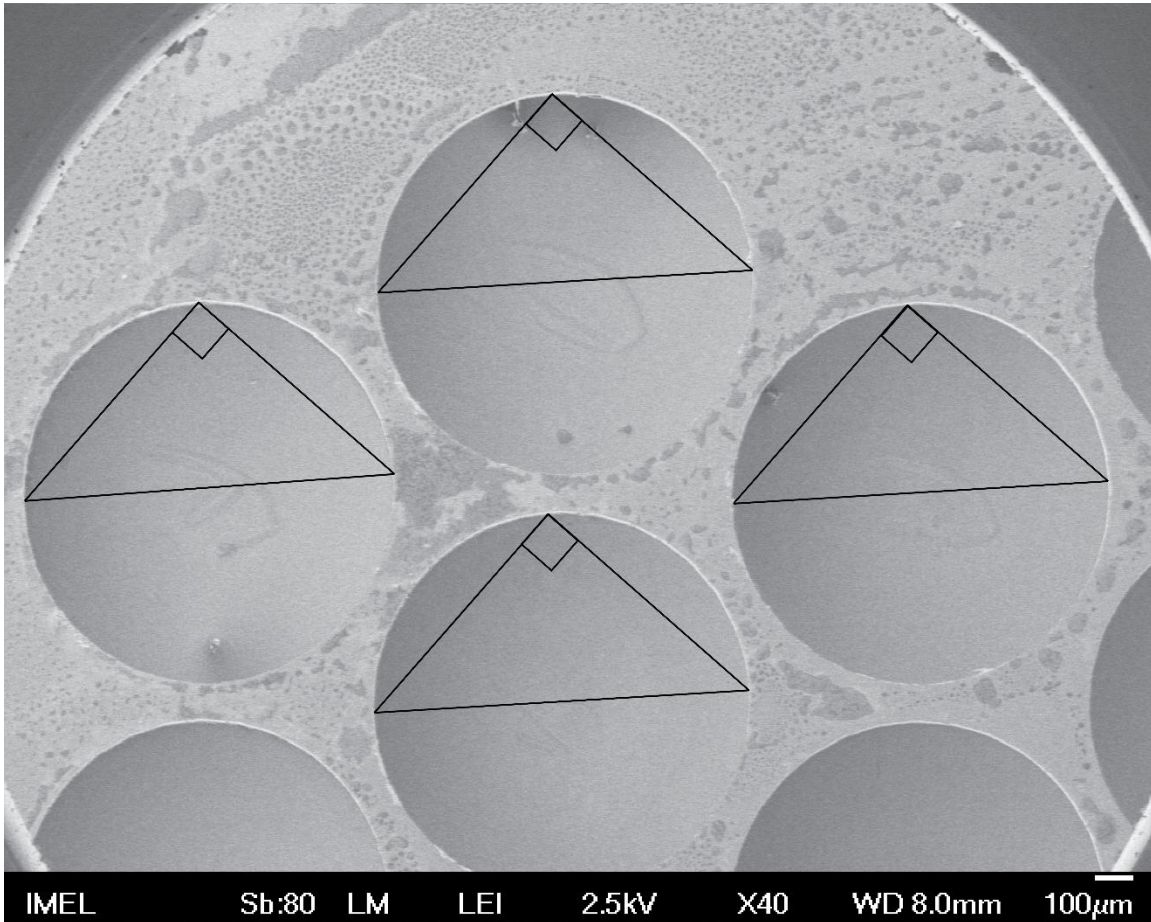


Figure 3.18. SEM image of the silicon die after DRIE process: Top view of the array of the 960 μm in diameter wells.

While the tolerance of critical dimensions is held in a submicron scale, the assembly process may result to severe height variation due to the stresses induced in the optical adhesive during UV exposure and curing. The roughness of the thick glass slide to prevent lenses displacement during this procedure is claimed to be in the nanometer scale, however the tilt that might be induced at the placement of this glass slide to the assembly holder may result in a gradually increasing lens height

along the array. To accurately examine the variation in the topography of the lens array a profilometer was used. From the extracted profile line the height of each lens was defined as the value corresponding to the local maximum and the center-to-center distance was extracted by the same values. The values depicted in Figure 18 are indicative of the entire array with the maximum height difference being at $4.7 \mu\text{m}$ and the center-to-center distance error not exceeding 0.02% of the nominal value. The promising results from the observation described here need to be confirmed by the image that each lens provides since any measurement of the topography may be highly affected by the instrument or human induced error. Particularly concerning the measurement conducted with the profilometer, the slightly increasing distance between the lenses across the extracted line may be indicative of the misalignment/tilt of the measurement line with respect to the axis of the lenses.

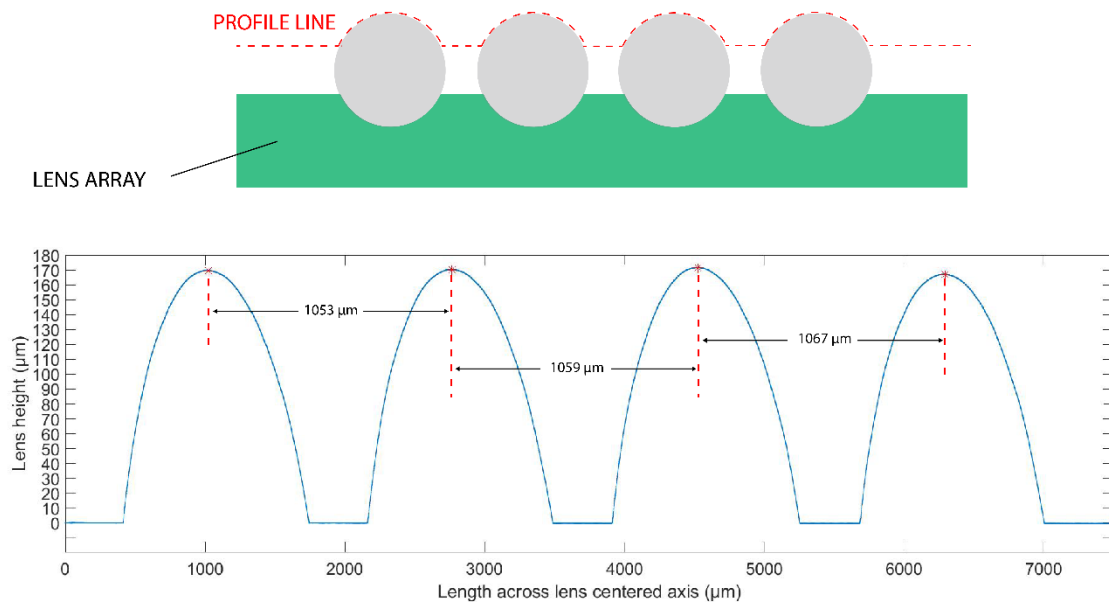


Figure 3.19. Profile line across lens – centered axis. The reference point was selected on the first step so that the measurement is held within the range of operation of the profilometer. Flat regions correspond to spaces between the lenses where the measurement is out of range for the instrument. The differences in height between the lenses have a mean value of $2.6344 \mu\text{m}$ with a maximum value of $4.6618 \mu\text{m}$.

2.4.5.2. Focal plane uniformity

Aiming at precisely determine the focal plane location, a laser beam at 655 nm was used by a collimated laser diode module (Thorlabs, CPS532) and expanded with an optical beam expander (Thorlabs, BE15M-A) to provide illumination with parallel monochromatic rays to the entire lens array simultaneously. The optimal focal plane was selected after scanning in vertical direction with the movement of the CMOS detector with a step of $20 \mu\text{m}$, as the one depicting minimum spot size for each lens. This plane was located at the bottom surface of the glass slide confirming the theoretical calculations and conducted simulations for the location of the focal plane. For the aforementioned plane the intensity of the created spots was plotted normalized with respect to the maximum value, the differences in light intensity being less than 5% of the maximum spot intensity.

The minimization of the spot size at the focal plane eventually leads to the demand to compare the spots produced by each lens. The pixel intensity distribution of each spot, illustrated in Figure 19.D, presents a circular imprint whose radius was calculated from the total surface of pixels with intensity higher than 0.2 a.u. (normalized intensity). The derived radii for all spots in the image remained within the range 2.2 pixels – 3.7 pixels.

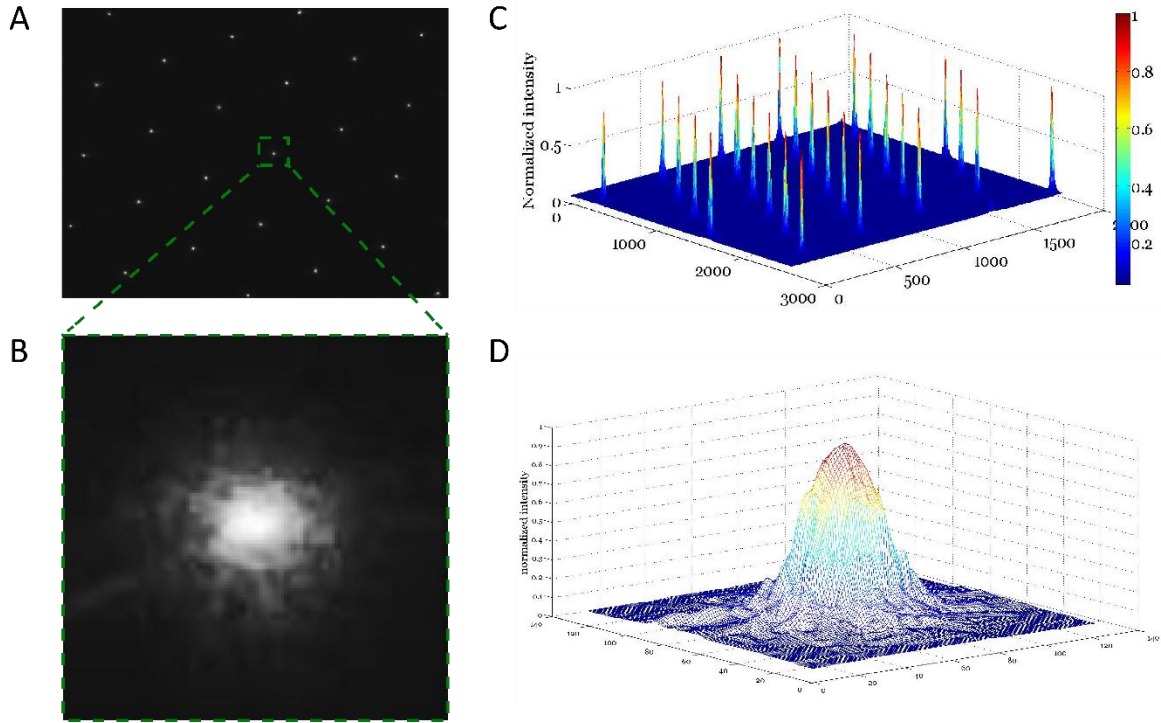


Figure 5. (A) Laser spot image at the focal plane of all lenses in the array. (B) Image of a spot produced by one lens. (C) Normalized pixel intensity values with respect to the coordinates of each pixel. The spots are presented as sharp peaks with almost identical intensity (variation: 5 %) (D) Light intensity distribution for a spot created by one lens.

2.4.5.3. Contrast and resolution uniformity

To quantify the error in resolution and contrast produced by each lens in the optimal focal plane a calculation of the in-focus factor and the contrast of an image of a blood smear film was performed. The in-focus factor is a metric indicating the ability of each lens to produce sharp, in-focus images and it is derived by the algorithmic calculation described by the curvature based autofocus method and the equations (2.24) – (2.26). Consequently, for each lens in the array the in-focus factor is increasing until the focal plane, followed by a decrease and it usually presents a bell shaped distribution. Defining the out-of-focus error as the difference in the in-focus factor from its maximum value (1 in the case of normalized values), the optimal focal plane for the entire array is selected as the one in which the averaged out-of-focus error – averaged for all lenses – was minimized. For the selected plane a plot of the in-focus factor normalized with respect to the maximum value of each lens clearly depicts that the out-of-focus error remains below 20 %.

Using the grayscale images of the focal plane, the contrast (C) was calculated based on the Michelson formula (Peli, 1990):

$$C = \frac{\text{standard deviation of the light intensity gradient}}{\text{mean value of the light intensity gradient}} \quad (3.27)$$

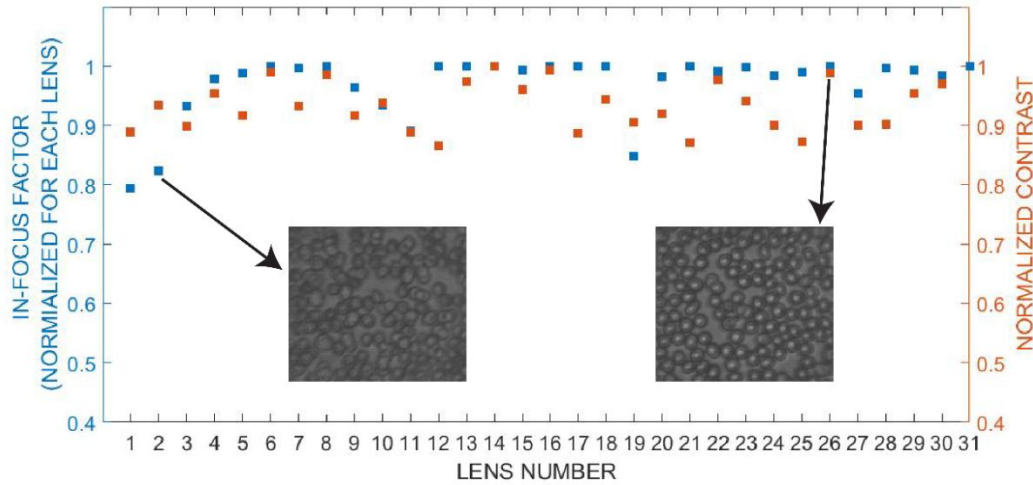


Figure 6. In-focus factor normalized for each lens within the array, as measured by images obtained from a blood smear test (left axis); Contrast of the image produced by each lens of the array (right axis); 5 lenses were excluded from this experiment as they did not produce high quality images.

The resulting variations of contrast factor prove that all lenses produce images within 12 % of the maximum contrast for this specific specimen of blood film. The contrast factor being highly dependent on the image features, will change if the experiment is repeated for a different type of object, the aforementioned experiment was selected as indicative of the performance of the optical system in imaging a relatively low contrast biological specimen.

3. The scanning head and the mechanical components of the micro-scanner

The motorized translation stage is mainly responsible for the movement of the optical head across the scanning direction. Thus, its design and manufacturing process, described in the following section, lean on the need to eliminate artifacts induced in the imaging procedure due to the repeated stepping process. A characterization experiment was performed for the quantification of the induced defocusing error across scanning direction while an automatically stitched image produced by a series of scanning steps from one lens is presented as a proof of optimal alignment of all mechanical components.

3.1. Design and fabrication of the mechanical parts of the micro-scanner

The motorized translation stage comprises of a high torque stepper motor (ST4118L) in size of NEMA 17 (42 mm) with 1.8° angle step (full step). The motor is connected through a motor flex coupler with a leadscrew upon which the scanning head is sliding, with a minimum stepping size of

5 μm . Two shafts, parallel to the leadscrew, are used to support the scanning head and prevent rotation of it around the leadscrew during sliding. The scanning head, hosting the optical components of the imaging system, is allowed to move across the scanning direction for covering a distance of 40 mm maximum length. A press button is used to prevent movement beyond zero position. The head is moving beneath the sample – either a typical microfluidic chamber or a glass slide – across its long axis. These components are held in place by a cubic enclosure made of PVC that has open side walls (Figure 21). The sample is placed on top of the device, hosted by the sample holder and kept fixed during scanning. The sample holder is a PVC component that is the lid of the entire enclosure. It contains an opening at the center of it to allow optical access from the optical head to the specimen. It can host a standard glass slide of 60 mm x 22 mm surface size, however, the scanned surface is defined by the CMOS effective area and the maximum scanning range provided by the stepper motor. The entire device has a volume of 128 mm (length) x 80 mm (width) x 107 mm (height). Its weight is approximately 1 kg. The illumination source – not illustrated in the schematic – is placed on top of the device, on the vertical axis to the scanning direction, and at a working distance of approximately 20 cm (see section 4). The scanning/imaging device together with the illumination source can be hosted in an opaque PMMA cage of 20 cm x 15 cm x 22 cm to prevent artifacts in acquired images due to ambient light.

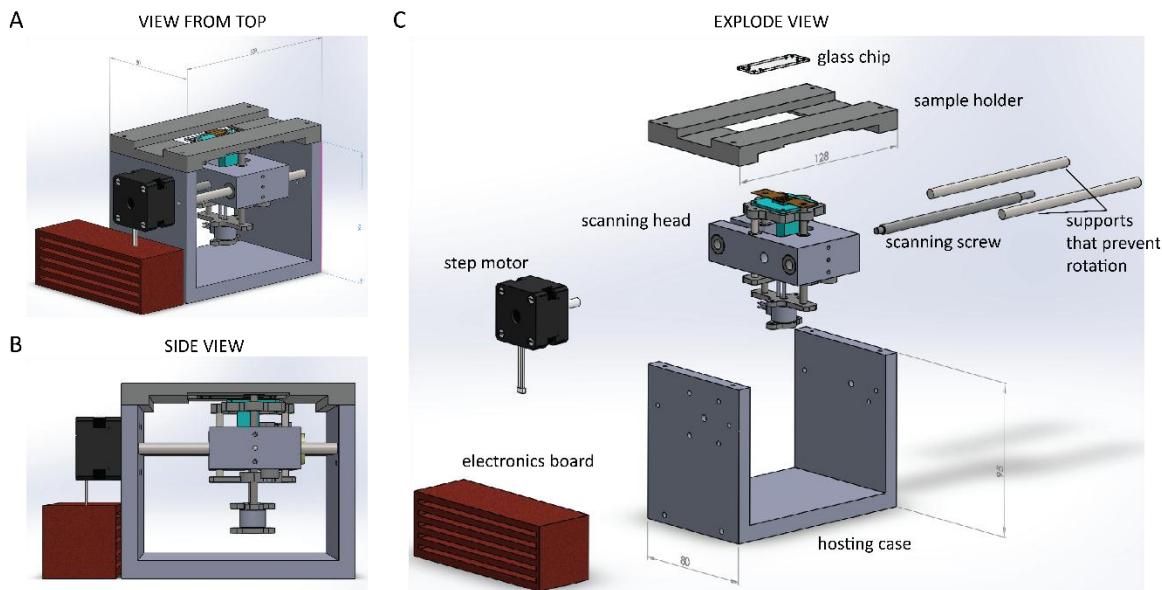


Figure 7. Schematic of the design of the scanning device seen from top side view (A), side view (B) and with all components illustrated after separation – explode view – (C).

Particularly concerning the scanning head, it comprises of the optical components of the system responsible for imaging the specimen: the lens array and the CMOS camera employed. It also hosts two small stepper motors in order to allow for vertical axis movement of the CMOS detector and the lens array with respect to the sample. The employed stepper motors (ST-PM35-15) for z-scanning and image focusing have a 7.5° stride angle and they are connected to a 3 mm in diameter drive shaft they can provide a minimum step length of 20 μm for a maximum length range of 3 mm.

To achieve focused sharp images in each configuration of separating position between the sample and the lens array – different magnification in the design described above – the maximum distance to travel with these step motors does not exceed 500 μm for the case of lens array positioning with respect to the sample and 2000 μm for the case of the detector with respect to the lens array. To prevent movement beyond these points and possible damage in the hosting scanning head components, three optical interrupters are used to stop any movement when the distances between the lens array holder, the sample holder and the camera holder are minimized. The scanning head contains supporting shafts for preventing any tilt or rotation of the lens array and the camera holder during focusing movement. It also contains an enclosure permanently attached to the leading screw to ensure the entire head follows the rotation of the screw during scanning.

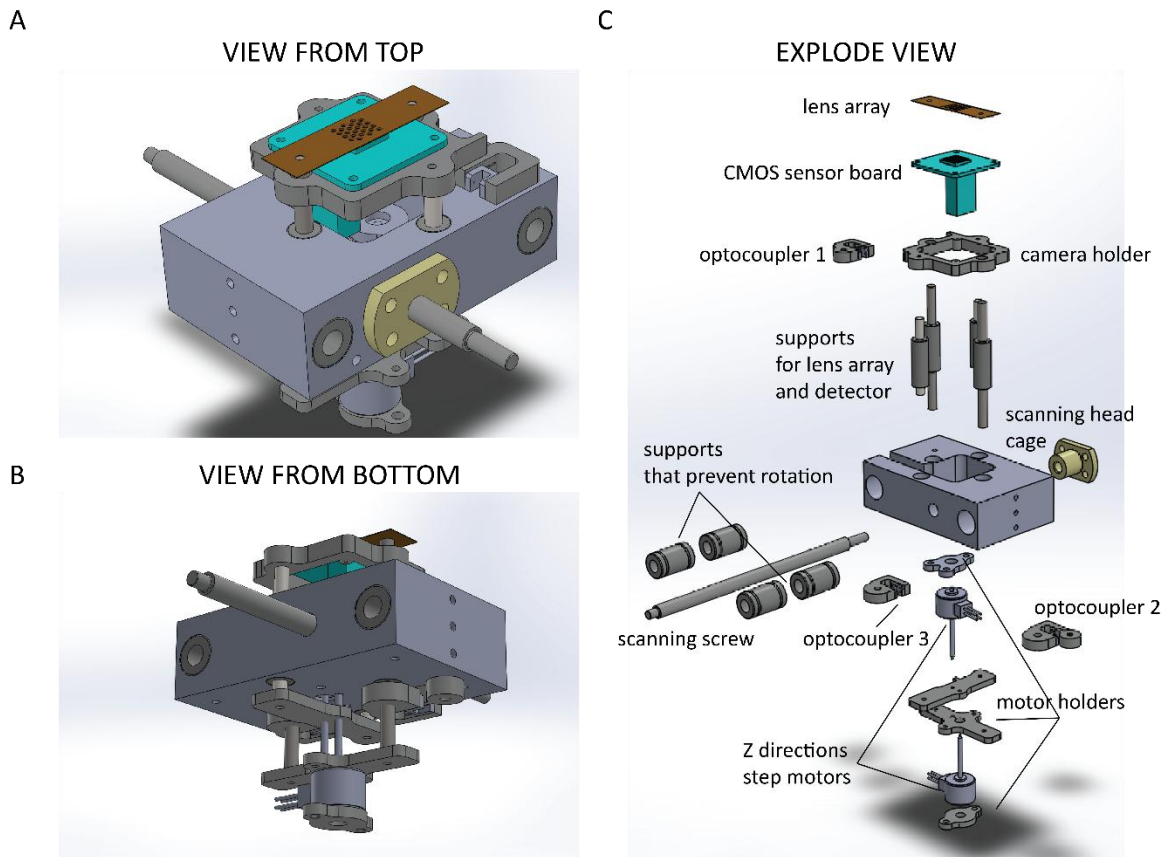


Figure 3.23. Design of the scanning head seen for top side (A) and bottom side view (B). The components it comprises of are illustrated in explode view (C).

All components of the scanning head were CNC (computer-numerical control) polyvinyl chloride (PVC) manufactured. The device enclosure is made of polymethyl methacrylate (PMMA) and manufactured with a CNC laser cutter. The screws and shafts used are off-the-shelf components of low cost. The manufacturing and assembly process was accomplished in N.C.S.R. Demokritos mechanical laboratory and in collaboration with Mechanical Engineering School of the National Technical University of Athens (Section of Mechanical Design and Automatic Control).

3.2. Characterization of the scanning performance

The accuracy of micro-positioning of the scanning head as well as the parallelism of all moving components with respect to the sample surface is of critical importance for the accurate performance of the imaging system. Additionally, the need to design a platform of decreased cost and complexity eventually leads to the exclusion of sophisticated alternatives in micro-positioning, but to choose for stepper motor movement solution, profiting of a series of advantages that compensate provided accuracy and cost of equipment. In the sections to follow, a quantification of micro-positioning and parallelism error is conducted based on the theoretical error of the motors employed and the artifacts induced in the acquired images across the scanning direction.

3.2.1. Micro-positioning stepper motors error

Stepper motors are brushless, synchronous electric motors that convert digital pulses into mechanical shaft rotation. The motor can take one step only at a time and the size of step is always the same, since each pulse sent causes the motor to rotate a precise angle. Thus, the stepper motor can be controlled without the need to integrate a feedback mechanism. For the scanning stepper motor and the leadscrew employed in the design, a minimum step size of 5 μm is provided. Provided that a hybrid stepper motor presents a precision error of 3 - 5 % of the minimum step, the error of positioning in the scanning direction is less than 250 nm. This error being non-cumulative from one step to the next, the accuracy of micro-positioning is much higher than the optical resolution provided by the system. Thus, no detectable artifacts are expected to be present in the automatic imaging and mosaicking of the acquired pictures.

For the stepper motors employed in the vertical direction the error is much higher – theoretically at 1 μm - with the minimum step being at 20 μm . However, this error is radically reduced by the gravitational force acting on the components of the optical head. Being in the vertical direction each moving part is positioned at the end of each step at the lower case of the error gap. Table 1 summarizes all specifications of the employed motors concerning movement accuracy, speed and induced error.

| | ST4118L | ST-PM35-15 |
|-------------------------|-----------------|------------------|
| Resolution | 1.8°/step | 7.5°/step |
| Minimum step length | 5 μm | 20 μm |
| Total travel length | 40 mm | 3 mm |
| Micro-positioning error | 250 nm | 1 μm |
| Size | 42 mm | 15 mm (diameter) |

Table 3.1. Micro-positioning specifications for the scanning and focusing moving parts based on the stepper motors employed and the shaft screws connected to them.

The repeatability of the system in accurate positioning of the scanning head at the same point (specific distance from the starting point) after a series of scans, was eliminated by effectively

programming the controller of the scanning motor to return to zero position after performing a scanning process. Thus, no detectable error is observed in a series of repeated scans.

3.2.2. Parallelism and defocusing error across scanning axis

Despite positioning, the sliding movement of the scanning head with respect to the sample surface has to be perfectly aligned so as no defocusing error is added while imaging away from the starting point. To quantify this error in parallelism a series of images is acquired from a blood smear test for equally spaced positions – the selected step is 1 mm – across a total length of surface scanning equal to 25 mm. The error quantification is based on the variations of the in-focus factor as this is described by the curvature autofocusing algorithm (Helmlí and Scherer, 2001) and the equations (3.24) – (3.26).

The variations in the in-focus factor, normalized with respect to the maximum value are below 5 % and are mainly attributed to the slight differences of the smear pattern imaged in each position. Though blood smear film presents no noticeable changes in detectable features, the size and shape of cells being identical across a blood smear, the reduction in the number of cells present away from the starting point may induce changes in the intensity of image pixels affecting overall light intensity and contrast, therefore affecting the measured in-focus factor. The images tested in this experiment are collected by one lens in the array to strictly measure uniformity across the scanning direction and exclude the error of non-uniformity within the array.

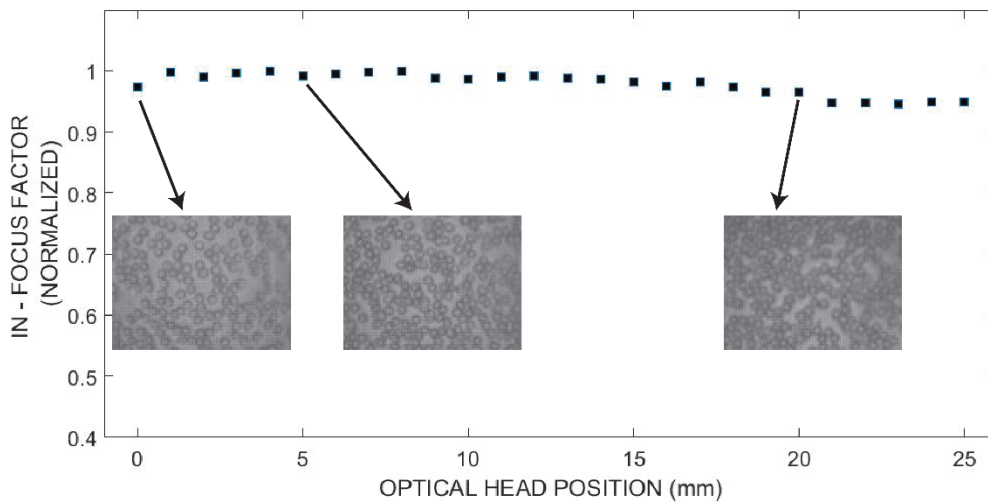


Figure 3.24. Variations in the in-focus factor calculated by a series of images of a blood film specimen acquired by one lens in the array in equidistance points across scanning direction. The scanning step was selected to be 1 mm and the total travel length is 25 mm. The calculation is based on autofocusing algorithm of image curvature (Helmlí and Scherer, 2001). No apparent drift is present in the images and the variations are attributed to the slight differences in imaging pattern – changes in the density of the sample across the smear blood test.

As a proof of the negligible errors in the scanning direction – both in micro-positioning and gradual defocusing – a series of images acquired by one lens with a selected scanning step of 100 μm across

a travel length of 2 mm, were stitched to create a mosaic of the entire FOV of the lens during the scanning process. Each of the 20 acquired images was cropped around the lens FOV, centered at the same point of the figure in each shot. The cropped images were subjected to vignetting effect correction and they were stitched based on an automatic algorithm in MATLAB environment. The automatic algorithmic stitching is based on a repeated translation of images in the order of acquisition for a specific distance with respect to the previous image. Since this length is identical for all images, any positioning error across scanning direction would have resulted in mismatching between neighboring images. The absence of any mismatching errors in the final stitched image proves that the positioning of the scanning head is accurately accomplished, with a misalignment error smaller than the resolution of the optical system. Thus, any misalignments cannot be observed by the employed detector.

Additionally, no apparent drift of the moving optical components with respect to the sample is present on the illustrated mosaic of blood smear specimen. The artifacts observed are mainly attributed to vignette effect, an aberration affecting light intensity in the FOV area, with gradual reduction of it away from the center of the lens. This effect is corrected based on the overall pixel intensity and contrast of each image and is affected by the imaged pattern in each area of the sample. With the vignette effect being highly dependent on distance from the lens center, evidently the selection of a smaller scanning step results in more uniform stitched image due to reduced fluctuations of light intensity within the same step. Irrespectively of the FOV of the lens in each step, the adjacent images are stitched by further cropping based on the selected scanning step. The stitching algorithm is based on weighted superposition of neighboring images and the overlap region between them is reduced to the strict minimum – an area of 2 pixels in width – so that the final image quality is not affected by the mosaicking process.

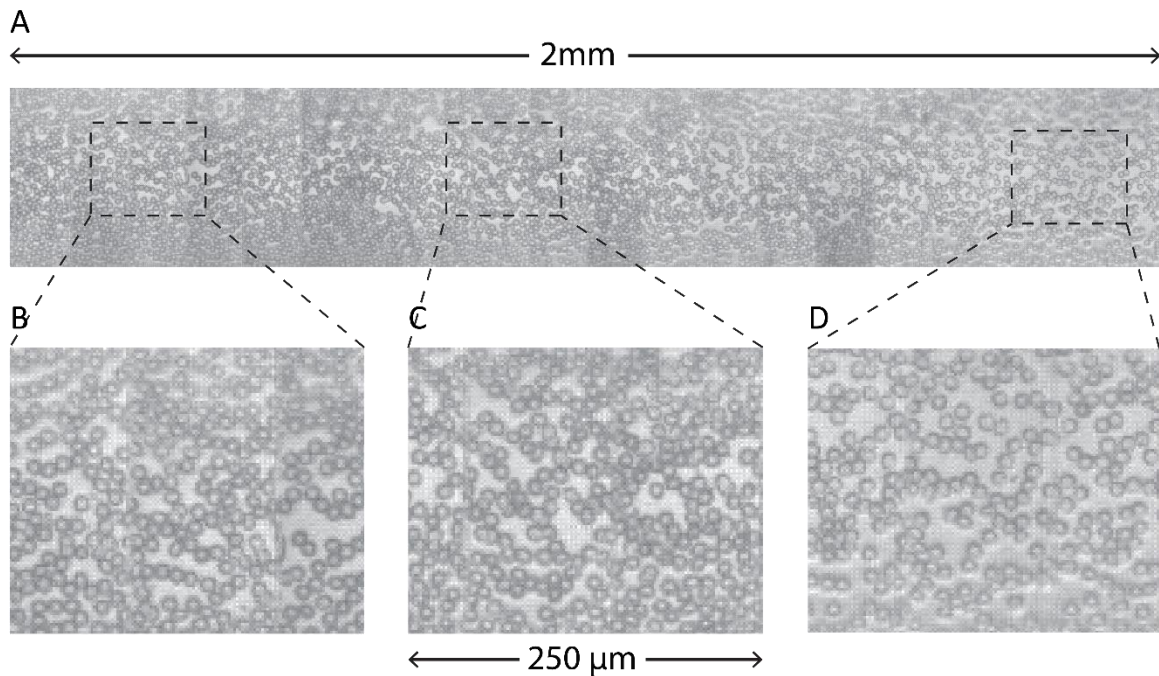


Figure 8. Automatically stitched images acquired by one lens of the array with a scanning step of $100\ \mu\text{m}$ and a total travel length of $2\ \text{mm}$. The 20 images were cropped in the FOV of the lens and the mosaic was extracted by an automatic stitching based on repeated translation of images for a specific distance. Thus, the micro-positioning error can be examined. Gradual defocusing of the image across the scanning direction is not noticeable.

4. The illumination scheme – transmission mode imaging

In transmission mode imaging, the illumination of the sample is provided by a square LED array (EDMUND OTPICS, #66-830). Refracted light, after being scattered by the sample is collected by the mini-lenses of the optical system. This light source consists of an LED array (operated at 24 V) covered by a diffuser. The emitted light is homogeneously diffused onto the biological sample and it is distributed over a surface 6 % wider than the surface of the source (square of a side length 5 cm). The entire scanner along with the light source is placed inside a PMMA opaque enclosure to prevent ambient light from entering the scanner. Since the illumination provided by the employed source is homogeneous, rays travelling at a wide angle with respect to the optical axis of each optical unit – each lens in the array - may cause severe blurring in the final image as a result of the superposition of images from distant areas of the sample, a phenomenon known as ‘crosstalk’, explained in details in section 2. In the following, the experimental examination focuses on determining the extent at which this phenomenon affects image quality and the description of an operating scheme aiming at the elimination of it.

4.1. Elimination of crosstalk phenomenon

To avoid the use of complex and costly optical components to achieve collimated illumination, the crosstalk phenomenon was examined with respect to the working distance of the light source from the sample. The distance between the light source and the sample affects the contrast of the

produced image. If that distance is short, the images obtained from neighboring lenses are projected onto overlapping areas on the CMOS sensor. In the case of a non-collimated light source, such as the employed LED array-based source, increasing the distance between the LED array and the sample can reduce crosstalk, as diverging rays originating from the source do not reach the sample (Tanida et al., 2001; Lee et al., 2017). To select the minimum illuminator – sample distance where crosstalk is adequately reduced, a contrast measurement experiment was performed as a factor indicative of the image blurring at different distances. The contrast factor is derived from the Michelson formulae described by equation (2.7) (Peli, 1990).

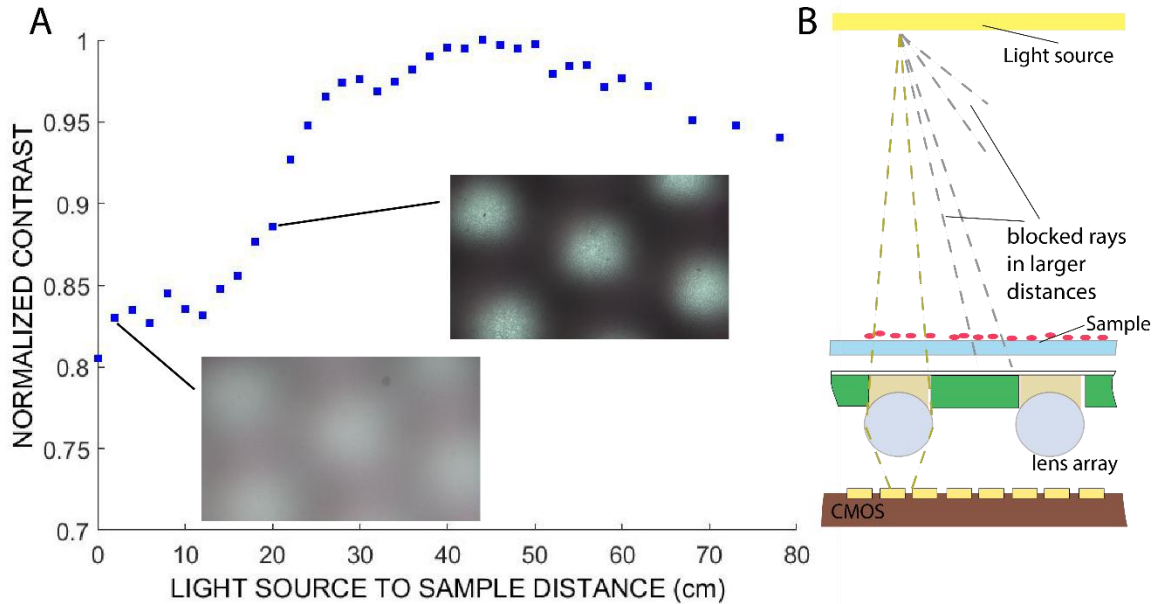


Figure 9. Normalized contrast versus light source – sample distance (A). Larger distances result in less crosstalk and clearer images as diverging rays do not reach the mini-lens array (B).

Observation of the resulting variations in image contrast with respect to the working distance separating the sample from the LED array source lead to an assumption of gradual decrease of the crosstalk phenomenon until a critical distance of approximately 45 cm. Further lengthening of this distance results to a decrease in image contrast as a result of the inadequate illumination intensity provided. The examination of produced image quality for distances closer than 45 cm proves that a clear sharp image is produced when the separation between the light source and the sample is greater than 20 cm. At this point the contrast factor is equal to 0.89 in a scale normalized with respect to the maximum contrast – provided at 45 cm working distance.

5. Electronic parts of the scanning system and computer-assisted control

The electronic parts of the scanning system are responsible for the control of scanning process and image acquisition. The electronics board is an Arduino Uno microcontroller board connected with stepper drivers to control the motion of stepper motors, with the CMOS sensor board to control image acquisition parameters – exposure time, gain, gamma factor – and it is also directly connected

with the optical interrupters and the scanning stop button to detect minimum distances between mechanical parts. An electronic board, additional to the Arduino Uno board is used to host all needed circuitry for the power supply, the stepper drivers-related electronic components and all necessary connectors. The power requirements for the scanning/imaging platform are particularly subdivided in the requirements of the stepper motors, the imaging board, the illumination source and the microcontroller employed. For the operation of the prototype setup the power supply is retrieved by external power supply devices or the PC connected to the device through a USB port. Computer assisted control of all scanning and imaging specifications is achieved through a LabVIEW code used for the implementation of a Graphical User Interface(GUI). In the following sections all aspects of electronic parts and software coding for automatic scanning and imaging of a sample are explained in details.

5.1. Schematic of the electronic parts circuitry

The electronic drawing of the board hosting all electronic components is illustrated in Figure 26. It contains a low-voltage stepper motor driver carrier (Pololu drivers - DRV8834) responsible for scanning stepper motor control and two identical micro-positioning stepper motors (Pololu drivers - DRV8825) for the control of vertical direction movement of the camera and the lens array with respect to the sample. Their operation specifications are presented in Table 2.

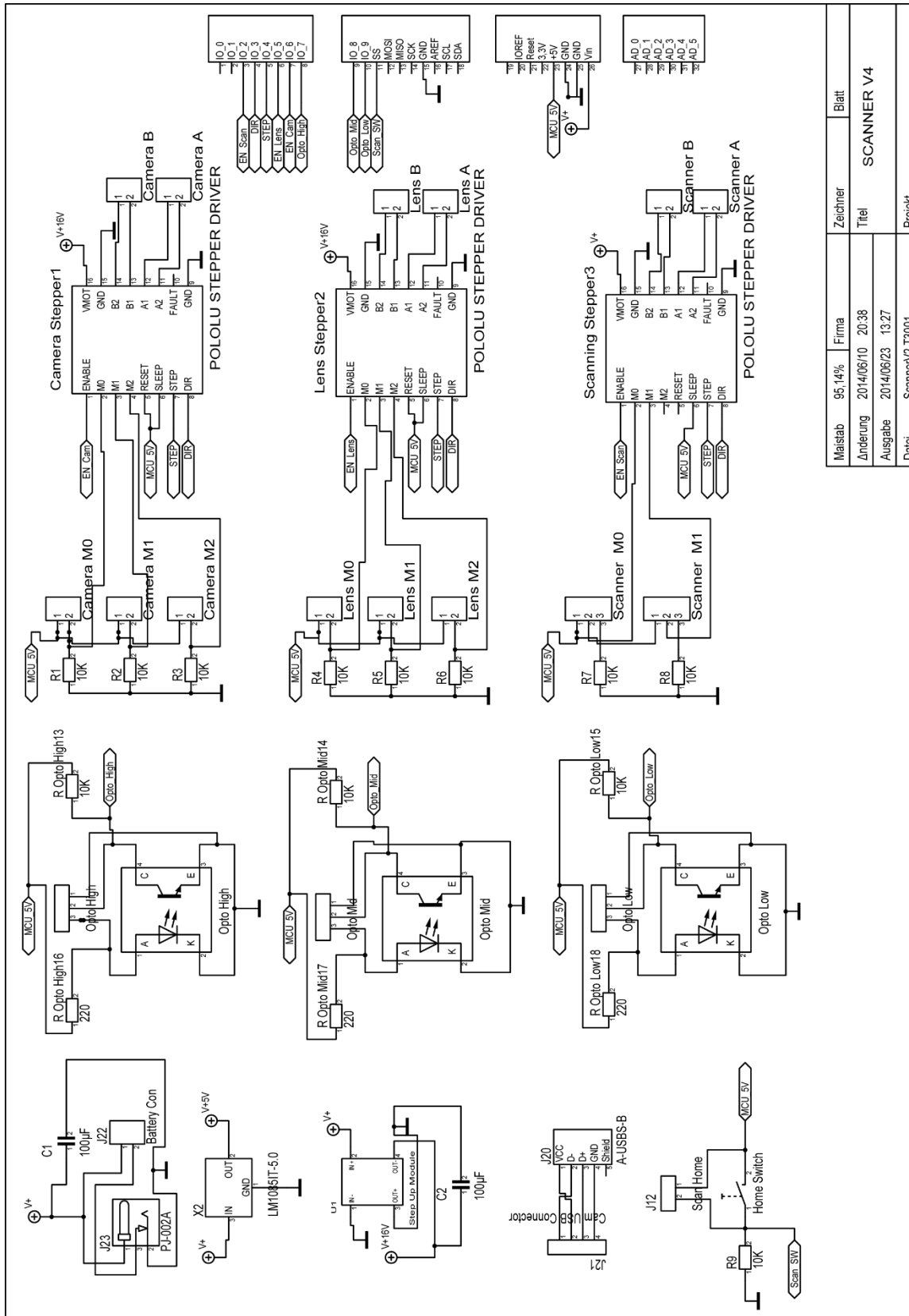
| | DRV8834 | RV8825 |
|------------------------------|----------------------------------------|----------------------------------------|
| minimum operating voltage | 2.5 V | 8.2 V |
| maximum operating voltage | 10.8 V | 45 V |
| continuous current per phase | 1.5 A | 1.5 A |
| maximum current per phase | 2 A | 2.2 A |
| minimum logic voltage | 2.5 V | 2.5 V |
| maximum logic voltage | 5.25 V | 5.25 V |
| micro-step resolutions | full, 1/2, 1/4, 1/8, 1/16, and 1/32 | full, 1/2, 1/4, 1/8, 1/16, and 1/32 |

Table 3.2. Operating specification of the employed stepper motor drivers

It also comprises of three opto-interrupters of high sensitivity and very small packaging (TR 20403). These optical interrupters are responsible for stopping the movement of the lens array and the CMOS camera when their positioning minimizes one of the distances separating the optical components of the system – the lens array, the camera boards and the sample holder. An additional switch connected to the circuit is used to inform homing of the scanning head, when this reaches the starting position.

All components are connected to the Arduino Uno Rev 3 (Code: A000066) separated board operating with an ATmega328P microcontroller. This microcontroller is programmed to send pulses to the stepper motor drivers so as to periodically control the movement in both axis and to receive the signals from the optical interrupters to stop the process when homing is reached. It

communicates with serial (USB) connection with a local computer in a master-slave mode so that the entire process is controlled by the user through the Graphical User Interface. Through this communication process, in every step the microcontroller receives a command line to perform a step and sends back a response command to inform the hosting computer for the successful accomplishment of it. The program code of the Arduino Uno board is available in Appendix 2.



| | | | | | |
|----------|-----------------|-------|--|------------|-------|
| Maßstab | 95,14% | Firma | | Zeichner | Blatt |
| Änderung | 2014/06/10 | 20:38 | | TITEL | |
| Ausgabe | 2014/06/23 | 13:27 | | SCANNER V4 | |
| Datei | ScannerV2.T3001 | | | | |
| Projekt | | | | | |

Figure 10. Schematic drawing of the electronic circuitry used in the scanning device.

ARDUINO UNO REV 3

| | |
|-------------------------|------------------------------------|
| Microcontroller | ATmega328P |
| Operating voltage | 5 V |
| Input voltage | 7-12 V |
| Input voltage (limit) | 6-20 V |
| Digital I/O pins | 14 (of which 6 provide PWM output) |
| PWM digital i/o pins | 6 |
| Analog input pins | 6 |
| DC current per I/O pin | 20 mA |
| DC current for 3.3V pin | 50 mA |
| Flash memory | 32 KB (ATmega328P) |
| SRAM | 2 KB (ATmega328P) |
| EEPROM | 1 KB (ATmega328P) |
| Clock speed | 16 MHz |
| Length | 68.6 mm |
| Width | 53.4 mm |
| Weight | 25 g |

Table 3.3. Specifications of the Arduino UNO REV 3 board.

5.2. External power supply

The power requirements of the system are a crucial aspect referring to the feasibility of reaching full portability of the developed device. In the described prototype the power supply is given by external devices. Power requirements for each component are listed in Table 4. The low demands of the particular components, keep the total power requirements of the device down to a limit of less than 7 W. Particularly concerning the Arduino UNO and the CMOS camera boards, they are exclusively powered by the USB port output power. An external programmable power supply (HAMEG – HMP2020) is used for DC power requirements of the circuit connected to the motorized translation stage. The power of the illumination source is provided by an AC (230 V) to DC (up to 32 V) converter connected with a rotor resistance to manually control light intensity.

| Component | Operating voltage | Current consumption | Power requirements |
|-----------------------------------------------------------------------|-------------------|---------------------|--------------------|
| Arduino UNO REV 3 | 5 V | ~100 mA | ~0.5 W |
| Electronics board hosting stepper motor control and opto-interrupters | 8.5 V | ~ 500 mA | ~4.25 W |
| CMOS board | 4.5 – 5.5 V | ~250 mA | ~1.25 W |
| Illumination source in transmission mode | 24 V | ~60 mA | ~ 1.44 W |

Table 3.4. Power requirements for all components of the scanning/imaging system

5.3. Graphical User Interface and computer-assisted control

A LabVIEW code was developed to perform automatic scans of samples in the device. The code offers a series of available tests for the user to select through a Graphical User Interface (GUI). It also operates as a master for sending commands to the Arduino UNO board (slave) and control the movement of the motorized stage. It controls the image acquisition, by the selection of specific values in parameters relevant to imaging with the employed CMOS sensor. In Table 5 the available tests are listed, while in Figure 27 the main GUI is illustrated. Prior to all available experiment setting the user can define imaging parameters such as the exposure time and gain of the CMOS sensor. In these experiments, a scanning process is usually accomplished either in the scanning direction or the vertical direction to define the optimal focusing position of the components participating in the system. As it is clear by the parameters participating in each process, no vertical movement is performed during scanning of the sample. In each step of the automatic scanning procedure the image acquired is saved to a specified folder. The main block diagram of the LabVIEW code is available in Appendix 2.

| Available tests Parameters | Depth of focus | Depth of field | Lens array focus position | Scanning process |
|---------------------------------------------|----------------|----------------|---------------------------|------------------|
| Scanner initial distance | ✓ | ✓ | ✓ | ✓ |
| Lens-to-object initial distance | ✓ | ✓ | ✓ | ✓ |
| Lens-to-CMOS initial distance | ✓ | ✓ | ✓ | ✓ |
| Object moving step | ✓ | | | |
| Lens moving step | | | ✓ | |
| CMOS moving step | | ✓ | | |
| Scanner step | | | | ✓ |
| Number of pictures | ✓ | ✓ | ✓ | ✓ |

Table 3. List of available tests in the GUI and the corresponding parameters of scanning process each test can control.

A second code was also developed offering to the user basic image processing tools for live investigation of the imaged sample. Among the available image parameters related to image enhancement can be altered while imaging the specimen and features borders' detection can be accomplished based on a series of algorithmic image segmentation processes. Particularly, brightness, contrast and gamma factor can be changed on live imaging with the processed image being presented in a different window. The image histogram is always available and the equalization

of it is an additional feature that can enhance specimen's features presentation. Basic detection of features in the image can be performed by the application of a series of edge detection algorithms, such as Prewitt algorithm, Sobel algorithm, Roberts algorithm and differentiation or gradient based detection. The live image processing GUI is illustrated in Figure 28. The main block diagram of the LabVIEW code is available in Appendix 2.

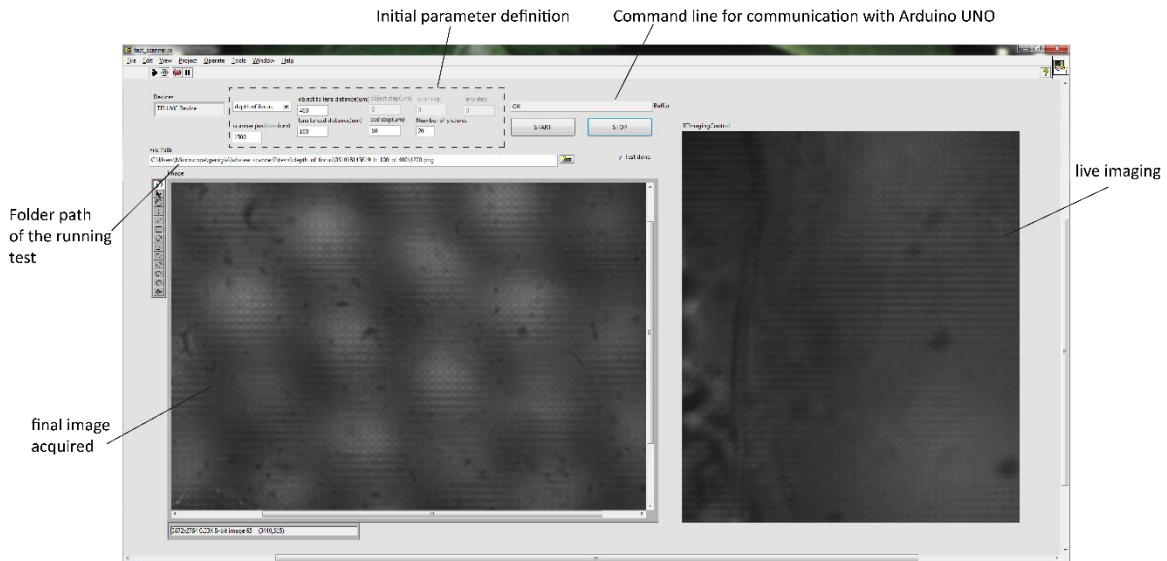


Figure 11. Main GUI for the control of the device components and the automatic scanning and imaging of the sample based on the specified parameters.

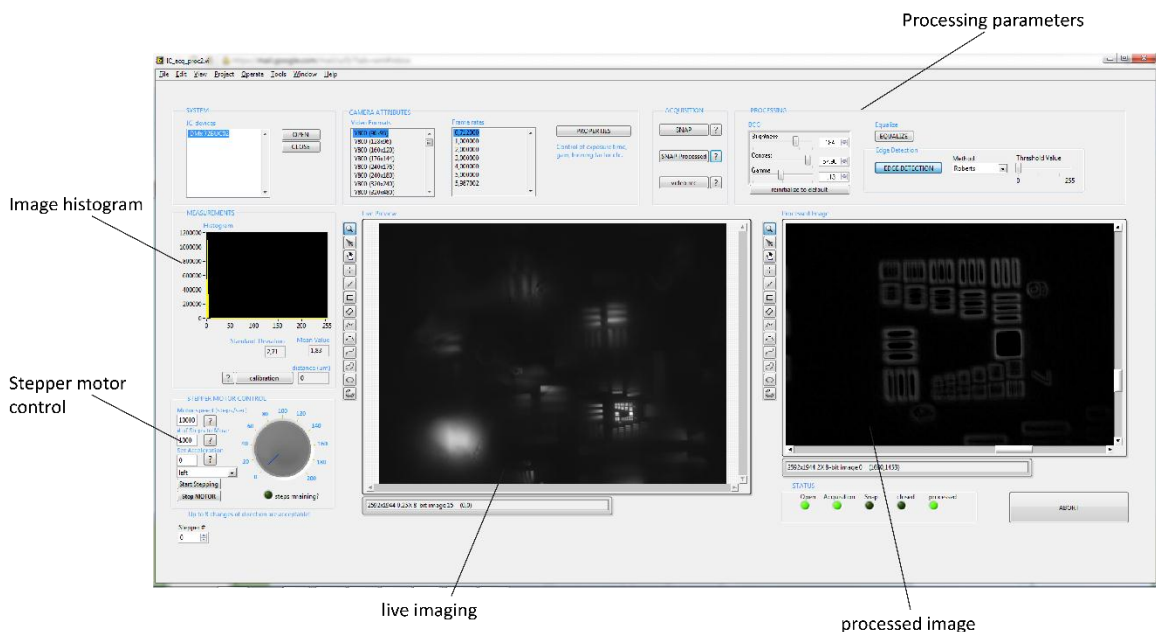


Figure 3.29. Live image processing GUI, for basic image enhancement and edge detection algorithms application, that allows the user to estimate resolution and image quality.

6. Image processing algorithms for image mosaicking, cell detection and counting

As a post procedure to the scanning and image acquisition of the specimen, the acquired set of images is subjected to an automatic stitching process and a cell detection and counting algorithm. The purpose for developing these automatically executed algorithms is to validate the feasibility of operation without expert user for step-by-step observation of the specimen and manual counting of cells. In the sections to follow, a detailed description of the algorithmic process is given, accompanied by an explanation of constraints to compensate, when imaging with a mini-lens array-based, low cost, scanning system. These obstacles refer to the parameters affecting image manipulation and enhancement, image feature extraction and computational requirements of automatically driven procedures.

The entire algorithmic procedure initiates with a preprocessing step that automatically isolates the parts of each image corresponding to the effective FOV of each lens in the array and performs basic image enhancement to correct image aberrations. In the stitching process, the cropped images acquired for all scanning steps are combined with reference to a specific lens in the array to form the entire image acquired by each lens during scanning. Final step of the mosaicking is the combination of these long images in a united picture of the entire sample, providing the ‘virtual slide’.

6.1. Preprocessing for lens aberrations correction and image enhancement

The picture acquired by the CMOS detector in each step of the scanning procedure contains the imaged regions of the sample that lie underneath each one of the 36 lenses in the array. Since a few rays scattered in a wide angle by the sample cannot be blocked by the silicon substrate of the lens array, they travel through the mini-lens and hit the detector surface in the regions of the picture located between the lenses. Thus the spaces between the lenses appear blurred and dark. The presence of a significant amount of dark – blackish grey – pixels severely affect image enhancement techniques implying the use of histogram specific algorithms to increase image quality (Hussain et al., 2018). In the case of dark areas created underneath lens array interspaces, the corresponding pixels do not contain any exploitable information of the imaged sample, therefore should be excluded by the image enhancement process.

Cropping of the initial image is performed in an automatic manner to maintain smaller images, each one corresponding to the effective FOV of a particular lens. The automation of this procedure is achieved through a calibration process of the imaging system that can be accomplished once prior to the first scanning process. In absence of any sample and by locating all optical components in the position of optimal focusing at the desired magnification, an image is acquired. This image corresponds to light intensity distribution over the detector surface. Light intensity surface plot presents local maxima in the center of each lens. Therefore, through the location of these local maxima, it is feasible to determine the coordinates of the center of image projected by each lens in the array on the sensor area. These coordinates can be used for locating the center of the cropping rectangle that corresponds to each lens FOV, for all scanning steps. The use of large, uniform illuminating surface over the entire scanned area, assures that the center of each lens is projected on the same point on the detector surface without the need the illumination source to follow the translation movement. The rectangles that define the cropped images are in this stage larger than the

effective FOV of the lens, to assure no loss of exploitable information, while they are further decreased during the stitching process.

Each cropped image is subjected to enhancement methods mainly intended to correct the effects of the spherical shape of the lenses. The barrel distortion aberrations are negligible in this part of the image as only the effective FOV is selected for each lens. Thus the size of cells appears to be the same for those cells that are located at the borders of the image and those at the center of it. This result is in full compliance with the theoretical estimation of the aberrations-free effective FOV prediction and the estimation of the lens aberrations by the use of the lines pattern (see section 2.4.2.). The vignetting effect induces severe light intensity decrease as the distance from the center of the image elongates. This inevitably creates a perspective view in the image giving a spherical distribution of brightness. To correct the flat field of the cells images we apply a bias correction algorithm (Zheng et al., 2009). This algorithm estimates the light intensity background field and proves to be more efficient compared to the performance of an automatic vignetting effect correction. With the selected algorithmic enhancement possible dislocation of the center of the lens at the previous cropping step does not affect image correction as with vignetting correcting algorithms where the center of the lens should coincide with the center of the image.

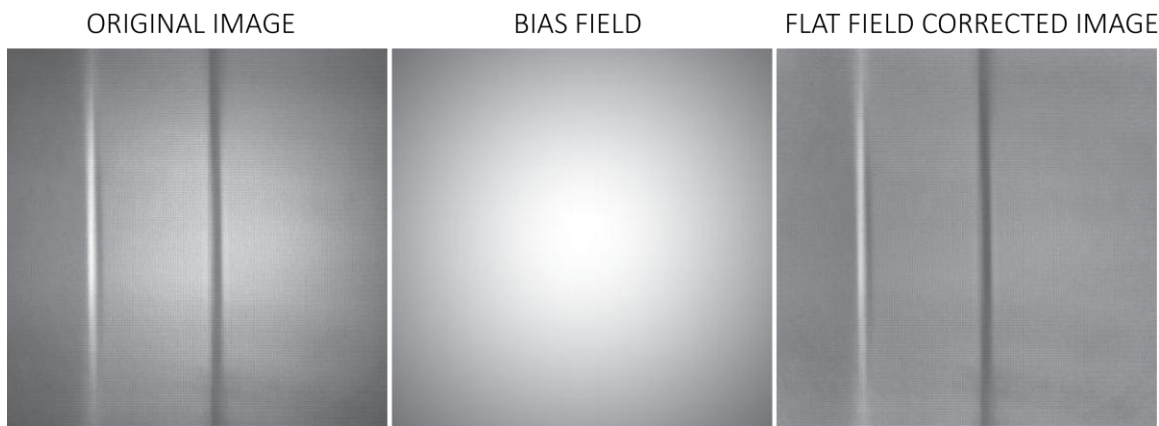


Figure 3.30. Flat field correction, required prior to the stitching process. This step is crucial for the entire image appearance as well as for the effective automatic detection of cells and features that depend on uniformly applied image segmentation techniques.

6.2. Image mosaicking of the ‘virtual slide’

The entire image of the scanned sample is formed by a two-step procedure: (a) The cropped images acquired during scanning by each lens are stitched to form the image of each of the 36 lenses. (b) Each one of the 36 stitched images is placed on the exact position with respect to neighboring lenses to form the mosaic of the final image. In both steps, the stitching process is based on the known translational movement of the lens array – the selected by the user scanning step – expressed in pixels. This conversion is based on the selected distances between the sample, the lens array and the detector, all determining the magnification. Thus, for a given magnification, the scanning step in pixels is given by the equation:

$$d(\text{in pixels}) = \frac{\text{scanning step (in } \mu\text{m)} \cdot \text{Magnification}}{\text{detector pitch (in } \mu\text{m)}} \quad (3.28)$$

Since the magnification is calculated based on imaged features of known size, with this calculation being restricted by the provided resolution of the system and the detector pitch, this mathematic expression was used only for the first estimation of the dislocation that should be imposed on each image. The final values used in the algorithmic process giving the exact position of each image with reference to the one acquired in the previous scanning step is defined by successional tests performed.

The selected stitching method was preferred over other automatic methods proposed in literature due to the robustness it provides in this specific application. Cross correlation is the most widely studied algorithmic process to perform image mosaicking (Nielsen and Yamashita, 1995; Rankov et al., 2005; Ma et al., 2007; Johar, Manjula and Namita, 2017). However, in the designed microsystem, this method has proven unreliable. Indeed, in the case of dense blood cell samples, such as whole blood smear tests, the cells form clusters, being packed the one next to the other resulting in frequently repeated patterns that have many features in common – same size of cells, perfectly circular shape and packed clusters. In the case of rather sparse samples – white blood cells captured on the surface of internal walls of a chamber with all other cells being washed away – the small size of the FOV of each lens results frequently in images free from cells, where no pattern exists to enable cross correlation sharp increase. The presence of repeated patterns or the total absence of a particular pattern present severe obstacles in this algorithmic process, while the serial nature of stitching images results in a serial repetition of an error even when this appears only once. The procedure is also affected by the small size of the images to stitch and the spatial distribution of brightness background field, that in many cases is not possible to be entirely smoothed.

The merging step of two adjacent images is accomplished by further cropping of the two images so that minimum overlap of 2 pixels wide is achieved followed by an alpha blending process whereby a weighted combination of the two images is used to create a composite image. This merging algorithm is preferred as being the simplest and fastest. Possible ghosting and registration errors that may cause blurring (Abdullah and Agha, 2013) are minimized by the limited width of the overlapping region. Thus, the resulting stitched image proves perfect alignment though subjected to frequent changes in flat field intensity (Figure 25).

The same methods are followed for image mosaicking of the 36 lenses' images, the location of each one being defined by a series of tests for the specified magnification. The final image of a glass biochip containing 2 chambers, of 7 routes each, is illustrated in Figure 31. The chambers' inner walls are functionalized with anti-CD45 antibody to capture white blood cells (WBCs) expressing CD45 biomarker on their surfaces.

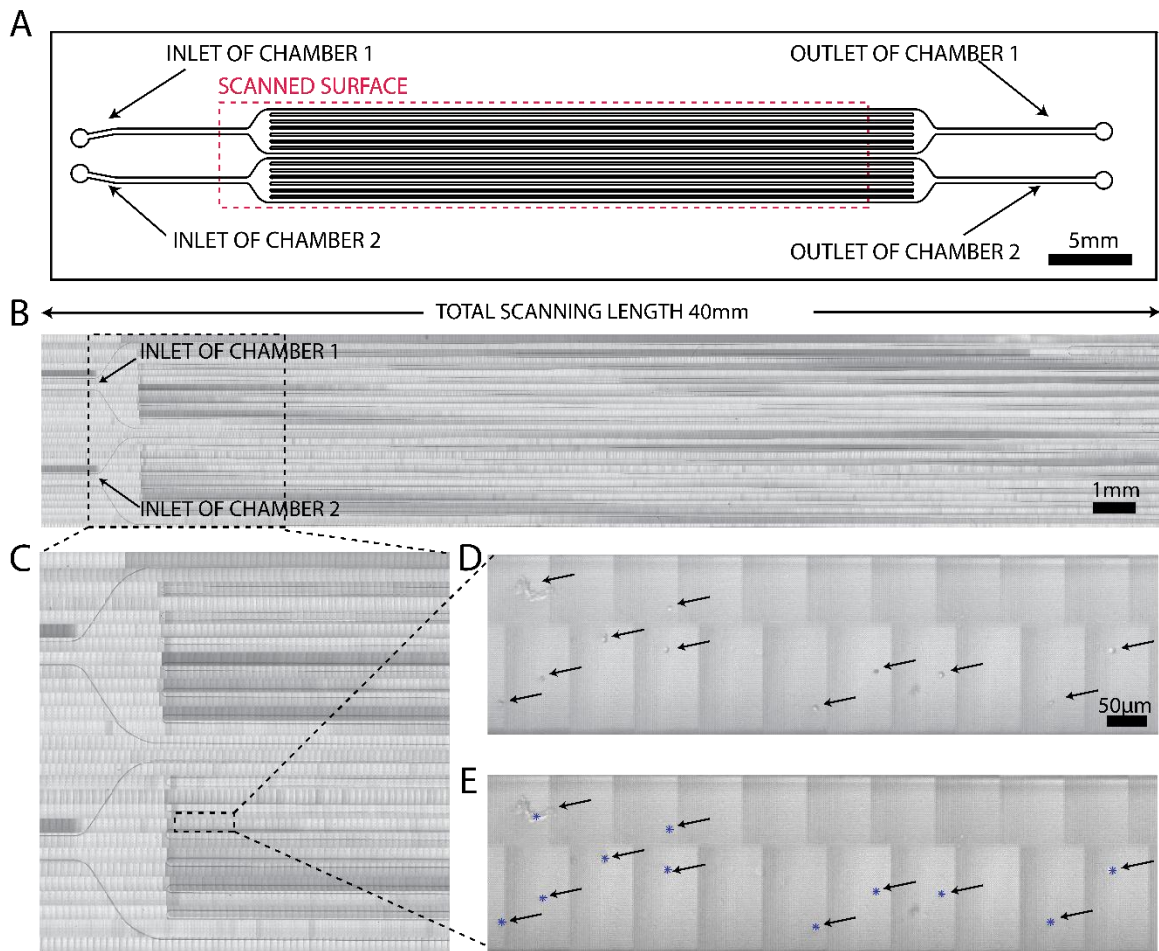


Figure 3.31. (a) Schematic of the microfluidic chip with 2 parallel chambers used for the experiment. Dotted square defines the scanned surface. (b) Stitched image of the 4 cm long microfluidic chip of two parallel chambers. (c) Zoom-in of the image in the region of inlets. (d) WBCs captured in the microfluidic chamber (e) automatically detected WBCs (indicated with an arrow) with Sobel operator image segmentation algorithm.

6.3. Cell detection/counting

The automatic detection of specific features in an image is a widely studied field of image processing; a study that has led to numerous algorithmic approaches but is still open to further investigation. The main reason lies in the restrictions imposed by the aim of the application and the target feature characteristics. Thus, in the case of the presented imaging platform technology, the automation of cell detection and counting should be classified by the blood cell population that each time needs to be measured.

Different cell populations and different methods of cell immobilization on the substrate result in different density of the sample, different size and shape of the cells as well as different contrast between the cells and their aquatic environment. Particularly, in normal whole blood smear film tests, the cells present a perfectly circular shape with slightly increased size compared to other tests of non-fixation methods, while exhibiting high contrast with the environment and easily detectable

boundaries (Adewoyin and Nwogoh, 2014). In cases of abnormal changes in the shape of cells in the peripheral blood smear film a blood related disease can be detected due to the non-disc shaped appearance of them, which still falls in the category of application based detection – e.g. sickle cell anemia can be diagnosed based on the sickle shape of red cells (Diez-Silva et al., 2010).

On the contrary, whole undiluted blood test of non-fixed cells simply inserted in a thin microfluidic chamber suffer from cell clusters formed due to the possibility of red blood cells to be squeezed (Pan et al., 2018). The red blood cells present a donut shape appearing both like disc shaped or linear shaped based on their stochastic tilted position with respect to the imaging axis. White blood cells in this case appear rather spherical, with distinguishable larger size compared to red blood cells, however, depending on the height of the microfluidic chamber they are frequently seated on the bottom side and covered by red blood cells, thus cannot be easily detected. Dilution of whole blood samples may seriously enhance automatic detection efficiency, however, it is not preferred since it requires sample preprocessing, undesirable in the case of point-of-care devices.

In applications where a blood cell population is isolated and the rest of the cells are washed away the sample appears rather sparse while the cells exhibit common characteristics. The isolation method is crucial for the shape of captured cells. In the case of a subpopulation of white blood cells, such as CD4⁺ T lymphocytes, capturing on a functionalized surface gives to this type of cells an irregular shape with their membrane being largely deformed while the nucleus retains its initial shape. This deformation results in larger surface projection of the cells but also in a radical decrease in the contrast with the aqueous solution (Khalili and Ahmad, 2015). Some white blood cells expressing CD3 or CD8 biomarkers and captured by the use of the corresponding anti-bodies tend to maintain their spherical shape presenting evidently higher contrast with the environment. This may be due to the elasticity of the specific cell population but also due to the biomarker density over the cell surface or the strength of the specific bonding type.

Apart from the target group of cells, the size of the image to be subjected to segmentation and registration algorithms is of crucial importance for the automation of the detection process. Therefore, when image size changes the parametric values concerning background noise removal, expected feature population or more importantly thresholding over the entire image can be severely non-effective. This is the case for image segmentation algorithms applied in the final extracted image of the entire sample that has been scanned. The density changes over a large sample area result in different contrast values observed in regional level, therefore a common threshold applied in the entire image will induce a large error of false detection or sub-detection spatially distributed. Moreover, the computational requirements in this case are prohibitive as the image needs to be maintained in high resolution while being in the order of G pixels in size. Inevitably the image segmentation algorithms need to be applied in each image retrieved by each lens in one step of the scanning process. The summation of the detected features can give the final count of the cell population. Double detection of cells located in the overlap between adjacent lenses can be avoided based on the stitching parameters. The overlap between the lenses is sufficiently wide to allow for effective detection of cells located in the borders of two images.

In the sections to follow a description of the algorithmic processes developed for two different types of blood cell population and immobilization methods takes place. Both algorithms intend to prove

the feasibility of cell detection given the provided resolution of the scanning platform that operates in a range of magnification much lower than bulk laboratory microscopes, for which most cell counting algorithms have been developed in literature.

6.3.1. Peripheral blood smear film cell detection

Peripheral unstained blood smear tests have been imaged in the proposed scanning platform by using a color CMOS camera (Imaging Source DFM-72BUC02-ML) of $2.2\ \mu\text{m}$ pixel size at the maximum provided magnification. The produced images exhibit a generally high contrast level with the cells' borders being clearly distinguishable by their environment, while both red and white blood cells exhibit a circular shape.

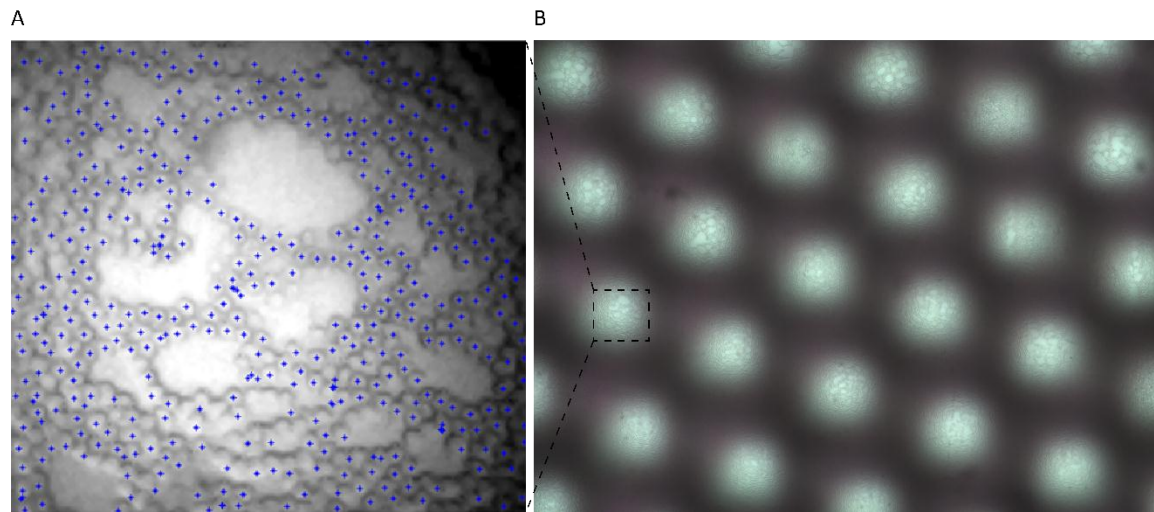


Figure 3.32. Blood cell detection performed on one lens image of an unstained smear whole blood film.

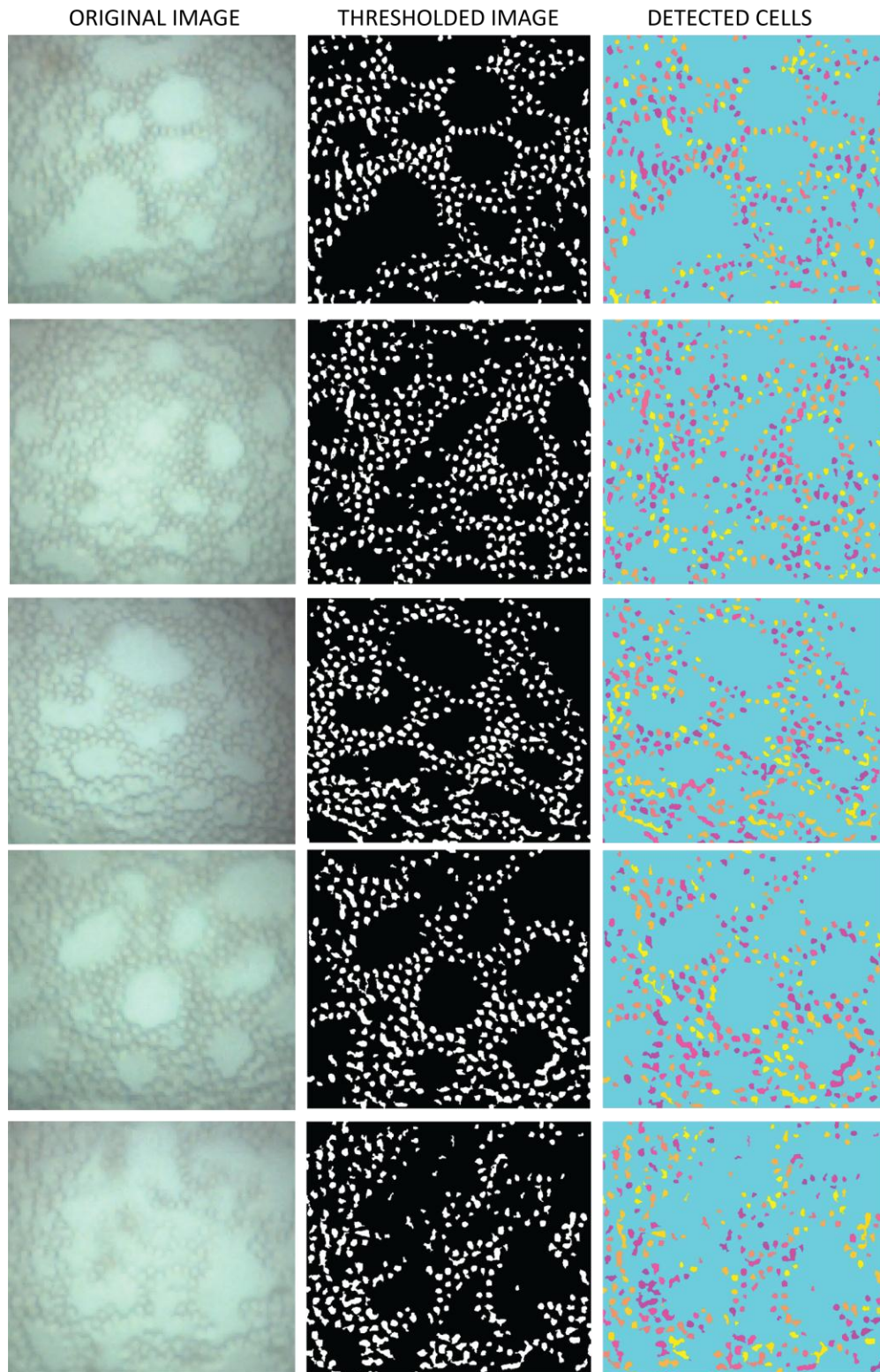


Figure 3.33. Thresholding and segmentation algorithm applied in 5 different lenses in the array exhibiting different contrast level.

The detection algorithm developed is based on image segmentation techniques using morphological operators. Mathematical morphology is well suited to biological and medical image analysis (Vincent, 1993; Nedzved, Ablameyko and Pitas, 2000; Ruberto et al., 2000; Di Ruberto et al., 2002), allowing for the isolation of features depending of their geometrical properties. Particularly concerning blood cell images (Ruberto et al., 2000; Di Ruberto et al., 2002; Mukherjee, Ray and Acton, 2004), this type of image segmentation appears to be highly efficient, while being at the same time simple, with minimum computational and time requirements.

Prior to image segmentation, resizing is used to enhance the ease of manipulation of small images; the cells in this magnification configuration occupy less than 25 pixels (diameter of approximately 8 pixels) in the original image. The removal of the background intensity variations together with small size debris or platelets is performed by blurring of the initial image and subtracting the extracted background level. The application of a threshold and filtering of the black and white resulting image so that it includes regions of a specific surface area value range is proven effective for the detection of the majority of cells within the FOV region of the lens (Buggenthin et al., 2013). The developed code contains a circularity check of the final detected features as well as a classification of them based on the detected diameter.

The above method is simple and rapidly executed without being computationally expensive. The main reason of the robustness that this algorithm exhibits, compared to other approaches, is that it was initially developed for microscopy images of much higher magnification that profited from intentional defocused position of the optical system to enhance image contrast (Buggenthin et al., 2013). Therefore, it can easily be applied in portable low magnification and resolution imaging platforms.

6.3.2. Automatic detection of white blood cells captured on anti-CD45 antibody functionalized surfaces of a typical microfluidic chip.

In reference with the case in which white blood cells or a subpopulation of them are captured on functionalized walls of a microfluidic chamber, the appearance of cells radically changes. The conducted experiment includes a microfluidic chamber, whom inner walls are functionalized with anti-CD45 antibody capable of capturing all white blood cells. All non-captured cells – red blood cells and platelets – are washed away. The majority of the immobilized cells exhibit a spreading behavior during incubation resulting in a non-spherical shape. Consequently, a radical decrease of the contrast is observed.

The developed algorithmic process is based on Sobel edge detection (Biswas and Ghoshal, 2016). This type of classical edge detection was selected due to the simplicity it presents, but mainly due to the increased sensitivity over slight changes in the neighboring pixel intensity (Maini and Aggarwal, 2009). Inevitably, this high sensitivity renders the algorithm vulnerable to noise detection, however, as illustrated in both Figures 31 and 34, the detected noise can be removed following a boundaries smoothing process. The entire procedure is described in details in Figure 34 where Sobel operator is applied in flat field corrected images of a single lens FOV. At first, all variations of light intensity inside the cell body are detected, together with the noise, mainly present in defocused – blurred – regions at the borders of the FOV. Enhancement of the detected lines can be performed by linear

structuring elements resulting in a dilated gradient image mask. Smoothing of the borders of the detected features, applied for at least 3 times will result in a completely clear, segmented image, where the cell is the only detected feature.

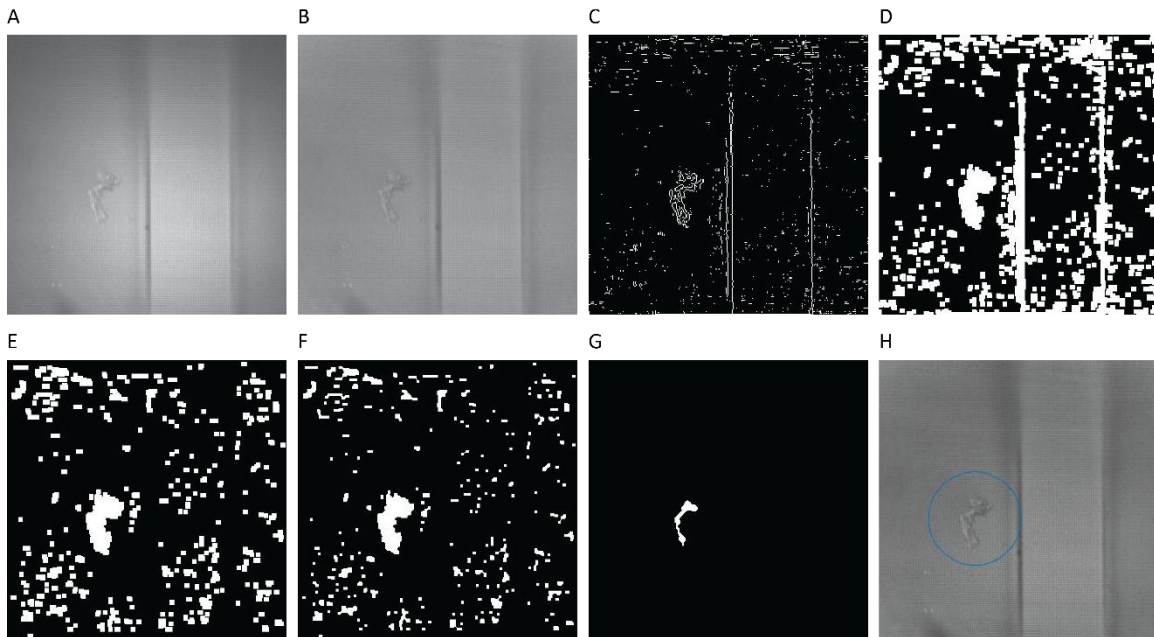


Figure 3.34. (A) Original image derived from cropping the FOV of a single lens in the array. (B) Flat field corrected image as described in section 6.1. (C) Binary gradient image after Sobel operator is applied. (D) Dilated gradient mask using linear structuring elements. (E) Binary gradient image after removal of the borders. (F) Clearing image after smoothing the detected objects' boundaries – initial step. (G) Segmented image completely clear from the detected noise after repetition of the previously applied function. (H) Original image in which the detected white blood cell is labeled.

This algorithm operates efficiently for images of samples containing low concentration of cells that express light variations in the inner part of their body, due to spreading over the functionalized surface. The cells at close vicinity to the boundaries of the microfluidic chamber cannot be detected as the borders are completely removed. There is no distinction between remaining red blood cells – due to ineffective washing procedure – and white blood cells of circular shape. Thus the detection error can be highly affected by a non-properly conducted sample washing step.

7. Discussion – Advantages, trade-offs and future perspectives

The designed and fabricated imaging/scanning platform is capable of monitoring single cells of a sample extended over a wide area of approximately 6 mm x 40 mm by profiting of a special design of a mini-lens array. The maximum provided resolution reaches 1 μm in 4X magnification configuration achieved through precise positioning of the employed micro-stepping motors. This system operates in white light transmission mode at a scheme minimizing the crosstalk phenomenon, frequently observed in optical systems employing micro-lens arrays. The characterization process of the mini-lens array proves a robust fabrication process of a perfectly

uniform array in reference to both the geometrical aspects of the unit lenses and the optical performance of them. Thus, large FOV imaging is achieved without resolution compensation, through whole slide scanning, completed in a few seconds.

As it was expected, based on the theoretical analysis of this novel design, complete imaging of a large surface of a blood cell sample is accomplished without loss of information that is assured by the overlap between the FOV regions of adjacent lenses in the array. To validate the device, image mosaicking has been conducted on images acquired by a microfluidic chamber surface containing white blood cells of a 3 μ l of blood. The extracted image is a proof of whole slide imaging capabilities, however, it exhibits increased computational and memory requirements, often not available in poor or restricted resources settings. Indeed, the prototype presented in this study, operates with a PC for the control of both the automatically driven scanning/imaging process and image manipulation process for single cell detection.

Several alterations can be performed in this design to improve the optical performance of it and to reach full portability. In the sections to follow, a detailed description is given on the improvements that need to be implemented towards this direction. The broad field of applications, this device can be useful at, is also analyzed, always in full compliance with the requirements for an effective device for point-of-care testing: portability, ease of use, minimized cost of production, operation and maintenance and low power and computational requirements.

7.1. Possible improvements on the design – optical components, mechanical parts and illumination scheme.

According to the optical performance of the employed, high numerical aperture lenses (Gulari et al., 2014), the provided image quality can be further enhanced, when combined with higher resolution detectors and at increased magnification schemes. Indeed, the system's resolution is limited by the pixel size of the CMOS detector employed, therefore, using a decreased pixel size and pitch camera can assure increased quality at the submicron level. The feasibility of higher magnification, without reducing the FOV of each lens or the entire surface of the imaged sample, can be assured by slight alterations in the design of the mini-lens array. Towards this direction the fabrication of the lens array entirely on sapphire substrate could consist a design of improved compactness, in which each unit lens is made of one material excluding the optical adhesive part of lower refractive index while, at the same time, cropping of lenses at their exact FOV will result in smaller pitch in the lens array and reduced dark spaces in the acquired image. An increased number of lenses fitting in the same area would ensure full coverage of the sample surface even at higher magnification ranges, beyond 4X.

The optical performance of the proposed system is affected by the air gap between the lens array and the specimen. An ultra-thin deformable PDMS membrane, containing oil, attached to the lens array, that could automatically deflect to reach the sample surface and fill this air gap, could improve the optical capabilities of the employed components. In accordance with the standard oil immersion lenses of bulk microscopy this configuration is expected to increase the numerical aperture of each unit lens in the array.

Concerning the mechanical components used to accomplish scanning, higher accuracy can be easily achieved by the integration of a PID feedback control in the system. The precision can be further increased with the use of ultra-sensitive, piezo motor driven, stages that can decrease the resolution and micro-stepping down to the sub-micron scale (Li and Xu, 2011), provided they are available with decreased power requirements, so as the feasibility of a fully portable device is not affected.

The developed illumination scheme integrates a homogeneously diffused white light source that evidently induces ghost effect - crosstalk – in the acquired image. To compensate the level of ghost beams travelling through neighboring lenses in the array, this light source is located at an extended working distance from the optical head of the scanning system. This effect could be eliminated by the use of a collimator/condenser system to provide parallel illumination to the sample, without the need for distant illumination.

7.2. Towards full portability and automation of the proposed device.

Though the current prototype operates connected with a PC, full portability of the system can be achieved with the employment of a microcontroller with adequate available memory and computational power such as a Raspberry pi or other equivalent board. These micro PCs, knowing great advances in the past decades, could be efficiently used to control all mechanical components, image acquisition, storage and manipulation for cell detection and counting. High throughput of the device can be achieved even in parallel execution of the sample scanning and image processing tasks. However, it still remains questionable if the entire image of the sample can be stored and displayed at the optimal resolution to the user. As the device is intended for use by the patient himself, such display possibilities are not necessary, provided that the automatic counting process is accomplished in the imaged acquired by each lens. A simple display of the resulting summation is sufficient for the tests completed.

Moreover, as it has been depicted by the power requirements of the developed setup (see Table 3) not exceeding 7 W, the device could effectively operate with a power bank. In the same direction the volume of the entire device can be further decrease by a new, more compact design to host all optical components, mechanical parts and electronics necessary for the control of the automatic processes.

The automation of the cell detection processes, at high accuracy level is dependent upon the imaged sample and the specific application for which the device is to be used. In the validation of the device developed in this study, accurate cell identification of whole blood cells in a smear blood film and of white blood cells captured in a microfluidic chamber were both proven, however, the number of the conducted experiments is not sufficient to provide accurate determination of the detection error. The significance of this error depends upon the application, while it is expected to be eliminated for low concentration blood cell populations such as white blood cells or a sub-category. Further improvement of the defects of the algorithmic processes' accuracy can be achieved with enhanced resolution of the optical components and with the use of microfluidic chips with minimum number of walls, severely affecting the detection of cells at the boundaries.

7.3. Application perspectives of this platform technology

This high resolution imaging/scanning system, capable of screening an extended sample area, provides a simple and inexpensive solution for microscopy observation of a blood sample at the point of care. It constitutes a platform technology that could apply to a wide variety of diseases and conditions that need to be observed or diagnosed, without the requirement for a hospital visit or without the presence of expert personnel and bulk equipment. In compliance with the requirements imposed by the WHO for point-of-care testing, that concern affordability of a single test, ease of operation by non-experts, robustness, portability and accuracy of provided results in terms of sensitivity and specificity, the developed platform imaging technology has proven, in this study, to be a promising tool for the diagnosis and monitoring of health conditions related to blood cell counts for both limited resources setting or in the developed world.

More precisely, HIV related blood cell counting tests intended to count CD4⁺ T cell lymphocytes for the observation of virus progress within the body and the determination of treatment adjustment, are tests that need to be driven at frequent intervals, while the epidemic of HIV affects countries of poor resources and infrastructure. The diagnostic procedure of malaria, also affecting low income countries, is based on microscopy observation of stained blood smears that could be easily accomplished with the proposed device. Sickle cell anemia, determined by the abnormal shape of red blood cell could be defined as well, while in a future improved version of this technology, reaching higher resolution, Tuberculosis, diagnosed by sputum stained thin films observation is an additional disease of application. In the developed world, medical examinations for white blood cell counts, conducted on a daily basis for patients undergoing cancer treatment, could be effectively accomplished even at home, protecting the patient from exposure to hospital infections and providing a patient-centered health care. It is among the visions of this study to provide a general purposed, single cell imaging platform that can be effectively used for blood related disorders monitoring, when combined with the advances in microfluidic technology for sorting and isolation of specific blood cell populations.

Chapter 4

Integration of an LED structure in a mini-lens array for the implementation of reflection mode illumination scheme in miniaturized optical devices.

Reflection mode illumination constitutes an irreplaceable part of microscopy imaging schemes that are necessitated either in cases of opaque samples or sample holders, not optically accessible by both sides, or with the intention to increase signal to noise ratio of the optical monitoring setup. This is the case of epi-fluorescent imaging where specific part of the sample can be effectively isolated from the surrounding features or backscattering dark-field imaging for enhanced contrast of non-stained samples. The wide field of applications dependent on epi-illumination scheme eventually leads to the necessity to develop simple, robust and inexpensive setups for constituting part of miniature imaging systems and devices at the point of care.

The criteria to examine for the determination of the efficiency and provided quality of reflected illumination, mainly concern the uniformity of the illuminating beam and the possibility of the setup to separate the excitation and the reflection beams. In conventional bulk microscopes, the illuminating beam shares the same optical elements used for image formation when the beam is reflected back or scattered by the sample. This configuration affects the provided signal-to-noise ratio and imposes the use of high quality expensive and complex optical compounds that place a severe impediment towards the reduction of the volume and production expenses. Despite the serious endeavor to meet the emerging challenge, the field still remains open to new proposals and ideas towards the integration of reflected illumination in portable optical monitoring systems, with the setups already developed failing to provide high quality reflection-based imaging without increasing the cost and complexity.

In this chapter, profiting from well-established CMOS compatible methods of LED microfabrication and the advances in high grade quality in micro-optics, a novel idea is presented for the integration of the illuminating source in the main optical element of the setup. Increased compactness is the apparent asset of the presented illuminating/optical module, as it can radically reduce the length of the excitation and reflection optical paths down to a few millimeters. However, the crucial benefit provided is the separation of excitation and emission optical paths, without the need to employ bulk off-axis elements, as in conventional reflection-based optical systems. In the sections to follow a detailed description of the operating principle and the design of the proposed illumination/collection module is presented together with a characterization of its performance in terms of power requirements, provided illumination intensity and uniformity. Possible restrictions of this design are also examined including the noise level that is induced by reflection on the interfaces between the different optical media in the beam path and the temperature increase due to LEDs operation. The proposed compound chip integrating illumination and collection elements, constitutes a platform illuminating/imaging scheme for use in portable compact optical monitoring devices, as it appears promising for a wide range of applications, from simple bright field reflection-based microscopy to epi-fluorescence with the implementation of slight alterations in the initial design.

1. Integration of an LED structure on a ball mini-lens array – design and operating principle of the compound chip.

The idea of the proposed device is based on the integration of an LED array structure in a silicon based mini-lens array. The silicon chip is patterned on both sides so that it can host the ball lenses on the one side and the LED structure on the opposite side. Precisely, the mini-lens array comprises of sapphire ball lenses of 1 mm in diameter that are placed on top of cylindrical through holes created on the silicon chip. These holes have a radius slight smaller than the radius of the lenses so that they are seated a few micrometers above the upper surface of the silicon die. The LED structure comprises of an array of LED illuminating rings that are formed by ring-shaped pn junctions on Silicon implanted with Phosphorus and Boron. These illuminating rings are patterned on the bottom side of the silicon wafer, so that they are concentric with the lenses placed on the top side. Thus, each LED ring surrounds each lens of the array, being responsible for the illumination of the area of the sample located underneath this specific lens. Precisely, in this design of the LED structure, the illuminating rings circle the holes that are patterned on the silicon chip to host the lenses on the opposite side of the chip.

This hybrid illumination/collection optics chip is intended for use in imaging setups. It is therefore, placed between a sample and a detector. The LED structure is an avalanche based p-n junction structure that emits light when reverse biased beyond a breakdown voltage. Thus, when appropriately supplied with power, the LED rings emit light towards a specimen that is located a few micrometers away from the bottom surface of the silicon chip. The light rays, released by the LED rings are scattered and reflected back by the sample surface and are collected by the ball lenses, so that the image of the sample is projected on the detector effective area located on the opposite side of the proposed device.

The distances between the sample, the LED/lens array chip and the CMOS detector employed can be adjusted by changing the position of the aforementioned elements vertically to achieve sharp, in-focus imaging. While the principle governing imaging with ball mini-lenses has been reported in details in the previous chapter, the LED operating principle is analyzed in this chapter, with reference to the illuminating process of the selected pn junctions, the illuminating intensity, the power consumption and provided efficiency and the aspects affecting imaging such as the uniformity of the emitted light and the temperature rise threatening the viability of biological specimens due to their location at close proximity to the LED structure.

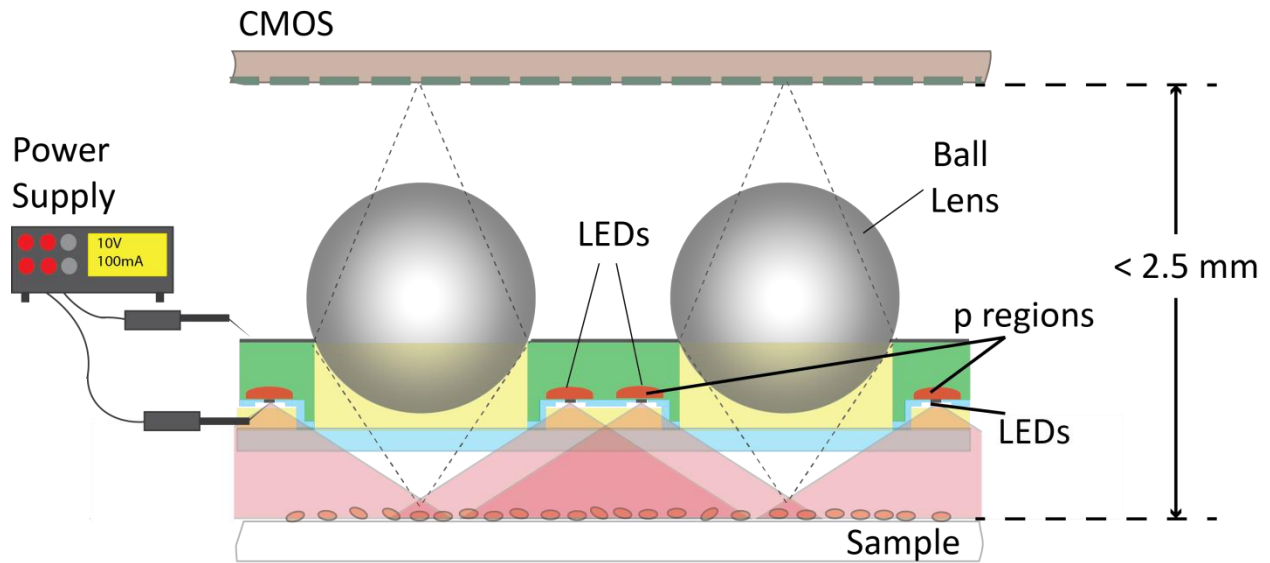


Figure 4.1. Schematic illustrating the illuminating/imaging principle of the proposed device. Light rays released by the ring shaped LEDs are scattered by the sample, which is located a few micrometers away (up to $300 \mu\text{m}$) and they are collected by the lenses to reach the detector, which is positioned on the other side of the Si chip. The entire setup achieves the reduction of optical path length down to a few millimeters ($< 2.5 \text{ mm}$).

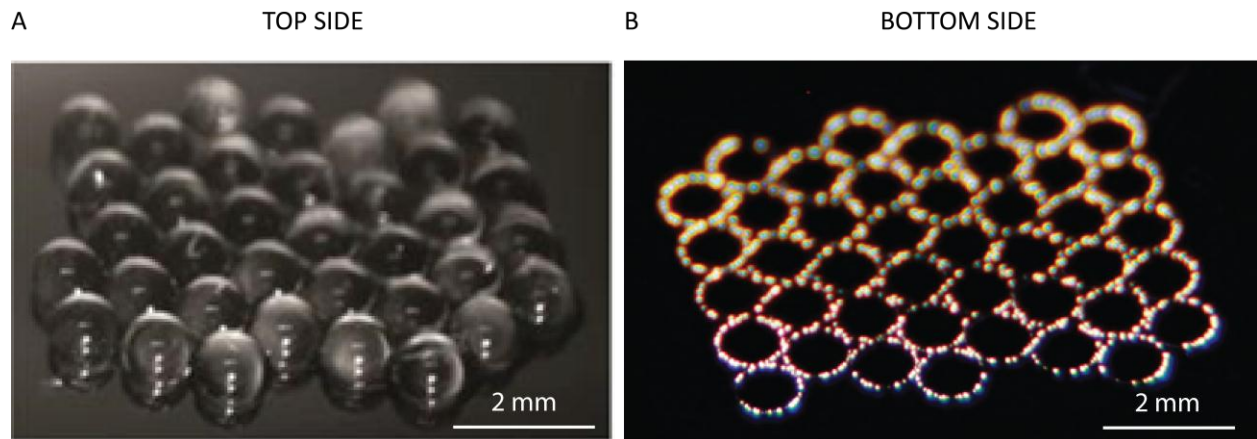


Figure 12. Top and bottom side of the proposed silicon based illuminating/imaging component. (A) Sapphire ball mini-lenses of 1 mm in diameter placed at close distances to each other to form an array able to cover the entire effective area of a CMOS detector of approximately 25 mm^2 . (B) Ring shaped LEDs patterned on the bottom side of the same silicon chip, in a way that they are concentric with the lenses seated on top. The LED ring illuminate when reverse biased beyond the breakdown voltage.

1.1. Light emission by the silicon based avalanche diode array structure.

The indirect band gap of silicon eventually leads to low and slow efficiency in the case of silicon-based forward biased light emitting diodes. It is indeed well known that the hole – electron pairs recombination in p-n junctions of silicon materials in forwards bias, present too low a rate to achieve photon emission (Xu et al., 2014). However, visible light illumination observed from silicon based p-n junctions under the presence of reverse biased high electric field has already been reported

back to the 1950s (Newman, 1955; Chynoweth and McKay, 1956). The breakdown is a result of secondary ionization in semiconductor junctions. For voltages lower than the breakdown voltage, applied in reverse biased p-n junctions, a number of electrons enter the reverse biased p-n junction from the P side. In this region of high electric field, the electrons will be accelerated to velocities up to 10^5 cm/s, therefore, their energy is sufficient to create hole-electron pairs, through the collisions with the valence electrons. A corresponding process takes place for the holes entering the N side of the junction. The newly generated carriers by impact ionization serve to maintain the discharge, their number being just sufficient to replenish the carriers swept out of the junction region by the field.

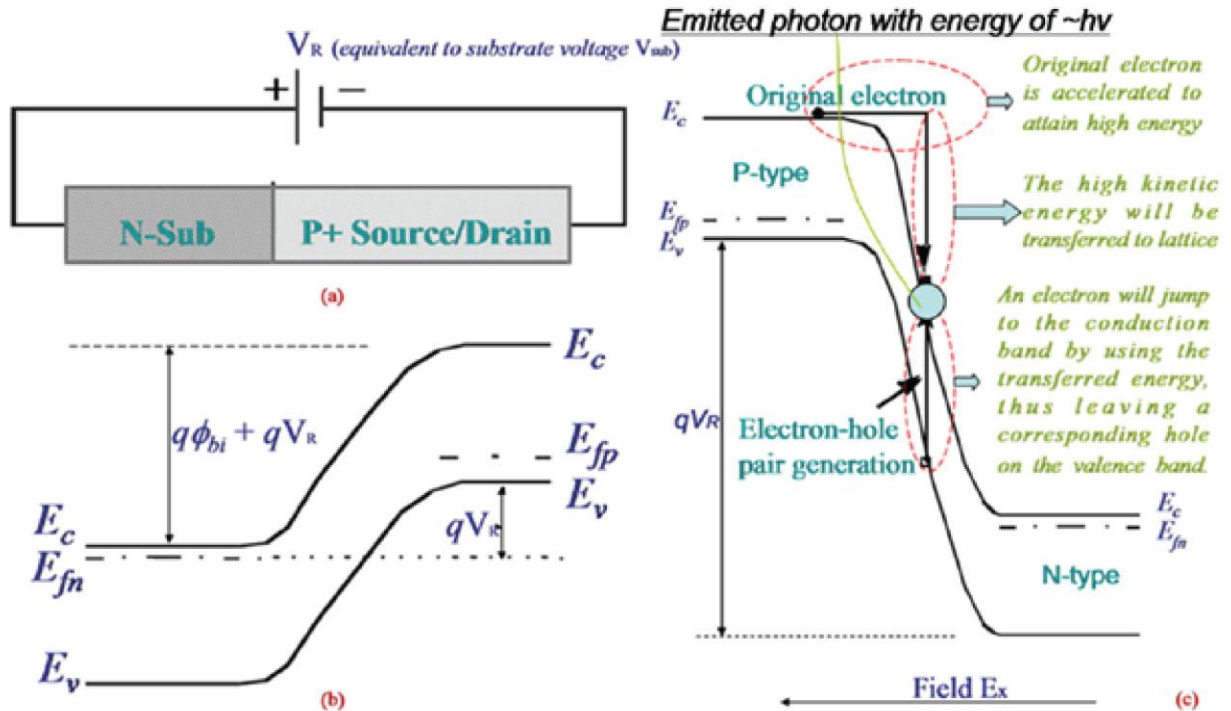


Figure 13. Energy band scheme of a PMOSFET-like device, regarded as a p-n junction, which demonstrates current amplification due to impact ionization and depicts radiative recombination of an e-h pair (Xu et al., 2014).

With the increase of applied voltage, the number of carriers entering the junction region is subjected to an increasing multiplication, leading to the well-known effect of avalanche multiplication at the breakdown voltage, where the multiplication factor approximates infinity (Moll and Van Overstraeten, 1963). Concerning the multiplication factor, based on analytical (Lerach and Albrecht, 1975) and experimental processes (Fulop, 1967), it has been shown that it depends upon the charge carrier ionization probability per distance travelled – therefore, the effective ionization coefficient – as a function of the applied electric field E :

$$\alpha = ae^{-\frac{b}{E}} \quad (4.1)$$

where a , b are constant values depending on the implantation of silicon and the silicon characteristics. When the multiplication is so large that both electrons and holes contribute to ionization, the multiplication factor M_n is given by the mathematical expression:

$$1 - \frac{1}{M_n} = \int_0^W a_n \cdot \exp \left[\int_0^x (a_n - a_p) dx' \right] dx \quad (4.2)$$

where a_n , a_p are the charge carrier ionization probability per distance travelled for electrons and holes respectively (Moll and Van Overstraeten, 1963).

The breakdown occurs when the integral of the probability density of ionizing scattering events over the entire depletion area W – being the probability distribution function – reaches the value of one (Lerach and Albrecht, 1975). Therefore, multiplication factor reaches infinity:

$$\int_0^W a_n \cdot \exp \left[\int_0^x (a_n - a_p) dx' \right] dx = 1 \quad (4.3)$$

The voltage where avalanche multiplication occurs, termed breakdown voltage, depends on the net dopant concentration N , the relative permittivity of the semiconductor ϵ_r and the maximum strength of the electric field F_b under breakdown condition (Lerach and Albrecht, 1975).

$$V_b = \frac{1}{2} \cdot F_b \cdot W = \frac{1}{2} \cdot F_b^2 \cdot \frac{\epsilon_r}{e \cdot N} \quad (4.4)$$

In the proposed design the p^+n junction is built on a n -type silicon of 0.1 ohm·cm resistivity and comprises of a phosphorus implanted region created by phosphorus implantation over the entire wafer area of $2 \cdot 10^{14}$ ions/cm² under 100KeV implantation energy and boron implantation for the creation of ring shaped p^+ type regions. The boron implant is given in two steps, of $5 \cdot 10^{15}$ ions/cm² under 60KeV and $1 \cdot 10^{15}$ ions/cm² under 20KeV, respectively. The expected breakdown voltage has been previously reported to approximate $V_b = 8V$ (Misiakos et al., 1998, 2001).

In avalanche breakdown condition, for values of applied voltage beyond the breakdown voltage, the generated electron-hole pairs recombine radiatively. The radiative transition between hot carriers emits photons of energy higher than the energy gap, E_g . The occurring luminescence presents a broad emission spectrum, which extends to $h \cdot \nu = 3 \cdot E_g$, depicting the energy separating the hottest electron by the hottest hole, provided the impact ionization energy is $\frac{2}{3} E_g$ (Pankov, 1971). At first, the radiation originates in the isolated spots in close proximity to the junction area; with the gradual increase of reverse biased voltage the spots merge into a single homogeneous emitting area (Xu et al., 2014).

Light intensity appears to be proportional to the reverse current, increasing with the number of bright spots developing in intensity at the first stage of the process, while a large increase in light output occurs as the relatively large regions of uniform brightness begin to contribute (Newman, 1955). Any apparent declination from the linear proportionality between emitted light intensity and

reverse current of the p-n junction is attributed to imperfections in the region of the junction. This is clearly depicted in previous studies by intentional imperfections in the surface of the device (e.g. scratches) correlating with a much softer transition in the breakdown condition (Figure 4). The illuminating uniformity at the last stage of homogeneous area emitting light rays is to be discussed in the following as it is believed to be susceptible to fabrication imperfections in the region of the junction (Newman, 1955).

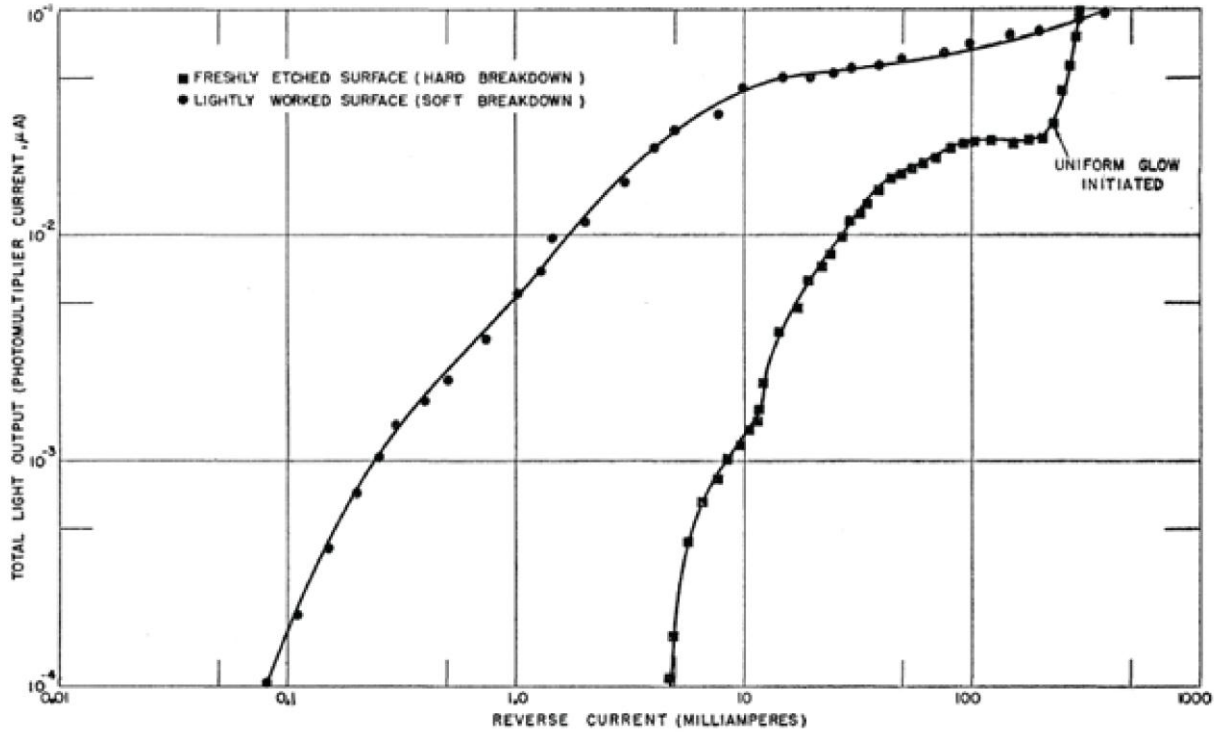
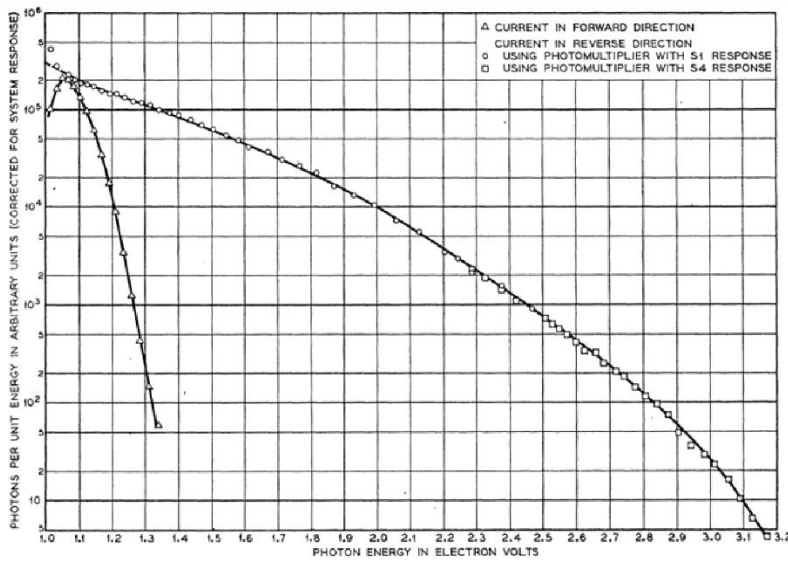


Figure 14. Two reverse current vs. total light output curves for a silicon p-n junction unit (Newman, 1955).

A



B

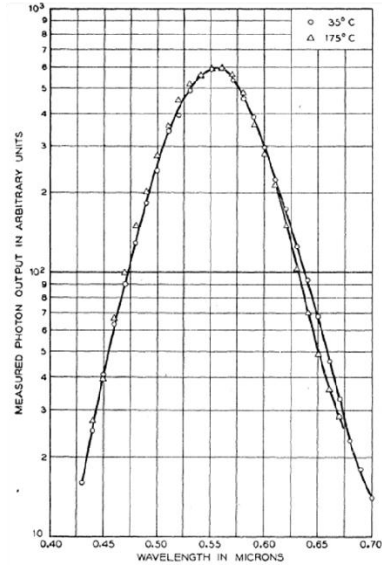


Figure 4.5. (A) Emission spectra from a p–n junction of Si for both forward and breakdown currents corrected for the spectral response of the spectrometer-photomultiplier system. (Pankov, 1971) (B) Uncorrected emission spectra at two different temperatures, normalized at their peak values (Chynoweth and McKay, 1956).

Based on analytical expression, the dependence of light intensity on the photon energy (in eV) for silicon p–n junctions present a peak at 2.2 eV, corresponding to yellowish light of approximately 565 nm (Gaijtan, Khokle and Garg, 1988). As previously reported, the spectral content of emitted light is generally expected to be broad, while specifically for the implemented fabrication protocol described above the spectrum was measured and it is illustrated in the Figure 6 (Misiakos et al., 1998).

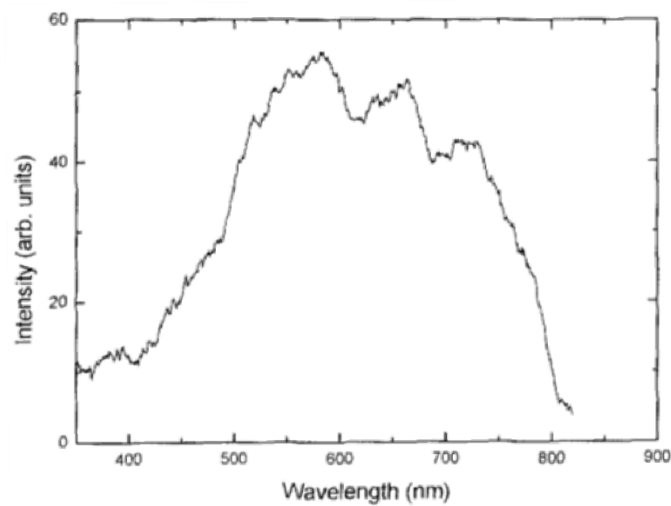


Figure 15. Spectral content of the Light Emitting Diodes of the selected concentration of Phosphorus and Boron ions for the p–n junctions (Misiakos et al., 1998).

Light emission efficiency has been studied specifically for boron and phosphorus implanted samples for various implantation and annealing conditions, depicting strong dependence upon these factors. The band-to-band luminescence of phosphorus implanted diodes is observed to increase by more than one order of magnitude upon rising the sample temperature from 80 K to 300 K and a maximum internal quantum efficiency of 2 % has been reached at 300 K (Kittler et al., 2005).

1.2. Non-uniformity of p-n junctions and light emission of microplasma spots.

In both theoretical and experimental study of light emission in avalanche breakdown in p-n junctions, the mechanism expressing the phenomena taking place becomes complicated due to the fact that actual junctions usually present local defects. These imperfections produce regions in which the breakdown condition – when multiplication reaches infinity – occurs at voltages substantially lower than the voltage at which breakdown would have occurred in the absence of any defects, for the same average impurity distribution in the junction (Goetzberger et al., 1963). For a perfectly uniform p-n junction – microplasmas free junction – the V-I characteristic curve is illustrated in Figure 7. The reference to “microplasmas” is a prerequisite for the assumption of Bremsstrahlung (Braking) radiation in the general p-n region over the entire spectra. Thus for a junction containing microplasma spots, created by striation patterns or dislocations, different ionization rates of electrons are observed, though still following the empirical law described in equation (3.1) (Chynoweth, 1960). The carrier photomultiplication in reverse bias junctions, being a function not only of the applied electric field but also of the location of the generated electron – hole pair, exhibits a deviation of the theoretically linear dependence of $1/M$ vs. V (Haitz et al., 1963). While a soft reverse characteristic curve is observed (Chynoweth and Pearson, 1958), the current flow occurs in the neighborhood of the defects (Chynoweth, 1960).

In general, in the case of microplasma spots being present, created either due to inhomogeneous doping during diffusion, or – in the absence of lattice imperfections – due to resistivity striations in the crystals, a non-uniform light emission is expected. As previously investigated, the illuminating spots vary statistically in size and brightness and do not have sharp outlines. The occurrence in clusters is also expected with the presence of large dark areas separating them (Goetzberger et al., 1963).

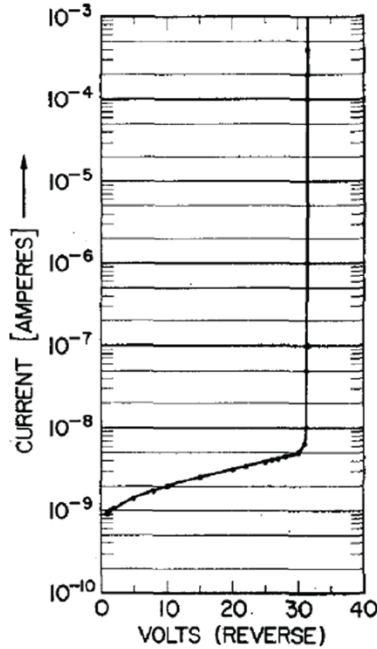


Figure 4.7. V-I curve at reverse bias of a p-n junction on Silicon free of microplasmas.

1.3. Theoretically predicted illumination with the designed LED micro-structure.

In the proposed design, the LED structure is intended for use in illumination of a specimen seated in close vicinity of the chip from the side of the ring shaped p-n junctions. The LED rings are patterned on the space between the lenses and each ring is responsible for the illumination of the area of the sample located underneath the corresponding lens. Taking into account the employed lenses' diameter – 1 mm – and the minimized distance separating them in the array structure – 50 μm – along with the geometric aspects of the silicon chip – the etched region for wells creation being 960 μm in diameter – the free space for the LED rings on the backside of the silicon is 90 μm wide (edge-to-edge distance). In this area, two LED rings are patterned to circle adjacent lenses, each one comprising of a ring shaped boron implanted region. Thus, each LED ring contains a double illuminating circle that surround the corresponding lens.

The distance, at which the sample is located, is of crucial importance to achieve successful illumination of the entire specimen area. To examine the effective illumination provided by this structure of light emitting diodes, a 3d COMSOL simulation was conducted, in which the double illuminating ring was placed inside a recess filled with the employed optical adhesive (NORLAND 60) of 1.56 refractive index and a glass cover slip of 150 μm thickness – piece of borosilicate glass sealing the device from the bottom side – with an index of refraction approximately 1.514. The light rays released from the double ring line were forced to obey to the lambertian spatial distribution with an axis vertical to the surface of the LED structure. The same simulation was conducted for hemispherical distribution of each point belonging to the illuminating edge, leading to similar results concerning the surface of interest which is located at the center of the ring with a radius of 200 μm . This disc space corresponds to the field of view of the lens as this was measured in transmission mode imaging setup (see chapter 2).

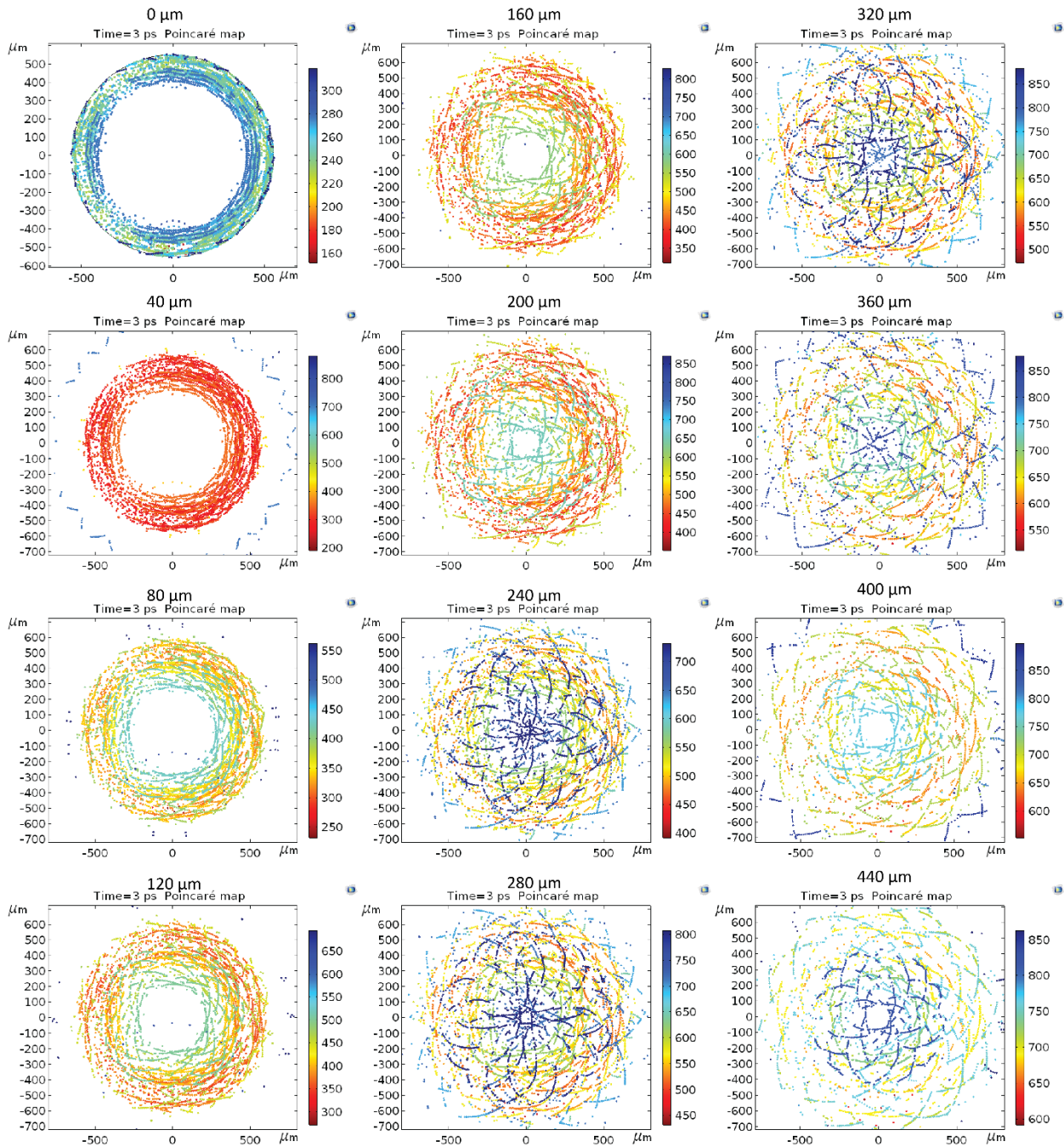


Figure 4.8. Poincaré maps depicting light rays hitting the sample surface for a distance separating the sample and the bottom side of the designed chip ranging from 0 – 500 μm . The simulation was conducted with a step of 20 μm for this distance range, while the selected images presented correspond to a step of 40 μm .

The poincaré map, illustrating the light rays hitting on the surface of the sample, was extracted for a range of distances between the sample and the bottom side of the chip, starting from the bottom side of the glass cover slip until a distance of 500 μm from it (Figure 8). The selected step for the simulation was 20 μm , while the presented figures correspond to a step of 40 μm . In this poincaré illustration the color-map expression was based on the distance that each ray has travelled within

different optical media of the optical path, which corresponds to a quality classification of different light intensity of the rays. According to the conducted simulations, a minimum distance of 200 μm should separate the sample from the LED structure so that the center of the disc is illuminated. Further increase of this distance will eventually lead to more rays reaching this point with a reduction of the intensity of light.

2. Fabrication of the proposed illumination/ imaging compound chip.

The fabrication of the integrated ring-shaped light emitting diodes on silicon-substrate requires 5 different lithography masks combined with well-established CMOS compatible micromachining methods. An n-type silicon wafer of 400 μm thickness and 0.1 $\Omega\cdot\text{cm}$ electric resistivity is used as a substrate. A ~ 1.5 μm deep recess is created with standard optical lithography and etching processes to host the light emitting diodes, on the one side of the Si wafer. Phosphorus implantation of $2 \cdot 10^{14}$ ions/ cm^2 is performed at 100 KeV to create a P⁺ type region approximately 100 nm into bulk Si, in the entire surface of it – no lithography step is needed. A SiO₂ of 600 nm thickness, is created at the top surface of the wafer through wet oxidation at 1050 °C for 120 min, followed by annealing process for 10 min. A lithography step and wet etching (BHF) are used to create Boron implantation mask. The windows on oxide mask are ring-shaped with internal diameter of 980 μm and width of 20 μm . A first doping step of $5 \cdot 10^{15}$ B ions/ cm^2 at 60 KeV followed by a second doping step of $1 \cdot 10^{15}$ B ions/ cm^2 at 25 KeV form the N⁺ type ring-shaped region on Si wafer. A second thin layer of SiO₂ is created through dry oxidation at 1050 °C for 70 min, followed by annealing process for 10 min. This thin oxide layer patterned with optical lithography and BHF wet etching process is used to form the windows for Aluminum interconnections. Ring-shaped windows, concentric to Boron implanted ring regions are opened to the oxide layer and an Aluminum thin film of 500 nm thickness is deposited on top. The oxide windows are narrower than N⁺ type Boron implanted rings to prevent contact of the Al pads with P type region. A final mask for Aluminum and unnecessary oxide removal is used to open optical windows over the p-n ring-shaped junctions and prevent blocking of light emitted by them.

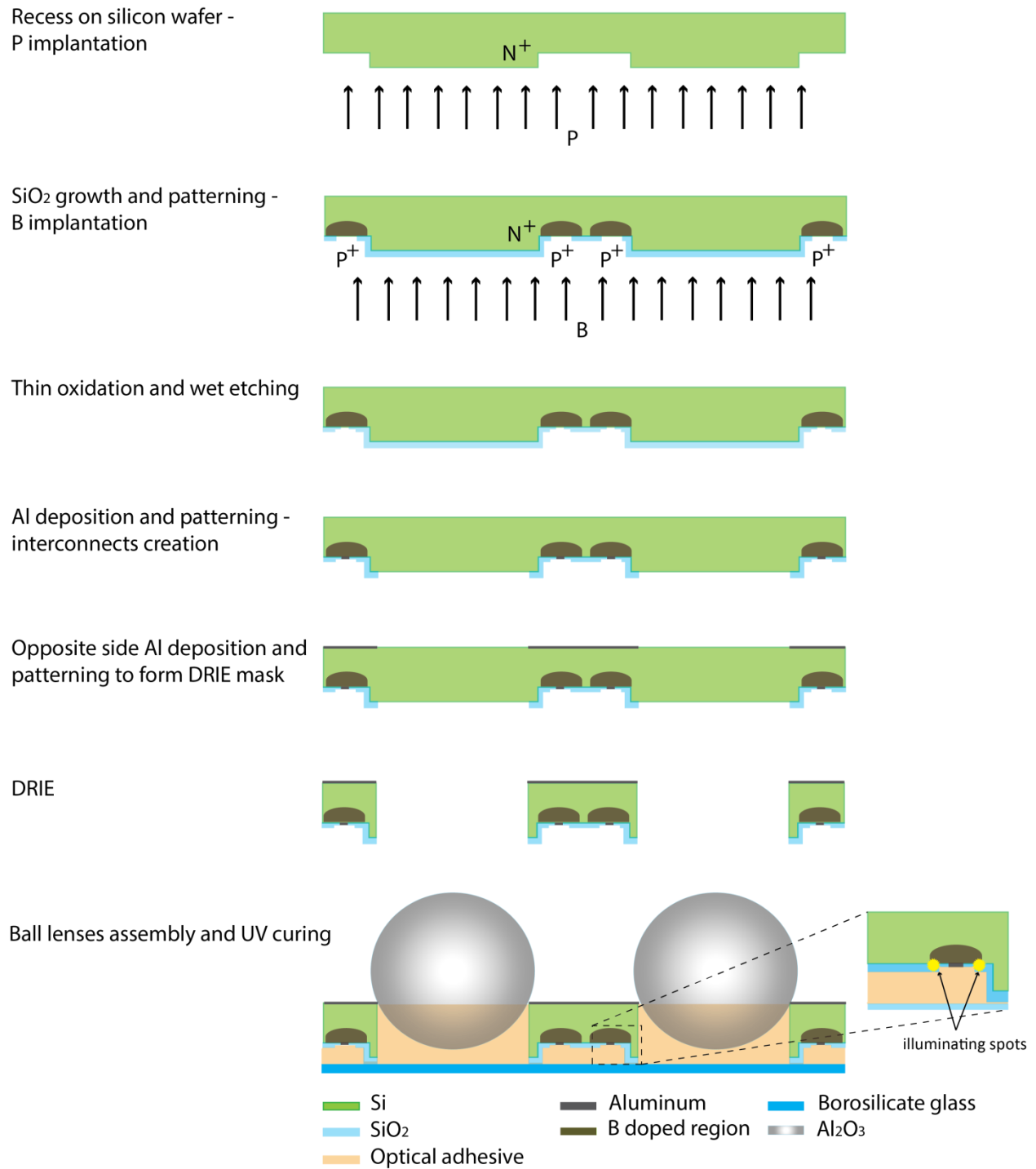


Figure 4.9. Schematic illustration of the fabrication steps of the ring-shaped LED array patterned on silicon-based sapphire ball mini-lens array. The procedure of LEDs on Silicon fabrication is followed by through holes opening on the backside of the silicon die. These holes which host the ball lenses; their fabrication being discussed in the previous chapter. The entire process relies on well-established CMOS compatible fabrication methods.

In this design all LED rings in the array are interconnected with neighboring rings so that voltage is applied to all P and N regions through the same power supply pad, formed by the 500 nm thick Aluminum film. For this reason, the aluminum film is patterned so that it contains ring shaped pads placed over each Boron implanted ring region, interconnected with adjacent rings on 6 points on the ring perimeter. This number, combined with Aluminum film deposition on all free areas (triangle shaped regions between the rings) is adequate to sufficiently minimize voltage drop for the rings located at the center of the array, with respect to those at the borders, while at the same time the number and width of interconnections crossing the illuminating circular edge are reduced enough not to block the emitted light (Figure 10).

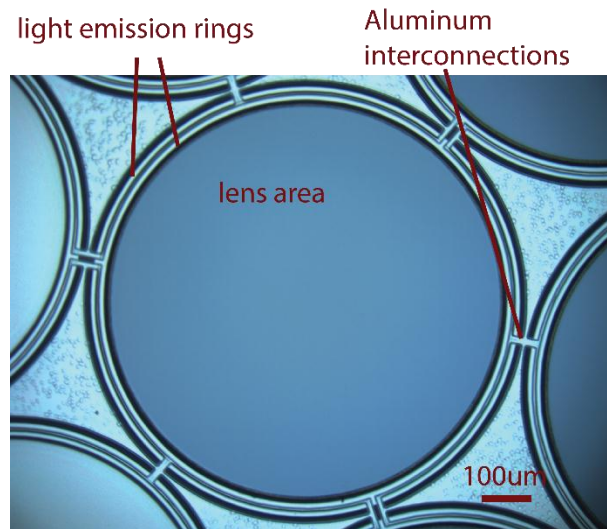


Figure 4.10. Top view of the structure of the ring LED array imaged with an optical microscope under 10X magnification objective lens. The aluminum ring-shaped regions that are used as power supply pads appear bright on top of the Boron implanted regions (dark thin rings). In the figure interconnections between neighboring rings can be observed.

The Si wafer is then pattern on the opposite side of the formed light emitting diodes. Deep Reactive Ion Etching (DRIE) process is performed with the use of the aluminum mask to create 36 through-holes on the Si wafer of a diameter of 960 μm each (Gulari, Tripathi and Chronis, 2012). These holes are equidistant from each other and concentric to the ring-shaped LEDs of the backside. They serve as wells on which 36 Sapphire ball mini-lenses (Edmund Optics #43-638) of 1 mm in diameter and 1.77 refractive index are placed. To form the wells a thin cover slip of 130-170 μm nominal thickness is placed on the side of the LEDs and permanently held with the use of a UV curable optical adhesive (Norland 60). The same adhesive is used to fill the wells prior to ball lenses placement. The structure leaves a 50 μm distance between adjacent lenses and a corresponding region 90 μm wide on silicon substrate. This region of the Si chip hosts on its backside the light emitting diodes.

The fabrication of this design was accomplished with the use of low cost on-film photolithography masks eventually affected by low resolution and artifacts of the size of 2 μm , according to the supplier. The resulting LED structure was imaged under optical microscope of high magnification to

examine the defects induced in the borders of each feature (Figure 11). According to the theoretical background concerning striations in the microfabrication process, the observed roughness of Boron implanted ring shaped regions are expected to be subjected to a microplasma radiation and spots-like illumination. As the defects are uniformly distributed over the mask surface, the spots are expected to develop a homogeneously illuminating ring region, beyond an increased voltage value, slightly higher than the predicted breakdown voltage of 8 V.

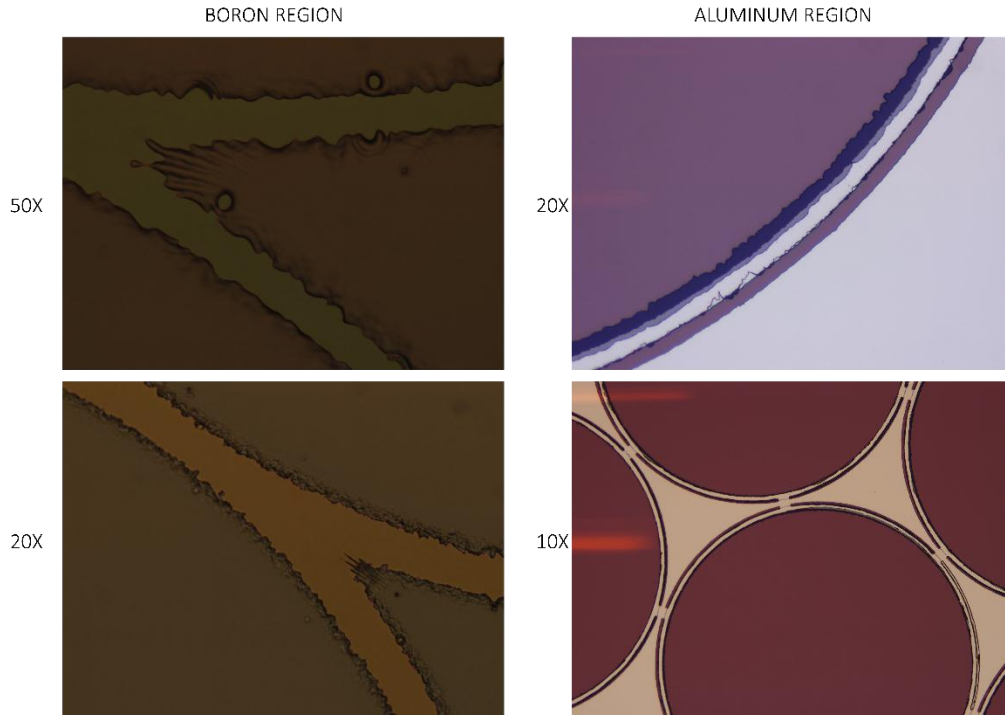


Figure 4.11. Defects in the fabrication process attributed to low resolution photolithography masks printed on film.

3. Characterization of the fabricated illumination/imaging chip.

To examine the performance and efficiency of the proposed device, 3 different designs were fabricated, in which different numbers of patterned LED rings and ball mini-lenses were combined. The first structure comprises of 2 ball lenses with the double LED-ring of each one patterned on the backside of the silicon chip. The second structure tested contains only 1 ball lens placed on a silicon die that is patterned on the backside to host 7 double LED rings – 1 double-ring surrounding the lens well and 6 neighboring LED rings without the corresponding through-holes or lenses. The third structure tested is the final proposed device containing 36 sapphire ball mini-lenses and the corresponding to each lens double ring LED. Though 36 sapphire mini-lenses are adequate to fill the effective area of the CMOS sensor employed in the imaging characterization setup (Imaging Source DMM 27UJ003-ML), 6 additional LED-ring units were used in the LED array structure to ensure adequate illumination in the borders of the imaged area. All three designs are illustrated in Figure 12 under illumination conditions – breakdown region – in which the side of the LED

structure was placed under a stereo microscope of low magnification (up to 2X) to achieve large field of view imaging.

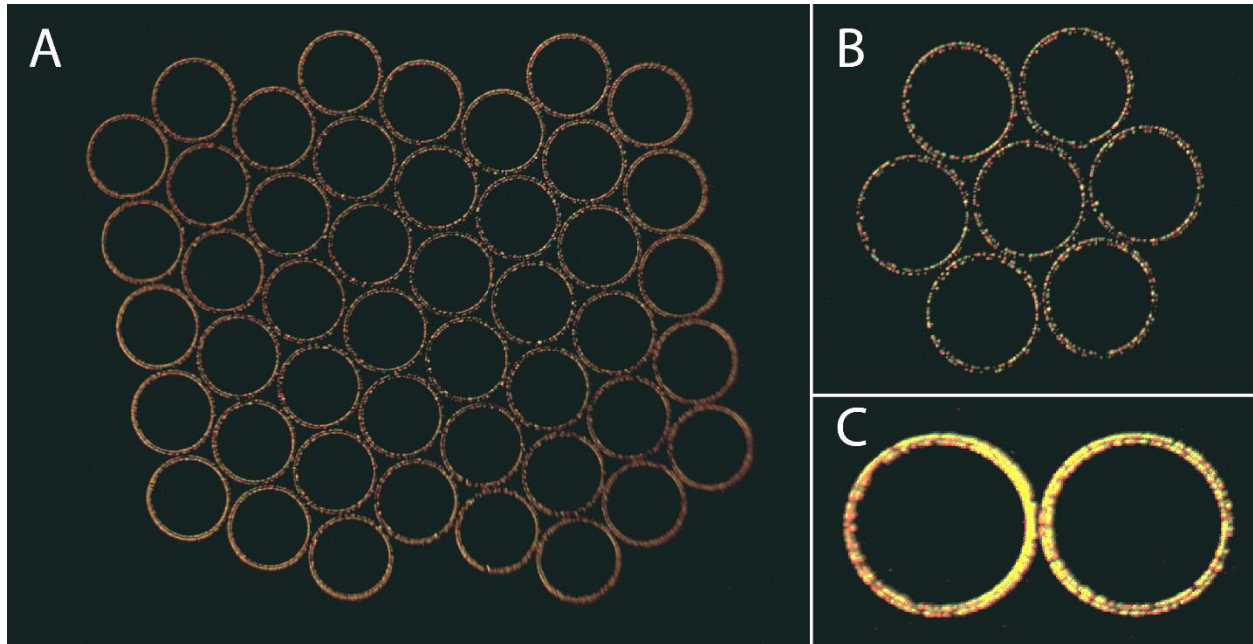


Figure 4.12. The differences in the tested structures lie on the number of double LED rings in each structure: we tested 2 ring LED array, 7 ring LED array and 42 ring LED array. Images from each structure when light emission occurs are captured under stereo microscope in figures (A), (B) and (C).

3.1. Electrical characterization.

For all 3 structures tested, the I-V characteristic curve was extracted for reverse bias mode. Reverse biased voltage from 0 to 12 V was applied to the LED-on-silicon array and the corresponding substrate current was measured. The resulting curves comply with the characteristic curve of a reverse biased p-n junction. A slight increase in the substrate current – leakage current in reverse bias operation – occurs until a specific voltage value is applied and avalanche multiplication dominates. In the structures tested, breakdown conditions appear at 9.5 V for both 2 and 7 LED structures, while a much softer breakdown transition is observed in the case of 42 LED rings structure. This soft transition in avalanche photo-multiplication process is attributed to the roughness in the illuminating edges, therefore the microplasma spots present in the junction regions. Additionally, the observed deviation of the breakdown voltage compared to the predicted one of approximately 8 V is believed to appear due to the thermal resistance which results from an increase in power dissipation (Haitz, 1967).

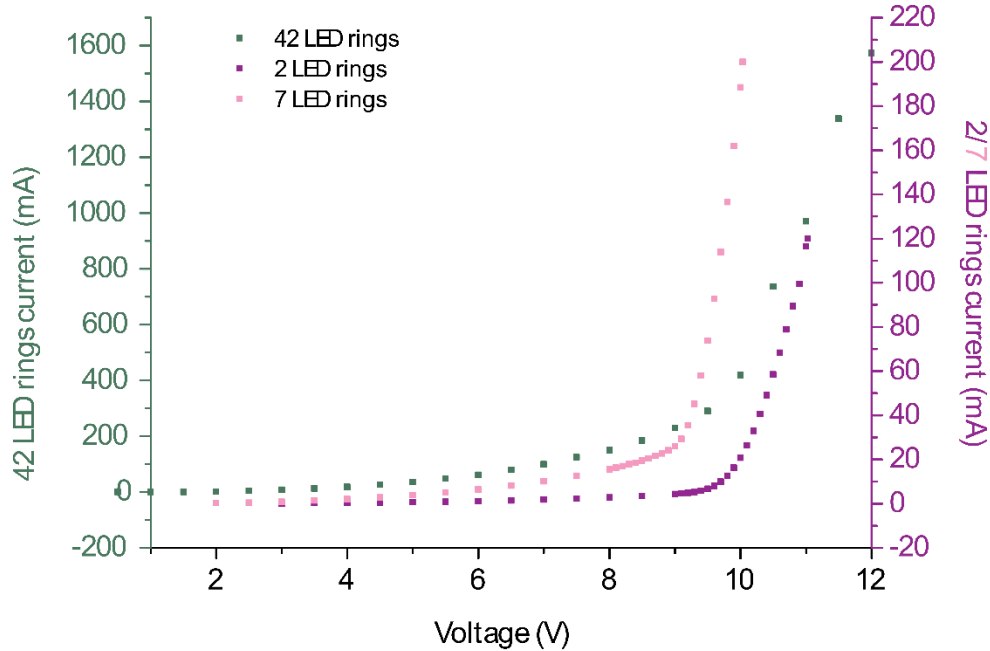


Figure 4.13. I-V curves acquired for 3 different structures of the ring LED on Silicon array.

Intensity of light emitted by these 3 tested LED array structures was measured with respect to the power consumption for light emission. The patterned silicon die was placed on a stereo microscope under a 2X magnification lens to assure adequate Field of View and imaging of a large area of the LED-structure surface (Figure 12). A sequence of images was acquired for different values of reverse voltage applied within the range of 0 to 12 V and the light intensity was calculated as the average pixel intensity in the acquired image. Prior to intensity calculations the acquired images were subjected to image enhancement to increase contrast. The values of light intensity were normalized with respect to the maximum intensity provided by each structure.

As theoretically predicted, the light intensity exhibits a voltage dependence identical to the reverse current (Figure 14). A slight increase in the average pixel value of the image is observed when the applied electric field is held below the breakdown condition, corresponding to the reverse leakage current. In this region, light emission occurs in non-uniformities of microplasma spots (Figure 15), entering the avalanche multiplication region earlier than the predicted breakdown voltage value of a microplasma-free diode of the same characteristics. As the applied voltage increases, the number of bright spots exhibits a corresponding increase, until the condition where each ring appears to illuminate as a homogeneous ring line. In all above measurements, the current corresponds to the substrate current. The LED rings being in parallel connection, as the number of included LED rings in the structure rises, a corresponding increase in the substrate current leads to a different increase in the illumination intensity of each ring, for the tested structures. Evidently, the power consumption is expected to be much higher in the case of 42 LED array than that of 2 or 7 LED structure, to reach relatively high output power – intensity of illumination.

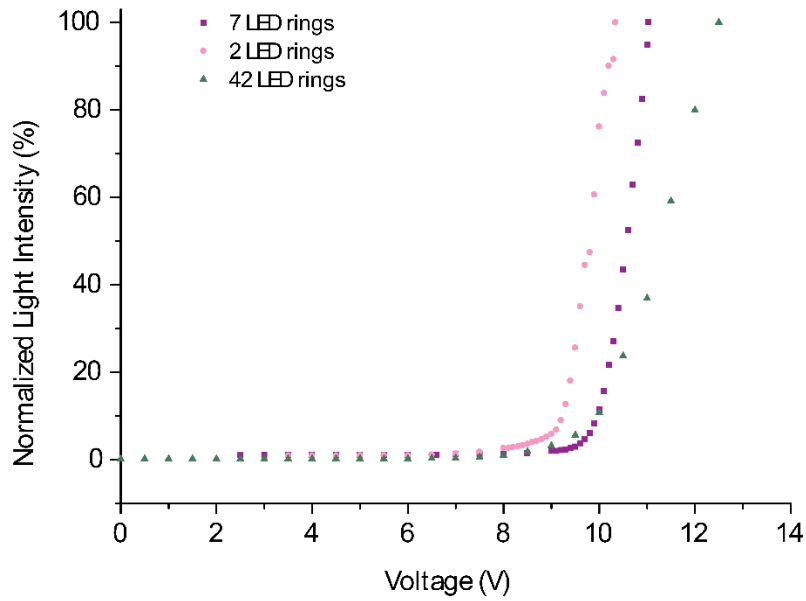


Figure 4.14. Light intensity graph vs. voltage applied in reverse bias. Light intensity value is extracted as the average pixel intensity in the images acquired under stereo microscope for the 3 different LED ring array structures. The intensity value is normalized with respect to maximum intensity provided by each structure. As expected, light emission occurs beyond breakdown voltage and appears to be linearly proportional to current that has been previously measured.

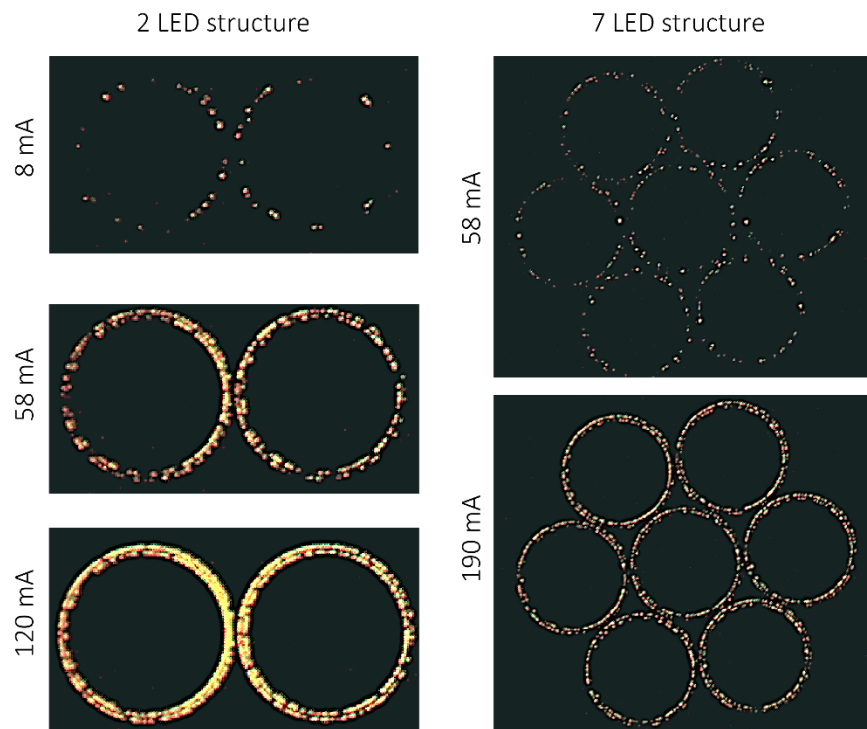


Figure 4.15. Pictures depicting the spot-like illumination occurring on the ring line of the LED structure. In the 2 LED structure the double illuminating ring can be easily observed.

3.2. Optical characterization – uniformity of emitted light and noisy image.

Imaging with a lens array should be uniform in terms of resolution, contrast and brightness of the image produced by each optical unit in the array. Though imaging uniformity with a lens array in transmission mode has been previously reported (chapter 2), illumination uniformity has been examined with respect to the variations across the illuminating ring and spatial distribution of light rays hitting the sample surface.

For the first experiment, direct imaging of the LED rings under a stereo microscope focused on the LED surface was used to detect intensity across the double ring LED. Standard deviation of the value of non-zero-pixels of the image was extracted as a metric of illumination uniformity provided by two LED rings. In the image acquired by this structure, the calculations, after exclusion of zero (dark) pixels, resulted in an estimation of 0.1556 a.u. standard deviation of light intensity and a mean value of 0.5325 a.u. after normalization with respect to the maximum pixel intensity. These values present a variation of light intensity lower than 30 % around the mean intensity – normalized with respect to the maximum value - provided by approximately 75 % of the pixels belonging to the LED ring region. This variation can be easily observed in the pseudo-color 3d illustration of spatial distribution of pixels' value presented in Figure 16 and it is attributed to the striations in the p-n junctions inducing microplasma spots. Though this variation of light, affecting illumination uniformity, can be easily improved by the use of high resolution impurities-free photolithography masks on soda lime or quartz, it is clearly depicted by the experiments described below that imaging can be accomplished even by the use of low-cost fabrication of on-film masks.

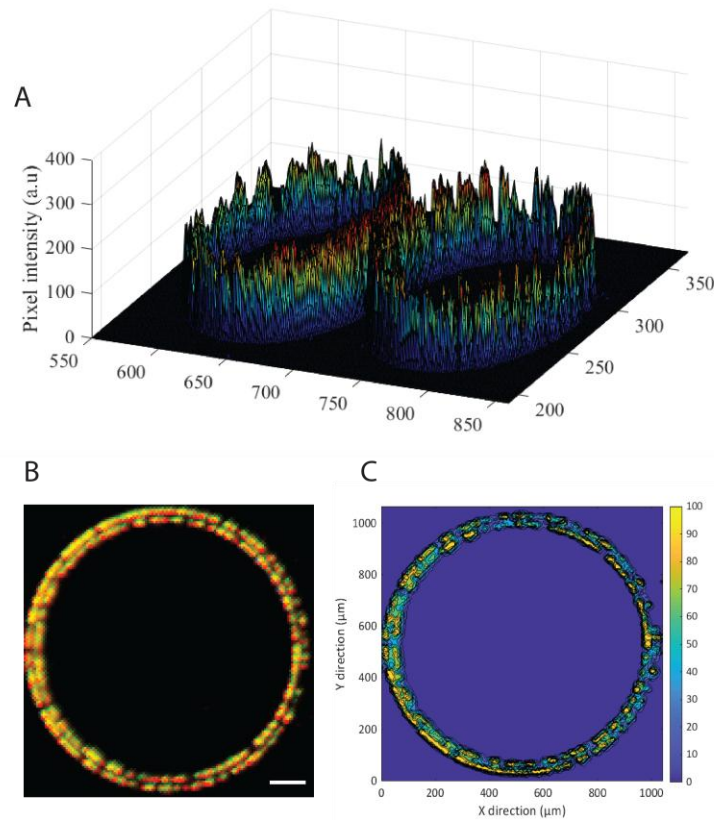


Figure 4.16. Surface plot of pixel intensity distribution over the area of the LED structure.

A second experiment was performed excluding the lenses, in which light rays, released by the LED array, directly hit the detector surface for different distances between the CMOS detector and the LED structure. The voltage applied to the LED structure was 11V and the measured substrate current was 450 mA. The CMOS detector was located in distances ranging from 20 μm up to 500 μm with a scanning step of 20 μm . Based on the expected wide angle light emission by the p-n junction, as this distance increases, the light rays will reach a wider area of the sample surface. At the same time, a decrease in the intensity of rays will be observed, as these are propagating for longer distances, through the optical media that participate in the optical path. Indeed, the conducted experiment resulted in images of higher mean value as the CMOS sensor moves away from the LED structure. This rise of the mean value is indicative of the number of pixels exhibiting higher or non-zero values as the detector is positioned far from the LED rings and consequently of the broader spatial distribution of light over the CMOS surface.

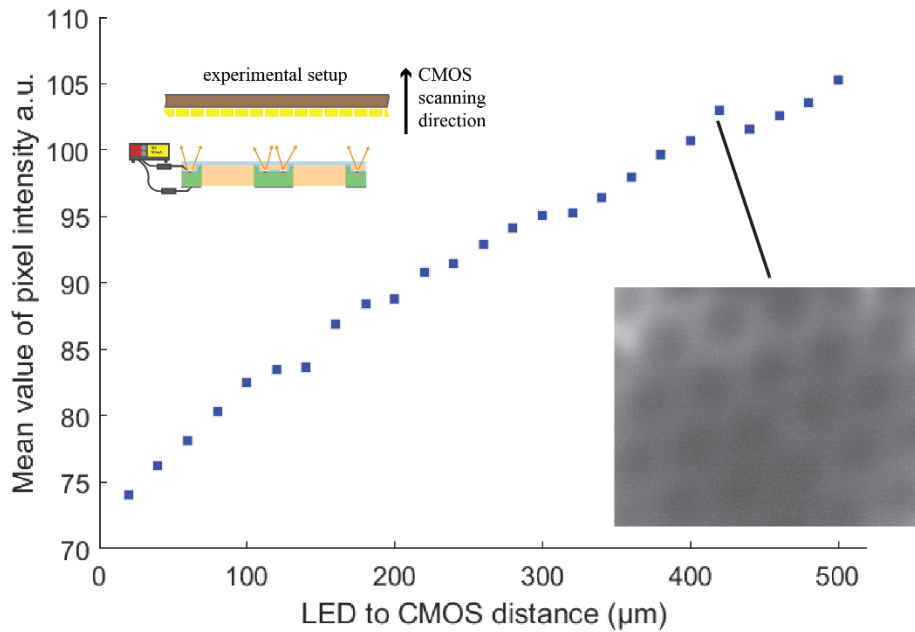


Figure 4.17. Spatial distribution of light directly hitting the sample surface, measured with the precise positioning of the CMOS detector in the place where the sample should be located. A series of images was acquired each one corresponding to a gradually increasing distance of the detector with respect to the LED structure.

While in the acquired images, an apparent non-uniformity of light distribution can be noticed, the result should be examined in reference to the intended use of the LED array along with the mini-lens array. The parts of the illuminated surface that can be imaged by the lens array in a single shot correspond to the field of view of the lenses that are disc shaped regions located in the center of each lens and presenting a maximum diameter of 300 μm. The light distribution over each disc is much more homogeneous with the standard deviation being held for all lenses below 1.7% of the maximum pixel intensity. This value has been extracted for all examined distances between the detector and the LED array. After cropping 15 areas corresponding to the field of view of the lenses, we have examined the increase in the mean value of each one with respect to the distance separating the sample from the LED structure. The variations observed between these areas are attributed to the light intensity slight decrease for the LED rings located in the center of the array compared to those at the borders. This decrease is mainly due to a small voltage drop at the interconnections of aluminum film. However, the small differences between the mean intensity of these areas indicate a uniformly illuminating array.

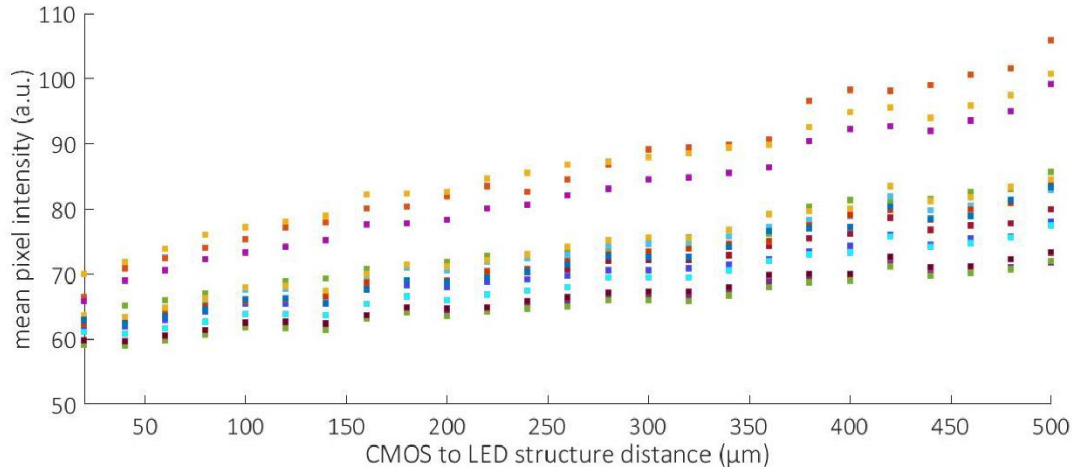


Figure 4.18. Mean pixel intensity measured for 15 regions in the array corresponding to the field of view of 15 lenses, with respect to the sample – to – LED structure distance.

3.2.1. Noise superimposed on image due to reflected light though the optical path.

As light rays propagate through the different optical media of the optical path – optical adhesive, glass cover slip, air, sample holder surface – until they reach the sample surface, some rays are reflected back from the interfaces between these media. A part of the reflected rays is reflected again towards the sample by the aluminum film deposited on the bottom side of the chip, exhibiting increased reflectivity. However, the fraction of the reflected rays that are able to pass through the lenses can reach the detector and induce a noise in the final image. To examine the level of the induced noise, an experiment was conducted, in which a mirror was employed in the place of the sample. Light rays reflected by the mirror travel through the lenses and hit the detector surface. For different positions of the CMOS sensor with respect to the lens array, ranging from 40 to 1000 and a vertical scanning step of 40 μm, the variations of light intensity in the entire acquired image were calculated. In this experimental setup, a fixed position of the mirror was selected with the distance measured from the LED surface being held at 150 μm and the LED ring array was power supplied with 5 W. The coefficient of variation was calculated as the standard deviation of pixel intensity over the mean pixel intensity.

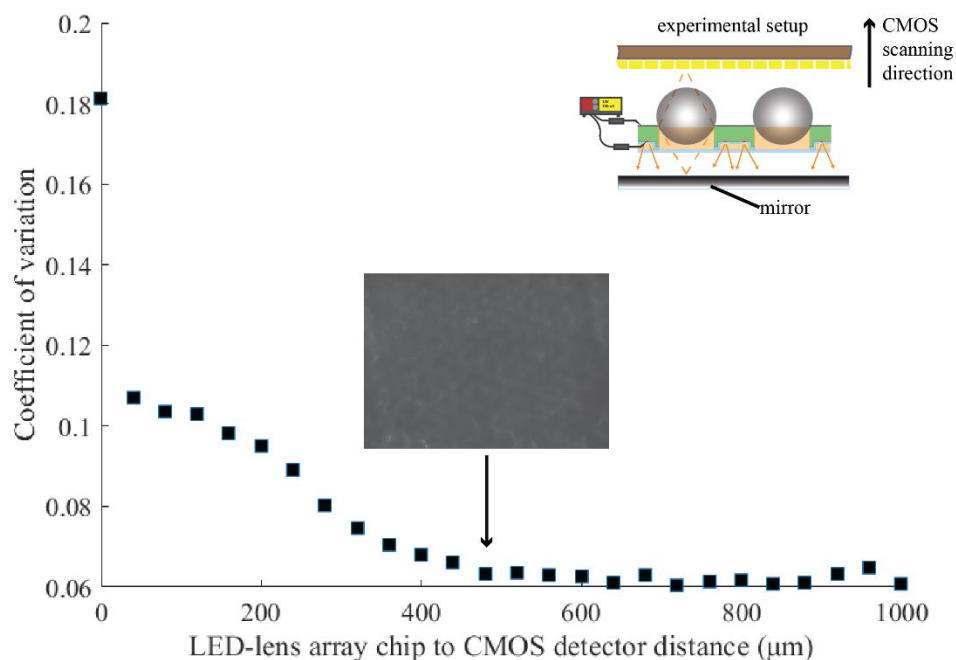


Figure 4.19. Experiment examining the noise level due to reflected light rays on the CMOS detector. A mirror was fixed in the position of the sample and a scanning of the detector was performed for a range of distances from the lens array from 40 to 1000 μm with a 40 μm . The coefficient of variation was extracted by the acquired images depicting a plateau of uniformly distributed noise level above a distance of 450 μm .

For positions of the detector close to the lens array, sharp imaging of the LED structure is performed, in which the bright spots appearing along the LED rings are easily noticeable after passing through the high numerical aperture lenses. As the detector moves away from the lens/LED chip these spots become blurred and consequently the coefficient of variation – calculated over the entire acquired image – reduces. After a specific point about 450 μm distant from the lens array the image becomes uniformly blurred and the metric of variation reaches a minimum plateau. The images acquired along this experiment are considered as noise images that will be superimposed on the sample image for the case a high reflectivity surface is used as a sample holder. Thus, the pixel intensity in these noise images has to be uniformly distributed over the entire CMOS surface and be held at a low level so as not to destruct the sample's features imaging.

3.3. Thermal characterization.

The performance and efficiency of the produced LED-based light source array is also examined concerning the temperature rise of the silicon chip as a result of the applied reverse biased voltage and the duration of operation time. With the intension of using the proposed optical/illuminating silicon chip as part of portable point-of-care imaging systems, and the necessity to place the imaged biological sample as close to this chip as possible for high magnification and high resolution imaging it becomes of great importance to assure temperature operation below a critical value of approximately 45 $^{\circ}\text{C}$ (Dewhirst et al., 2003). Indeed, the sample has to be located in close proximity to the LED-ring array (within the range of 0-500 μm), while long exposure time is necessary to

capture a high quality image of it. Thus, possible raise over 45 °C may permanently damage cells or tissue samples. Under increased reverse voltage conditions, temperature of the silicon die was measured by a thermocouple, placed on the surface of the glass cover slip which is in direct contact with the silicon LED chip. In this experimental setup, the temperature dependence on the substrate current was measured, with each measurement being taken after 3 min of continuous operation (steady state condition). The temperature rise exhibits a linear proportionality to the substrate current, presenting a maximum value of approximately 65 °C when the substrate current rises up to 1200 mA.

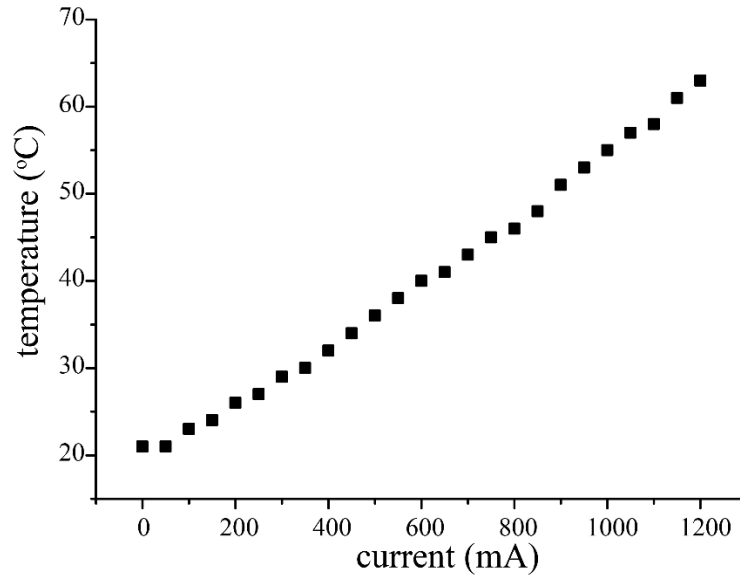


Figure 4.20. Temperature rise occurring on the surface of the silicon-based LED structure, measured by a thermocouple in direct contact with the bottom side of the chip, as a result of the substrate current of the silicon die.

The same experimental configuration was used to detect the temperature evolution over the operating time for a high value of substrate current reaching 1000 mA. The total duration of the experiment was 3 min and the resulting curvature of temperature proves a plateau of approximately 35 °C higher than the starting temperature of the environment. This plateau has been reached within the first 30 s of operation.

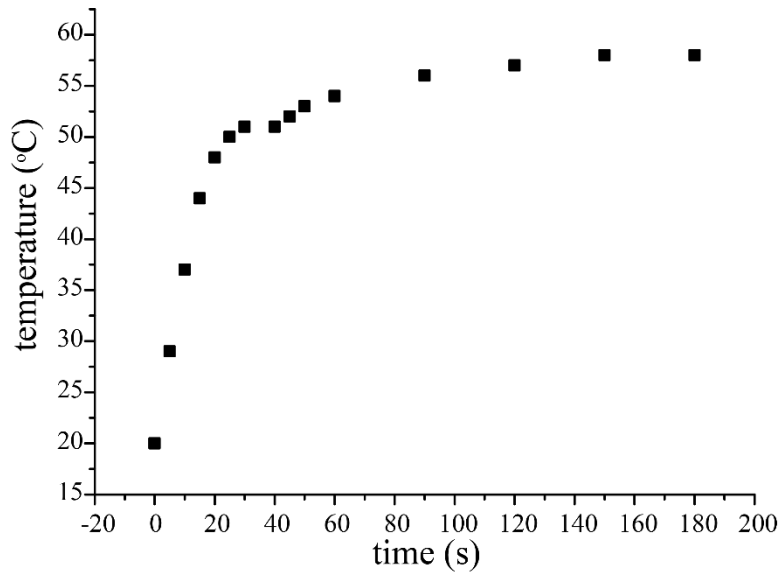


Figure 4.21. Temperature rise over time of operation measured with the use of a thermocouple in direct contact with the bottom side of the silicon chip.

A similar experiment was conducted with the use of an IR thermal camera combined with a FLIR T197214 close-up lens. In this configuration, the IR thermal camera was placed at a distance of 3 cm from the imaged surface with a tilt of approximately 20° to prevent ambient light reflection from the aluminum film. IR thermal monitoring was performed by direct imaging of the aluminum film surface, without the presence of the glass cover slip. The lens/LED array chip was placed on a holder that touched it in two points located approximately 1.5 cm away from the LED array on both side. This holder used as part of the imaging setup, acts as a heat sink, therefore a deviation from the values measured above is expected.

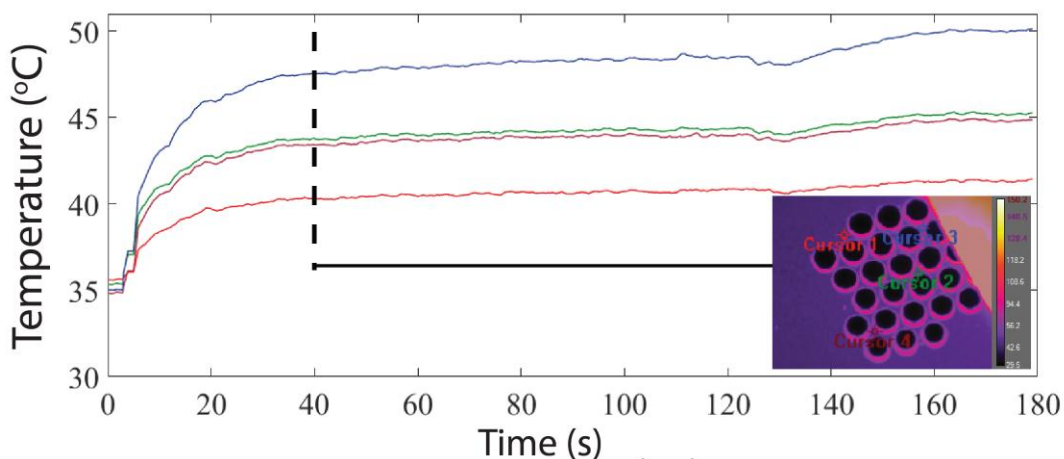


Figure 4.22. Temperature rise with respect to the operation time measured at 4 points of the LED surface with the use of an IR thermal camera.

4 different points/cursors were selected on the surface of the LED array indicating the spatial differences of temperature over the silicon chip. As expected, the points close to the LED rings presented a higher plateau of temperature while those in the spaces between the LED rings were held slightly colder. The overall reduction of 10 °C in the temperature rise is attributed to the placement of the LED/lens array on a metallic holder used as part of the scanning/imaging setup. With the same experimental setup two different values of the selected operation time were tested under switching configuration. Short time switching configuration of serial intervals of 10 and 20 s were used to examine the temperature raise and fall within the operation cycle and possible temperature increase over a long number of cycles. Total operation time was therefore selected to approximate 3 min. The selected values are much higher than the exposure time required by the detector to collect light scattered by the sample in most cases. However, they were used as indicative of the temperature rise with respect to the total operation time (after a large number of repeated images are acquired).

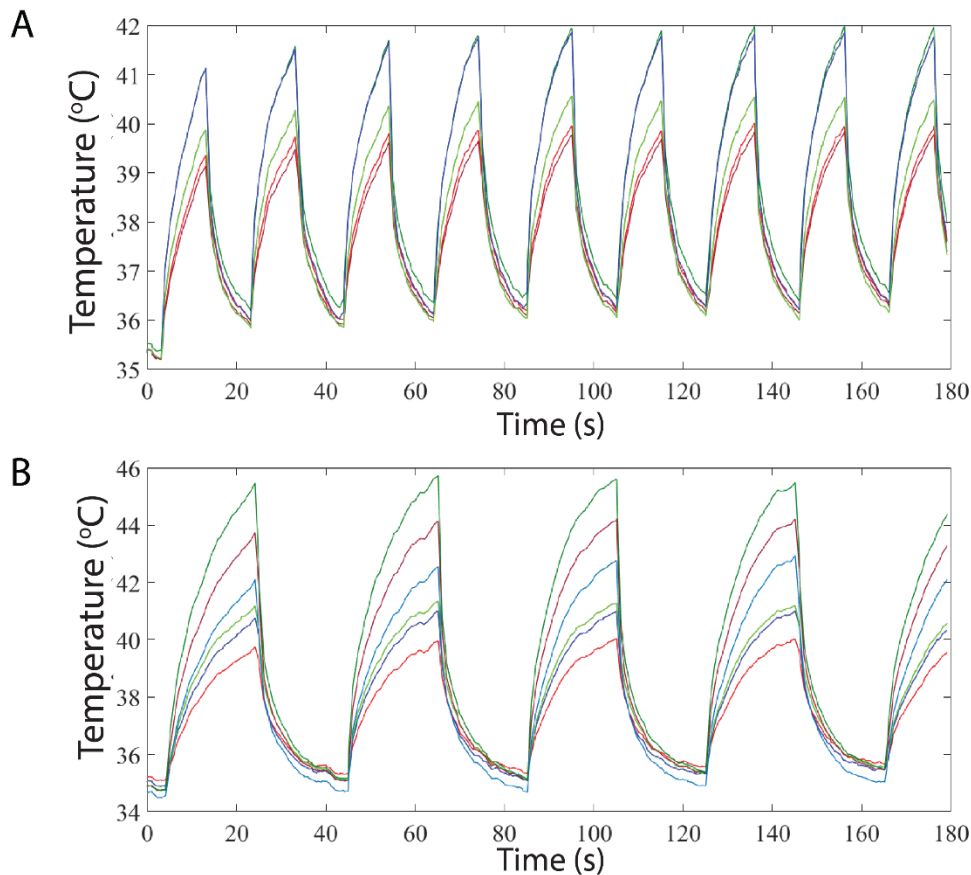


Figure 4.23. Temperature rise over long time of operation of switching intervals with a duration of (A) 10 s and (B) 20 s, measured for 6 points on the LED surface with an IR thermal camera.

The results, illustrated in Figure 23, present a negligible overall temperature raise, less than 0.3 °C for 9 cycles of 10 s operating time, while in the case of 20 s interval no rise of the overall plateau is observed. The maximum value reached (plateau) was 10 °C higher than the starting room

temperature for the case of 20 s intervals and only 7 °C above room temperature when switching intervals are 10 s long. The maximum value (plateau) is held in both cases under the critical point of 45 °C, proving the potential to use of this type of illumination even in biological samples at close distance to the LED array.

3.4. Imaging with the LED/lens array device.

To complete the characterization process of the proposed device, bright field reflection mode imaging with the use of this silicon-based LED/mini-lens array chip was accomplished. The experimental setup comprises of a CMOS detector, placed close to the mini-lens/LED array chip – from the side of the ball lenses – and a sample holder, located close to the LED array – at the bottom side of the Si chip. 2 different precision micro-stepping motors with a minimum step of 20 μm are employed to precisely change the distances between the mini-lens/LED chip, the CMOS sensor and the sample holder.

For bright field reflected illumination scheme, USAF 1951 resolution chart (Edmund Optics #58-198) was used to determine the resolution provided by the aforementioned system. In this negative polarity resolution chart, chromium film is deposited on glass, while the features of line pairs of known width are etched regions of the chromium film. Thus, when light rays released by the LED structure reach the surface of the resolution chart, the chromium film reflects back the rays leaving dark the etched patterns in the image projected on the detector. A 2 sec exposure time of the CMOS detector was selected for this experiment with equivalent operation time applied to LED array source. High voltage of 10 V in reverse biased mode was applied to the LED array to assure maximum intensity of light illuminating the sample. The entire setup was controlled by an Arduino Uno microcontroller board to perform vertical scanning of the CMOS detector (from 0 to 800 μm distance from the lens-array chip) for a fixed – 150 μm – distance between the sample and the LED source. To control the entire setup, a Graphical User Interface (GUI) was developed in LabVIEW environment for the simultaneous, automatic control of the micro-stepping movements in the employed setup, the imaging parameters – exposure time and gain of the detector – and the aspects of the LED power supply – voltage applied, current threshold and operating duration (APPENDIX 2). The captured images were subjected to salt and pepper de-noise filtering algorithm (in MATLAB environment) and image contrast adjustment to enhance image quality (APPENDIX 2).

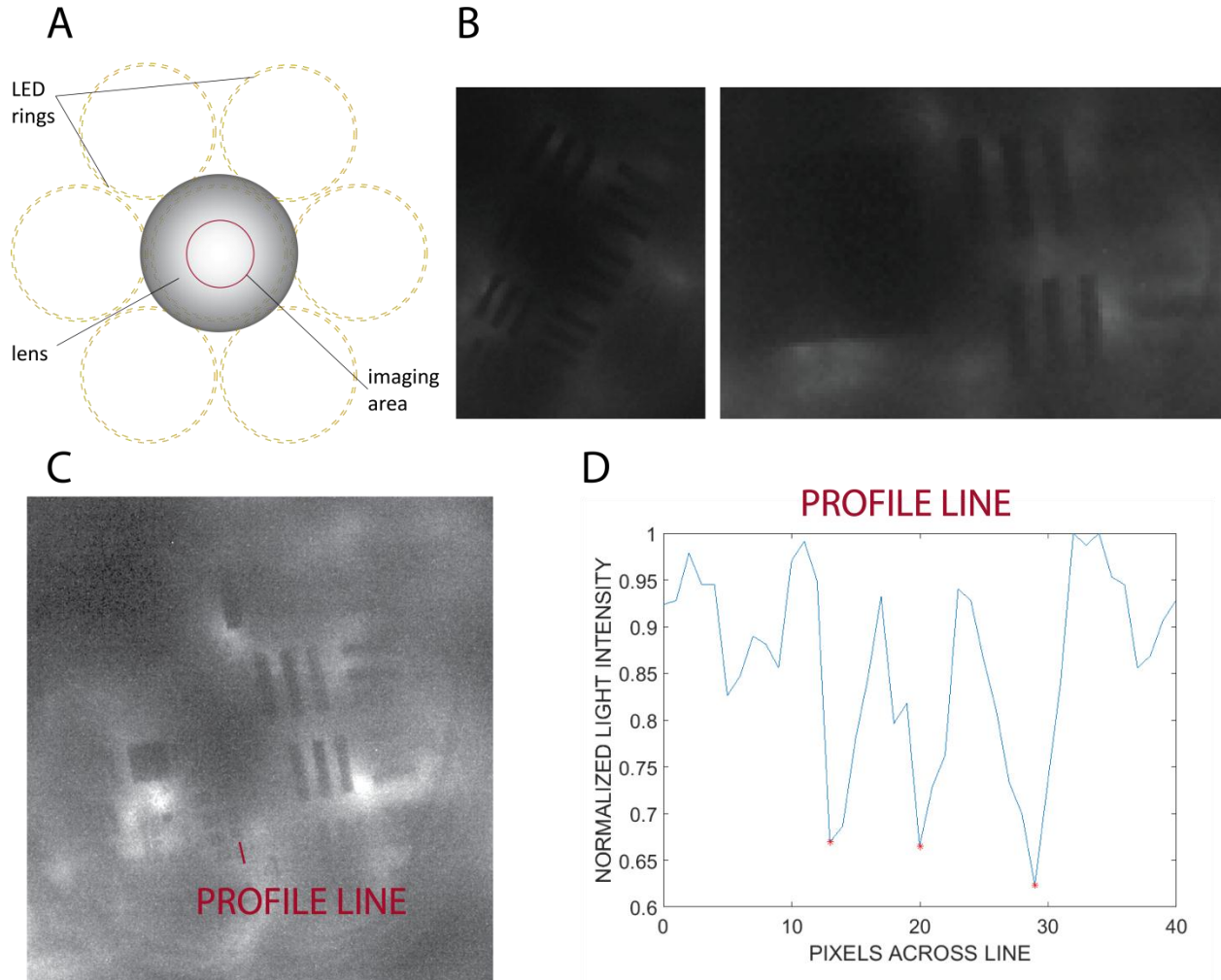


Figure 4.24. Epi-illumination imaging in bright field. (A) Sharpest image acquired through focus scanning process. (B) Part of the image containing the narrowest line pairs detected – maximum resolution. (C) Profile line of the lines pattern of maximum resolution (8.8 μm lines width).

Bright field epi-illumination imaging of a resolution chart (USAF 1951, Edmund Optics) resulted in 8.8 μm resolving power of the proposed device. The image was acquired through vertical scanning to determine the distances between the sample, the LED/lens array and the CMOS detector that provide sharp, in-focus images. The selected pattern exhibits high reflectivity due to the thin polished film of chromium deposited on the glass piece. The resolution was defined as the width of the thinner lines pattern that provided clearly distinguishable peaks in the profile line in MATLAB. In the 8.8 μm line pairs the pixel values corresponding to dark lines were approximately 30 % lower than their separating bright lines, therefore, they could be automatically detected by the selected criterion.

4. Discussion – Advantages and tradeoffs, improvements and future perspectives.

A micro-optical array integrating excitation and collection optics on the same silicon chip has been developed and presented, with the intention to be used in reflection mode imaging setups and

miniaturized point-of-care devices. The fabrication and characterization process clearly depict the increased compactness of the proposed chip, with the total optical path length being held below 2.5 mm, rendering this design suitable for all miniaturized optical setups for epi-illumination imaging. The bulk complex optical systems, usually employed for epi-illumination scheme, are excluded, while miniaturized optical elements – mini-lenses of 1 mm in diameter – are used instead. Key element for the reduction of the size and volume is the integration of the illuminating structure on the optical element, without affecting the field of view of the imaging system. It is indeed of crucial importance to implement a lens array that is capable of reducing the volume of the optical components, while providing successful screening of a wide area; a surface of more than 5 mm² is feasible simultaneously by the lenses, in the presented design.

Apart from the successful miniaturization, the proposed hybrid optical element achieves the separation of the excitation and emission beam optical paths, which, in conventional reflection-based setups, share the same optical components affecting eventually the signal-to-noise ratio in the provided image. In conventional epi-illumination microscopy, the separation of the two beams is achieved by the employment of filters. In the proposed design, the characterization process indicates the feasibility of imaging in bright-field reaching a resolution of 8.8 μm, without the use of any filtering coatings or other bulk filtering components.

The temperature rise of the silicon chip is dependent on the duration of its operation under increased reverse voltage conditions, therefore on the exposure time required by the CMOS detector. This aspect is crucial for the feasibility of integrating the developed optical/illuminating chip in biological imaging systems, provided that the sample should be located at close vicinity to the illuminating structure (up to 300 μm away from it). While the temperature increase, for 3 min total duration, is expected to affect the sample reaching 65°C, it can be easily controlled through miniaturized heat sink devices, in many cases constituting part of the hosting setup, as in the micro-setup presented in this chapter. Furthermore, the automatic control of the switching time, limiting the operation of the LED structure to the strict requirement of detector's exposure time - up to 2 s being adequate to capture a high quality image – and extending the non-operation time to suppress high temperature value, have been depicted as simple ways for controllable thermal effects in the chip and the entire setup.

The resolution provided by this silicon chip is not limited by the optical lens array as it is proven by the optical performance characterization of the lens array in transmission mode imaging (see chapter 2). The uniformity variations of the emitted light are considered as the main factor affecting the resolving power. These uniformity variations are attributed to imperfections of the LED rings in the fabrication process – non-uniformity along the LED ring- or to the geometrical characteristics of the design – spatial non-uniformity over the entire sample area as a result of the radius of the designed LEDs. The characterization process illustrated both the gradual decrease of light intensity in the center of each lens area as well as the possibility to image high reflectivity samples as the one selected in the imaging experiment (USAF resolution pattern, polished chromium film deposited on glass). However, simple alterations in the design and the fabrication protocol, discussed in the sections to follow, have the potential to further improve image quality in reflection mode based applications.

4.1.Improvements on the geometrical design and fabrication process, to achieve increased quality performance.

The fabrication process described above includes the employment of low-cost photolithography masks printed on film that resulted in rough boarder lines separating the p and n regions of the LEDs. The uniformity of emitted light along the p-n junction could radically improve by the use of high resolution photolithography masks on soda lime or quartz, containing low density of impurities of decreases size. Such an option will eventually increase the cost of fabrication but is believed to lead to higher resolution and decreased power requirements for the same LED array structure design.

Improvements on the geometry of the proposed excitation/collection micro-optics array may result in increased resolution to reach the lens limit of optical resolution (Korompili et al., 2018). To further increase the illuminated area and the provided light intensity, more space is needed for the LED structure to be patterned on the bottom side of the silicon chip. Additionally, it is clearly depicted by the lens array imaging performance in transmission mode that the lens aperture could be reduced to the size of a disc equal to the field of view of each lens, down to a radius of 150 μm without loss of information. Thus a fabrication process that would result in a broader space for the LED structure is strongly believe not to affect imaging but also to improve the spatial distribution of light over the sample surface.

Towards this direction, a Silicon on Insulator (SOI) wafer (Bruel, 1995) could be employed, in which the thin device layer, hosting the LED array could be etched through along with the buried oxide over a disc area of 250 – 300 μm in diameter, being always centered to the lens placed on top (bulk silicon layer). In this case, the edge to edge distance of the bottom side of the wells would increase up to 850 μm without any displacement of the lenses in the array, thus achieving equivalently wide field of view imaging. Compared to the presented structure of 90 μm , this increase of almost 850 % will provide the space for the integration of up to 9 times the number of LED rings for each lens. This number together with the radically smaller radius of the LED rings will result in much more uniform illumination, while at the same time the increased intensity of provided illumination is believed to lead to reduced requirements of operating time. Possible drawbacks of such a design could be the temperature rise affected by the multiplied density of the LED structure as well as the extension of the fabrication process – more steps and photolithography masks are necessary. An entailed increase in the fabrication cost of the device is also included among main trade-offs of the proposed alteration.

A similar idea towards improved spatial distribution of light over the field of view area includes anisotropic wet silicon etching - e.g. KOH (Bean et al., 1978; Monteiro et al., 2015) - as an alternative micromachining technique of the wells hosting the lenses. In this case, the resulting design of the wells would present a squared shape instead of circular one with oblique walls instead of vertical, giving a narrower aperture opening at the bottom side. While, such a fabrication benefits from reduced complexity and production cost, it may restrict the density of the lenses in the array, therefore, result in reduced optical field of view in the acquired image. Additionally, the ring-shaped design might need to be altered to a square-shaped with decreased dimensions. In both wet etching and silicon-on-insulator designs, blocking of undesired light coming from neighboring regions of the

sample will also be feasible, leading to an improved signal-to-noise ratio and elimination of crosstalk effect, severely affecting micro-lens array-based, miniaturized, microscopy platforms.

4.2. Alterations in the fabrication process to improve power consumption and high illuminating efficiency.

Increased light efficiency combined with lower power consumption can be achieved with the use of different LED technologies according to recent advances in the field of solid state lighting (Tan et al., 2012; Pust, Schmidt and Schnick, 2015). In particular, the great interest this field has gained over the years, led to both brighter LEDs produced or lower power requirements to run the device at the required illumination level. The proposed system integrating an LED ring-shaped structure with a mini-lens array can be considered as a platform design that can be implemented with a different LED protocol and materials either to provide white light of higher luminous efficacy or narrow band light for specific applications, such as fluorescent imaging described below.

4.3. Alterations in the fabrication process to achieve reflection based fluorescent imaging.

The described platform design could be highly beneficial in the case of fluorescent imaging, mainly due to its capability to separate the excitation and emission optical paths. It is indeed obvious that these two beams do not share the same optical components, a fact that has been the ultimate requirement for reduced noise, reflection-based imaging. To perform epi-fluorescence, simple alterations of the design should be included. Different substrate and p-n regions materials are to be used to produce light of narrow band wavelength to excite the specimen. Typical example of non-white light LED structures are GaN, that can be used to limit excitation light to the blue region (400 – 450 nm) (Nakamura, Pearton and Fasol, 1999) or AlInGaN to illuminate the sample in the UV region (below 400 nm) (Khan, Balakrishnan and Katona, 2008). In these cases, the excitation – narrow wavelength band light beam hits the fluorescent sample by direct propagation without passing through the lenses. The scattered light beam released by the sample's features is collected by the lens array and projected on the detector's effective area.

Further improvement on the efficiency and provided image quality in the above described application could be reached by the decrease of superimposed reflected noisy image. The noise that might be induced is attributed to high reflectivity of the sample holder employed. Therefore, antireflective coatings deposited on all optical media participating in the optical path could lead to noise elimination without affecting transmitted light intensity. This technique could be combined with thin film flexible filters placed between the lens-array and the detector or filter coatings directly deposited on camera sensor surface, to block the excitation wavelength according to the application, and achieve successful fluorescent imaging of increased specificity and sensitivity, with the proposed hybrid excitation/collection micro-optical array.

Chapter 5

A microfluidic bio-chip for enhanced surface capturing of white blood cells or a sub-population: extensive study of factors affecting capturing efficiency.

Surface functionalization for specific cell population capturing is widely used due to the simplicity of the method, the low cost of production compared to other techniques, such as micro-machined structures for cell filtration, and because of the radically increased throughput in comparison with the bulk laboratory cell counters used in large healthcare infrastructures. Additionally to these reasons, this method offers the possibility of diagnosis based on minute volume of blood, 1-10 μl , collected even by patients' finger. It can be easily applied to standard, cheap, commercially available, microfluidic chips and portable microscopy platforms for cell detection. Therefore, it has been proven promising for the diagnosis at the point of care, leading to a more patient-centered healthcare.

Numerous approaches, targeting different cell populations, can be applied in a wide range of diseases or health conditions. Among them, CD4^+ T lymphocytes can be captured on surfaces activated with anti-CD4 antibody (Watkins et al., 2013), as they express this specific biomarker on their cellular membranes, contributing to the effective diagnosis of the progress of HIV virus within the body of HIV infected individuals (WHO, 2015b). White blood cell counts, frequently tested even in healthy individuals but also in patients undergoing cancer treatment, can be performed by surface affinity isolation method from whole blood samples, with the use of anti-CD45 antibody, specifically binding to the corresponding biomarker on WBCs' membrane (Chen *et al.*, 2014). Other developed devices target rare circulating tumor cells (CTCs) in blood as a predictive test for cancer metastasis through blood circulation (Didar and Tabrizian, 2010).

Except for the confronted challenges in each specific case study, the specificity and sensitivity of the aforementioned cell isolation technique has proven to be promising, however, poorly researched in reference with the crucial factors that restrict accurate results of the developed microfluidic functionalized chips. Towards this need, the sections to follow are dedicated to the fabrication of a microfluidic dual chamber bio-chip regarded as a platform technology that could be used in cells isolation of various cases, according to the specific anti-body functionalization. The characterization study concerns the aspects of the geometrical design, the functionalization protocol and the conditions of washing out non-captured cells with regard to the provided efficiency in terms of specificity and sensitivity.

1. Design of the microfluidic dual channel bio-chip for surface capturing of specific cell types

The developed microfluidic chip comprises of two parallel chambers of a volume approximately equal to 1.5 μl each. Four different designs have been studied, in both theoretically described performance and experimentally based capturing behavior. In all four designs examined, there are several key aspects, in reference to the selected geometrical characteristics that are used to enable high efficiency in cell adhesion on the walls of the chambers and to prevent detachment of captured

cells during washing of unbound cell populations. Moreover, the proposed designs are intended for use in the imaging scanning platform developed in this study, while, at the same time, the required volume of whole blood sample is sufficient to provide accurate results of cell counts presenting reduced concentration in blood, such as WBCs or subpopulations of them. This volume needs to be reduced to the strict minimum to enable finger withdrawal via pricking method, for use at the point of care.

1.1. Key geometrical aspects of the design to enhance capturing efficiency

Particularly, the selected thickness of all four designs developed is reduced to only 17 μm , a height much smaller than the one selected in previously reported works, that is always above 30 μm (Zhang et al., 2005; Cheng, Irimia, Dixon, Sekine, et al., 2007; Cheng, Irimia, Dixon, Ziperstein, et al., 2007; Deng et al., 2014) up to 57 μm (Sin et al., 2005). This reduction in microfluidic chamber height is expected to enhance capturing efficiency, as the target cells - mainly WBCs with a diameter in normal conditions being 8 - 15 μm (Prinyakupt and Pluempitiwiriyaewej, 2015) – are forced to come in contact with the walls of the chamber rather than travel in the free space between them. This particular value of chamber's thickness approximates one and a half of the normally expressed WBCs mean diameter value, therefore, a single cell is not allowed to travel above an occupied region of the chamber without touching the top wall of it, while it is blocked from travelling in spaces where both top and bottom walls are occupied by captured cells (Figure 1). In the majority of cases, WBCs that are captured on a surface through anti-body specific binding mechanism, exhibit a spreading behavior; the cellular membrane is spread on the functionalized surface. The shape of the cell appears consequently to have an elliptical cross section with the height of the cell from the surface being reduced compared to the original diameter of the spherical shape of non-captured cells (Kwon et al., 2007; Khalili and Ahmad, 2015). Thus, enough space is given to the rest of blood components, mainly RBCs exhibiting a highly compressible behavior, to travel within the chamber without the possibility of clogging affecting the flow of the blood sample.

The reduced thickness of the microfluidic chamber is expected to increase the flow resistance of the chamber therefore, affect the rate of blood sample flowing into the chamber, given the specific value of applied pressure. The same effect is expected to be observed in the increasing value of flow rate in the washing step, required to remove all unbound cells. In the first case, the surface binding protocol employed is based on static blood incubation for cell capturing (see section 2.1.), where no flow appears, thus, capturing efficiency is not affected by the increased resistance of the chamber. In the second case the increased washing agent flow rate, proportional to the shear stress induced to the immobilized cells may lead to their detachment from the functionalized walls. To examine this effect, several designs were developed containing different chamber widths and lengths (Table 4.1). The theoretical and computational analysis of the proposed designs resulted in different flow resistance of each one. The functionalization efficiency has been tested in all different designs with a characterization process conducted for each one, in reference to the spatial distribution of antibodies on their inert walls.

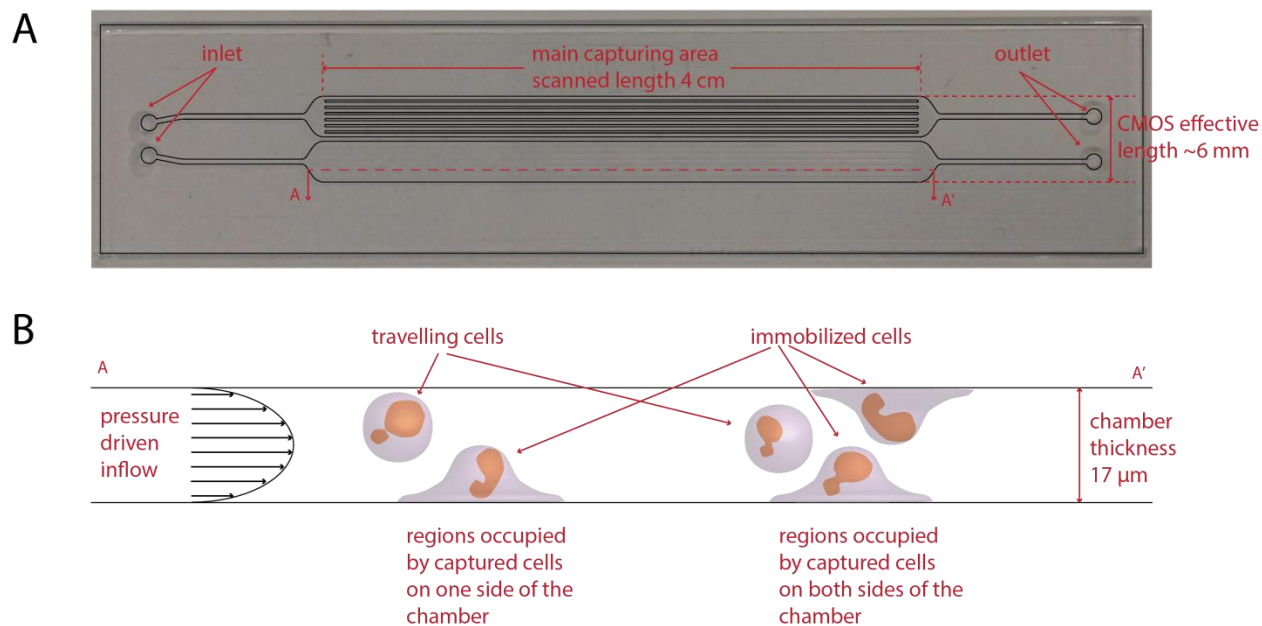


Figure 5.1. Schematic of the proposed microfluidic chip design illustrating key elements of the geometry. (A) Top view, where the effective area for cell capturing is indicated. This region is designed to comply with the specifications imposed by the developed imaging/scanning platform as this is described in the previous chapters. (B) Cross section view, where the selected height is linked with the cases of regions occupied by captured cells and the expected behavior of travelling cells in these regions.

The different microfluidic devices proposed in this study, have a total effective binding area from top view equal to the scanning area of the proposed imaging/scanning platform, reported in the previous chapters. Thus, a total length of 4 cm is selected for the main chamber of each microfluidic chip, while the width occupied by the two chambers participating in each chip is slightly smaller than the large size of the CMOS sensor active area (~6 mm).

Based on the specified dimension of each chamber, the volume of whole blood sample required to fill each chamber is in the range of 1.4 to 1.8 μl based on the specific design. Provided that each chip contains two identical microfluidic chambers, the aforementioned volume is adequately reduced to be retrieve by patients' finger through pricking method, and sufficient to provide accurate results for most cell populations count. The accuracy of the counting results is determined by the specific application and it is expected to be higher for target cells presenting higher concentration in blood such as WBCs (Bond and Richards-Kortum, 2015). The dual chamber of this platform technology can be used either to increase the processed whole blood volume, or to detect different populations in blood at the same time, provided functionalization of the chambers with different anti-bodies. In Table 4.1, the different designs are illustrated accompanied by the measurement of volume in the initial design and the estimated increased volume of the chamber based on the followed fabrication process.

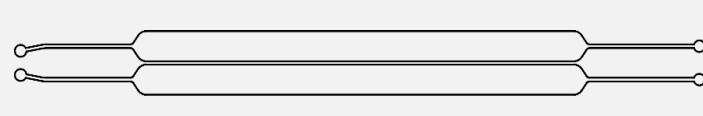
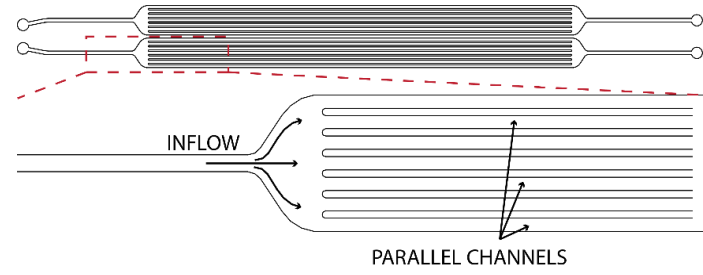
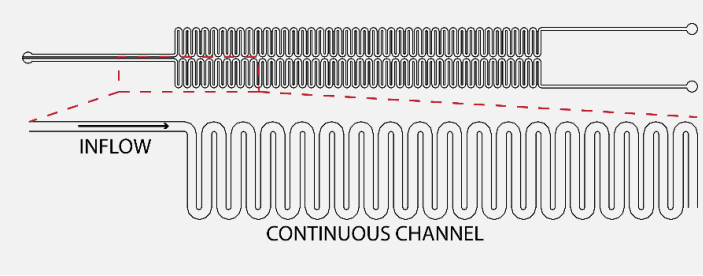
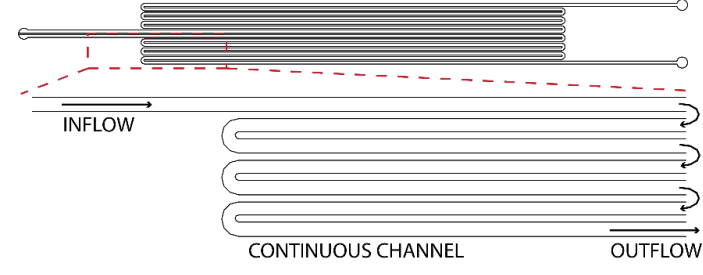
| Microfluidic chip design | Required volume based on mask design (μl) | Required volume based on fabrication (μl) | Surface to volume ratio ($1/\text{m}$) |
|-------------------------------------------------------------------------------------|--------------------------------------------------------|--------------------------------------------------------|------------------------------------------|
|  | 1.75 | 1.78 | 0.118 |
|  | 1.25 | 1.4 | 0.14 |
|  | 1.02 | 1.14 | 0.12 |
|  | 1.24 | 1.4 | 0.12 |

Table 5.1. Designs of microfluidic chambers tested in this study. For each case the initially designed volume based on the microlithography mask is reported and the estimated final volume based on the over-etching effect of the employed fabrication method is also indicated.

1.2. Theoretical calculations of flow resistance of each design

For the microfluidic device developed in this study, particular interest is gained by the exhibited hydraulic resistance of each proposed design, mainly affecting the shear force imposed on captured cells during washing. In the step of insertion of whole blood sample into the microfluidic chamber, there is little interest in the flow rate as a blood incubation step follows, in which cells are allowed to bind to the functionalized walls in rest – no pressure drop is applied between the inlet and outlet of the chamber, thus no flow is expected to appear. However, computational analysis has been

conducted to determine the resistance of each chamber in the washing process. In this analysis, both water and blood (at 37 °C) can be considered as non-compressible fluids exhibiting Poisseuille flow inside the microfluidic chamber, where the hydraulic resistance R_{hyd} can be considered as the ratio between the applied pressure drop Δp and the corresponding volumetric flow rate Q (Bruus, 2006):



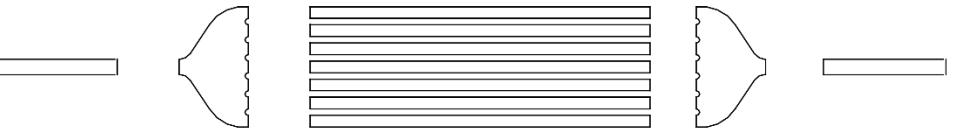
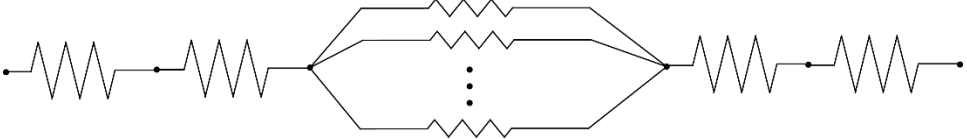
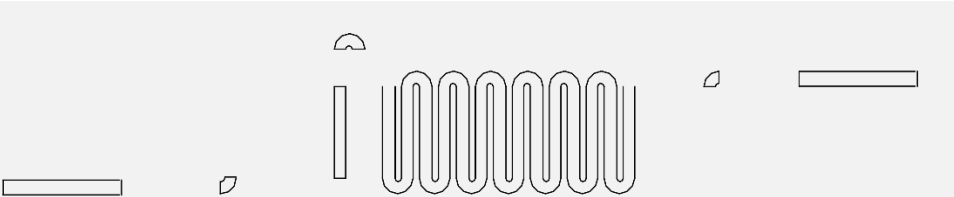

$$R_{\text{hyd}} = \frac{1}{G_{\text{hyd}}} = \frac{\Delta p}{Q} \quad (5.1)$$

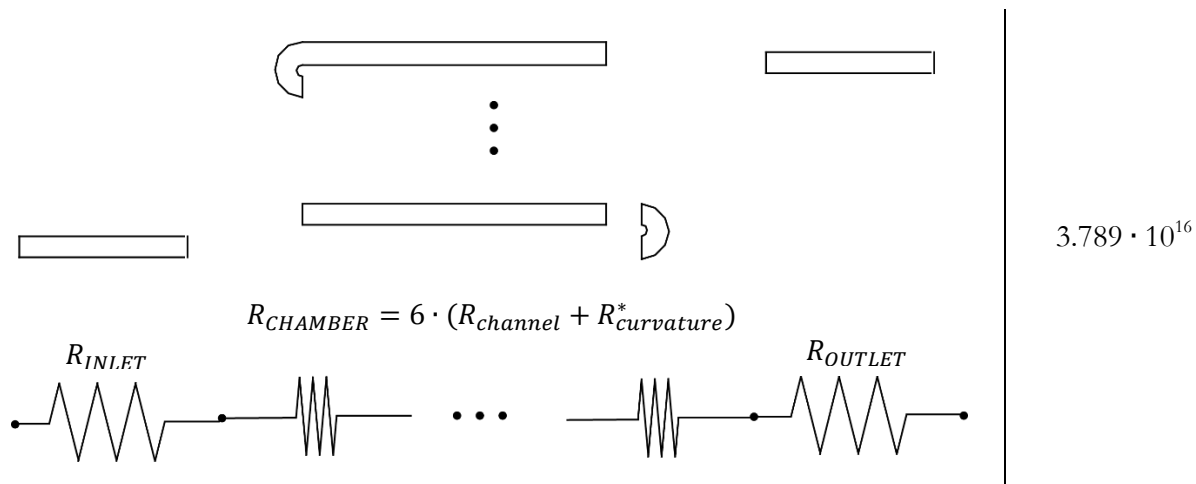
The developed microfluidic chambers are assumed to have a rectangular cross section vertical to the flow direction, despite the curved angles that are expected to appear to this cross section due to the microfabrication process. The different parts of each microfluidic chamber – inlet, main chamber, and outlet – have different flow resistance according to the geometry of each one. For the calculation of the entire fluidic resistance, each chamber is subdivided into smaller parts and analyzed either by a combination of numerical (computational fluid dynamics - CFD) and resistive electrical circuit modeling (Oh et al., 2012). For the parts of each design of rectangle top-view (straight channel) the hydraulic pressure is calculated based on the equation:

$$R_{\text{hyd}} = \frac{12 \cdot \eta \cdot L}{(1 - 0.63 \cdot \frac{h}{w}) \cdot h^3 \cdot w} \quad (5.2)$$

where L is the length of the straight channel part, w is the width of this part – that should be constant across the entire length L – h is the height of the chamber and η is the dynamic viscosity of the fluid inside the chamber.

For all parts containing either a curvature in the top view or a gradually increasing or decreasing width, a COMSOL fluid flow simulation was conducted and the hydraulic resistance was calculated as the slope in the ΔpQ (pressure drop – volumetric flow rate) derived curve. For these calculations the selected fluid was blood and the density of it (at 37°C) was 1047.37 kg/m³, while the dynamic viscosity was set at 2.78 mPa·s (Anton Paar, 2000; Ranucci et al., 2014). In this specific application, only laminar flow is expected to appear, due to the very low Reynolds number (below than the critical value of 2000) in microfluidic devices. Thus, in the COMSOL simulations velocity and pressure field are computed for a single-phase fluid in the laminar flow regime. Blood is assumed to be incompressible fluid for a constant temperature and it is also simulated as a Newtonian fluid. The time dependent solution of the Navier-Stokes equations, for an increasing field of pressure applied between the inlet and the outlet of the device, resulted in a proportionally increasing volumetric flow rate and the hydraulic resistance is derived as the division of these two values, held constant with time, as expected.

| Design | Hydraulic resistance $\left(\frac{\text{Pa} \cdot \text{s}}{\text{m}^3}\right)$ |
|-----------------------------------------------------------------------------------------------------------------------------------------------------------------------------------------------------------------------------------------------------------------------------------------------------------------------------------------------------------------------------------------------------------------------------------|------------------------------------------------------------------------------------|
|  <p data-bbox="212 506 1133 541"> R_{INLET} R_{NECK}^* $R_{CHAMBER}$ R_{NECK}^* R_{OUTLET} </p>  | $4.895 \cdot 10^{14}$ |
|  <p data-bbox="542 821 808 884"> $R_{CHAMBER} = \frac{R_{channel}}{7}$ </p> <p data-bbox="212 863 1133 905"> R_{INLET} R_{NECK}^* R_{NECK}^* R_{OUTLET} </p>  | $4.811 \cdot 10^{14}$ |
|  <p data-bbox="423 1293 927 1335"> $R_{CHAMBER} = 83 \cdot (R_{channel} + R_{curvature}^*)$ </p> <p data-bbox="212 1356 1133 1398"> R_{INLET} R_{NECK}^* R_{NECK}^* R_{OUTLET} </p>  | $3.715 \cdot 10^{17}$ |



* These values were extracted through COMSOL laminar flow simulations

Table 5.2. Total hydraulic resistance for each specific design extracted as the different parts resistance connected either in parallel or in series, according to the corresponding geometry.

1.3. Fabrication of the microfluidic chips

The fabrication of the microfluidic chips was performed entirely on glass with standard wet BHF etching and anodic bonding processes. One photolithography mask was required and it is available in Appendix A. The channels were created on a thick glass wafer of 700 μm thickness and they were then bonded on an unprocessed glass wafer, 145 μm thick. The holes of the inlet and outlet were created with powder blast technique and have a conical shape with the top circular opening 1500 μm ($\pm 150 \mu\text{m}$) in diameter and the bottom opening, that touches the microfluidic chamber being 1000 μm ($\pm 150 \mu\text{m}$). The thickness of the chambers was at 17 μm with a tolerance of $\pm 0.5 \mu\text{m}$, according to the manufacturer – Micronit microtechnologies. Due to the wet etching process an over-etching effect is expected with all features participating in the chamber being 17 μm wider in both sides. This over-etching was predicted by the design and resulted in slightly larger volume of the microfluidic chamber (Table 1). Following the fabrication on 4 inch square wafer, the chips were diced in rectangular shape of 64 mm ($\pm 300 \mu\text{m}$) length and 14 mm ($\pm 300 \mu\text{m}$) width.

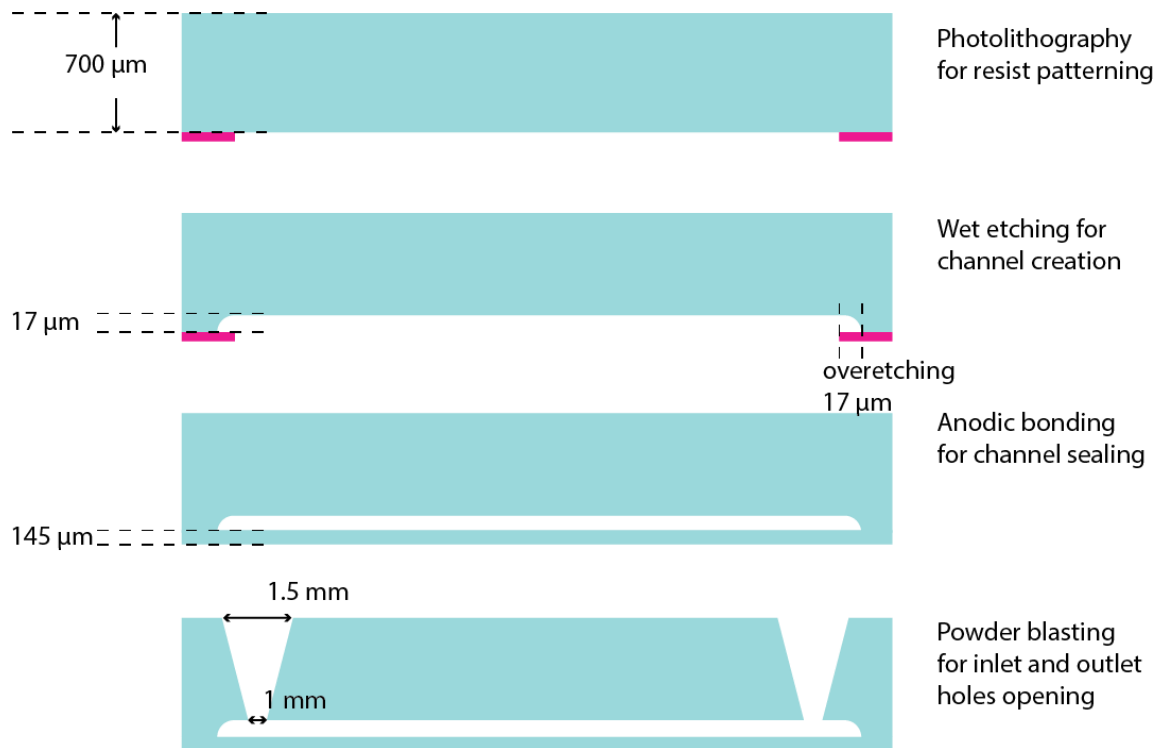


Figure 5.2. Fabrication process for microfluidic channels, based on wet (BHF) etching, anodic bonding and powder blasting techniques. The process was performed by Micronit microtechnologies company.

2. Functionalization protocol for WBC and subpopulations surface capturing.

The surfaces of the developed microfluidic chips were bio-activated with bio-active molecules aiming at specific binding with target cell populations, through specific binding to biomarkers expressed on the cell surface. The protocol of surface activation was based on standard processes followed in literature to functionalize glass surfaces with anti-CD45, anti-CD3 and anti-CD8 antibodies to immobilize specific cell types on the microfluidic chip walls. Particularly, protein tyrosine phosphatase, receptor type, C – also known as PTPRC or cluster of differentiation 45 – is a pan-leukocyte protein expressed on the surface of all WBCs, therefore is also referred to as leukocyte common antigen (LCA) and it is used to isolate WBCs in whole blood samples (BD biosciences, 2010). Cluster of differentiation 3 is a T cell receptor expressed on the surface of CD8⁺ naïve T cells and of CD4⁺ naïve T cells, therefore anti-CD3 antibodies can be effectively used for specific binding to these T cell populations (Chetty and Gatter, 1994; Bio-Rad Laboratories Inc., 2016). Cluster of differentiation 8 is a transmembrane glycoprotein that serves as a co-receptor predominantly expressed on the surface of all cytotoxic T-cells (Leong, Cooper and Leong, 1998). Several parameters of the standard protocols were modified to enhance capturing efficiency. These varying parameters were selected in order to examine the factors that affect cell surface adhesion and distribution over the available surface area or the factors that enable the detachment of captured cells during the washing process, which aims at the removal of unbound cells only.

Prior to the functionalization process, thorough cleaning of the microfluidic chambers is performed with 30 min in acetone bath in ultrasonic, 20 min of piranha 1:1 process, ethanol (70%) and deionized water. Moisture removal is accomplished with placement of the chips on hotplate at 100°C for 10 min, while a plasma exposure for 5 min completes the preprocessing step with the creation of hydroxyl groups on the glass substrate surface. The functionalization process initiates with the introduction of 4 % v/v of 3-(Trimethoxysilyl)-1-propanethiol (3-MPS) in absolute ethanol, followed by incubation at room temperature for 30 min. The chips are then washed with ethanol absolute and an annealing process is performed on hotplate at 100°C for 30 min. In this step three methoxy (CH₃O-) groups of 3-MPS are replaced with 3 hydroxyl groups (OH-) on the surface, thus forming strong covalent -Si-O-Si- bonds (Asghar et al., 2016). This process prepares the substrate for the crosslinker N-(g-Maleimidobutyryloxy)succinimide ester (GMBS) (Hermanson, 2008) that is to be inserted in the following step. 1 mM of GMBS working solution in ethanol absolute is inserted in the microfluidic chamber and incubated at room temperature for 30 min (Thermo Fisher Scientific, 2006). In this particular step maleimide reactive groups of GMBS react with -SH groups at 3-MPS, forming stable thioether linkages (Asghar et al., 2016). Washing with ethanol absolute and phosphate buffered saline (PBS) 1X is followed by introduction of neutrAvidin, a deglycosylated version of avidin that retains biotin binding affinity while it expresses minimized non-specific interactions with the negatively-charged cell surface compared to avidin (Marttila et al., 2000). 150µg/ml neutrAvidin in PBS 1X is inserted into the microfluidic chambers and it left for 1.5 h for incubation at 4°C, followed by washing with PBS 1X and PBS 1 % BSA. The NHS-ester end of GMBS couples with amines located at neutrAvidin to form stable amide bonds (Thermo Fisher Scientific, 2006). The used antibodies are biotinylated, thus specific biotin-avidin interaction occurs with the insertion of anti-CD45 monoclonal, biotinylated antibody at various concentrations (purchased from R&D systems, #BAM1430). The very specific interaction of biotin and avidin is characterized by the strongest known non-covalent bonding (Dugas, Elaissari and Chevalier, 2010). Incubation for 30 min at room temperature, washing with PBS 1% BSA and blocking with PBS 1 % BSA at room temperature for 30 min complete the entire functionalization process.

Blood sample retrieved by finger pricking method or through the vein following the standard venipuncture protocol is collected in heparin tube and inserted into the microfluidic chamber with a Hamilton syringe. An incubation step of total duration 8-15 min, depending on the specific chamber design, is performed; removal of unbound cells and blood components is performed with PBS 1X containing 0.001M EDTA pH 8.0 washing step. The applied pressure for washing out the non-targeted blood compounds is adjusted to 2 mbar for designs 1 and 2 of the microfluidic chambers, ~12 mbar for design 4 and 300 mbar for design 3, with the total duration ranging from ~16 min to ~1 h depending on the hydraulic resistance and the total volume of each specific chamber; the washing process is considered sufficient after introduction of a total volume of 3 times the volume of the chamber.

For the experimental process, imaging of the captured cells is accomplished under optical microscope with DAPI filter and in bright field illumination scheme. Thus, the specificity and sensitivity of the proposed bio-chip can be quantified. For fluorescent imaging Hoechst staining (3:1000 in PBS 1X) is introduced in the microfluidic device. The introduction scheme used is from

both the inlet and outlet of the chamber, 2 times each, every 20 min. With such a scheme successive staining of captured blood cells is observed, even in cells located at the center of the microfluidic chambers.

2.1. Key aspects of functionalization process.

Key aspect of the previously described functionalization protocol is the incubation of whole blood sample within the chamber. This step excluded from other approaches for surface affinity based isolation of cells is expected to enable enhanced capturing efficiency. The WBCs, that travel in the space between the chambers walls without touching them during flow, are able to settle down during incubation where no flow is present. The increased concentration of RBCs is expected to affect the possibility of WBCs to find the route towards the functionalized surface. Therefore, periodical stirring is performed during incubation time. This stirring is accomplished with manual rotation of the chip towards both directions every minute of the incubation time. This stirring process forces WBCs to slide to neighboring regions not occupied by cells – either WBCs or RBCs – and come in contact with the functionalized wall. The total incubation time is dependent on the channel hydraulic resistance and the time needed blood to come to rest – in thermodynamic equilibrium, after removal of the external pressure drop applied during insertion (Bruus, 2006). The incubation time also depends on the possibility of blood coagulation, especially in channels with narrow routes, that need to be washed in shorter times after blood introduction.

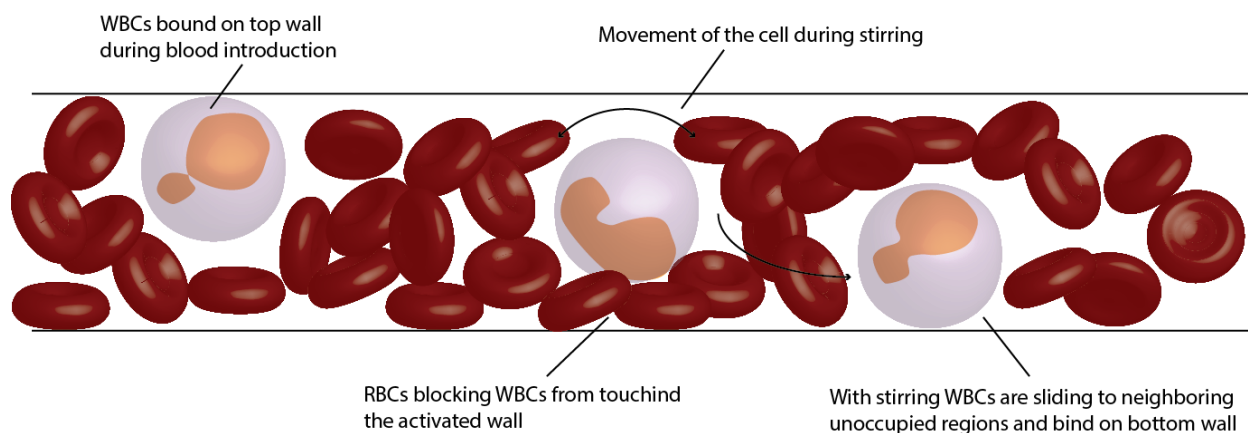


Figure 5.3. White blood cells movement in stirring process during incubation time, where no flow occurs.

Crucial aspect of the followed bio-activation protocol is the introduction scheme of the proteomic agents participating in surface functionalization into the microfluidic channels. Increased molecular weight solutions, such as neutrAvidin, antibody and Hoechst staining solutions were observed not to be evenly distributed over the chamber' surfaces (Kamholz and Yager, 2001), with the phenomenon being at increased intensity in chambers presenting increased hydraulic resistance. Therefore, these solutions are introduced into the chamber by both inlet and outlet, while several schemes of repetition of the introduction process being examined.

Final key aspect of the protocol described is the washing process aiming at the removal of unbound cells and other blood components. A successful washing procedure refers to the removal of all

unbound cells, in order to achieve maximum selectivity of the quantification process in bright field imaging, as well as to the non-detachment of captured cells from the functionalized walls, in order not to affect the resolution of the device. This detachment occurs under high flow rate of blood or washing solution that applies shear stress to the immobilized cells. The detachment is highly dependent on a series of factors: the strength of the bond between the cell receptor and the ligand molecules anchored on the chamber's wall (Hassani-Ardekani, Niroomand-Oscuii and Khismatullin, 2015), the number of specific surface bio-markers expressed on each cell type membrane (Davis et al., 1998), the cell size and deformability when attached to an antibody-functionalized surface (Khalili and Ahmad, 2015). The flow rate when increased above a critical limit may result in extensive cell loss. The flow rate was accordingly adjusted with a corresponding adjustment of the applied pressure drop during washing, taking into account the hydraulic resistance of each microfluidic chamber as theoretically analyzed in previous sections. The aforementioned adjustment is based on computational analysis through COMSOL fluid flow simulations that examine the applied shear stress induced to a cell during washing. Despite the numerous efforts in literature towards this analysis (Kuo, Hammer and Lauffenburger, 1997; Simone et al., 2012; Hassani-Ardekani, Niroomand-Oscuii and Khismatullin, 2015; Torney, Saxman and Hammer, 2015), in this attempt, a deformation of the cell is taken into account to provide more accurate results of the simulations, based on the specific geometry of the proposed microfluidic channels.

2.2. Shear force imposed on immobilized/captured cells during washing, based on COMSOL simulations.

To estimate the shear forces that are applied on a cell attached on a functionalized surface through pressure driven flow in a microfluidic channel, a computational fluid dynamic (CFD) analysis was performed in COMSOL fluid-structure interaction module software. In the developed model, the microfluidic chamber is assumed to comprise of a parallel plate configuration with infinite aspect ratio in the cross-sectional dimensions, as the comparison of the captured cell size is much smaller compared to the chamber's width and length in all four proposed designs. The total length of the designed microfluidic channel in the model was 300 μm in the flow direction. A second assumption of the conducted simulations refers to the dome-shape of the cell after attachment on the functionalized surface, attributed to the cell membrane deformation. The dome-shaped geometry employed, depicted in Figure 4, corresponds to a real image of a deformed cell attached on a bio-activated surface provided by cellular observation under standard optical microscope in increased magnification (50X) in trans-illumination bright field scheme.

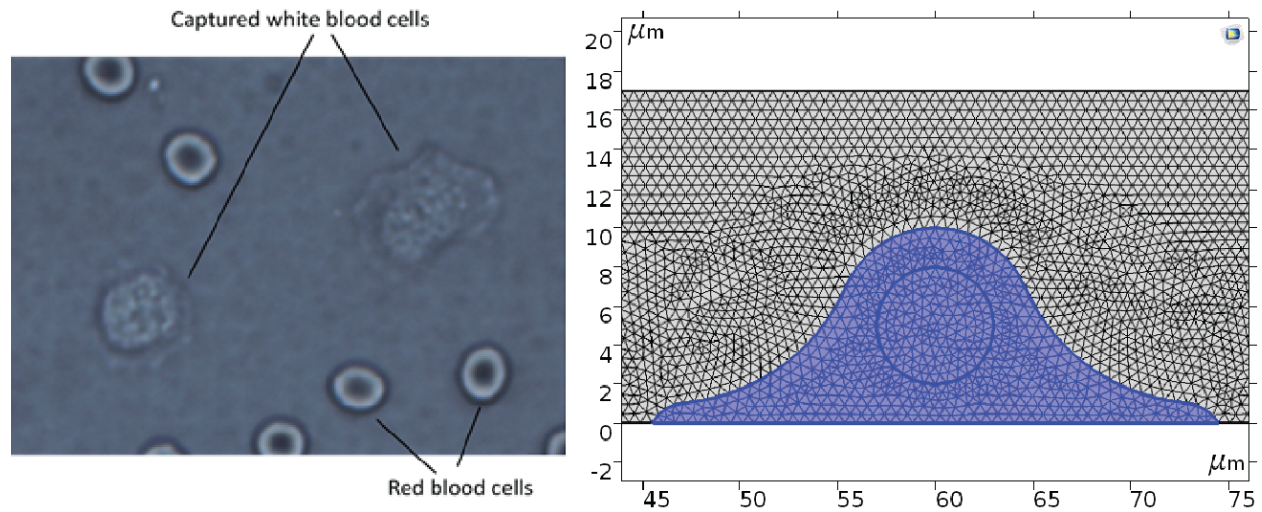


Figure 5.4. (A) Deformation of a White Blood Cell due to the adhesion of PTPRC surface biomarkers of its membrane to an activated glass surface with anti-CD45 antibody. The red blood cells that are also visible in the image serve to the comparison of resulting cell diameter after spreading over the surface. (B) The geometry used in COMSOL simulations resembling to dome-shaped cells attached on a surface. The cell nucleus exhibits no deformation and it is simulated as a sphere of 5 μm diameter. The model's mesh edge size is selected in the range of 0.017 μm and 0.59 μm .

In this model the heterogeneous intracellular structure is ignored aiming at a quantification of the macroscopic response of a cell to an external stimulus provided by water flow within the chamber. The cell cytoplasm is simulated as a hyperelastic nearly incompressible material, with a mechanical response described by the neo-Hookean model (Zhou, Lim and Quek, 2005), in which stresses and strains are computed from a strain energy density function

$$\Psi = \frac{\mu}{2} (\bar{I}_1 - 3) + \frac{\kappa}{2} (J_{el} - 1)^2 \quad (5.3)$$

where μ is the shear modulus, κ is the bulk modulus, J_{el} is the elastic volume ratio and \bar{I}_1 represents the isochoric first invariant. The same model is used for cell nucleus with different values for shear and bulk moduli, indicated in Table 3.

| | Shear modulus μ (N/m^2) | Bulk modulus κ (N/m^2) | Density (kg/m^3) |
|----------------|-------------------------------------------|---------------------------------------------|-----------------------------|
| Cell cytoplasm | 70 | 10^6 | 1500 |
| Cell nucleus | 5000 | $5 \cdot 10^6$ | 1200 |

Table 5.3. Shear and bulk moduli and density of cell nucleus and cytoplasm used in COMSOL model simulation (Haider and Guilak, 2000; Zhou, Lim and Quek, 2005).

The simulation was conducted for a volumetric flow rate applied in the inlet described by the time dependent expression

$$Q = \frac{U \cdot t^2}{\sqrt{t^4 - 0.07 \cdot t^2 + 0.0016}} \quad (5.4)$$

where U is a parametric variable of the system with a value in range between 1 nl/s and 7 nl/s with a step of 1 nl/s. The simulations were also conducted for the range 10 nl/s to 110 nl/s, with a step of 10 nl/s. The time dependent study of the model was computed within time steps from 0 s to 0.75 s – with a time step of 0.005 and from 1 s to 4 s with a time step 0.25 s, for each parametric solution of the model. The solution was repeated for maximum simulated value of volumetric flow rate at 12 nl/s, with all time-dependent variables retained.

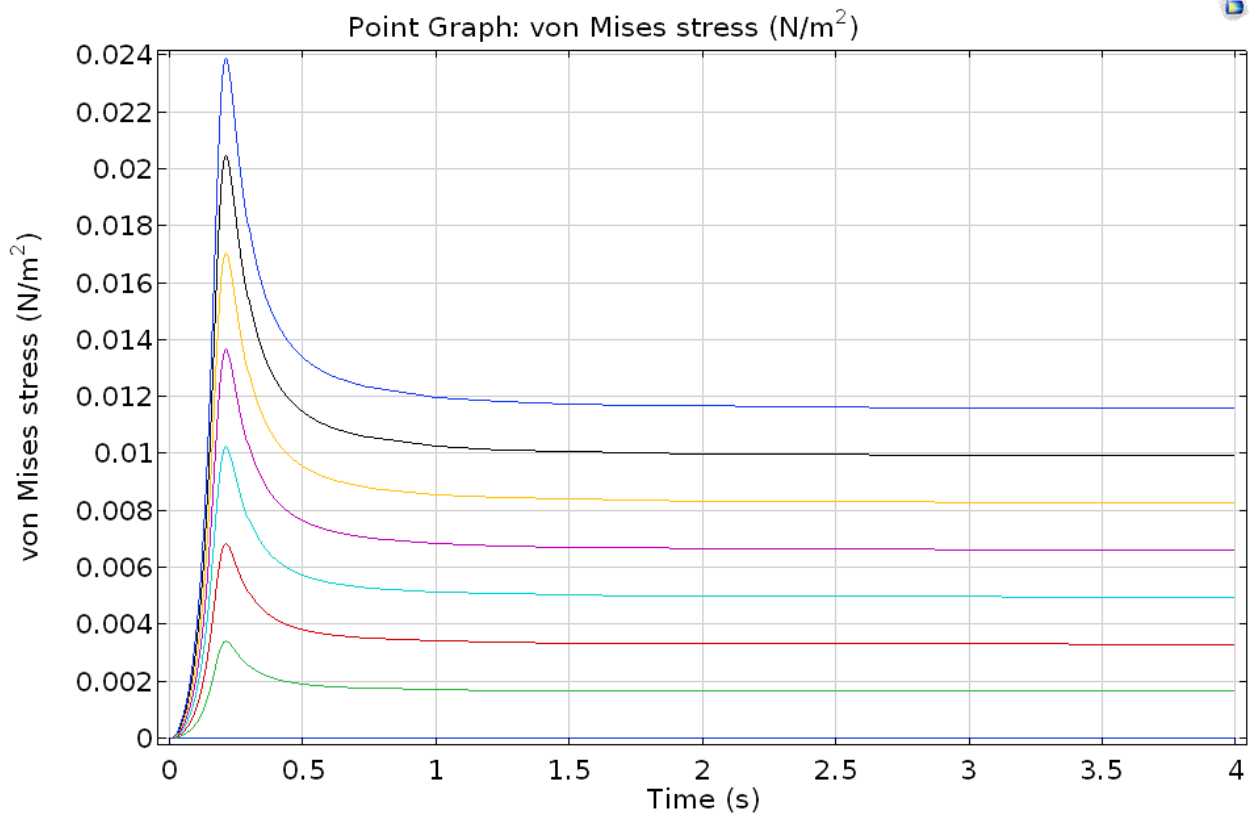


Figure 5.5. von Mises imposed on the first point of cellular cytoplasm that touches the bio-activated glass substrate. The derived time-dependent curves correspond to all different volumetric flow rate values that have been simulated and follow the curve of it as it is defined in the computed problem.

The derived von Mises stresses imposed on the first point of the cell that touches the functionalized substrate are indicated for all parametric values – $Q = \text{range} \left(1 \frac{\text{nl}}{\text{s}}, 1 \frac{\text{nl}}{\text{s}}, 7 \frac{\text{nl}}{\text{s}} \right)$ – in the time-dependent graph of Figure 5. As expected, the stress follows the curve of the determined volumetric flow rate, described in eq. (5.4). The extracted von Mises stress over the entire cellular space, together with the velocity field of the fluid travelling within the chamber is illustrated in Figure 6, for four different volumetric flow rates, at the steady state flow – 4 s.

The magnitude of reaction force in the direction of the flow (x-axis) that needs to be applied by the substrate on the cell, in the interface between cellular cytoplasm and glass chamber's walls, in order to prevent detachment of the cell during flow, is also extracted and illustrated in Figure 7. These values refer to the time value in which the volumetric flow rate maximizes – $t=0.215$ s – for imposed steady state volumetric flow rate regimes 4 nl/s and 5 nl/s.

Finally, the predicted by the system, displacement of the cell during flow, is depicted for the maximum volumetric flow rate in the time dependent solution six different parametric values corresponding to 2 nl/s – 7 nl/s with a step of 1 nl/s. The selected plotted values in time – $t = 0.215$ s – illustrated in Figure 8, correspond to the maximum observed displacement of a point of the cellular body within time. This displacement is expected to be retained below 1 μm , while in the steady state condition is expected to be less than 1 nm.

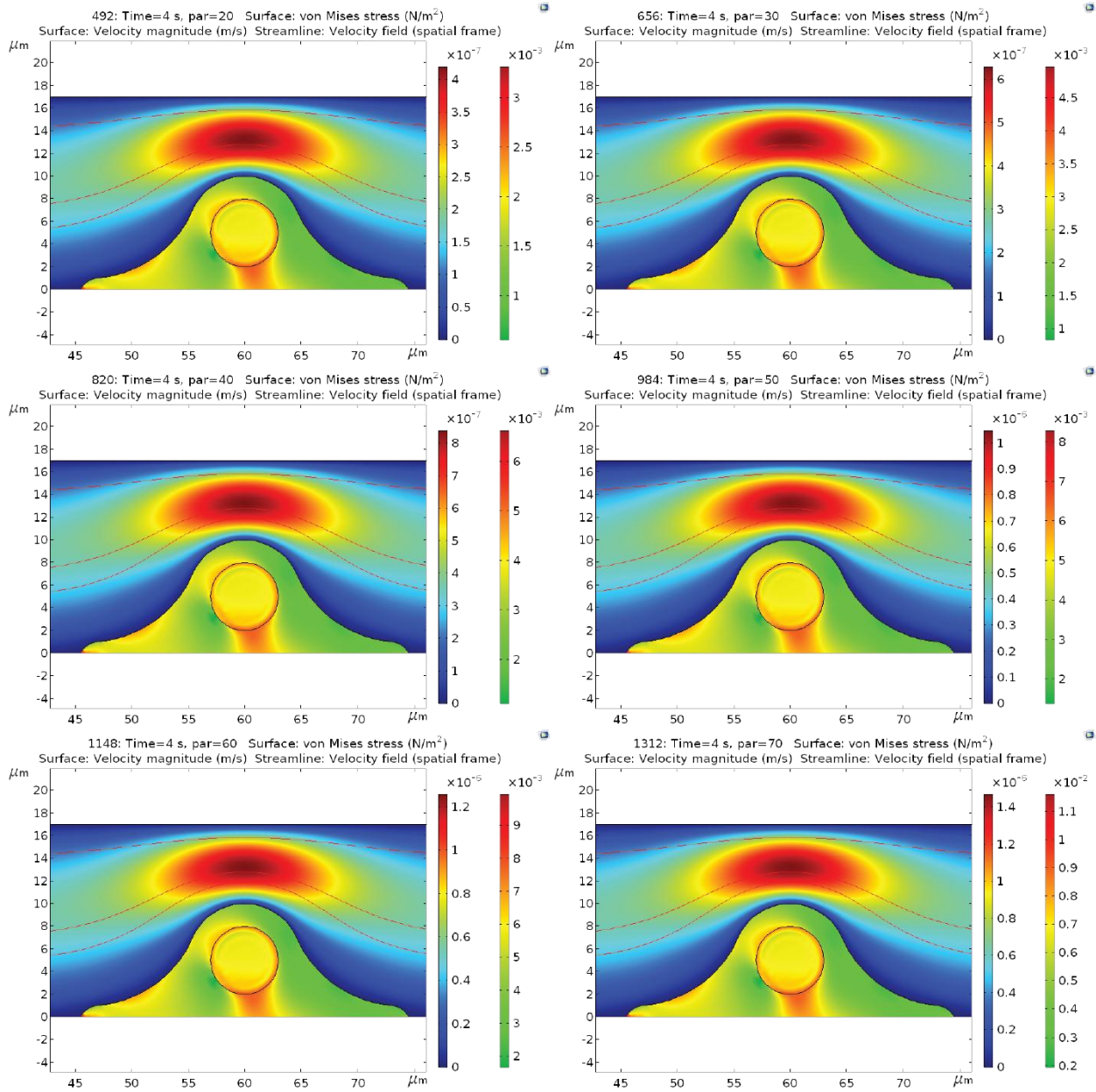


Figure 5.6. Parametric time dependent solution of computational fluid-structure interactions of the presented COMSOL model, where von Mises stresses induced on the cell volume and fluid velocity field are depicted for different volumetric flow rates applied in the inlet. The presented graphical illustrations refer to the near equilibrium state of steady flow ($t = 4$ s).

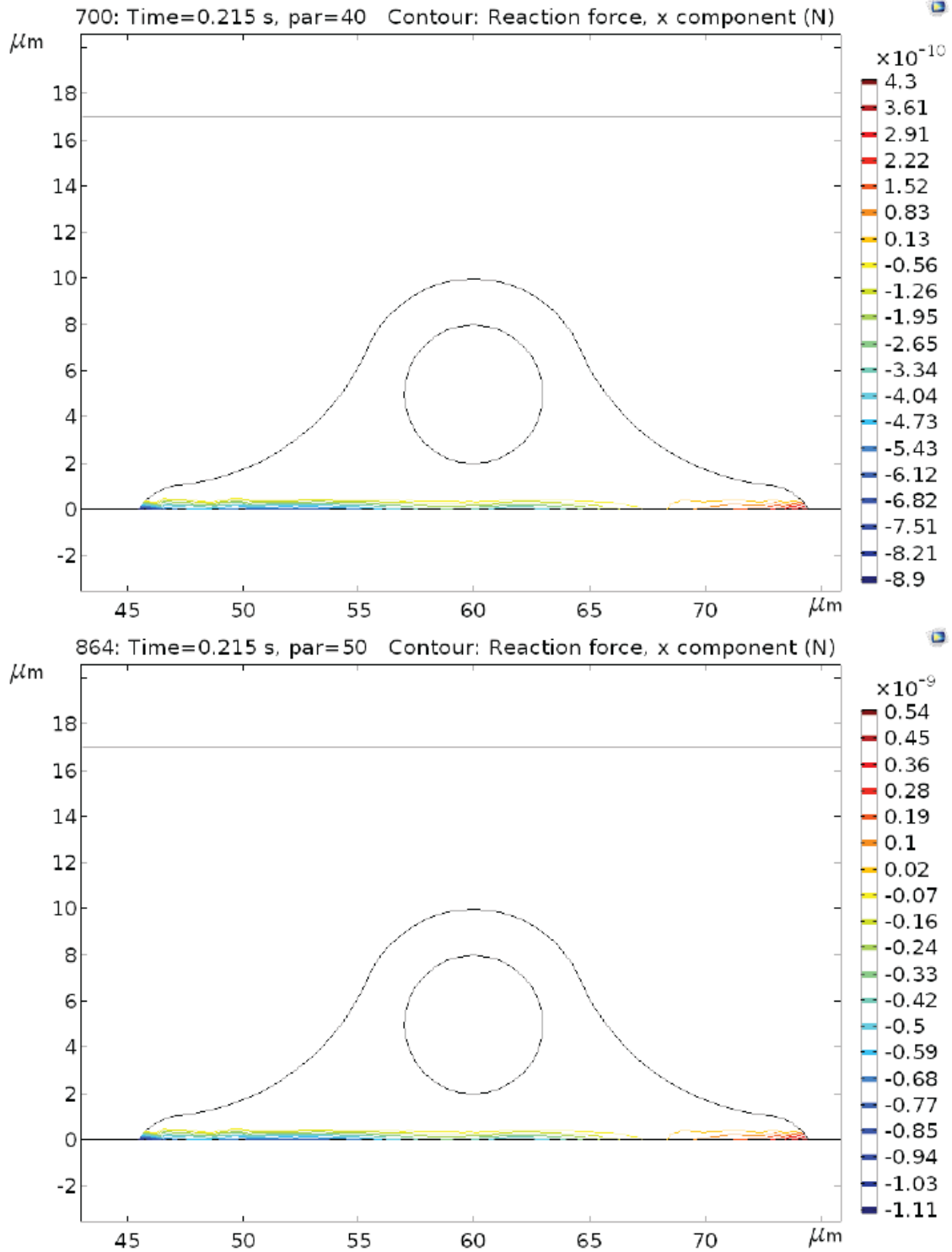


Figure 5.7. Magnitude of reaction force imposed on the cellular-substrate interface at the time of maximization of the time dependent applied volumetric flow rate, for the steady state cases of 4 nl/s and 5 nl/s. The reaction force is expected to be observed in the direction of the flow, while the vertical component presents a 0 value.

The aforementioned factors are studied in comparison with the bonding strength of the cell-on-surface adhesion. An estimation of this linkage strength is based on the density of the available receptors on the cell surface that participate in the adhesion bonds, with the binding force at each couple of receptor-ligand being measured in literature to vary from 40 pN (carbohydrate-carbohydrate) to 150 pN (streptavidin-biotin) (Simone et al., 2012). The number of total number of receptors on the cell surface is a variable to be defined for each specific application – CD4 receptor has been reported to exhibit a range of $0.5 - 1.45 \cdot 10^5$ copies of the surface of CD4⁺ T lymphocytes (Siiman and Burshteyn, 2000; Wang et al., 2014) while CD3 and CD8 receptors are available over a range of $6.6 - 7.8 \cdot 10^5$ and $0.5 - 2.1 \cdot 10^6$ respectively (Siiman and Burshteyn, 2000). However, these values are not only believed to vary with respect to patient related health state (Shabtai et al., 1993), but also presenting a rather heterogeneous density distribution over the cells of the same sample (El Hentati et al., 2010). Moreover, the distribution of the receptors over entire cell surface eventually reduces the available number of receptors that can participate in the adhesion bonding to a flat substrate surface at least to one half. Based on the above, an estimation of the mean adhesion strength of a white blood cell on a functionalized surface is assumed to be in the order of 10^{-8} N, which is comparable to the maximum reaction force occurring during flow for 10 nl/s as depicted by the conducted finite element analysis simulations. Based on this analysis and assuming a possible declination of the extracted values of at least one order of magnitude, the volumetric flow rate, considered to be safe for preventing decohesion of the cells during washing removal of unbound blood components is selected to be below 5 nl/s. This flow rate regime gives a maximum applied force of less than 10^{-9} N, therefore is believed not to affect cells immobilization.

| | Design 1 | Design 2 | Design 3 | Design 4 |
|----------------------|-----------------|-----------------|-----------------|-----------------|
| Pressure drop | 2 mbar | 2 mbar | 300 mbar | 11.367 mbar |
| Flow rate | 4.085 nl/s | 4.15 nl/s | 3 nl/s | 3 nl/s |
| Washing time | 21 min | 16.86 min | 50 min | 19 min |

Table 5.4. Pressure drop that should be applied on each design of the microfluidic chamber to assure no detachment of the bound cells. The corresponding flow rate and the time needed to accomplish washing of unbound cells are also depicted. The washing time is calculated based on the assumption that a total volume of washing solution equal to 3 times the volume of the chamber is needed for sufficient cleaning of the channel.

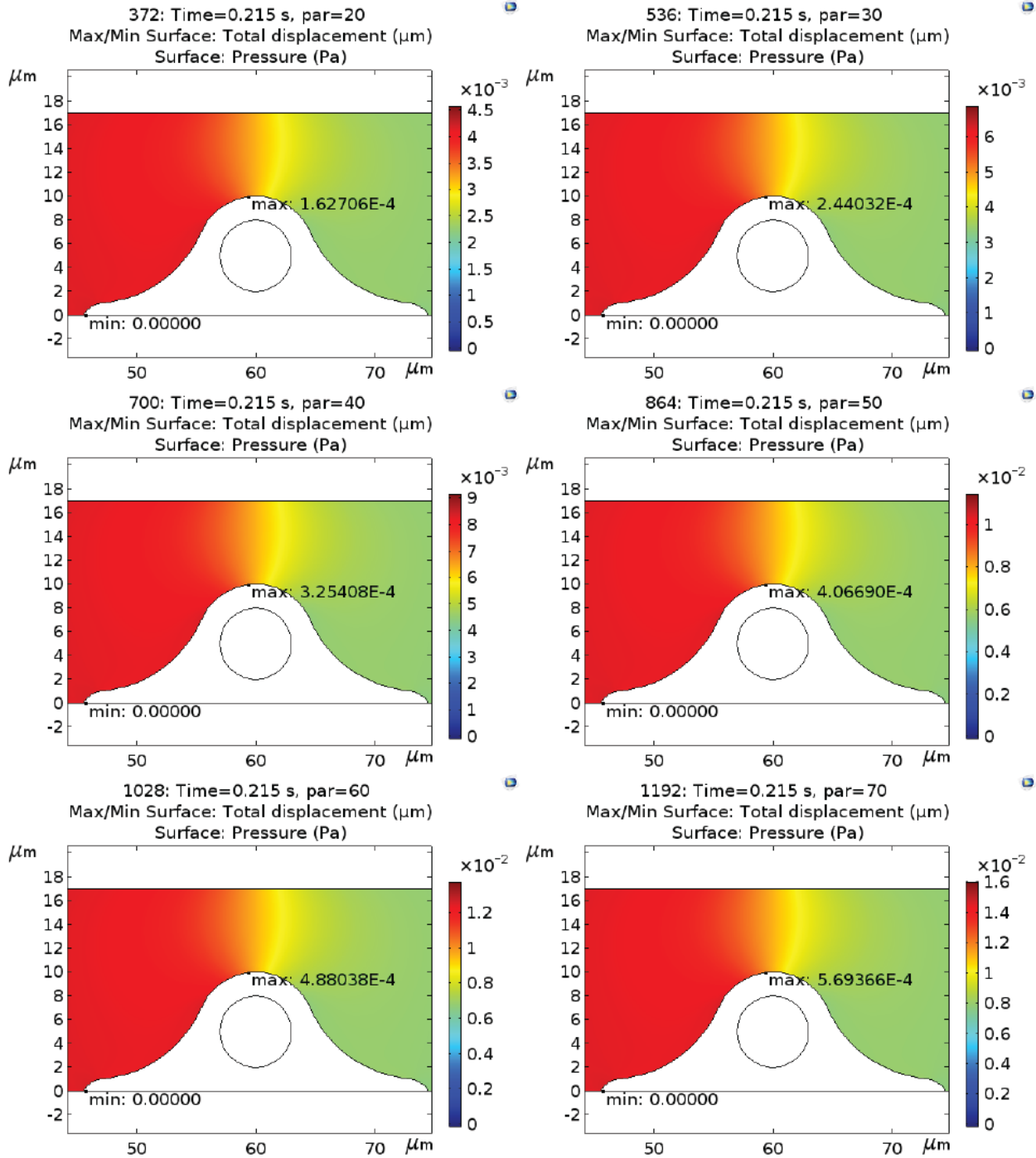


Figure 5.8. Time-dependent total maximum displacement and fluid pressure field for a cell-fluid interaction model for different parametric values of the conducted simulations. The initial pulse in the volumetric flow rate induced maximum displacement of the cell skeleton retained below 0.6 nm in the direction of the flow.

3. Characterization of capturing performance based on factors affecting cell surface adhesion.

The characterization process is based on a series of experiments that emphasize on the functionalization protocol aspects affecting capturing efficiency. Therefore, the optimal concentration of all proteomic solutions participating in this activation protocol is obtained, but also the introduction scheme and incubation time that result in a uniform distribution of molecules over the entire chip surface. To quantify spatial distribution, fluorescent imaging is accomplished; therefore, staining with fluorescent dyes is used, specifically binding on the molecules of interest. To minimize the error in the quantification method, all stains were introduced by both sides of the microfluidic chip under test, four times alternatively by the inlet and outlet of the device, at the beginning of the incubation process. In the case of cell specific fluorescent staining, where Hoechst staining was used, the acquired bright field images were used as a reference for successive staining of the cells.

3.1. Optimal neutrAvidin concentration and uniformity of distribution over chamber surface.

The distribution of neutrAvidin over the chamber's surface area is crucial for the capacity of the channel in hosting the antibodies and consequently for profiting from the entire channels surface to capture the target cells. The theoretical estimation of adequate neutrAvidin concentration for covering the entire chip surface were extracted, based on the molecular size of neutrAvidin, being approximately equal to $5.6 \text{ nm} \cdot 5 \text{ nm} \cdot 4 \text{ nm}$ (Livnah et al., 1993; Erickson, 2009) and its molecular weight, being 60 KDa (Polysciences Inc., 2008). The imprint of a molecule of neutrAvidin deposited on the glass surface of the chamber could be assumed equal to 25 nm^2 . According to the calculations of the volume and the surface-to-volume ratio of each particular design, the number of neutrAvidin molecules that is sufficient to cover the entire chip surface is derived and presented in Table 4. The corresponding minimum number of molecules that should be present in the entire chamber volume is also depicted. This minimum molecular population was multiplied by the molecular weight ($60 \text{ KDa} = 9.96 \cdot 10^{-20} \text{ g}$) and divided by the chip's volume to give the theoretical prediction of minimum neutrAvidin solution concentration, being approximately equal to 3.984 ng/ml . This solution concentration is the minimum that should be provided, with the incubation process providing the time to neutrAvidin molecules to find the non-occupied regions of the chip surface and bind to GMBS crosslinker. However, the particular distance between the molecules of the aforementioned molecular weight in this concentration would result in partial coverage of the surface (Erickson, 2009). Thus, in the experimental process, the concentration values tested were above $1 \text{ } \mu\text{g/ml}$ for neutrAvidin molecular solution.

| Microfluidic design | Number of neutrAvidin molecules sufficiently covering the chip surface | Corresponding number of molecules present in the microfluidic chamber |
|---------------------|------------------------------------------------------------------------|-----------------------------------------------------------------------|
| Design 1 | $8.4 \cdot 10^6$ | $7.1186 \cdot 10^7$ |
| Design 2 | $7.84 \cdot 10^6$ | $5.6 \cdot 10^7$ |
| Design 3 | $5.472 \cdot 10^6$ | $4.56 \cdot 10^7$ |
| Design 4 | $6.72 \cdot 10^6$ | $5.6 \cdot 10^7$ |

Table 5.5. Theoretically estimated values of neutrAvidin molecules population needed to cover the internal surfaces of the proposed microfluidic chips.

To experimentally examine the adequate neutrAvidin concentration neutrAvidin-biotin complex was inserted in microfluidic chamber of the second presented design while the used solution contained 1:1 neutrAvidin:Biotin with variant concentration values: 1 $\mu\text{g/ml}$, 10 $\mu\text{g/ml}$, 50 $\mu\text{g/ml}$, 150 $\mu\text{g/ml}$, 250 $\mu\text{g/ml}$ and 500 $\mu\text{g/ml}$. The insertion of the solution was performed by both inlet and outlet every 22.5 min, counting a total incubation time of 1.5 h. This introduction scheme was observed to provide optimal distribution of the molecules in the center of the microfluidic chamber, since high molecular weight solution as this, are expected to present low rate of diffusion inside microfluidic channels (Bicen and Akyildiz, 2013).

To quantify the results, fluorescent imaging of the covered surface was performed with streptavidin Alexa Fluor staining, under fluorescent epi-mode illumination in 10X magnification of standard optical microscope. The tested channel was divided in five regions: inlet, near inlet, channels, near outlet and outlet. Seven sub-regions were quantified for each segmentation and the mean pixel intensity provided by in the acquired images was calculated. The derived neutrAvidin distribution over the channel is depicted in Figure 9. The provided values were subjected to subtraction of the background noise, calculated as the mean intensity value in regions outside the microfluidic chip in each acquired image.

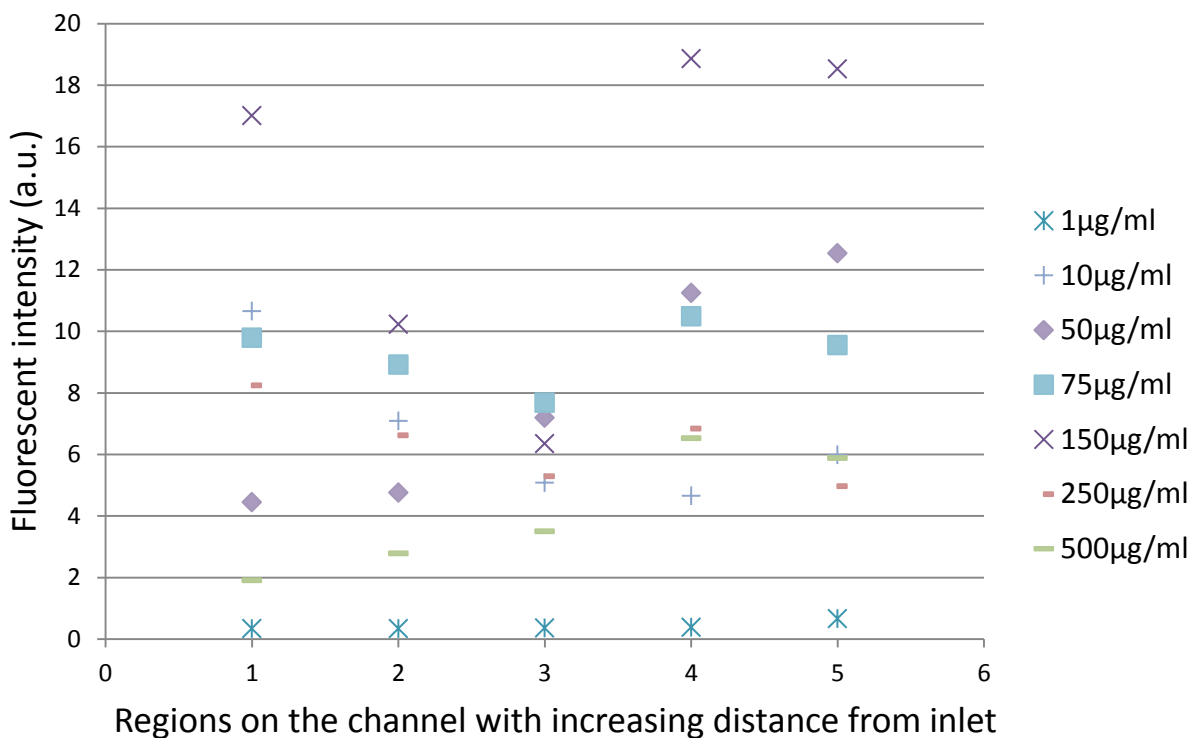


Figure 5.9. NeutrAvidin distribution in the microfluidic channels of design 2, for different concentration values and introduction scheme including two times insertion from both the inlet and outlet of the device every 22.5 min.

As the concentration increases, the number of molecules that bind on the surface of the chamber is expected to increase; the values of tested concentrations would never reach the packed scheme in which the neutrAvidin molecules are distant from each other with a center-to-center distance equal to their molecular volume (approximately equal to 112 nm^3). However, this does not present to be the case, as the intensity value reaches a plateau for a concentration above $50 \text{ }\mu\text{g/ml}$. The optimal concentration is selected to be at $150 \text{ }\mu\text{g/ml}$, providing higher uniformity of light intensity between the inlet and outlet regions. The uniformity of the aforementioned concentration value is a proof of equivalently uniform distribution of GMBS solution of the previous step of functionalization protocol.

3.2. Optimal antibody concentration and uniformity of distribution over chamber surface.

In reference to the previous analysis on the theoretical estimation of minimum adequate neutrAvidin concentration, the concentration of the biotinylated antibody is based on the binding sites available for biotin binding on neutrAvidin molecule. Containing four biotin binding sites, each neutrAvidin molecule (Jain and Cheng, 2017) is to be bind with four antibody molecules. The biotinylated antibodies normally contain up to 10 molecules of biotin as a further increase of this number of biotin molecules tends to denature the antibodies, make them sticky and therefore unspecific.

Aiming at maximizing the concentration of antibodies being present on the surface of microfluidic channels, the minimum provided number of biotinylated monoclonal antibody molecules should exceed four times the number of minimum number of neutrAvidin molecules that are considered to cover the entire chip surface. The extracted values, depicted for each specific design in Table 6, result in a minimum concentration of antibody solution of 53.12 ng/ml. However, the particular distance between the molecules of the aforementioned molecular weight in this concentration would result in partial coverage of the surface (Erickson, 2009). Thus, in the experimental process, the concentration values tested were above 1 µg/ml for biotinylated monoclonal antibody solution and it is based on the recommendations of the supplier (Thermo Fisher Scientific, 2018).

| Microfluidic design | Number of biotinylated antibody molecules sufficiently covering the chip surface | Corresponding number of biotinylated antibody molecules present in the microfluidic chamber |
|----------------------------|-----------------------------------------------------------------------------------------|----------------------------------------------------------------------------------------------------|
| Design 1 | $3.36 \cdot 10^7$ | $2.8744 \cdot 10^8$ |
| Design 2 | $3.136 \cdot 10^7$ | $2.24 \cdot 10^8$ |
| Design 3 | $2.19 \cdot 10^7$ | $1.824 \cdot 10^8$ |
| Design 4 | $2.688 \cdot 10^7$ | $2.24 \cdot 10^8$ |

Table 5.6. Theoretically estimated values of monoclonal biotinylated antibody molecules population needed to cover the internal surfaces of the proposed microfluidic chips.

The examined concentration values were 1 µg/ml, 10 µg/ml, 50 µg/ml, 75 µg/ml and 150 µg/ml anti-CD45 monoclonal biotinylated antibody. When the introduction in the microfluidic chamber was accomplished by the inlet only, a radical decrease in the fluorescent intensity value was observed across the channel as the distance from the inlet increases. The experiment was conducted with fixed incubation time for 1 h. The optimal distribution via this specific introduction scheme was provided by 150 µg/ml concentration that was capable of reaching approximately equal fluorescent intensity between the inlet region and the middle region of the chamber.

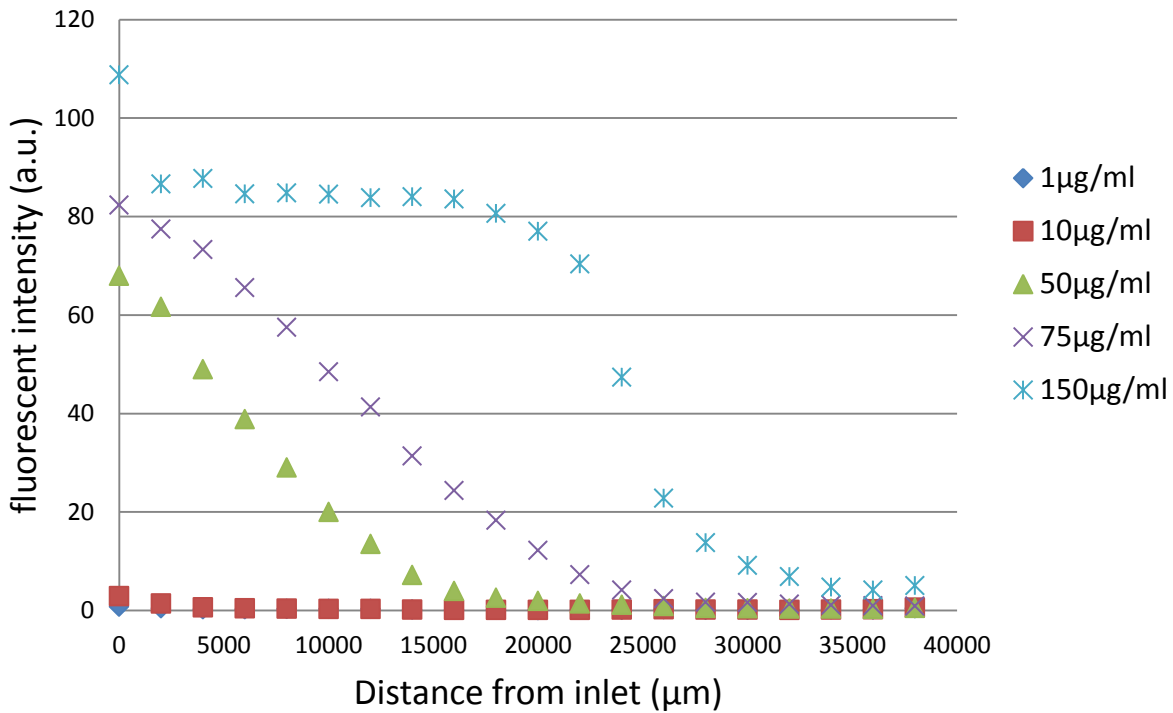


Figure 5.10. Distribution of fluorescent intensity (Alexa Fluor staining) for different values of antibody concentration introduced only once from the inlet.

The incubation time has also been examined with time durations 10 min, 30 min, 1 h and 2 h, with the corresponding fluorescent intensity being plotted for equidistant points in the chamber – distance between them 2 mm – between the inlet and the outlet. The derived intensity values measured as average pixel intensity in acquired images prove little relativity of the incubation time with the distribution and adhesion of the antibody molecules. Therefore it is assumed that as the initial impulse pressure, applied for inserting the solution in the chamber, dominates the distribution process of the molecules within the chamber. The above experiment was conducted for a concentration of antibody CD45 solution of 150 μg/ml.

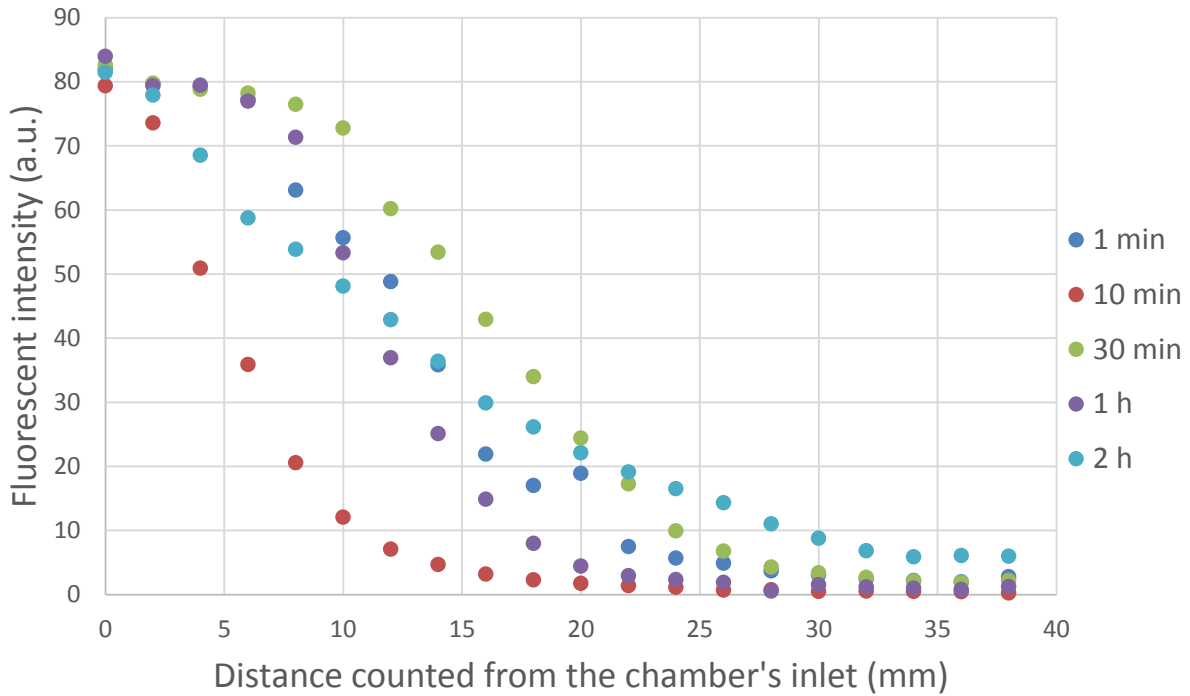


Figure 5.11. Distribution of CD45 antibody molecules into the chamber (design 1) for different incubation times.

The problem of non-uniform distribution of the antibody molecules on the microfluidic channel's surface eventually increases in intensity in the case of high hydraulic resistance of the chamber. The case of the final design with a resistance of the order of $10^{16} \frac{\text{Pa}\cdot\text{s}}{\text{m}^3}$ was tested for a concentration of $75 \mu\text{g}/\text{ml}$ with an introduction scheme of six times alternatively from the inlet and the outlet of the device and for a concentration of $150 \mu\text{g}/\text{ml}$ with an introduction scheme of four times alternatively from the inlet and outlet. The comparison of the acquired fluorescent images (Alexa Fluor staining of the antibody) proves a much more uniform distribution in the case of $150 \mu\text{g}/\text{ml}$, though fluorescent intensity is in the same level in the inlet and outlet regions. This value is considered to be the optimal concentration for antibody solution for the case of microfluidic chambers with increased hydraulic resistance and increased travel length in the flow direction. The value of $75 \mu\text{g}/\text{ml}$ is considered sufficient for the case of design 1 and 2 of the proposed microfluidic chambers.



Figure 5.12. Fluorescent images depicting CD45 antibody molecules distribution over the chip surface for the case of design 3 exhibiting increased hydraulic resistance.

3.3. Cell capturing efficiency

After selection of optimal concentration values for all proteomic solutions participating in the functionalization protocol as well as the optimal introduction scheme and incubation time for each step, the cell capturing efficiency of the proposed microfluidic devices of reduced height has been extensively studied. Particular emphasis has been placed on the role of red blood cells in the achieved sensitivity of the device. In the conducted experiments Hoechst staining has been used to selectively stain only the targeted cell population and distinguish them from unbound cells that have not been effectively washed away during the washing process. For this purpose, imaging under DAPI fluorescent filtering was accomplished and compared to images acquired under bright field illumination. The distribution of the captured cells on the surface of the chip is also examined as a factor of efficiency of the proposed design. The resulted white blood cell counts or the count of a subpopulation have been compared to the corresponding counts by standard whole blood cell count medical examination conducted for the same samples, by the official doctor in the medical department of N.C.S.R. Demokritos.

3.3.1. The role of red blood cells in decreased capturing efficiency of white blood cells.

Based on the theoretical analysis previously described, the presence of red blood cells in the tested samples being at increased concentration rates, interfere with white blood cells' attachment capability to the microfluidic chip. This theoretical assumption was verified with a comparison in the captured WBCs for an experiment conducted with whole blood sample – retrieved from the finger through finger pricking method – and a second experiment conducted for the same blood sample diluted 10 times. The experiments were both performed with 75 $\mu\text{g/ml}$ CD45 antibody solution, introduced three times alternatively from the inlet and outlet of the microfluidic chip, a total incubation time for antibody solution of 30 min and incubation time for blood 5 min. The second design was used for this testing. The resulting captured cells count was 1600 cells for undiluted whole blood and 340 cells for 1:10 diluted blood sample. The corresponding concentrations of WBCs – assuming a volume capacity of the effective imaging area of the microfluidic chip equal to 1.27 μl – is 1260 cells/ μl and 2677 cells/ μl , respectively. An important increase of 112 % has been

observed to the capturing efficiency of the device attributed entirely on the presence of decreased number of red blood cells in the diluted sample.

Nevertheless, aiming at the future use of the microfluidic device at the point of care, dilution cannot be opted for; elimination of sample preprocessing is a prerequisite. Towards this need, a manual vertical stirring performed periodically over both directions of the chip was examined as a method to provide to the unbound WBCs the required minor movement towards unoccupied neighboring regions of the bio-activated surface, without being blocked by the present RBCs. The aforementioned experiment has been repeated with a vertical stirring applied every 1 min of blood incubation process, without changing the total duration of this step. The resulting capturing efficiency has been increased to 3080 cells/ μl . A further increase of the total blood incubation duration up to 10 min with a vertical stirring applied every 2 min with continuous stirring for 5 s, led to a corresponding increase of the captured cells count of approximately 53 % giving a count of 4717 cells/ μl . Final optimization of the functionalization factors led to the repetition of the experiment with optimum conditions of antibody insertion scheme and pressure drop applied for washing giving a total WBC count of 5570 cells/ μl , in which 15 min of blood incubation were interrupted every min for manual stirring. Based on the aforementioned result the proposed microfluidic device presents a capturing efficiency of approximately 83% when the reference value is derived by a whole blood cell count performed with a compact laboratory blood cell analysis instrument (Muse Cell Analyzer – Merck Millipore Inc.).

3.3.2. Captured cells distribution over functionalized surface.

The distribution of immobilized cells over the entire chip surface is an aspect of crucial importance depicting the capacity of the designed microfluidic chip to participate in its entity in the capturing process. In the case where an uneven distribution of captured cells is observed, blank regions of the chip can be considered not to participate in the isolation protocol, therefore reducing the efficiency of the device, or – in the cases of maximized efficiency – requiring unnecessarily higher volume of blood sample. The volume capacity of the proposed microfluidic designs is reduced to the strict minimum that is required to provide accurate results, with a further decrease in the volume rendering questionable whether the proportionality and correlation with real values – total blood cell count in the body – is retained. The surface to volume ratio of the proposed devices is rather low compared to other approaches containing posts in the main body of the chamber, thus, the available surface should be in its entity profitable for count result extraction to provide high accuracy. Among the reasons that may lead to blank – non-used – regions on the chamber's internal walls, the uneven distribution of proteomic solution in the functionalization process is of crucial importance, therefore discussed and optimized in previous sections. The possibility of target white blood cells – expressing increased volume in comparison with other blood cell populations – to travel along the entire chip, without being blocked by cells clusters and coagulated parts, is examined in order to provide equally concentrated regions across the entire chip volume. The distribution of cells is also tested in smaller regions of the chip to check the tendency of cells to be bound in spaces close to the boarder of the chip. The curvature of the microfluidic channel, emerging as an unavoidable result of the micro-

fabrication process, induces imaging problems that reduce the efficacy of automatically performed detection algorithms as it was depicted in chapter 3.

To experimentally examine the aforementioned distribution factors, imaging of the entire microfluidic chip surface has been performed under standard optical microscope. Bright field illumination scheme was first used, while DAPI filtering in epi-illumination mode was used to confirm the selectivity of the proposed devices, with the use of Hoescht staining. The microscopic imaging of the entire surface was accomplished with an automatic x-y scanning algorithm developed in LabVIEW that was set to control the movement of a motorized stage attached to the optical microscope. The algorithmic process also controls the image capturing parameters for every step of the scanning process. Automatic correction of the defocusing error induced by the non-parallel movement of the stage with respect to the objective lens of 10X magnification is performed to provide high quality images. The algorithm provided the resulting mosaic image of the entire chip along with the images acquired in each step.

Cell counting can be performed manually based on this mosaic image or can be automatically accomplished with increased accuracy based on the fluorescent images provided in each step of the scanning process. The scanning step is calculated so that adjacent images overlap and cells occurring in the overlap region are counted once in the automatic detection code developed in MATLAB environment. The specific space coordinates of each detected cell are plotted on a 2D plot (Figures 13 and 14). The main aspects affecting the efficient detection of cells in fluorescent mode imaging is the uneven distribution of proteomic staining solution over the entire chip volume and the stain residues that may interfere in the measurement by increasing the detected number of cells; the algorithmic process presents an eliminated error as it is based on high contrast fluorescent imaging. Bright field images provided by the scanning process can be used as a control to the detection error induced and the plotted distribution present a total detection error of less than 5%, evenly distributed over the entire imaged surface.

The distribution of WBCs was examined in the cases of two microfluidic chambers of highly deviating hydraulic resistance – designs 2 and 4 – functionalized with anti-CD45 antibody. A perfectly uniform distribution is observed, however, an increased number of cells are bound close to the borders of the microfluidic channels, imposing an obstacle to the detection of cells when only bright field imaging is used.

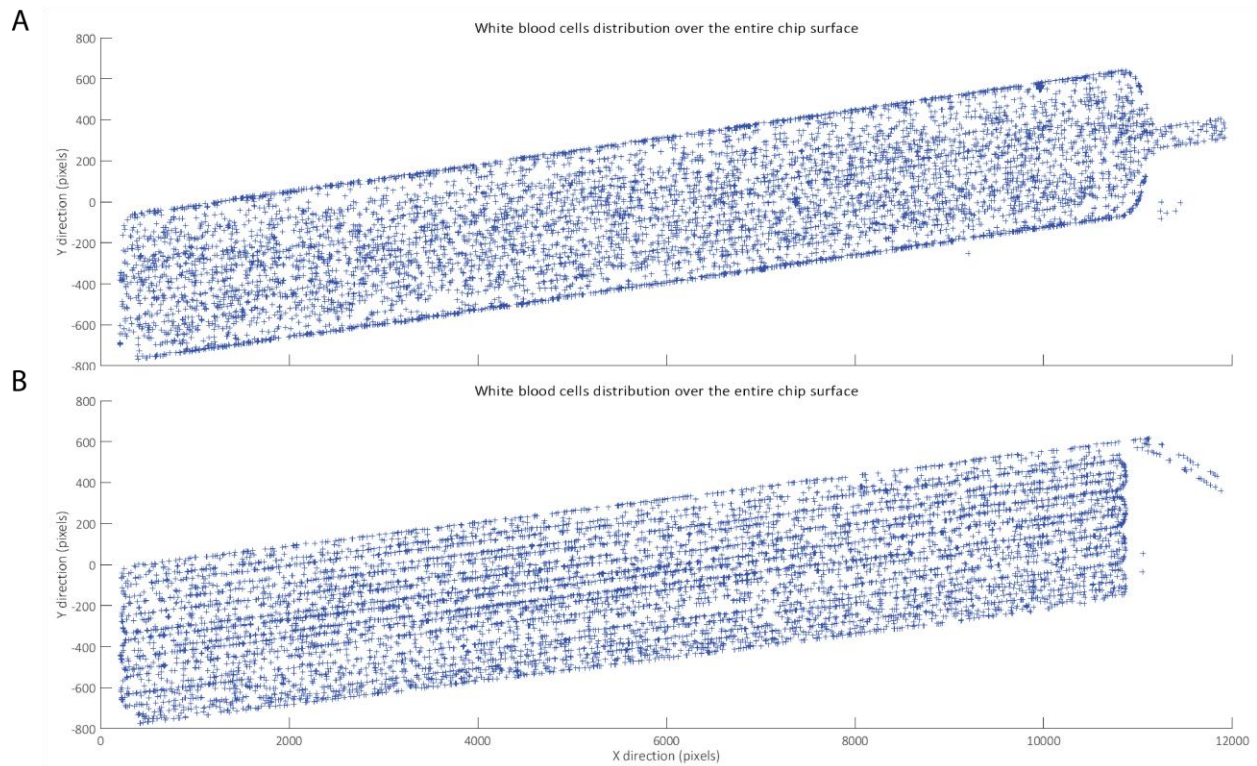


Figure 5.13. Spatial coordinates of WBCs captured in two microfluidic chambers expressing highly deviating hydraulic resistance – proposed design 2 (A) and 4 (B) – functionalized with anti-CD45 antibody. The cells were automatically detected in MATLAB image processing algorithm of images acquired under DAPI fluorescent epi-illumination optical microscope. Unbound cells that were not efficiently washed away do not interfere with the above detection due to the use of Hoescht specific staining of WBCs only. Perfectly uniform distribution of cells over the chip surface is observed in both designs, while an increased concentration of cell bound in regions close to the microfluidic channel's borders is also remarked.

The spatial distribution of specific lymphocytes populations presenting radically decreased concentration in blood was also examined, through bio-activation of the microfluidic chamber of design 2 with anti-CD3 and anti-CD8 antibodies. The expected total number of captured $CD3^+$ T cells and $CD8^+$ T cells is expected to be in the range of 58 % - 87 % of total lymphocytes count and 12 % - 42 % of total lymphocytes count, respectively. The total $CD3^+$ T cells count detected was 1082 cells/ μ l and the total $CD8^+$ T cells count was 523 cells/ μ l. Even in the case of $CD8^+$ T lymphocytes presenting a concentration of one order of magnitude lower than WBCs the uniformity of the spatial distribution proves a perfectly uniform concentration of blood cell populations in the entire volume of the channel.

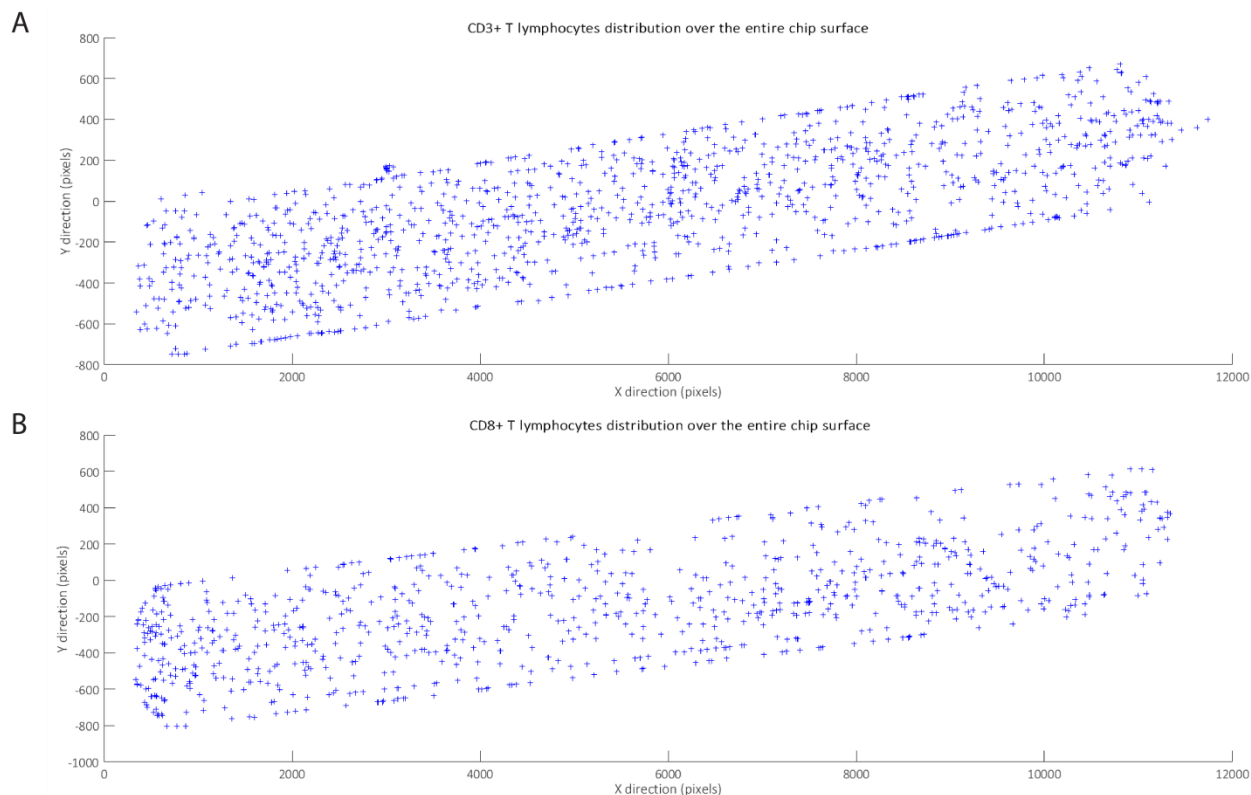


Figure 5.14. Spatial distribution of captured CD3⁺ T lymphocytes and CD8⁺ T lymphocytes in the microfluidic chamber of design 2. Even the reduced total count of these WBCs sub-populations – is evenly distributed over the entire chip surface proving a proportionally uniform distribution of anti-CD3 and anti-CD8 molecules over the surface and a uniformly concentrated blood sample in regions close to the inlet, in the middle and close to the outlet of the device.

3.3.3. Capturing efficiency achieved in white blood cells, CD3⁺ and CD8⁺ T lymphocytes counts.

Capturing efficiency of the device was based on the comparison of immobilized blood cell counts with the derived by the standard medical examination corresponding counts, of the same sample. The samples used in these experiments were retrieved by the vein of healthy volunteers, since the total volume required for the medical examination is much larger than the volume of blood sample that can be retrieved by finger pricking method. The experimental process was performed for the same blood sample to eliminate the error induced in the cell counts attributed to variations of cell counts between vein retrieved and finger retrieved blood samples (Ponampalam, Fook Chong and Tan, 2012).

By employing anti CD45 antibody in the functionalization process, total WBCs population was targeted with the comparison of derived counts, between the experimental protocol of bio-activation of the proposed microfluidic device and the standard medical examination, giving minor deviation of less than 3.8% for both the low and high hydraulic pressure designs. The use of anti CD3 antibody targeting all CD3⁺ T lymphocytes exhibits a decreased efficiency restricted in the level of 78 % of the count measured through medical test. Similarly, the efficiency of the device when

targeting CD8⁺ T lymphocytes is measured to be close to 84 % of the corresponding count of the medical test performed. The decreased efficiency of the device when targeting CD3⁺ and CD8⁺ T cells is attributed to the higher variations of corresponding surface receptors distribution in cells within the same sample, thus, higher levels of detachment for these types of cells during the washing process.

The performance of the proposed microfluidic chamber as a dual cell population count device was proven with the extraction of CD4⁺ T lymphocytes. This count was extracted as the subtraction of CD8⁺ T lymphocytes count by the total count of CD3⁺ T lymphocytes, giving a sensitivity of the device for this configuration close to 77 % compared with the total number of CD4⁺ T cells counted by medical examination of the blood sample volume. Though this count is affected by the efficiency error of the device in counting the corresponding cell populations, it provides an accurate result of CD4⁺ T lymphocytes, with efficient exclusion of monocytes expressing CD4 receptor on their surface.

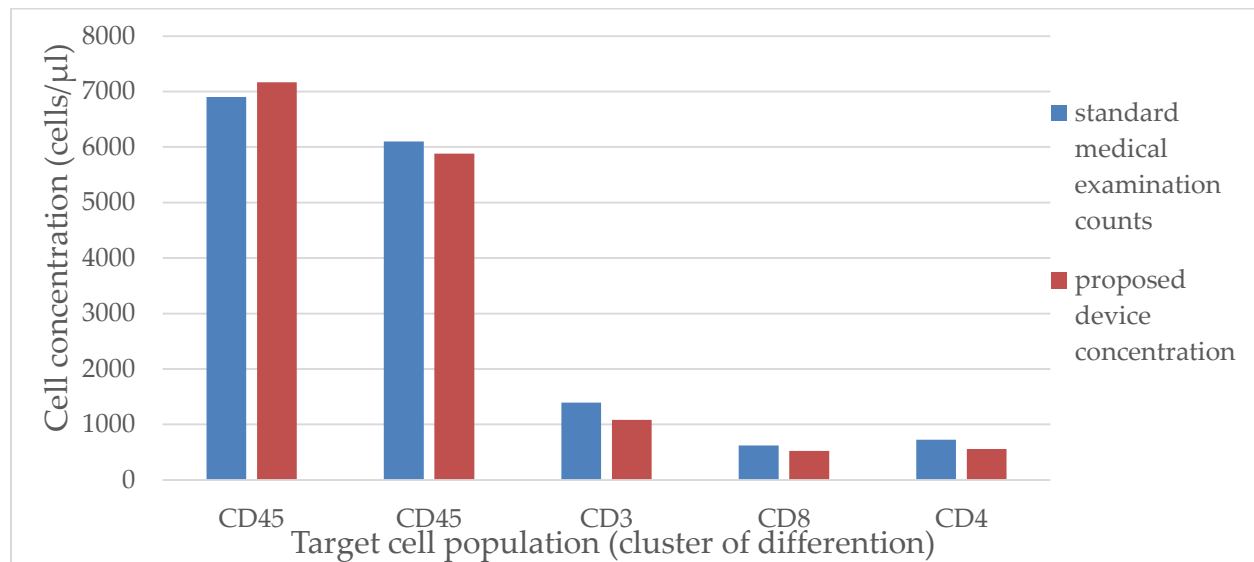


Figure 5.15. Comparison of target blood cell counts of different cluster of differentiation measured with standard medical examination process and through the experimental process employing the proposed microfluidic chip.

4. Discussion – Advantages and tradeoffs, improvements and future perspectives.

In this study, four different designs of a microfluidic cell capturing device have been proposed and investigated with reference to the factors affecting cell immobilization efficiency. Common aspect of all proposed designs is the reduced height of the microfluidic chamber, considered to be the main reason for reduced efficiency of similar devices proposed in literature. This geometrical feature is combined with an optimized functionalization protocol to achieve increased efficiency of WBCs capturing, subjected to a clinically negligible error of less than 3.8 %. The device profits from blood incubation under no flow conditions where the number of effectively immobilized cells increases (Nagrath et al., 2007). A periodically performed manual stirring of the microfluidic device during this incubation time has been proven to be highly profitable in eliminating the problems occurring in

rare circulating blood cells from the presence of highly concentrated RBCs. Thus, it is depicted to achieve increased efficiency with the use of whole blood samples without the need to preprocess them with dilution or RBCs lysing procedures.

Each one of the designs contains two identical chambers giving the possibility of performing dual functionalization and differential counting of blood cell populations. This is the case for CD4⁺ T lymphocytes, a count used to determine the HIV virus progress within the body of infected individuals. Previously developed devices using anti – CD 4 antibody, were subjected to an error induced by the immobilization of monocytes together with the target population, as CD4 receptor is also expressed on the surface of monocytes. CD4⁺ T lymphocytes can be extracted as the subtraction of CD8⁺ T lymphocytes count by the CD3⁺ T lymphocytes count, thus, dual functionalization is necessary.

However, the capturing efficiency is still restricted in lower levels in the case of CD3⁺ T lymphocytes and CD8⁺ T lymphocytes. This problem is attributed to the higher variations of targeted surface receptors in cells within the same sample, rendering them – among all lymphocytes – the most vulnerable to detachment during washing of unbound cells. Moreover, bright field imaging of the aforementioned lymphocytes led to an observed round shape after immobilization on the activated surface. It is to be further investigated whether these types of cells exhibit a less deformable behavior reducing the number of bound receptors on the surface and to the exposure of an increased height on the vertical flow during washing process.

4.1. Alterations and deeper investigation towards further increase in capturing efficiency

Due to the decreased height of the proposed devices, a proportional increase of the hydraulic resistance they present is unavoidable. Among the designs tested, two present a relatively low resistance due to the use of wide channels (design 1) or due to parallel connection of narrower channels (design 2). These devices exhibit an optimized behavior in the way the proteomic solutions are inserted, with easily achieved perfectly uniform distribution over the entire chip area. This factor is crucial for the efficiency of the device and the maximization of profitable chip surface. In the contrary, great difficulty is observed in handling the designs of increased hydraulic resistance, being in the order of $10^{17} \frac{\text{Pa}\cdot\text{s}}{\text{m}^3}$. Though optimization of the functionalization protocol aspects has been performed and resulted in even distribution for these chips, the distribution of proteomic solutions is considered to be vulnerable to non-controllable initial impulse of pressure applied in the introduction process.

To compensate this problem, pressure driven insertion of the functionalization solutions should be performed with an automatic pressure controller. Such a choice would lead to further investigation on the effect of the initial pressure on the uniformity of distributed protein molecules and might result in the reduction of incubation time or of the required concentration of proteomic solutions. In this case a further reduction of the time for functionalization protocol but also of the cost of the proposed devices should be expected.

The reported maximum resolution provided by the device should be subjected to further investigation especially in reference with the repeatability of the results. A large number (>100) of

identical experiments should be performed and compared to corresponding values retrieved by standard medical examination process of flow cytometry, considered to be the gold standard. The efficiency of the device should be in full compliance with the conducted research in the fields of medical conditions changing the mechanical behavior of target cells or the number of cell receptors expressed on their surfaces. Deeper investigation of these factors is a prerequisite for full application of the proposed platform technology of microfluidic cell capturing in the medical diagnostic procedures.

4.2.Future perspectives: fields of application for a platform technology of microfluidic cell capturing device.

The microfluidic chambers investigated in this work consist of a platform technology that can be applied in a broad range of diagnostic processes in reference with blood cell population isolation and imaging. Proven by the analysis conducted in the previous section, WBCs count can be effectively performed by whole blood samples of minute volume approximately in the range of 1 μ l to 3 μ l. The functionalization of the proposed device with different antibodies can efficiently result in the diagnosis of HIV virus progress providing highly accurate CD4⁺ T lymphocytes count excluding monocytes isolation.

In the future this device can be effectively used for the detection of rare blood circulating tumor cells (CTCs) by surface functionalization with a chimeric monoclonal antibody directed to the cell surface expressed epithelial adhesion molecule (EpCAM) (Saucedo-Zeni et al., 2012). The isolation, imaging and enumeration of CTCs is a research field attracting increasing interest, as it can be used in the early diagnosis and decision making in the treatment of cancer patients (Dotan et al., 2009; Krebs et al., 2010) or act as a prognostic test in the metastatic behavior of previously expressed cancer (Hou et al., 2011). Going further into research achievements, surface functionalization and cell surface biomarkers can be used in the isolation of a wide range of cell populations (Gallacher et al., 2000; Takaishi et al., 2009).

Representing a platform technology, the proposed design is proven to fully comply with the requirements for point-of-care testing by the World Health Organization. Requiring minute sample volume, eliminating blood sample preprocessing and being affordable based on mass production cost and functionalization expenses, it is believed to promote a patient-centered healthcare with the diagnosis performed at the point of care.

Discussion

Overall valuation of the suggested system for efficient blood cell identification and counting at the point of care

The present thesis is dedicated to the design and development of a device for blood cell identification and counting. The device comprises of a miniaturized imaging/scanning system that is able to screen a large sample volume – approximately 2 cm² of a blood cells monolayer or a total blood volume of 3 μ l – profiting by the great advances in micro-optics and micro-machining methods. This system can be combined with a micro LED/lens array hybrid chip that has been developed. This optical emission/collection chip enables epi-illumination microscopy imaging in miniaturized optical setups. A microfluidic device of unique geometrical properties has been studied for specific cell isolation, based on optimized surface immobilization technique. An extended characterization process and profound analysis of the factors that affect efficient performance of the proposed device have been conducted. The designed system has eventually succeeded in responding to crucial technical challenges imposed in the field of miniaturized microscopy – trans- or epi-illuminated - and cell fractionation efficiency, based on surface functionalization with specific antibodies. The technical problems solved and the requirements for further optimization are thoroughly discussed in the corresponding chapters. An overall valuation of the entire system is attempted in this final chapter, including a summary of the innovative aspects of the proposed design and an estimation of the contribution of the conducted research in the corresponding scientific fields. The extent at which the entire system complies with the generic requirements for point-of-care testing is also examined. In this direction, a profound statistical analysis on the accuracy and precision of the entire system is imperative as part of the future research steps. The potential application of the proposed system in various medical pathologies along with the route towards a general purpose blood cell counter for use at the point of care illustrate the social impact of the proposed platform technology.

1. Innovative aspects and contribution to the corresponding research fields

The design of the imaging setup benefits from high quality micro-optics – defined as optical elements with a size up to 1 mm. High resolution and large field of view imaging is simultaneously achieved through the implementation of a special geometry in the structure of the employed mini-lens array. The lens-array is micromachined on a silicon substrate that hosts the lenses and it is capable of performing one direction scanning of the sample under observation. Through the scanning process and based on the geometrical specifications of the array – there is a tilt of the array with respect to the scanning direction - all lenses in the array contribute to the formation of the final 2D image of the sample. This geometrical structure depicts a new approach towards the integration of micro-lens arrays in miniaturized imaging systems, promising to combine increased compactness with a significant decrease in complexity of both the optical and scanning setups. Indeed the optical

path length is minimized and it does not exceed 2.5 mm while the scanning process included translation of the moving parts across one direction without the requirement for focusing in each step. The characterization process and the validation of the developed setup evince the factors affecting high quality imaging with 2 D lens arrays and the means to overcome the emerging limitations: the 'ghost image' effect, the contrast decrease due to crosstalk, the flatness imperfections and the uniformity errors attributed to the fabrication and assembly processes that affect final image sharpness.

The miniaturization of the optical system was attained in epi-illumination scheme, often suffering from bulk complex optical compounds, with a suggested novel design integrating the emission and the collection elements in one chip. The innovative element in this approach is the special geometrical design of the LED array that allows for the integration of them in the lens array chip. The developed hybrid LED/lens array chip, additionally to the minimized optical path length, demonstrates a separation of the excitation and emission optical paths, since the emitted beam and the reflected by the sample light beams do not share the same optical components. This design is proven therefore promising to provide significant increase of the signal-to-noise ratio in the final images, derived from reflection-based illuminating scheme. Such a design does not require the use of bulk expensive and complex optical elements or the placement of them off-the optical axis that eventually result in bulk optical setups. Through the characterization process it is clearly indicated that the developed chip achieves an 8.8 μm resolution in bright field epi-illumination mode, with the possibility of reduced temperature rise with controllable time scheme of its operation. Though further optimization is necessitated, the suggested architecture settles the groundwork for a new advantageous setup, applicable to a wide range of miniaturized optical imaging systems for biological specimen.

In the last part of this study, in reference to the field of microfluidics and specifically of cell fractionation, a study of the factors that affect cell capturing within antibody-activated microfluidic chambers is attempted. The conducted research includes both computational analysis and experimental investigation of the corresponding factors, among which the height of the microfluidic channel, the presence of red blood cells in whole unprocessed blood samples and the flow rate imposing high shear stress on immobilized cells are considered to dominate the low efficiency of the aforementioned devices. The reduced height of the suggested designed chamber – 17 μm – and the blood incubation scheme under no flow conditions both constitute unique elements enabling increased capturing yield. During incubation process, a manually performed vertical periodical stirring is proposed as a means to unblock targeted white blood cells and enable their sliding towards unoccupied regions of the activated walls. This technique, easily amendable to full automated systems, leads to increased immobilization yield of white blood cells without preprocessing steps of dilution or red blood cells lysing. The pressure driven flow rate for the washing process of unbound cells that would effectively prevent immobilized cells detachment was defined through finite element analysis, in which a spreading dome-shaped structure of cell attached on surface was used with the cytoplasm and cell nucleus obeying at the neo-Hookean model of hyperelastic nearly incompressible materials. The analysis of the aforementioned factors along with the optimization of the functionalization process with respect to the solutions' concentration set the basis towards highly

efficient microfluidic cell fractionation devices and contribute to the determination of all factors limiting their applicability in point-of-care testing.

2. Compliance with generic specifications for point-of-care testing.

The ASSURED criteria, imposed by the WHO for efficient and accurate examinations at the point of care, delineate a set of generic requirements that each medical testing process or tool should fulfill when intended for use at the point of care, independently of the employed technology. The extent, at which a specific medical tool complies with the aforementioned criteria, should be extracted via deep investigation of the specifications of each medical tool. However, an estimation of this level of compliance can be derived by the characterization process of the proposed platform technology that is conducted in this research study.

Particularly, the sensitivity of the proposed technology of single cell identification and counting is subdivided into the provided sensitivity of the detection system – the imaging/scanning platform – in both illuminating schemes and the sensitivity of the microfluidic device. In reference to the imaging platform, the resolving power of the system – 1 μm in 4X magnification – and its capability to perform whole slide screening without loss of information constitutes a proof of a highly sensitive imaging tool. It is, indeed, proven that the developed setup is capable of imaging and automatically detecting single cells in both smear blood tests and white blood cells immobilized on a functionalized microfluidic chip. The distinction of cell types based on their geometrical properties through the applied algorithmic process requires the employment of different CMOS sensor of decreased pitch size or the operation of the device at higher magnification ranges. The suggested microfluidic chip can provide increased accuracy in white blood cells count with a clinically negligible error of less than 3.8% between the detected count and the actual concentration of cells depicted via flow cytometry. The accuracy of the device in other cell types such as CD3 and CD8 lymphocytes is slightly lower; therefore a deeper investigation of the linearity of the results is required in reference to the factors that affect capturing yield in these types.

Towards the need for a fully portable and automated device of eliminated requirement in external power, external equipment, laboratory environment and users' expertise, the suggested technology has the potential to comply in its entity with the relevant criteria of the WHO. It exhibits increased compactness, high throughput – less than 10 min required for scanning process and less than 30 min for final image extraction and counting – absence of blood preprocessing requirement and low power demands. Further automation can be accomplished with the use of a small single-board computer such as a Raspberry pi and inclusion of automated stirring and washing processes in the final design of the device. Image storage must be excluded and final image display should be excluded to provide higher throughput and lower computational requirements.

The cost of fabrication of the current prototype does not exceed 1000 €, while it is expected to be reduced to less than a half of this price in mass production. The cost of a single test, mainly based on the cost of fabrication of the chip is currently approximately 400 €. However this cost refers to a reusable glass microfluidic chip that has been micromachined only in a few copies, with the employment of expensive micro-lithography techniques. Mass production, use of lower-cost micromachining methods, such as 3D printing, and cheaper materials, such as plastic, can ensure the

reduction of the consumable chip production cost and the suppression of a single test price down to 5-10 €.

Based on the above characteristics the deliverability of the final device is assured at all cases of primary health-care, either in the developing world or poor-income countries.

| Criterion | Compliance level of current prototype | Expected compliance level of the final medical device |
|------------------------------------|-----------------------------------------------------------------------------------------------------------------------------------------------------------------------------------------------------------------------------------------------------------------------------------------------------------------------------------------------------------------------------------------------|----------------------------------------------------------------------------------------------------------------------------------------------------------------------------------------------------------------------------------------------------------------------------------------------------------------------------------------------------------------|
| Affordability | Device fabrication cost < 1000 €, reusable glass microfluidic chip fabrication cost 400 €. | Mass production is expected to reduce the fabrication cost of the device below 500 € and the cost per single test < 10 €. |
| Sensitivity and specificity | Microfluidic device: - WBCs counting error: 3.8% - CD3 lymphocytes count error: 22% - CD8 lymphocytes count error: 16% - differential CD4 lymphocytes count error: 23% Technology providing high purity yield through specific binding of cells on antibodies Detection algorithm and resolving power of the detection system enabling single cell observation and counting | Specific determination of the final capturing yield demands linearity, accuracy, precision and interference study of the optimized final device. Design alterations of the developed platform technology can further improve its performance, while deeper investigation is required in reference to the factors affecting the microfluidic chip linearity. |
| User-friendliness | All aspects of scanning and imaging are automatically controlled via a LabVIEW GUI, easily operated by a researcher. | One button process should be provided, full automation of the washing process is required, external power supply should be eliminated. All these aspects can be easily accomplished with a Raspberry pi or equivalent board. |
| Rapidity and robustness | < 10 minutes for scanning and image storage, < 30 minutes for image processing and final large image display. The disposable microfluidic chip is the unique consumable. | Excluding image storage and display is suggested as a means of throughput and computational requirements reduction. The repeatability error should be statistically examined as part of the final device characterization. |
| Equipment-free operation | Externally powered, computer-based operating, off-site data analysis, easy sample handling | Battery-based operation and on-site data analysis for fast cell count extraction and decision making are achievable in the next generation of the device, based on the power and computational requirements. |
| Deliverability | Compact prototype (20 x 15 x 8 cm), light weighted (1 kg) | Increased compactness can be achieved based on the volume requirements of the current device |

Table 5.7. Analysis of the extent of compliance with the ASSURED criteria described by the WHO for point-of-care testing tools and procedures. The compliance of the current prototype is examined, along with the potential of the proposed technology to fully obey to the imposed specifications.

3. Towards a medical tool for point-of-care blood cell analysis: future investigation and validation requirements

The conducted research aimed at proving the feasibility of the suggested platform technology as a general purpose cell optical counter operating at the point of care. Towards the development and characterization of the derived medical tool a profound analysis of the statistical behavior of it is necessary. Such a research study is among the first steps to follow and concerns the determination of the provided linearity, accuracy and precision (ICH Harmonised Tripartite Guideline, 2005). These factors examined over a large amount of repeated laboratory studies aim at the validation of the proposed technology and its performance characteristics.

Particularly, in the accomplished work, the specificity of the device, targeting specific cell types through surface binding with antibodies fictionalized chip has been proven. Sensitivity tests have been conducted to an adequate extent depicting the potential of the suggested technology to operate as a single cell identifier and counter. These two aspects define clearly the accuracy of the device, depicting the agreement of the provided count values in comparison with a reference value, derived from flow cytometry tests. However, it is beyond the purpose of this study to accurately determine the precision of the device, defined as the variability in the data from replicates of the same sample under normal operating conditions. This study is to be accomplished in future work, along with the determination of linearity of the provided results. A series of blood samples containing different concentrations of target cell populations should be used for both linearity and operating range validation. All aforementioned aspects should be tested for different target cells, in parallel with equivalent optimization of the functionalization protocol followed in the activation of the microfluidic chip.

Towards this direction, the automated device for blood sample screening and single cell detection has to be validated, in reference with the application requirements and specifications. The validation process of the imaging scanning system should be accomplished based on instrument qualification (Bansal *et al.*, 2004) and software validation (U.S. Food and Drug Administration, 2002) where specifically installation qualification (IQ), operation qualification (OQ) and performance qualification(PQ) must be determined.

4. Social impact and future perspectives: current fields of application and the potential of a general purpose blood cell analysis device

The optical blood cell counter demonstrated in this work presents great societal impact, touching the medical need for frequent cell counting examinations that are related to the diagnosis or monitoring of a wide range of diseases. The development of a compact portable blood cell counter of high efficiency can transfer the medical tests performed in central clinics by the patient's bedside, therefore, at the point-of-care. Such a practice is proven to be highly advantageous not only for the convenience of the patient but also for the economic burden that is related with the aforementioned

medical examinations. Indeed, the patient himself will be able by the use of the presented blood cell counter to monitor his health status through white blood cell count extraction within a few minutes, without the need for a hospital visit. Consequently, the exposure of patients prone to infections is minimized and the health-care is more patient-oriented as the patient can perform blood cell counting at a regular basis without affecting his every day activities. Except for the provided convenience, the employment of the device either by the patients themselves or by primary health-care infrastructures would lead to a radical decrease of the expenses dedicated to this type of routine medical tests.

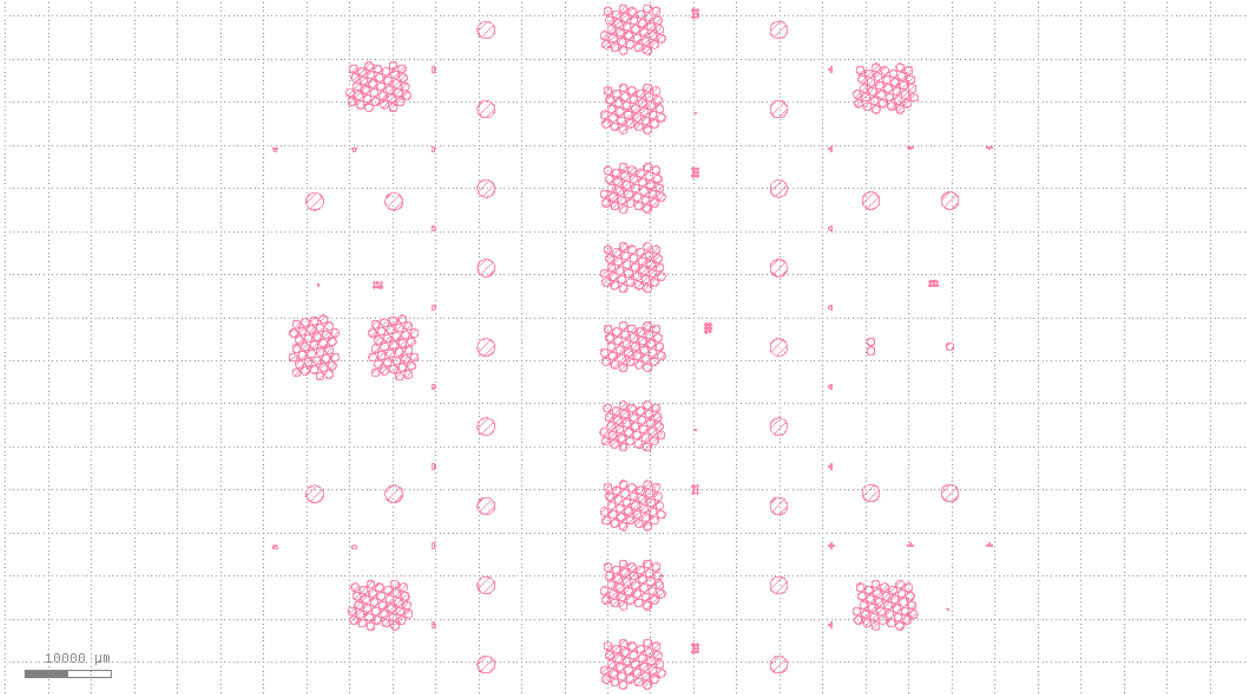
In the case of poor resources settings the economic burden imposed by the examination of blood cells counts with the conventional bulk laboratory equipment is frequently prohibitive for monitoring the population's health status and acts as severe handicap in the early detection of a blood related disorder. The suggested technology evidently proposes an alternative medical tool for blood screening that is able to operate with minimum requirement in power supply, laboratory environment, expert personnel and computational power. It can therefore effectively promote the accessibility of the population to blood screening examination and contribute to the prolongation of life expectancy in low-income countries.

The potential of the proposed technology to cover a wide range of blood cell types counting – white blood cells, CD3, CD8 and CD4 lymphocytes – has been demonstrated through the present thesis targets a range of disorders and infections diagnosis and treatment. Among them HIV infection, cancer related chemotherapy side effects, leukemia and opportunistic infections can be effectively monitored. Additionally this technology settles the groundwork for further application in other cell types gaining great interest for specific diseases monitoring – e.g. CTCs can also be counted with different functionalization protocol employed. Blood smears screening, accomplished with the proposed optical imaging setup, is related to a series of infections as part of the diagnostic process. Sickle cell disease and malaria smears stained with Giemsa can be effectively monitored and diagnosed. In the same direction the potential use of the epi-illumination scheme with the integration of the LED/lens array chip can further expand the field of applications in fluorescent imaging of increased resolution, thus, in specific diseases diagnostic procedures, such as tuberculosis sputum screening.

Finally, the developed imaging/scanning technology provided the capacity to image a large area of the sample within a few minutes and accomplish automatic detection of specific features present. Therefore, its use as a low-cost, increased-accuracy, biological specimen screener can be highly beneficial among research laboratories and educational institutions. Based on the demonstrated imaging performance, it can be considered as an alternative to bulk and expensive equipment used as part of the scientific laboratories, for the investigation of blood or sputum film tests, thin tissue imaging, specific cell identification and counting, in both bright field and fluorescent microscopy.

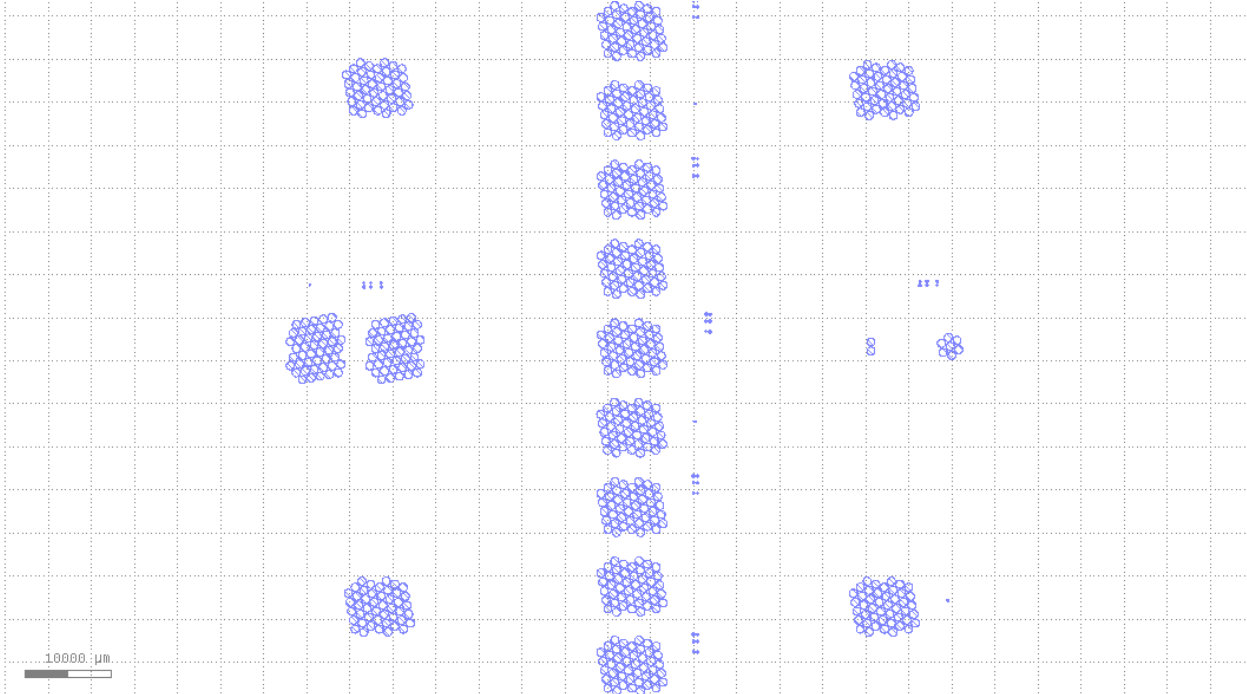
APPEENDIX 1 DESIGN DOCUMENTS

1. Mask of the lens array

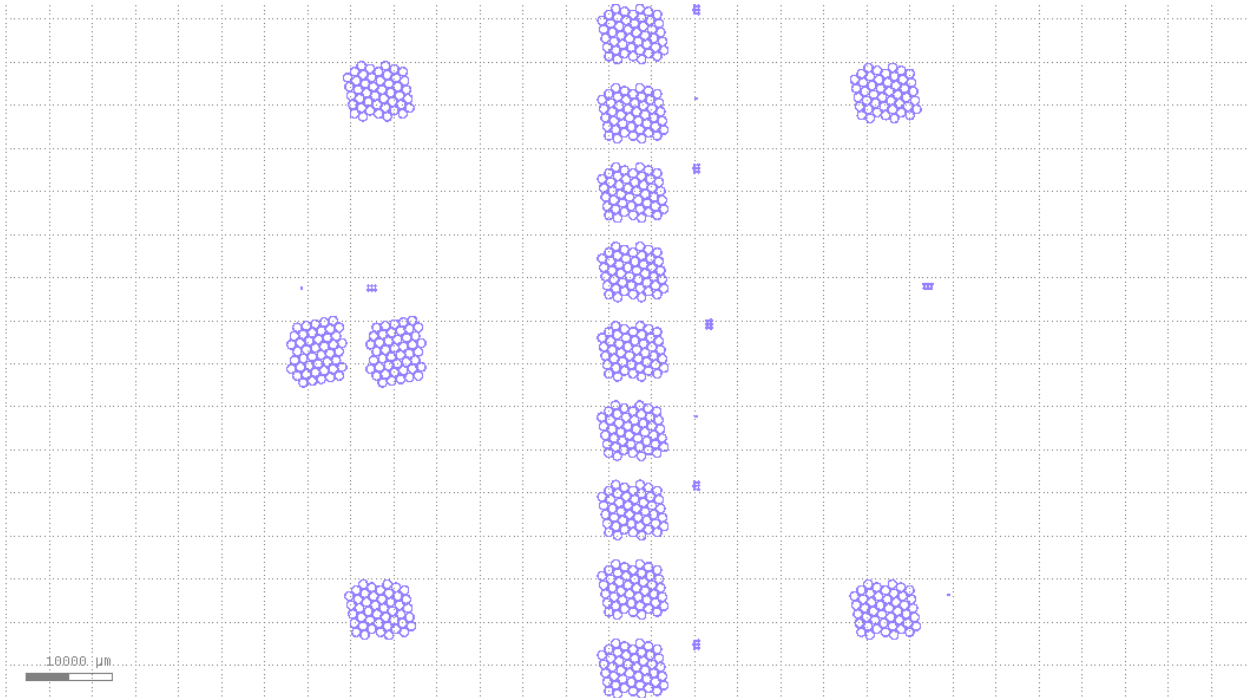


2. Masks of the LED on silicon lens array

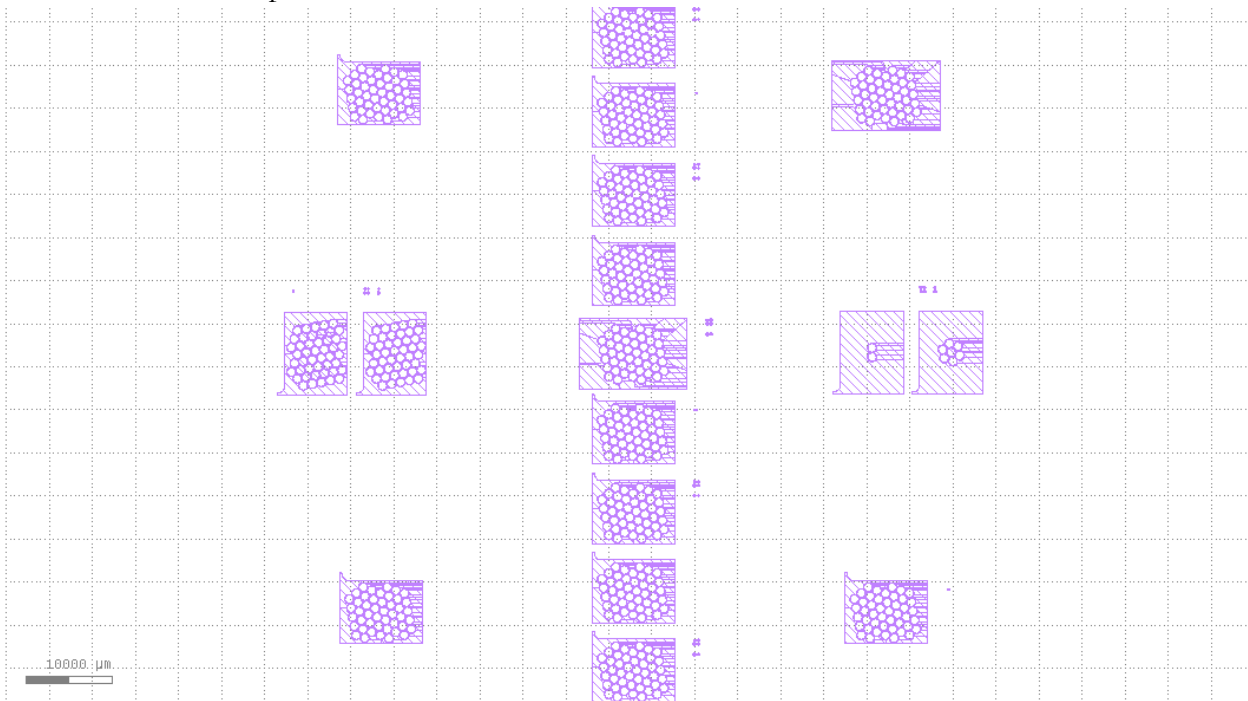
2.1. Recess mask



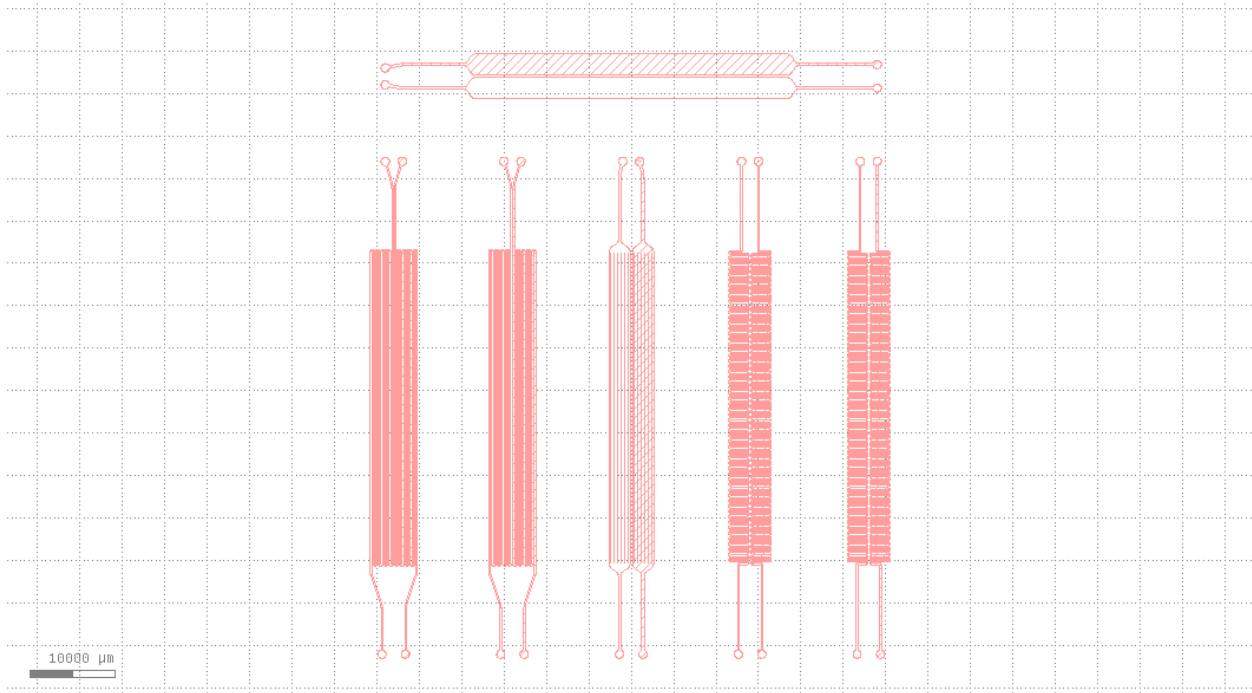
2.2. Boron Implantation mask



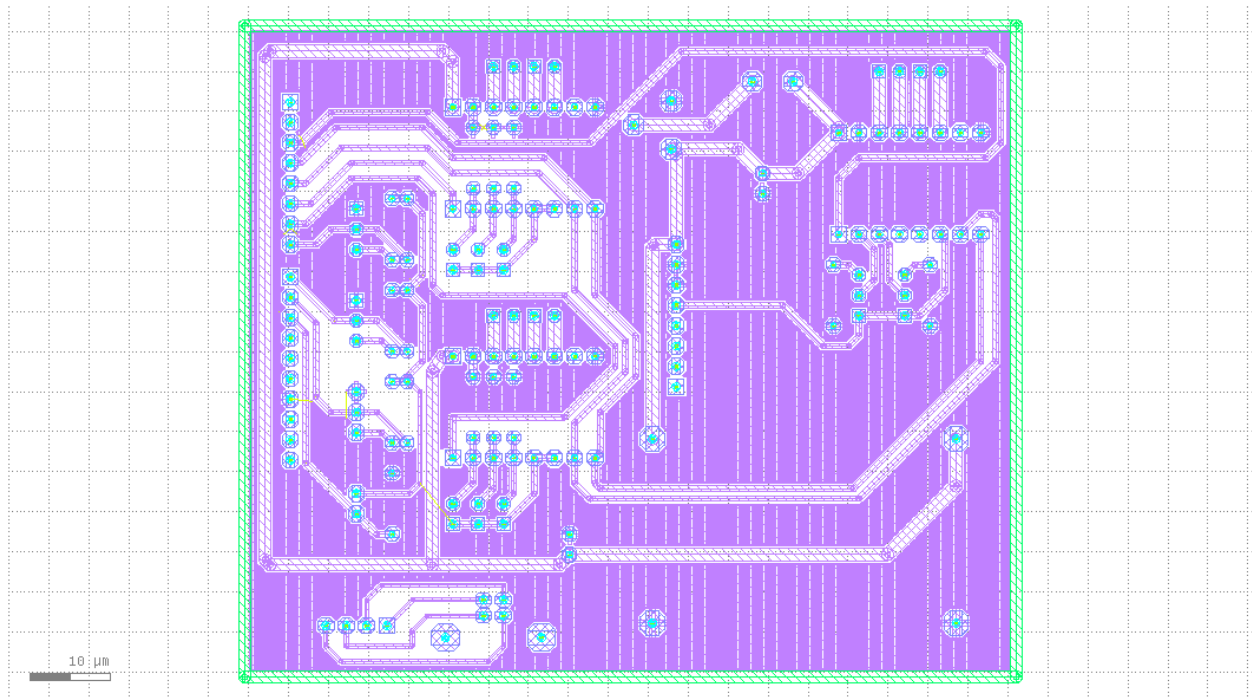
2.3. Aluminum deposition mask



3. Masks for the micro-fluidic chip

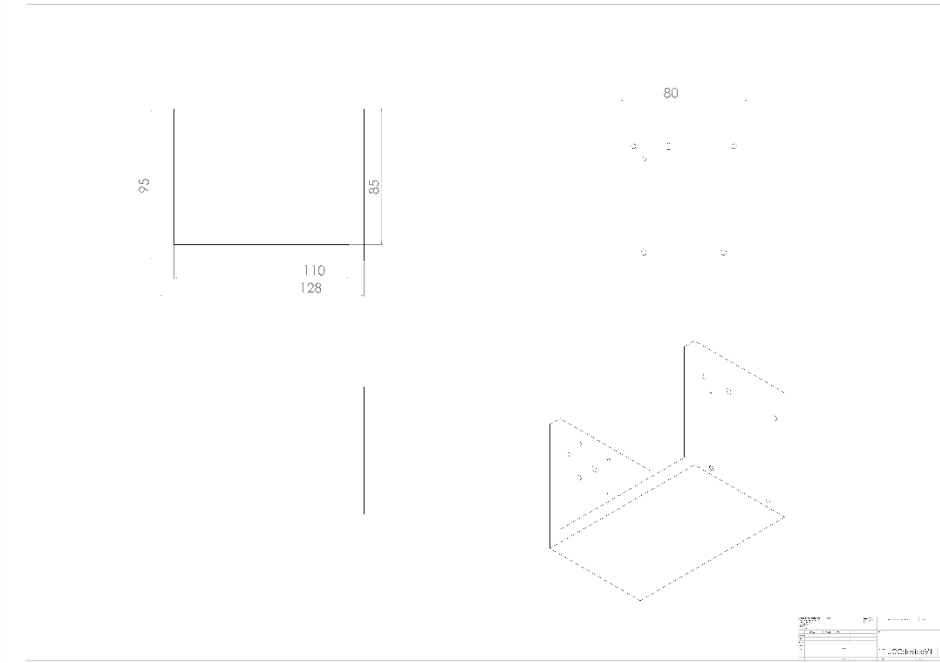


4. Electronics board design

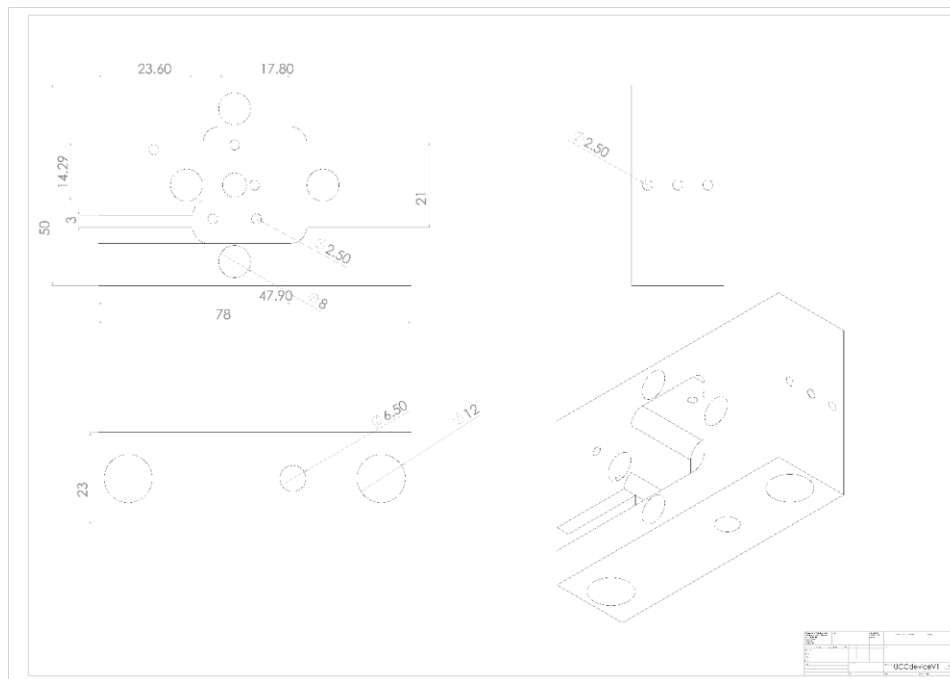


5. Drawings of the platform's mechanical parts

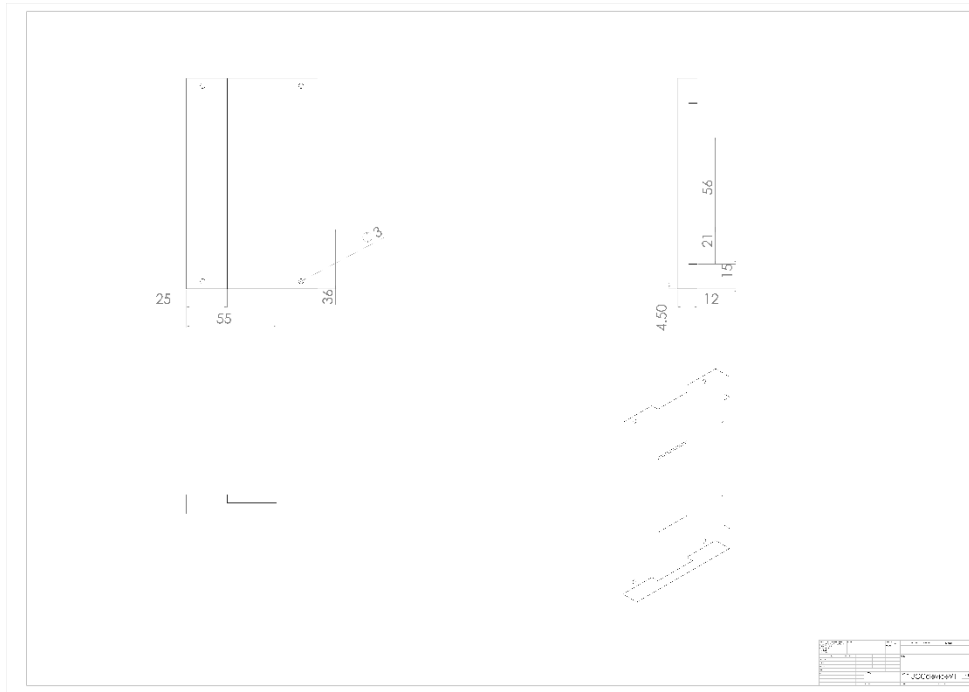
5.1. Case



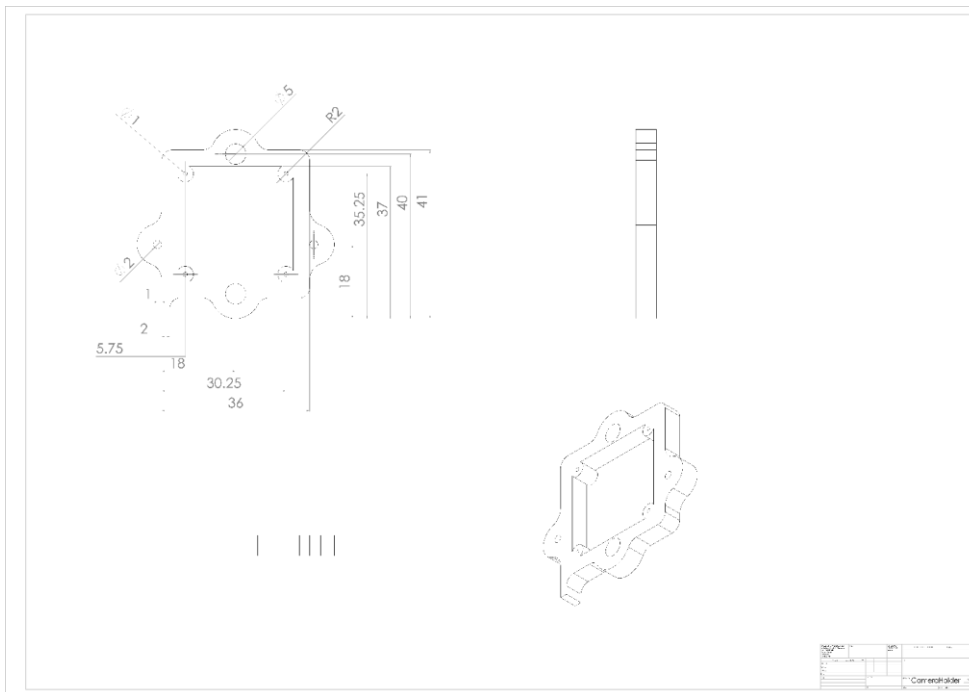
5.2. Optical head



5.3. Sample Holder

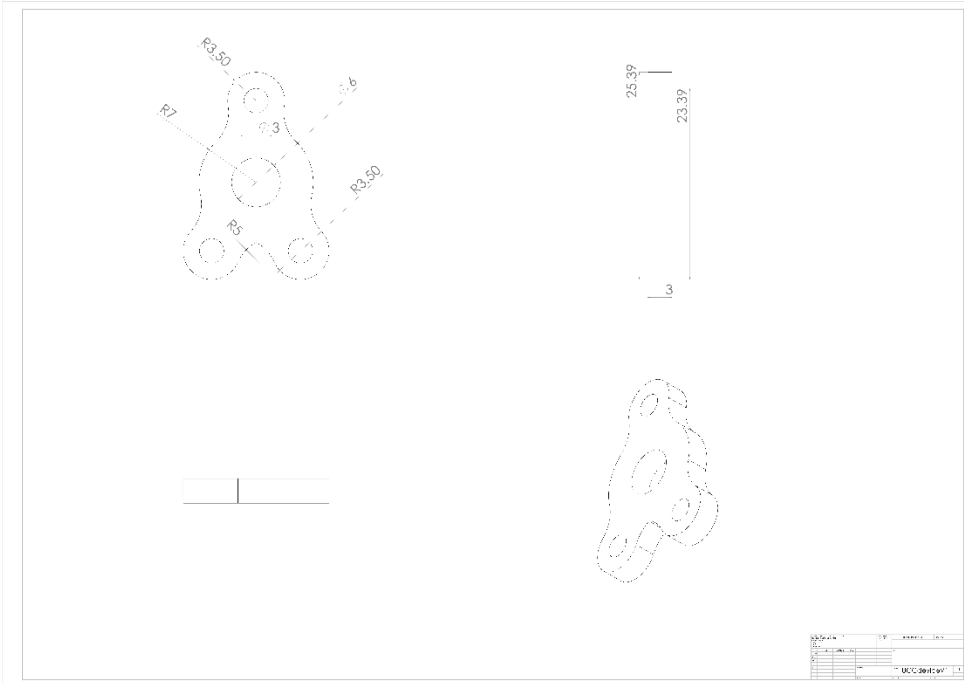
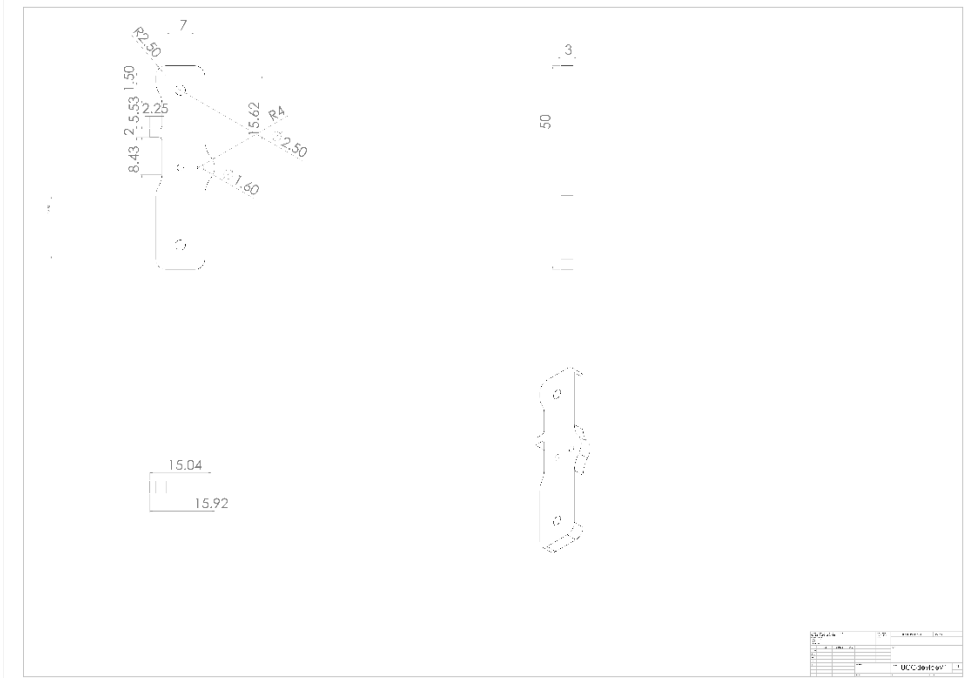


5.4. Camera Holder

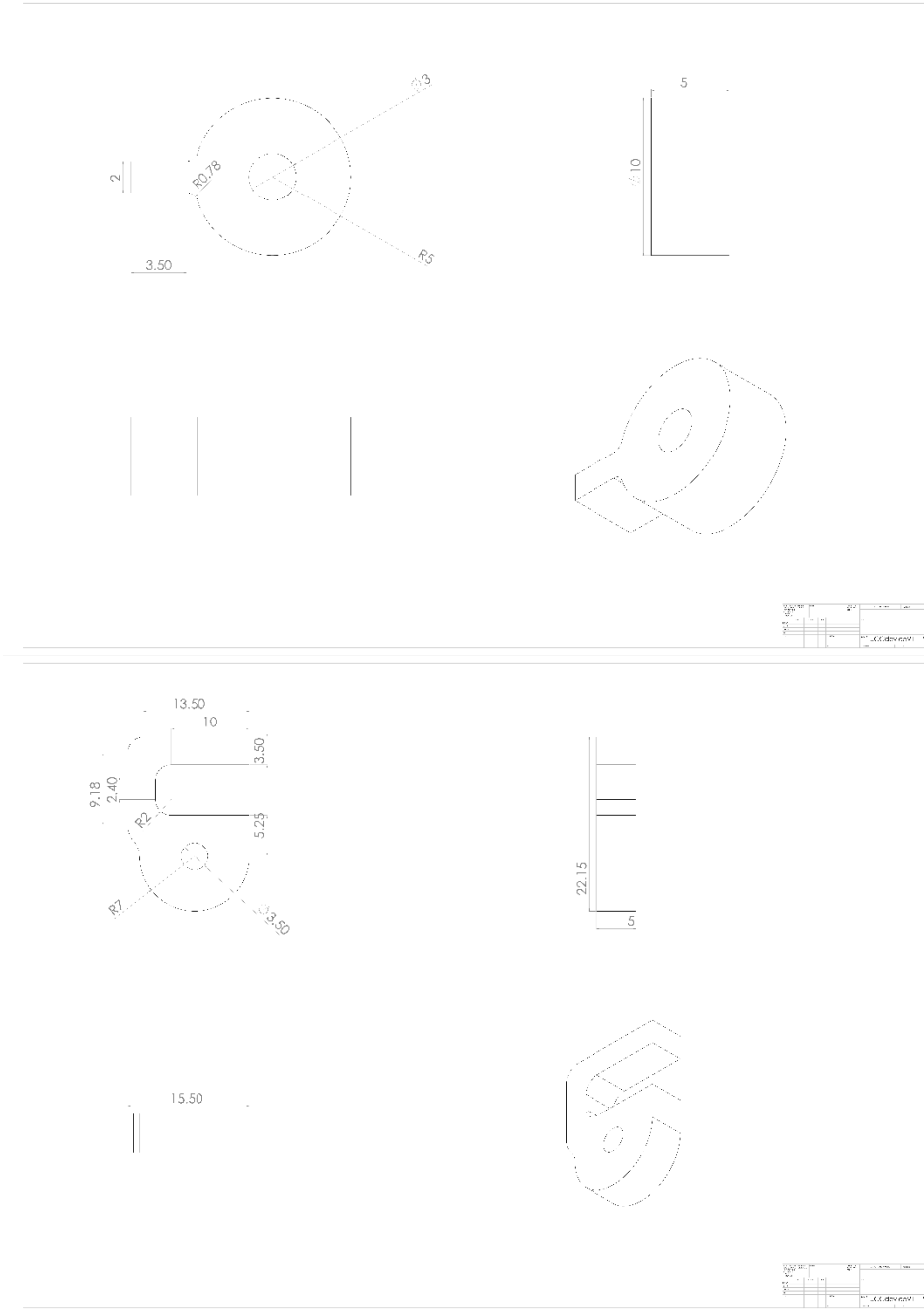


5.5. Z scanning components

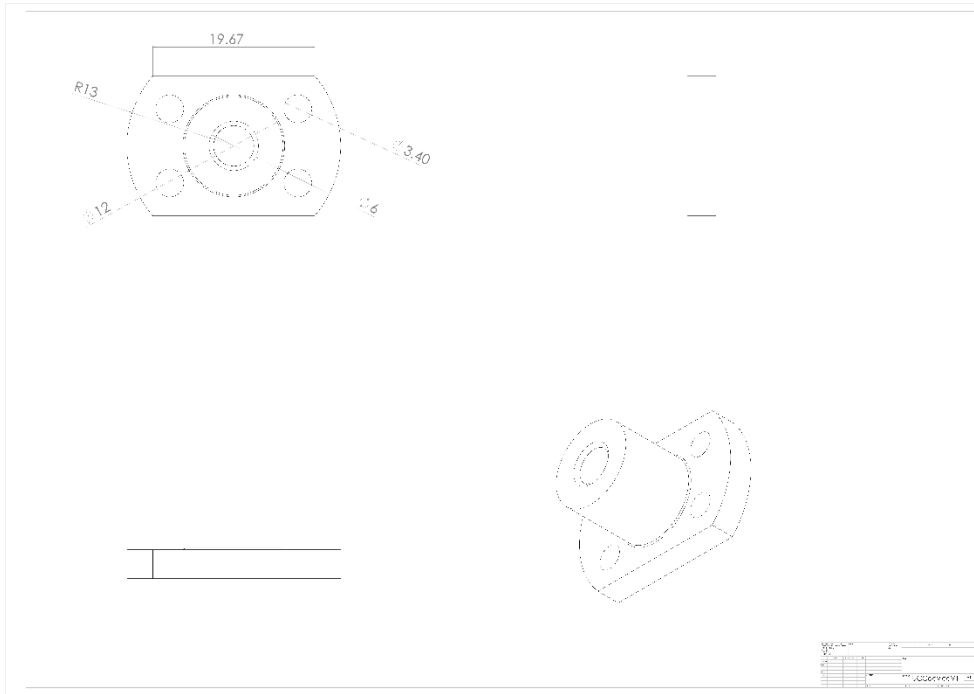




5.6. Optocoupler components



5.7.X scanning coupler



APPEENDIX 2 SOFTWARE CODE

1. Arduino platform programming software

```
#define DIR 3
#define STEP 4
#define EN_Scan 2
#define EN_Lens 6
#define EN_Cam 5
#define SW_Scan 10
#define SW_Low 9
#define SW_Mid 8
#define SW_High 7
String inputString = ""; // a string to hold incoming data
String XString = ""; // a string
boolean stringComplete = false; // whether the string is complete
boolean MotStopFlag = false;
long CamDelay=7000;
long LensDelay=7000;
long ScanDelay=600;
long CamMaxPos=340;
long LensMaxPos=100000;
long ScanMaxPos=8900;
long CamPos;
long LensPos;
long ScanPos;
long RelPos;
long AbsPos;
long Pos;

void setup() {
  // initialize serial:
  Serial.begin(115200);
  // initialize I/O:
  pinMode(SW_Scan, INPUT);
  pinMode(SW_Low, INPUT);
  pinMode(SW_Mid, INPUT);
  pinMode(SW_High, INPUT);
  pinMode(DIR, OUTPUT);
  pinMode(STEP, OUTPUT);
  pinMode(EN_Lens, OUTPUT);
```

```

pinMode(EN_Cam, OUTPUT);
pinMode(EN_Scan, OUTPUT);

digitalWrite(DIR, LOW);
digitalWrite(STEP, LOW);
digitalWrite(EN_Lens, HIGH);
digitalWrite(EN_Cam, HIGH);
digitalWrite(EN_Scan, HIGH);

// reserve 200 bytes for the inputString:
inputString.reserve(200);

}

void loop() {
  RX();
  InputCase();
}

void RX(){
  while (Serial.available()) {
    // get the new byte:
    char inChar = (char)Serial.read();
    // add it to the inputString:
    inputString += inChar;
    // if the incoming character is a newline, set a flag
    // so the main loop can do something about it:
    if (inChar == char(13)) {
      stringComplete = true;
      int StrLen=inputString.length();
      inputString=inputString.substring(0,StrLen-1);
      //Serial.println(inputString);
    }
  }
}

void Move(char Axis, long Steps){
  int Delay;
  switch (Axis){
    case 'C':

```

```

if (Steps > 0){
    digitalWrite(DIR, HIGH);
}
else {
    digitalWrite(DIR, LOW);
}
digitalWrite(EN_Cam, LOW);
Delay = CamDelay;
break;
case 'L':
if (Steps > 0){
    digitalWrite(DIR, HIGH);
}
else {
    digitalWrite(DIR, LOW);
}
digitalWrite(EN_Lens, LOW);
Delay = LensDelay;
break;
case 'S':
if (Steps < 0){
    digitalWrite(DIR, HIGH);
}
else {
    digitalWrite(DIR, LOW);
}
digitalWrite(EN_Scan, LOW);
Delay = ScanDelay;
break;
}
//Serial.println(Steps);
for (long i=0; i <= abs(Steps)-1; i++){
switch (Axis){
case 'C':
    if (Steps>0 && digitalRead(SW_High)) {digitalWrite(EN_Cam, HIGH);return;}
    if (Steps<0 && digitalRead(SW_Low)) {digitalWrite(EN_Cam, HIGH);return;}
    break;
case 'L':
    if (Steps>0 && digitalRead(SW_Low)) {digitalWrite(EN_Lens, HIGH);return;}
    if (Steps<0 && digitalRead(SW_Mid)) {digitalWrite(EN_Lens, HIGH);return;}
    break;
}
}

```

```

    case 'S':
        if (Steps<0 && digitalRead(SW_Scan)){digitalWrite(EN_Scan, HIGH);return;}
        break;
    }

RX();
if (inputString.substring(0,1)="X"){
    inputString = "";
    stringComplete = false;
    digitalWrite(EN_Cam, HIGH);
    digitalWrite(EN_Lens, HIGH);
    digitalWrite(EN_Scan, HIGH);
    return;
}
//Serial.println(Steps);
//Serial.println(i);
digitalWrite(STEP, HIGH);
delayMicroseconds(Delay);
digitalWrite(STEP, LOW);
delayMicroseconds(Delay);
switch (Axis){
    case 'C':
        if (Steps>0 ){CamPos=CamPos++;}
        if (Steps<0 ){CamPos=CamPos--;}
        break;
    case 'L':
        if (Steps>0 ){LensPos=LensPos++;}
        if (Steps<0 ){LensPos=LensPos--;}
        break;
    case 'S':
        if (Steps>0 ){ScanPos=ScanPos++;}
        if (Steps<0 ){ScanPos=ScanPos--;}
        break;
    }
}
// Serial.println(CamPos);
// Serial.println(LensPos);
// Serial.println(ScanPos);
delayMicroseconds(1000);
digitalWrite(EN_Cam, HIGH);
digitalWrite(EN_Lens, HIGH);

```

```

    digitalWrite(EN_Scan, HIGH);
}

void InputCase() {
    if (stringComplete) {
        long Steps;
        char FirstChar;
        char SecondChar;
        char ThirdChar;
        String str = inputString;
        int str_len = str.length() + 1;
        char AllChar[str_len];
        str.toCharArray(AllChar, str_len);
        FirstChar=AllChar[0];
        SecondChar=AllChar[1];
        ThirdChar=AllChar[2];
        switch (FirstChar) {
            case 'C':
                switch (SecondChar){
                    case 'A':
                        AbsPos = inputString.substring(2).toInt();
                        inputString = "";
                        stringComplete = false;
                        if (AbsPos<0 || AbsPos>CamMaxPos) {break;}
                        Steps = AbsPos - CamPos;
                        Move('C', Steps);
                        Serial.println("OK");
                        break;
                    case 'R':
                        RelPos = inputString.substring(2).toInt();
                        inputString = "";
                        stringComplete = false;
                        if (RelPos+CamPos<0 || RelPos+CamPos>CamMaxPos) {break;}
                        Move('C', RelPos);
                        Serial.println("OK");
                        break;
                    case 'H':
                        inputString = "";
                        stringComplete = false;
                        Move('C', 20);
                        Move('C', long(-pow(10,9)));
                }
            }
        }
    }
}

```



```

    CamPos = 0;
    Serial.println("OK");
    break;
case 'V':
    CamDelay = inputString.substring(2).toInt();
    inputString = "";
    stringComplete = false;
    break;
case 'C':
    if (ThirdChar=='+') {
        inputString = "";
        stringComplete = false;
        Move('C', long(pow(10,9)));
        Serial.println("OK");
    }
    else if (ThirdChar=='-') {
        inputString = "";
        stringComplete = false;
        Move('C', long(-pow(10,9)));
        Serial.println("OK");
    }
    else {
        inputString = "";
        stringComplete = false;
    }
    break;
}
inputString = "";
stringComplete = false;
break;
case 'L':
    switch (SecondChar) {
        case 'A':
            AbsPos = inputString.substring(2).toInt();
            inputString = "";
            stringComplete = false;
            if (AbsPos<0 || AbsPos>LensMaxPos) {break;}
            Steps = AbsPos - LensPos;
            Move('L', Steps);
            Serial.println("OK");
            break;

```

```

case 'R':
    RelPos = inputString.substring(2).toInt();
    inputString = "";
    stringComplete = false;
    if (RelPos+LensPos<0 || RelPos+LensPos>LensMaxPos){break;}
    Move('L', RelPos);
    Serial.println("OK");
    break;
case 'H':
    inputString = "";
    stringComplete = false;
    Move('L', 20);
    Move('L', long(-pow(10,9)));
    LensPos = 0;
    Serial.println("OK");
    break;
case 'V':
    LensDelay = inputString.substring(2).toInt();
    inputString = "";
    stringComplete = false;
    break;
case 'C':
    if (ThirdChar=='+'){
        inputString = "";
        stringComplete = false;
        Move('L', long(pow(10,9)));
        Serial.println("OK");
    }
    else if (ThirdChar=='-'){
        inputString = "";
        stringComplete = false;
        Move('L', long(-pow(10,9)));
        Serial.println("OK");
    }
    else {
        inputString = "";
        stringComplete = false;
    }
    break;
}
inputString = "";

```

```

stringComplete = false;
break;
case 'S':
switch (SecondChar){
case 'A':
AbsPos = inputString.substring(2).toInt();
inputString = "";
stringComplete = false;
if (AbsPos<0 || AbsPos>ScanMaxPos){break;}
Steps = AbsPos - ScanPos;
Move('S', Steps);
Serial.println("OK");
break;
case 'R':
RelPos = inputString.substring(2).toInt();
inputString = "";
stringComplete = false;
if (RelPos+ScanPos<0 || RelPos+ScanPos>ScanMaxPos){break;}
Move('S', RelPos);
Serial.println("OK");
break;
case 'H':
inputString = "";
stringComplete = false;
Move('S', 200);
Move('S', long(-pow(10,9)));
ScanPos = 0;
Serial.println("OK");
break;
case 'V':
ScanDelay = inputString.substring(2).toInt();
inputString = "";
stringComplete = false;
break;
case 'C':
if (ThirdChar=='+'){
inputString = "";
stringComplete = false;
Move('S', long(pow(10,9)));
Serial.println("OK");
}
}

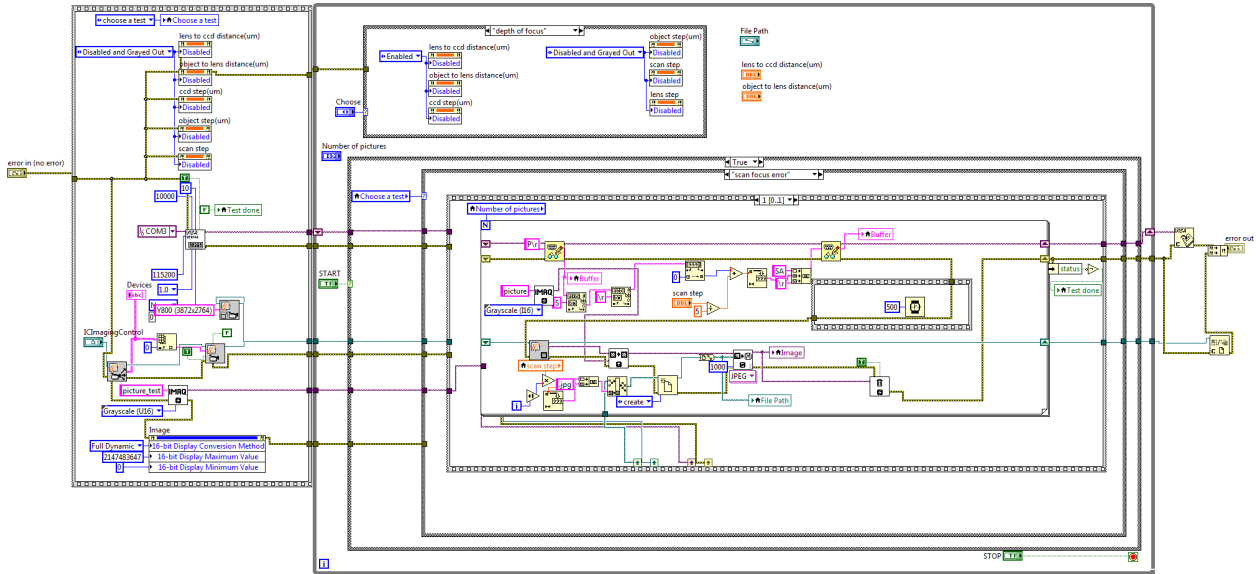
```

```

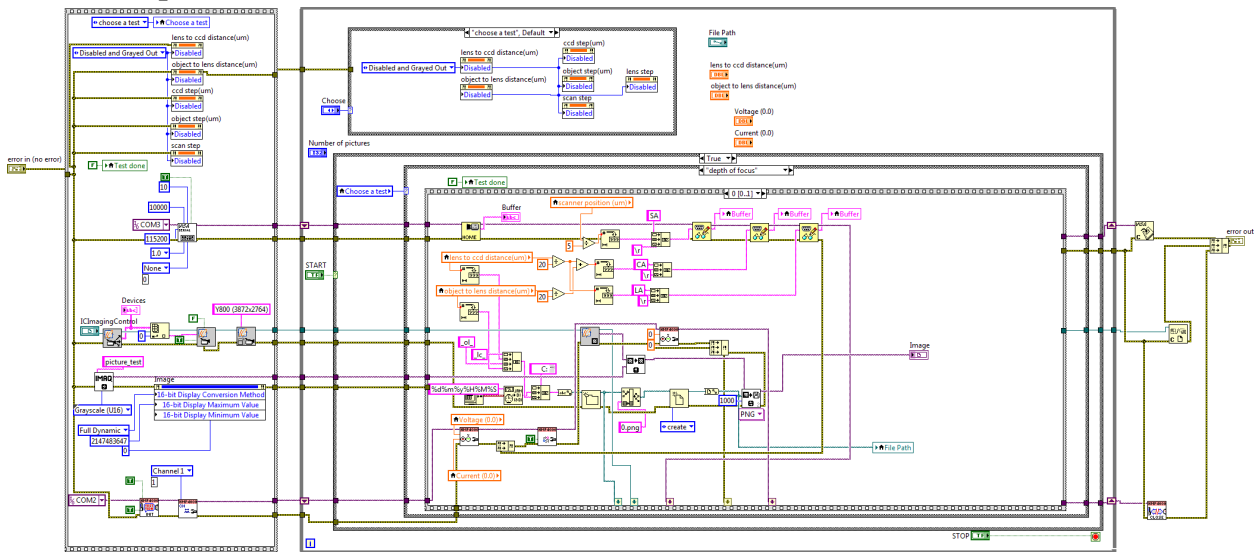
else if (ThirdChar=='-'){
    inputString = "";
    stringComplete = false;
    Move('S', long(-pow(10,9)));
    Serial.println("OK");
}
else {
    inputString = "";
    stringComplete = false;
}
break;
}
inputString = "";
stringComplete = false;
break;
case 'P':
    inputString = "";
    stringComplete = false;
    XString="C"+String(CamPos)+"L"+String(LensPos)+"S"+String(ScanPos);
    Serial.println(XString);
    break;
inputString = "";
stringComplete = false;
}
inputString = "";
stringComplete = false;
}
}

```

2. LabVIEW main block diagram for scanning platform operation



3. LabVIEW block diagram for the control of LED power supply and image acquisition setup



4. MATLAB code for image stitching

```
function [im_corrected,im_bias]=biasCorrection_bipoly(im_given,varargin)
% biasCorrection_bipoly can estimate and remove bias field in gray or
% color images.
% Reference:
% Y. Zheng, M. Grossman, S. Awate, J. Gee "Automatic Correction of
% Intensity Nonuniformity From Sparseness of Gradient Distribution in
% Medical Images," in MICCAI 2009: the 12th International Conference on
% Medical Image Computing and Computer Assisted Intervention, London, UK,
```

% September 20-24, 2009

```
if nargin==0
    error('You need to provide image data for biasCorrection_bipoly.m. Try "help
biasCorrection_bipoly" to get more information.');
```

end

```
[D,itrNum,alpha]=parseInputs(nargin-1,varargin);
epsilon=0.0001;% perturbation on B
shift=1; % shift to avoid computation of log(0)
numsz=length(size(im_given_sampled));
if numsz==3
    DIM=3;
    im_gray=rgb2gray(uint8(im_given_sampled));
else
    DIM=1;
    im_gray=im_given_sampled;
end
im_data=double(im_gray);
sz=size(im_data);
numPixels=sz(1)*sz(2);
disp('Preparing ...');
Z_shift=log(im_data+shift);
Lvxny=[getLv(sz,2);getLv(sz,1)];
numCoeff=(D+1)*(D+2)/2;
myI=speye(numCoeff,numCoeff);
vector_W=ones(numPixels*2,1);
W=W_vec2sparse(vector_W);
[Cx,Cy]=biPoly_getC(sz(1:2),D);
C=[Cx';Cy'];
Gamma1=epsilon*myI;
colNum=itrNum+1;
ims{1}=im_given_sampled; tts{1}='Given Image';
ims{colNum+1}=uint8(ones(sz(1),sz(2))*255); tts{colNum+1}='Initial Bias';
ims{2*colNum+1}=uint8(reshape(vector_W(1:numPixels),sz)*255); tts{2*colNum+1}='Initial
Weight';
for i=1:4
    disp(['IRLS: iteration ' num2str(i) ' ... ...']);
    right=W*Lvxny*Z_shift(:);
    A=W*C;
    warning off all;
    a=((A'*A+Gamma1)\(A'*right));
    B=poly2d(sz(1:2),D,a);
```

```

S1=abs(Lvxny*B(:)-Lvxny*Z_shift(:)); S2=alpha*(S1).^(alpha-1);
vector_W=exp(-S1).*(1-exp(-S2));
vector_W_temp=[vector_W(numPixels+1:end);vector_W(1:numPixels)];
vector_W=(vector_W+vector_W_temp)/2;
W=W_vec2sparse(vector_W);
image_W=uint8(reshape(vector_W(1:numPixels),sz)*255);
B=B-mean(B(:));
b=exp(B-(max(B(:))));% such that b is within [0 1], for display
image_b=reshape(b,sz);
image_b=uint8(image_b*255);
X=log(double(im_given_sampled)+shift)-repmat(reshape(B,sz(1),sz(2)),[1 1 DIM]);
x=exp(X)-shift;
x=uint8(x);
ims{1+i}=x; tts{1+i}=['Corrected: Iter ' num2str(i)];
ims{colNum+1+i}=image_b; tts{colNum+1+i}=['Bias: Iter ' num2str(i)];
ims{2*colNum+1+i}=image_W; tts{2*colNum+1+i}=['Weight: Iter ' num2str(i)];
end
im_bias=imresize(image_b,[size(im_given,1) size(im_given,2)],'bicubic');

% bias corrected image
im_bias_4compute=reshape(exp(B),sz)*255;
im_bias_4compute=imresize(im_bias_4compute,[size(im_given,1) size(im_given,2)],'bicubic');
data_bias=double(im_bias_4compute)/255; %data_bias=data_bias %mean(data_bias(:));
X=log(double(im_given)+shift)-repmat(log(data_bias),[1 1 DIM]);
x=exp(X)-shift;
im_corrected=uint8(x);

function [D,itrNum,alpha]=parseInputs(numVar,vars)
% default
D=5;% smoothness
itrNum=4;
alpha=0.1;%diff 2 weight %smaller alpha means more contingent or sharper

% read input
if numVar>=1
    D=vars{1};
end
if numVar>=2
    itrNum=vars{2};
end
if numVar>=3

```

```

alpha=vars{3};
end

```

```

function [If] = stitch_one_lens( I, n, rect, d )
%This function performs automatic cropping of the FOV of one lens (defined %in n) based on the
corresponding rectangle (defined in rect) for all %pictures acquired during scanning (given in cell
variable I).
%Each cropped region is subjected to bias brightness
%correction to create a flat background field. The cropped images are then
%stitched based on the known dislocation (the scanning step measured in
%pixels, given in input variable d). The final stitched image is given in %output variable If.
for i=1:size(I,2)-1
    Ic{i}=imcrop(I{i},rect);
    imwrite(Ic{i}, strcat(sprintf('G:\georgia back
up\scan_focus_error\041217191239_lc_960_ol_200\cropped\lens%d',n),sprintf('\%dbefore.jpg',i)));
    [Ic{i},im_bias]=biasCorrection_bipoly(Ic{i},2,4,0.1);
    imwrite(Ic{i}, strcat(sprintf('G:\georgia back
up\scan_focus_error\041217191239_lc_960_ol_200\cropped\lens%d',n),sprintf('\%d.jpg',i)));
    imwrite(im_bias, strcat(sprintf('G:\georgia back
up\scan_focus_error\041217191239_lc_960_ol_200\cropped\lens%d',n),sprintf('\%dbias.jpg',i)));
end
for i=1:size(I,2)-1
    if i==1
        C=Ic{1};
    else
        A=Ic{i};
        B=C;
        if size(A,1)>d(1)+1
            A=imcrop(A, [0 0 size(A,2) (size(A,1)-(size(A,1)-d(1))/2 +1)]);
            B=imcrop(B, [0 size(A,1)-d(1)-2 size(B,2) (size(B,1)-(size(A,1)-d(1)-2))]);
            d_new=size(A,1)-2;
        else
            d_new=d(1);
        end
        RA = imref2d(size(A));
        RB = imref2d(size(B));
        RB.XWorldLimits = RB.XWorldLimits;
        RB.YWorldLimits = RB.YWorldLimits+d_new;
    end
end

```



```

        [C,RC]=imfuse(A,RA,B,RB,'blend');
    end
end
figure (n);
imshow(C);
If=C;
imwrite(If,strcat(sprintf('G:\\georgia back
up\\scan_focus_error\\041217191239_lc_960_ol_200\\cropped\\lens%d',n),sprintf('\\final
%d.jpg',n)));
end

```

```

function [stitched_image]=stitch_adjacent_lenses(lens1,lens2,d)
%This function performs stitching of two adjacent lenses according to the %dislocation of the
second lens2 with respect to the first lens1 defined in 2 %elements vector d
    if size(lens1,2)>d(1)+3
        lens1=imcrop(lens1, [0 0 size(lens1,2)-(size(lens1,2)-d(1))/2+3 size(lens1,1)]);
        lens2=imcrop(lens2, [size(lens1,2)-d(1)-6 0 size(lens2,2)-(size(lens1,2)-d(1)-6)
size(lens2,1)]);
        d(1)=size(lens1,2)-6;
    end
    A=lens1;
    B=lens2;
    RA = imref2d(size(A));
    RB = imref2d(size(B));
    RB.XWorldLimits = RB.XWorldLimits+d(1);
    RB.YWorldLimits = RB.YWorldLimits+d(2);
    [stitched_image,RC]=imfuse(A,RA,B,RB,'blend');
    %figure;imshow(stitched_image);
end

```

```

function [ Final, rect] = stitching_complete( If)
%This function performs automatic stitching of all lens images previously %stitched If
    for i=size(centers,1):-1:1
        if i==size(centers,1)
            stitched_image=stitch_adjacent_lenses(If{i},If{i-1},[d(i,1) d(i,2)]);
        else
            stitched_image=stitch_adjacent_lenses(stitched_image,If{i-1},[d(i,1) d(i,2)]);
        end
        imwrite(stitched_image,sprintf('G:\\georgia back
up\\scan_focus_error\\041217191239_lc_960_ol_200\\stitched_image%d.jpg',i-1));
    end
end

```

```

imwrite(stitched_image,'G:\georgia back
up\scan_focus_error\041217191239_lc_960_ol_200\Final.jpg');
end

```

5. MATLAB code for cell detection and counting

```

function [ sum,grain_areas ] = smear_cell_detection_final( Iin )
%This function is used to detect cells captured in a smear whole blood film.
%The functions parameters are adjusted so that the function works efficiently
%for one lens image.
    figure;imshow(Iin);
    imwrite(Iin,'F:\georgia back up\HIV\Experiments2\scanner\matlab
code\matlab_code_stitching_cell_detection\detection counting\smear cell detection
test\lens1mat.tif');
    % [Icorr,im_bias]=biasCorrection_bipoly(Iin,2,4,0.1);
    I1=im2double(rgb2gray(Iin));
    figure;imshow(I1);

    I=imadjust(imresize(I1,4));
    imwrite(I,'F:\georgia back up\HIV\Experiments2\scanner\matlab
code\matlab_code_stitching_cell_detection\detection counting\smear cell detection
test\lens1matresize.tif');
    figure ;imshow(I);%
    [background,interp]=bgest(imadjust(imresize(I1,4)),80);
    figure;imshow(background);%
    NHOOD=[1 1 1;1 1 1;1 1 1];
    I=I-background;
    figure;imshow(I);%
    level = graythresh(I);
    bw = im2bw(I,0.5*level);
    figure;imshow(bw);
    bw = bwareaopen(bw, 20);
    bw=imfill(bw,'holes');
    bw_sub = bwareaopen(bw, 500);
    bw_sub=imfill(bw_sub,'holes');
    bw=bw-bw_sub;
    [L,bw] = splitCells(I,bw,100,300,0.7,1,1);
    figure;imshow(bw);
imwrite(bw,'F:\georgia back up\HIV\Experiments2\scanner\matlab
code\matlab_code_stitching_cell_detection\detection counting\smear cell detection
test\lens1matbw.tif');
    cc = bwconncomp(bw,4);

```

```

labeled = labelmatrix(cc);
RGB_label = label2rgb(labeled, @spring, 'c', 'shuffle');
figure;imshow(RGB_label);%
imwrite(RGB_label,'F:\georgia back up\HIV\Experiments2\scanner\matlab
code\matlab_code_stitching_cell_detection\detection counting\smear cell detection
test\lens1 matrgblabel.tif');
graindata= regionprops(cc,'all');
k=0;
grain_areas=[];
centers=[];
for i=1:size(graindata,1)
    if ((4*graindata(i).Area/(graindata(i).Perimeter^2)>=0))
        grain_areas(i-k) = graindata(i).Area;
        centers(i-k,1)=graindata(i).Centroid(1);
        centers(i-k,2)=graindata(i).Centroid(2);
    else
        k=k+1;
        4*graindata(i).Area/(graindata(i).Perimeter^2);
    end
end
edges=[min(grain_areas):40:max(grain_areas)];
if isempty(grain_areas)
else
    figure;hist(grain_areas,edges);%
    %%title('Histogram of cell Area');
end
if isempty(centers)
    sum=0;
else
    sum=size(centers,1);
    %%centroids = cat(1,graindata.Centroid);
    %%subplot(10,10,image);
    %%subplot(3,2,6);
    figure;imshow(imresize(Iin,4));hold on;
    plot(centers(:,1),centers(:,2), 'b*');hold off;
end
end

```

```

function [ZI,interp]=bgest(I,binsize)
%% This function is used to remove background intensity variations in images %% of smear blood
tests in bright field (Buggenthin et al., 2013)

```

```

%%% init
fprintf('init...\n')
imgsize=size(I);
x = nan(floor((imgsize(1)-binsize)/binsize*2*(imgsize(2)-binsize)/binsize*2),1);
y = nan(floor((imgsize(1)-binsize)/binsize*2*(imgsize(2)-binsize)/binsize*2),1);
z = nan(floor((imgsize(1)-binsize)/binsize*2*(imgsize(2)-binsize)/binsize*2),1);
featuremat = nan(floor((imgsize(1)-binsize)/binsize*2*(imgsize(2)-binsize)/binsize*2),5);
imgwidth=size(I,2);
imgheight=size(I,1);
counter=0;
fprintf('getting tiling features...\n')
for i = 1:binsize/2:imgsize(1)-binsize
    for j=1:binsize/2:imgsize(2)-binsize
        sub = I(i:i+binsize, j:j+binsize);
        counter=counter+1;
        y(counter) = i+binsize/2;
        x(counter) = j+binsize/2;
        z(counter)= mean(sub(:));
        featuremat(counter,:)=([std(sub(:)) skewness(sub(:)) max(sub(:))/min(sub(:))
kurtosis(sub(:)) var(sub(:))/mean(sub(:)) ]);
    end
end
%%% cluster it
fprintf('clustering %d points...\n',counter)
[classess,type]=dbscan(featuremat,size(featuremat,2)+1,[]);
if ~(size(classess,2)==size(type,2))
    classess(:,size(classess,2)+1)=type(:,size(type,2));
end
if numel(unique(classess))==1
    daclass = unique(classess);
else
    classstd = [];
    for c = unique(classess)
        if numel(featuremat(classess == c & type == 1,1))>200
            classstd(end+1)= mean(featuremat(classess == c,1));
        else
            classstd(end+1) = inf;
        end
    end
end
[~,daclass] = min(classstd(2:end));
daclass = daclass+1;

```

```

    daclasstemp = unique(classes);
    daclass = daclasstemp(daclass);
end
interp=sum(classes == daclass& type==1);
fprintf('using %d interpolation points...\n',interp)

%%% interpolate
[XI YI] = meshgrid(1:imgwidth,1:imgheight);
F=TriScatteredInterp(x(classes == daclass& type == 1),y(classes ==daclass& type == 1)
,z(classes ==daclass& type == 1),'natural');
ZI=F(XI,YI);

%%% extrapolate
for i=find(sum(~isnan(ZI(1:imgheight)))>1)
    ZI(:,i)=interp1(find(~isnan(ZI(:,i))),ZI(~isnan(ZI(:,i))),i, 1:imgheight,'linear','extrap');
end
for i=find(sum(~isnan(ZI(:,1:imgwidth)))>1)
    ZI(i,:)=interp1(find(~isnan(ZI(i,:))),ZI(i,~isnan(ZI(i,:))), 1:imgwidth,'linear','extrap');
end
%%% fix strange extrapolations
ZI(ZI<min(I(:)))=min(I(:));
ZI(ZI>max(I(:)))=max(I(:));
fprintf('done\n')
end

```

```

function [ centers] = captured_cells(I)
%This function is used for the detection of cells that are captured on a %functionalized surface. The
algorithm is applied on a single lens image %after flat field correction

```

```

[~, threshold] = edge(I, 'sobel');
fudgeFactor = .8;
BWs = edge(I_stretch,'sobel', threshold * fudgeFactor);
figure(2);imshow(BWs);
se90 = strel('line', 3, 90);
se0 = strel('line', 3, 0);
BWsdil1 = imdilate(BWs, [se90 se0]);
BWdfill1 = imfill(BWsdil1, 'holes');
figure(3);imshow(BWdfill1);
BWsdil=BWdfill1;
figure(6);imshow(BWsdil);
BWnobord = imclearborder(BWdfill1, 26);
figure(7); imshow(BWnobord), title('cleared border image');

```

```

seD = strel('diamond',1);
BWfinal = imerode(BWnobord,seD);
figure(8); imshow(BWfinal);
for i=1:7
    BWfinal = imerode(BWfinal,seD);
end
figure(9), imshow(BWfinal), title('segmented image');
cc = bwconncomp(BWfinal,4);
labeled = labelmatrix(cc);
RGB_label = label2rgb(labeled, @spring, 'c', 'noshuffle');
figure (10);imshow(RGB_label);%
graindata= regionprops(cc,'all');
for i=1:size(graindata)
    centers(i,1)=graindata(i).Centroid(1);
    centers(i,2)=graindata(i).Centroid(2);
end
k=0;
figure;imshow(I_stretch);hold on;
for i=1:size(centers(:,1))
    circle(centers(i,1),centers(i,2),10,10);hold on;
end
hold off;
end

```

APPEENDIX 3

SURFACE FUNCTIONALIZATION PROTOCOL

1. Functionalization protocol for White Blood Cells (WBCs) capturing

PREPARATION

1. Microfluidic chip is cleaned with acetone in ultrasonic bath for 30min
2. Microfluidic chip is cleaned with piranha 1:1 (clean room) for 20min
3. Working surfaces are cleaned with 70% ethanol
4. Microfluidic chip is washed with dH₂O
5. Microfluidic chip is washed with 70% ethanol
6. Microfluidic chip is baked at 100°C for 10min, on the hotplate
7. Plasma exposure to the reactor for 5min (recipe 9)

SURFACE FUNCTIONALIZATION

1. Introduction of 4%v/v 3-MPS in ethanol absolute, 30min incubation at RT
2. Washing with ethanol absolute
3. Annealing at 100°C for 30min, on the hotplate
4. Introduction of 1mM GMBS working solution in ethanol absolute, 30min incubation at RT (GMBS stock solution is diluted in DMSO anhydrous and maintained under anhydrous conditions at 4°C)
5. Washing with ethanol absolute
6. Washing with PBS 1X
7. Introduction of 150µg/ml Neutravidin in PBS 1X in the dark, 1.5h incubation at 4°C (Neutravidin is introduced 4X times, every 22.5 min successively from the inlet and the outlet)
8. Washing with PBS 1X
9. Washing with PBS 1% BSA
10. Introduction of 75µg/ml anti-CD45 monoclonal, biotinylated antibody (BAM1430, R&D), 30min incubation RT (BAM1430 is introduced 4X times, every 7.5 min successively from the inlet and the outlet)
11. Washing with PBS 1% BSA
12. Blocking with PBS 1% BSA for 30min at RT or O/N at 4°C

BLOOD INTRODUCTION, WASHING AND CELL IMAGING

1. Blood collection in a heparin tube (either fingerpick or vein blood sample)
2. Blood introduction to the microfluidic chip with Hamilton syringe, 8-15min incubation (depending on the microfluidic channel's design)
3. Washing with PBS 1X containing 0.001M EDTA pH 8.0 with washing pump pressure adjusted to 2mbar and washing duration depending of the microfluidic channel's design and ranging between 45min to 1.5h

4. Introduction of Hoechst staining (3:1000 in PBS 1X). Hoechst is introduced 2X times, every 20min successively from the inlet and the outlet
5. Microscopic observation and channel scanning under DAPI and Bright field specific filters

Bibliography

- Abdullah, A. and Agha, Z. (2013) 'Efficient Poisson Blending for Seamless Image Stitching'.
- Adams, D. L. *et al.* (2014) 'The systematic study of circulating tumor cell isolation using lithographic microfilters', *RSC Advances*, 4(9), pp. 4334–4342. doi: 10.1039/c3ra46839a.
- Adewoyin, A. S. and Nwogoh, B. (2014) 'Peripheral Blood Film - a Review', *Ann. Pg. Med.*, 12(2), pp. 71–79.
- Alapan, Y. *et al.* (2016) 'Emerging point-of-care technologies for sickle cell disease screening and monitoring', *Expert Review of Medical Devices*. Taylor & Francis, 13(12), pp. 1073–1093. doi: 10.1080/17434440.2016.1254038.
- Anton Paar (2000) *Application Report: Viscosity Measurement of Whole Blood*.
- Arrow, K.J.; Panosian, C.; Gelband, H. (ed.) (2004) 'A Brief History of Malaria.', in *Saving Lives, Buying Time: Economics of Malaria Drugs in an Age of Resistance*. Washington (DC): National Academies Press (US);
- Asghar, W. *et al.* (2016) 'Engineering long shelf life multi-layer biologically active surfaces on microfluidic devices for point of care applications', *Scientific Reports*. Nature Publishing Group, 6(February), pp. 1–10. doi: 10.1038/srep21163.
- Ashraf, S. *et al.* (2012) 'Developing standards for malaria microscopy: External competency assessment for malaria microscopists in the Asia-Pacific', *Malaria Journal*, 11, pp. 1–10. doi: 10.1186/1475-2875-11-352.
- B.L., J. (2002) 'Point-of-care testing for HIV: HIV counselling and testing', *Canadian Journal of Infectious Diseases*, 13(2), pp. 85–88. Available at: <http://ovidsp.ovid.com/ovidweb.cgi?T=JS&PAGE=reference&D=emed5&NEWS=N&AN=2002240667>.
- Baek, D. *et al.* (2014) 'Time-lapse microscopy using smartphone with augmented reality markers', *Microscopy Research and Technique*, 77(4), pp. 243–249. doi: 10.1002/jemt.22335.
- Bansal, S. K. *et al.* (2004) 'Qualification of analytical instruments for use in the pharmaceutical industry: A scientific approach', *AAPS PharmSciTech*, 5(1), pp. 151–158. doi: 10.1208/pt050122.
- Barretto, R. P. J., Messerschmidt, B. and Schnitzer, M. J. (2009) 'In vivo fluorescence imaging with high-resolution microlenses', *Nature Methods*. Nature Publishing Group, 6(7), pp. 511–512. doi: 10.1038/nmeth.1339.
- BD biosciences (2010) 'Human and Mouse CD Marker Handbook', pp. 1–47.
- Bean, K. E. *et al.* (1978) 'Anisotropic Etching of Silicon', *IEEE TRANSACTIONS ON ELECTRON DEVICES*, 25(10), pp. 1185–1193.

- Bhagat, A. A. S. *et al.* (2010) ‘Microfluidics for cell separation’, *Med Biol Eng Comput*, 48, pp. 999–1014. doi: 10.1007/s11517-010-0611-4.
- Bicen, A. O. and Akyildiz, I. F. (2013) ‘Molecular transport in microfluidic channels for flow-induced molecular communication’, in *2013 IEEE International Conference on Communications Workshops, ICC 2013*, pp. 766–770. doi: 10.1109/ICCW.2013.6649336.
- Bio-Rad Laboratories Inc. (2016) *The T Cell Marker, CD3 Antigen and Antibodies*. Available at: <https://www.bio-rad-antibodies.com/minireview-cd3-antibody.html>.
- Bishara, W. *et al.* (2011) ‘Holographic pixel super-resolution in portable lensless on-chip microscopy using a fiber-optic array’, *Lab on a Chip*, 11(7), pp. 1276–1279. doi: 10.1039/c0lc00684j.
- Biswas, S. and Ghoshal, D. (2016) ‘Blood Cell Detection Using Thresholding Estimation Based Watershed Transformation with Sobel Filter in Frequency Domain’, *Procedia Computer Science*. The Author(s), 89(December), pp. 651–657. doi: 10.1016/j.procs.2016.06.029.
- Bond, M. M. and Richards-Kortum, R. R. (2015) ‘Drop-to-drop variation in the cellular components of fingerprick blood: Implications for point-of-care diagnostic development’, *American Journal of Clinical Pathology*, 144(6), pp. 885–894. doi: 10.1309/AJCP1L7DKMPCHPEH.
- Boppart, S. A. and Richards-Kortum, R. (2014) ‘Point-of-care and point-of-procedure optical imaging technologies for primary care and global health’, *Sci Transl Med*, 6(253), pp. 165–171. doi: 10.1016/j.chemosphere.2012.12.037.Reactivity.
- Breslauer, D. N. *et al.* (2009) ‘Mobile phone based clinical microscopy for global health applications’, *PLoS ONE*, 4(7), pp. 1–7. doi: 10.1371/journal.pone.0006320.
- Bruel, M. (1995) ‘Silicon on insulator material technology’, *ELECTRONICS LE77ERS*, 31(14), pp. 1201–1202.
- Bruus, H. (2006) *Theoretical Microfluidics, Department of Micro and Nanotechnology Technical University of Denmark*. doi: 10.1111/j.1574-6968.2009.01808.x.
- Buggenthin, F. *et al.* (2013) ‘An automatic method for robust and fast cell detection in bright field images from high-throughput microscopy’, *BMC Bioinformatics*. BMC Bioinformatics, 14(1), pp. 1–10. doi: 10.1186/1471-2105-14-297.
- Casutt, S. (2012) ‘Focus tunable lenses for LED lighting with variable spot sizes’, (34), pp. 50–52.
- Chen, J. *et al.* (2013) ‘A microfluidic chip for direct and rapid trapping of white blood cells from whole blood’, *Biomicrofluidics*, 7(3), pp. 1–8. doi: 10.1063/1.4808179.
- Chen, W. *et al.* (2013) ‘Surface-Micromachined Microfiltration Membranes for Efficient Isolation and Functional Immunophenotyping of Subpopulations of Immune Cells’, *Advanced Healthcare Materials*, 2(7), pp. 965–975. doi: 10.1002/adhm.201200378.
- Chen, Y. *et al.* (2014) ‘Rare cell isolation and analysis in microfluidics’, *Lab Chip*, 14(4), pp. 626–645.

doi: 10.1038/jid.2014.371.

Cheng, X., Irimia, D., Dixon, M., Ziperstein, J. C., *et al.* (2007) 'A microchip approach for practical label-free CD4+ T-cell counting of HIV-infected subjects in resource-poor settings', *Journal of Acquired Immune Deficiency Syndromes*, 45(3), pp. 257–261. doi: 10.1097/QAI.0b013e3180500303.

Cheng, X., Irimia, D., Dixon, M., Sekine, K., *et al.* (2007) 'A microfluidic device for practical label-free CD4+ T cell counting of HIVinfected subjects', *Lab on a chip*, 7, pp. 170–178. doi: 10.1038/jid.2014.371.

Cheson, B. D. *et al.* (2003) 'Revised Recommendations of the International Working Group for diagnosis, standardization of response criteria, treatment outcomes, and reporting standards for therapeutic trials in acute myeloid leukemia', *Journal of Clinical Oncology*, 21(24), pp. 4642–4649. doi: 10.1200/JCO.2003.04.036.

Chetty, R. and Gatter, K. (1994) 'CD3: Structure, function, and role of immunostaining in clinical practice', *The Journal of Pathology*, 173(4), pp. 303–307. doi: 10.1002/path.17111730404.

Chronis, N. *et al.* (2003) 'Tunable liquid-filled microlens array integrated with microfluidic network', *Optics Express*, 11(19), p. 2370. doi: 10.1364/OE.11.002370.

Chynoweth, A. G. (1960) 'Uniform silicon p-n junctions. II. Ionization rates for electrons', *Journal of Applied Physics*, 31(7), pp. 1161–1165. doi: 10.1063/1.1735795.

Chynoweth, A. G. and McKay, K. G. (1956) 'Photon emission from avalanche breakdown in silicon', *Physical Review*, 102(2), pp. 369–376. doi: 10.1103/PhysRev.102.369.

Chynoweth, A. G. and Pearson, G. L. (1958) 'Effect of dislocations on breakdown in silicon p-n junctions', *Journal of Applied Physics*, 29(7), pp. 1103–1110. doi: 10.1063/1.1723368.

Co-operative, D. E. and Oxford, E. C. (2015) 'Point-of-care tests for malaria'.

Crawford, J., Dale, D. C. and Lyman, G. H. (2004) 'Chemotherapy-Induced Neutropenia: Risks, Consequences, and New Directions for Its Management', *Cancer*, 100(2), pp. 228–237. doi: 10.1002/cncr.11882.

Daily, D. (2000) *Microlens arrays, Physics Education*. Taylor & Francis Group, LLC. doi: 10.1088/0031-9120/29/3/009.

Davies, N., McCormick, M. and Brewin, M. (1994) 'Design and analysis of an image transfer system using microlens arrays', *OPTICAL ENGINEERING*, 33(11), pp. 3624–3633.

Davis, K. A. *et al.* (1998) 'Determination of CD4 antigen density on cells: Role of antibody valency, avidity, clones, and conjugation', *Cytometry*, 33(2), pp. 197–205. doi: 10.1002/(SICI)1097-0320(19981001)33:2<197::AID-CYTO14>3.0.CO;2-P.

Davis, K., Schoenbaum, S. C. and Audet, A. M. (2005) 'A 2020 vision of patient-centered primary care', *Journal of General Internal Medicine*, 20(10), pp. 953–957. doi: 10.1111/j.1525-1497.2005.0178.x.

- Deng, Y. *et al.* (2014) ‘An Integrated Microfluidic Chip System for Single-Cell Secretion Profiling of Rare Circulating Tumor Cells’, *Scientific Reports*, 4. doi: 10.1038/srep07499.
- Dewhurst, M. *et al.* (2003) ‘Thermal dose requirement for tissue effect: experimental and clinical findings’, 4954, p. 37. doi: 10.1117/12.476637.
- Diagnostics, H. I. V, Reliability, E. T. H. E. and Results, O. F. T. (2015) ‘IMPROVING HIV-RELATED POINT-’, (December).
- Didar, T. F. *et al.* (2013) ‘Separation of rare oligodendrocyte progenitor cells from brain using a high-throughput multilayer thermoplastic-based microfluidic device’, *Biomaterials*. Elsevier Ltd, 34(22), pp. 5588–5593. doi: 10.1016/j.biomaterials.2013.04.014.
- Didar, T. F. and Tabrizian, M. (2010) ‘Adhesion based detection, sorting and enrichment of cells in microfluidic Lab-on-Chip devices’, *Lab on a Chip*, 10(22), pp. 3043–3053. doi: 10.1039/c0lc00130a.
- Diez-Silva, M. *et al.* (2010) ‘Shape and Biomechanical Characteristics of Human Red Blood Cells in Health and Disease’, *MRS Bull.*, 35(5), pp. 382–388. doi: 10.1146/annurev.neuro.31.060407.125627.Brain.
- Ding, Y. *et al.* (2008) ‘Freeform LED lens for uniform illumination’, *Optics Express*, 16(17), p. 12958. doi: 10.1364/OE.16.012958.
- Dotan, E. *et al.* (2009) ‘Circulating Tumor Cells: Evolving Evidence and Future Challenges’, *The Oncologist*, 14, pp. 1070–1082. doi: 10.1634/theoncologist.2009-0094.
- Douglass, K. M. *et al.* (2016) ‘Super-resolution imaging of multiple cells by optimized flat-field epi-illumination’, *Nature Photonics*. Nature Publishing Group, 10(11), pp. 705–708. doi: 10.1038/nphoton.2016.200.
- Dugas, V., Elaissari, A. and Chevalier, Y. (2010) ‘Surface Sensitization Techniques and Recognition Receptors Immobilization on Biosensors and Microarrays’, in *Recognition Receptors in Biosensors*. Springer Science+Business Media, LLC, pp. 1–863. doi: 10.1007/978-1-4419-0919-0.
- Duparre, J. and Reinhard, V. (2007) ‘Novel Optics / Micro-Optics for Miniature Imaging Systems’.
- Eisner, M. and Weible, K. J. (2003) ‘Miniaturized imaging systems’, 68, pp. 461–472.
- Elson, D. S. *et al.* (2002) ‘Fluorescence Lifetime Imaging with a Blue Picosecond Diode Laser’, *Optics Letters*, 27(16), pp. 1409–1411. doi: 10.1364/OL.27.001409.
- Engelbrecht, C. J., Voigt, F. and Helmchen, F. (2010) ‘Miniaturized selective plane illumination microscopy for high-contrast in vivo fluorescence imaging’, *Optics Letters*, 35(9), p. 1413. doi: 10.1364/OL.35.001413.
- Erickson, H. P. (2009) ‘Size and shape of protein molecules at the nanometer level determined by sedimentation, gel filtration, and electron microscopy’, *Biological Procedures Online*, 11(1), pp. 32–51. doi: 10.1007/s12575-009-9008-x.

- Fan, X. *et al.* (2015) 'A microfluidic chip integrated with a high-density PDMS-based microfiltration membrane for rapid isolation and detection of circulating tumor cells', *Biosensors and Bioelectronics*. Elsevier, 71, pp. 380–386. doi: 10.1016/j.bios.2015.04.080.
- Flusberg, B. A. *et al.* (2008) 'High-speed, miniaturized fluorescence microscopy in freely moving mice', *Nature Methods*, 5(11), pp. 935–938. doi: 10.1038/nmeth.1256.
- Frenette, P. S. and Atweh, G. F. (2007) 'Science in medicine Sickle cell disease : old discoveries , new concepts , and future promise', *The Journal of Clinical Investigation*, 117(4), p. 850–58 doi:10.1172/JCI30920. doi: 10.1172/JCI30920.850.
- Fulop, W. (1967) 'Calculation of Avalanche Breakdown Junctions', *Solid state electronics Pergamon Press*, 10, pp. 39–43.
- Furlani, E. P. (2007) 'Continuous Magnetophoretic Separation of Blood Cells from Plasma at the Microscale', *J. Phys. D: Appl. Phys.*, 40, pp. 1313–1319. doi: 10.1088/0022-3727/40/5/001.
- Gajtam, D. K., Khokle, W. S. and Garg, K. B. (1988) 'PHOTON EMISSION FROM REVERSE-BIASED SILICON P-N JUNCTIONS', *Solid-Slate Electronics*, 31(2), pp. 219–222.
- Gale, M. T. and Knop, K. (1983) 'The Lens', in *Proc. SPIE 0398, Industrial Applications of Laser Technology*,. doi: 10.1117/12.935397.
- Gallacher, L. *et al.* (2000) 'Isolation and characterization of human CD34(-)Lin(-) and CD34(+)Lin(-) hematopoietic stem cells using cell surface markers AC133 and CD7.', *Blood*, 95(9), pp. 2813–20. Available at: <http://www.bloodjournal.org/content/95/9/2813.abstract>.
- Gaskill, M. M., Launiere, C. a and Eddington, D. T. (2012) 'Optimization of Protein Immobilization in Microfluidic Devices for Circulating Tumor Cell Capture', *Journal of Undergraduate Research*, 1.
- Ghaznavi, F. *et al.* (2013) 'Digital Imaging in Pathology: Whole-Slide Imaging and Beyond', *Annual Review of Pathology: Mechanisms of Disease*, 8(1), pp. 331–359. doi: 10.1146/annurev-pathol-011811-120902.
- Ghosh, K. K. *et al.* (2011) 'Miniaturized integration of a fluorescence microscope', *Nature Methods*, 8(10), pp. 871–878. doi: 10.1038/nmeth.1694.
- Giuliano, K. and Grant, M. (2002) 'Blood analysis at the point of care: issues in application for use in critically ill patients', *AACN Clinical Issues*, 13(2), pp. 204–220.
- Goedhart, P. T. *et al.* (2007) 'Sidestream Dark Field (SDF) imaging: a novel stroboscopic LED ring-based imaging modality for clinical assessment of the microcirculation', *Optics Express*, 15(23), p. 15101. doi: 10.1364/OE.15.015101.
- Goetzberger, A. *et al.* (1963) 'Avalanche Effects in Silicon p - n Junctions. II. Structurally Perfect Junctions', *Journal of Applied Physics*, 34(6), pp. 1591–1600. doi: 10.1063/1.1702640.
- Gogoi, P. *et al.* (2016) 'Development of an Automated and Sensitive Microfluidic Device for

Capturing and Characterizing Circulating Tumor Cells (CTCs) from Clinical Blood Samples', *PLoS one*, 11(1), p. e0147400. doi: 10.1371/journal.pone.0147400.

Greenbaum, A. *et al.* (2012) 'Imaging without lenses: Achievements and remaining challenges of wide-field on-chip microscopy', *Nature Methods*, 9(9), pp. 889–895. doi: 10.1038/nmeth.2114.

Grimm, R. H., Neaton, J. D. and Ludwig, W. (1985) 'Prognostic importance of the white blood cell count for coronary, cancer, and all-cause mortality.', *Jama*, 254(14), pp. 1932–7. doi: 10.1001/jama.1985.03360140090031.

Gross, H. *et al.* (2005) *Handbook of Optical Systems, Image* (Rochester, N.Y.).

Gulari, M. N. *et al.* (2014) 'An optofluidic lens array microchip for high resolution stereo microscopy', *Micromachines*, 5(3), pp. 607–621. doi: 10.3390/mi5030607.

Gulari, M. N., Tripathi, A. and Chronis, N. (2012) 'Microfluidic-based oil-immersion lenses for high resolution microscopy', in *The Sixteenth International Conference on Miniaturized Systems for Chemistry and Life Sciences (μ TAS 2012)*, pp. 112–115. doi: 10.1016/j.rmcl.2015.08.002.

Guo, M. *et al.* (2018) 'Single-shot super-resolution total internal reflection fluorescence microscopy', *Nature Methods*, 15(6), pp. 425–428. doi: 10.1038/s41592-018-0004-4.

Gupta, S., Baker, A. C. and Tang, W. C. (2013) 'Microfluidic platforms for capturing circulating tumor cells', *IEEE International Conference on Nano/Molecular Medicine and Engineering, NANOMED*, pp. 1–4. doi: 10.1109/NANOMED.2013.6766305.

Hadjiiski, L. *et al.* (1996) 'Neural network correction of nonlinearities in scanning probe microscope images', *Journal of Vacuum Science & Technology B (Microelectronics and Nanometer Structures)*, 14(2), pp. 1563–1568. doi: 10.1116/1.589139.

Haider, M. A. and Guilak, F. (2000) 'Integral Model for Incompressible Linear Viscoelasticity: Application to the Micropipette Aspiration Contact Problem', *Transactions of the ASME*, 122(June 2000), pp. 236–244.

Haitz, R. H. *et al.* (1963) 'Avalanche Effects in Silicon p - n Junctions. I. Localized Photomultiplication Studies on Microplasmas', *Journal of Applied Physics*, 34(6), pp. 1581–1590. doi: 10.1063/1.1702639.

Haitz, R. H. (1967) 'Noise of a self-sustaining avalanche discharge in silicon: Low-frequency noise studies', *Journal of Applied Physics*, 38(7), pp. 2935–2946. doi: 10.1063/1.1710027.

Hallek, M. *et al.* (2008) 'Guidelines for the diagnosis and treatment of chronic lymphocytic leukemia: A report from the International Workshop on Chronic Lymphocytic Leukemia updating the National Cancer Institute-Working Group 1996 guidelines', *Blood*, 111(12), pp. 5446–5456. doi: 10.1182/blood-2007-06-093906.

Haney, K. *et al.* (2017) 'The Role of Affordable, Point-of-Care Technologies for Cancer Care in Low- and Middle-Income Countries: A Review and Commentary', *IEEE Journal of Translational*

Engineering in Health and Medicine, 5(July), pp. 1–14. doi: 10.1109/JTEHM.2017.2761764.

Hassani-Ardekani, H., Niroomand-Oscuii, H. and Khismatullin, D. (2015) ‘Computational Determination of the Detachment Time of the Leukocyte Under Different Kinetic Dissociation Rate Parameters’, *Journal of Biological Systems*, 23(03), pp. 457–469. doi: 10.1142/S0218339015500230.

Helmlı, F. S. and Scherer, S. (2001) ‘Adaptive shape from focus with an error estimation in light microscopy’, *ISPA 2001. Proceedings of the 2nd International Symposium on Image and Signal Processing and Analysis. In conjunction with 23rd International Conference on Information Technology Interfaces (IEEE Cat.*, pp. 188–193. doi: 10.1109/ISPA.2001.938626.

Heng, X. *et al.* (2007) ‘An optical tweezer actuated, nanoaperture-grid based Optofluidic Microscope implementation method’, *Optics Express*, 15(25), pp. 16367–16375. doi: 10.1364/OE.15.016367.

El Hentati, F. Z. *et al.* (2010) ‘Variability of CD3 membrane expression and T cell activation capacity’, *Cytometry Part B - Clinical Cytometry*, 78(2), pp. 105–114. doi: 10.1002/cyto.b.20496.

Hermanson, G. T. (2008) *Bioconjugate techniques*. 2nd edn. Pierce Biotechnology, Thermo Fisher Scientific, Rockford, Illinois, USA.

Hosokawa, M. *et al.* (2010) ‘Size-selective microcavity array for rapid and efficient detection of circulating tumor cells’, *Analytical Chemistry*, 82(15), pp. 6629–6635. doi: 10.1021/ac101222x.

Hou, J. M. *et al.* (2011) ‘Circulating tumor cells as a window on metastasis biology in lung cancer’, *American Journal of Pathology*. Elsevier Inc., 178(3), pp. 989–996. doi: 10.1016/j.ajpath.2010.12.003.

Huang, G. *et al.* (2013) ‘Digital imaging scanning system and biomedical applications for biochips.’, *Journal of biomedical optics*, 13(3), p. 034006. doi: 10.1117/1.2939402.

Hussain, K. *et al.* (2018) ‘A histogram specification technique for dark image enhancement using a local transformation method’, *IP SJ Transactions on Computer Vision and Applications*. IPSJ Transactions on Computer Vision and Applications, 10(1). doi: 10.1186/s41074-018-0040-0.

Hvichia, G. E. *et al.* (2016) ‘A novel microfluidic platform for size and deformability based separation and the subsequent molecular characterization of viable circulating tumor cells’, *International Journal of Cancer*, 138(12), pp. 2894–2904. doi: 10.1002/ijc.30007.

ICH Harmonised Tripartite Guideline (2005) ‘VALIDATION OF ANALYTICAL PROCEDURES: TEXT AND METHODOLOGY Q2(R1)’, 1994(November).

Im, H. *et al.* (2018) ‘Design and clinical validation of a point-of-care device for the diagnosis of lymphoma via contrastenhanced microholography and machine learning’, *Nature Biomedical Engineering*. Springer US, 2, pp. 666–674. doi: 10.1038/s41551-018-0265-3.

Ishmukhametov, R. R. *et al.* (2016) ‘A Simple low-cost device enables four epi-illumination techniques on standard light microscopes’, *Scientific Reports*. Nature Publishing Group, 6(1), p. 20729. doi: 10.1038/srep20729.

- Isikman, S. O. *et al.* (2010) ‘High-throughput blood analysis on a chip using lensless digital holography’, *14th International Conference on Miniaturized Systems for Chemistry and Life Sciences 2010, MicroTAS 2010*, 2(11), pp. 1424–1426. doi: 10.1364/OL.30.000468.
- Isikman, S. O. *et al.* (2011) ‘Field-portable lensfree tomographic microscope’, *Lab on a Chip*, 11(13), pp. 2222–2230. doi: 10.1039/c1lc20127a.
- Iwamoto, T. (2013) ‘Clinical Application of Drug Delivery Systems in Cancer Chemotherapy: Review of the Efficacy and Side Effects of Approved Drugs’, *Biological and Pharmaceutical Bulletin*, 36(5), pp. 715–718. doi: 10.1248/bpb.b12-01102.
- Jackson, E. L. and Lu, H. (2014) ‘Advances in microfluidic cell separation and manipulation’, *Curr Opin Chem Eng.*, 2(4), pp. 398–404. doi: 10.1016/j.coche.2013.10.001.Advances.
- Jain, A. and Cheng, K. (2017) ‘The Principles and Applications of Avidin-Based Nanoparticles in Drug Delivery and Diagnosis Akshay’, *Control Release*, 245, pp. 27–40. doi: 10.2144/000114329.Functional.
- Jiang, G. *et al.* (2000) ‘Red diode laser induced fluorescence detection with a confocal microscope on a microchip for capillary electrophoresis’, *Biosensors and Bioelectronics*, 14(10–11), pp. 861–869. doi: 10.1016/S0956-5663(99)00056-1.
- Johar, S., Manjula, G. R. and Namita, M. V (2017) ‘Image Stitching Using Correlation Method’, *Imperial Journal of Interdisciplinary Research (IJIR)*, 3(7), pp. 282–290.
- Kallings, L. O. (2008) ‘The first postmodern pandemic: 25 Years of HIV/AIDS’, *Journal of Internal Medicine*, 263(3), pp. 218–243. doi: 10.1111/j.1365-2796.2007.01910.x.
- Kamholz, A. E. and Yager, P. (2001) ‘Theoretical analysis of molecular diffusion in pressure-driven laminar flow in microfluidic channels’, *Biophysical Journal*. Elsevier, 80(1), pp. 155–160. doi: 10.1016/S0006-3495(01)76003-1.
- Khalili, A. A. and Ahmad, M. R. (2015) ‘A Review of cell adhesion studies for biomedical and biological applications’, *International Journal of Molecular Sciences*, 16(8), pp. 18149–18184. doi: 10.3390/ijms160818149.
- Khan, A., Balakrishnan, K. and Katona, T. (2008) ‘Ultraviolet light-emitting diodes based on group three nitrides.pdf’, *Nature Photonics*, 2, pp. 77–84.
- Kim, S. and Demetri, G. (1996) ‘Chemotherapy and neutropenia’, *HEMATOLOGY /ONCOLOGY CLINICS OF NORTH AMERICA*, 10(2), pp. 377–395.
- Kittler, M. *et al.* (2005) ‘Silicon-based light emission after ion implantation’, *Optical Materials*, 27(5), pp. 967–972. doi: 10.1016/j.optmat.2004.08.045.
- Korompili, G. *et al.* (2018) ‘A portable, optical scanning microsystem for large field of view, high resolution imaging of biological specimens’, *Sensors and Actuators, A: Physical*, 279. doi: 10.1016/j.sna.2018.06.034.

- Kosack, C. S., Page, A.-L. and Klatser, P. R. (2017) 'A guide to aid the selection of diagnostic tests', *Bulletin of the World Health Organization*, 95(9), pp. 639–645. doi: 10.2471/BLT.16.187468.
- Krebs, M. G. *et al.* (2010) 'Circulating tumour cells: Their utility in cancer management and predicting outcomes', *Therapeutic Advances in Medical Oncology*, 2(6), pp. 351–365. doi: 10.1177/1758834010378414.
- Kuo, S. C., Hammer, D. A. and Lauffenburger, D. A. (1997) 'Simulation of detachment of specifically bound particles from surfaces by shear flow', *Biophysical Journal*, 73(1), pp. 517–531. doi: 10.1016/S0006-3495(97)78090-1.
- Kurkuri, M. D. *et al.* (2011) 'Plasma functionalized PDMS microfluidic chips: Towards point-of-care capture of circulating tumor cells', *Journal of Materials Chemistry*, 21(24), pp. 8841–8848. doi: 10.1039/c1jm10317b.
- Kwon, K. W. *et al.* (2007) 'Label-free, microfluidic separation of human breast carcinoma and epithelial cells by adhesion difference', *TRANSDUCERS and EUROSENSORS '07 - 4th International Conference on Solid-State Sensors, Actuators and Microsystems*, pp. 699–702. doi: 10.1109/SENSOR.2007.4300226.
- L.Frost & M. Reich (2008) 'How do good health technologies get to poor people in poor countries?'
- Lakshminarayanan, V. and Fleck, A. (2011) 'Zernike polynomials: A guide', *Journal of Modern Optics*, 58(7), pp. 545–561. doi: 10.1080/09500340.2011.554896.
- Larsson, A., Greig-Pylypczuk, R. and Huisman, A. (2015) 'The state of point-of-care testing: A european perspective', *Upsala Journal of Medical Sciences*. Informa Healthcare, 120(1), pp. 1–10. doi: 10.3109/03009734.2015.1006347.
- Laurell, T., Petersson, F. and Nilsson, A. (2007) 'Chip integrated strategies for acoustic separation and manipulation of cells and particles', *Chemical Society Reviews*, 36(3), pp. 492–506. doi: 10.1039/b601326k.
- Le, T. *et al.* (2013) 'Enhanced CD4+ T-Cell Recovery with Earlier HIV-1 Antiretroviral Therapy', *New England Journal of Medicine*, 368(3), pp. 218–230. doi: 10.1056/NEJMoa1110187.
- Lee, J. *et al.* (2017) 'Analysis and Reduction of Crosstalk in the Liquid Lenticular Lens Array Analysis and Reduction of Crosstalk in the Liquid Lenticular Lens Array', 9(3). doi: 10.1109/JPHOT.2017.2695645.
- Lee, M., Yaglidere, O. and Ozcan, A. (2011) 'Field-portable reflection and transmission microscopy based on lensless holography', *Biomedical Optics Express*, 2(9), p. 2721. doi: 10.1364/BOE.2.002721.
- Lee, S. A. *et al.* (2014) 'Imaging and identification of waterborne parasites using a chip-scale microscope', *PLoS ONE*, 9(2), pp. 4–8. doi: 10.1371/journal.pone.0089712.
- Lee, S. A. and Yang, C. (2014) 'A smartphone-based chip-scale microscope using ambient illumination', *Lab on a Chip*, 14(16), pp. 3056–3063. doi: 10.1039/c4lc00523f.

Leong, A. S.-Y., Cooper, K. and Leong, F. J. W.-M. (1998) *Manual of Diagnostic Antibodies for Immunohistology, Journal of Experimental Psychology: General*. Greenwich Medical Media Ltd.

Lerach, L. and Albrecht, H. (1975) 'Analytical solution for the avalanche breakdown voltage of p+n junctions and schottky diodes. Anomalous behaviour of low energy bandgap high-mobility semiconductors', *Physica Status Solidi (a)*, 30(2), pp. 625–636. doi: 10.1002/pssa.2210300224.

Leslie, T. *et al.* (2012) 'Overdiagnosis and mistreatment of malaria among febrile patients at primary healthcare level in Afghanistan: Observational study', *BMJ (Online)*, 345(7867), pp. 5–9. doi: 10.1136/bmj.e4389.

Levoy, M. *et al.* (2006) 'Light field microscopy', *ACM SIGGRAPH 2006 Papers on - SIGGRAPH '06*, p. 924. doi: 10.1145/1179352.1141976.

Levoy, M., Zhang, Z. and McDowall, I. (2009) 'Recording and controlling the 4D light field in a microscope', *Journal of Microscopy*, 235(2), pp. 144–162.

Li, X. *et al.* (2014) 'Continuous-flow microfluidic blood cell sorting for unprocessed whole blood using surface-micromachined microfiltration membranes', *Lab Chip*, 14(14), pp. 2565–2575. doi: 10.1080/10937404.2015.1051611.INHALATION.

Li, Y. and Xu, Q. (2011) 'A Totally Decoupled Piezo-Driven XYZ Flexure Parallel Micropositioning Stage for', *IEEE TRANSACTIONS ON AUTOMATION SCIENCE AND ENGINEERING*, 8(2), pp. 265–279.

Lim, J. *et al.* (2013) 'Micro-optical lens array for fluorescence detection in droplet-based microfluidics', *Lab on a Chip*, 13(8), pp. 1472–1475. doi: 10.1039/c3lc41329b.

Lim, L. S. *et al.* (2012) 'Microsieve lab-chip device for rapid enumeration and fluorescence in situ hybridization of circulating tumor cells', *Lab on a Chip*, 12(21), pp. 4388–4396. doi: 10.1039/c2lc20750h.

Livnah, O. *et al.* (1993) 'Three-dimensional structures of avidin and the avidin-biotin complex.', *Proceedings of the National Academy of Sciences*, 90(11), pp. 5076–5080. doi: 10.1073/pnas.90.11.5076.

Lochhead, M. J. *et al.* (2010) 'Low-cost fluorescence microscopy for point-of-care cell imaging', 7572, p. 75720B. doi: 10.1117/12.842099.

Lohmann, A. W. (1989) 'Scaling laws for lens systems', *Applied Optics*, 28(23), pp. 4996–4998.

Ma, B. *et al.* (2007) 'Use of Autostitch for automatic stitching of microscope images', *Micron*, 38(5), pp. 492–499. doi: 10.1016/j.micron.2006.07.027.

Maamari, R. N. *et al.* (2014) 'A mobile phone-based retinal camera for portable wide field imaging', *British Journal of Ophthalmology*, 98(4), pp. 438–441. doi: 10.1136/bjophthalmol-2013-303797.

Maini, R. and Aggarwal, D. H. (2009) 'Study and comparison of various image edge detection techniques', *International Journal of Image Processing*, 3(1), pp. 1–11. doi:

<http://www.doaj.org/doi?func=openurl&genre=article&issn=19852304&date=2009&volume=3&issue=1&spage=1>.

Manroe, B. L. *et al.* (1979) 'The neonatal blood count in health and disease.', *The Journal of Pediatrics*, 95(1), pp. 89–98. doi: 10.1016/S0022-3476(79)80096-7.

Marttila, A. T. *et al.* (2000) 'Recombinant NeutraLite Avidin: A non-glycosylated, acidic mutant of chicken avidin that exhibits high affinity for biotin and low non-specific binding properties', *FEBS Letters*, 467(1), pp. 31–36. doi: 10.1016/S0014-5793(00)01119-4.

McCall, B. *et al.* (2011) 'Toward a low-cost compact array microscopy platform for detection of tuberculosis', *Tuberculosis*. Elsevier Ltd, 91(SUPPL. 1), pp. S54–S60. doi: 10.1016/j.tube.2011.10.011.

Miller, A. R. *et al.* (2010) 'Portable, battery-operated, low-cost, bright field and fluorescence microscope', *PLoS ONE*, 5(8), pp. 8–10. doi: 10.1371/journal.pone.0011890.

Misiakos, I. *et al.* (1998) 'Monolithic integration of light emitting diodes, detectors and optical fibers on a silicon wafer: a CMOS compatible optical sensor', *International Electron Devices Meeting 1998. Technical Digest (Cat. No.98CH36217)*, pp. 25–28. doi: 10.1074/jbc.M000664200.

Misiakos, K. *et al.* (2001) 'Monolithic silicon optoelectronic biochips', *Technical Digest-International Electron Devices Meeting*, pp. 359–362. doi: 10.1109/IEDM.2001.979511.

Mitchell, M. J., Castellanos, C. A. and King, M. R. (2012) 'This article has been accepted for publication and undergone full peer review but has not been through the copyediting, typesetting, pagination and proofreading process which may lead to differences between this version and the Version of Record. Please', *Environmental Microbiology*, (86), pp. 1–43. doi: 10.1002/art.

Modell, B. and Darlison, M. (2008) 'Global epidemiology of haemoglobin disorders and derived service indicators', *Bulletin of the World Health Organization*, 86(6), pp. 480–487. doi: 10.2471/BLT.06.036673.

Moll, J. L. and Van Overstraeten, R. (1963) 'Charge Multiplication in GaP p-n Junctions', *Solid state electronics Pergamon Press*, 6, pp. 147–157. doi: 10.1063/1.1728804.

Monteiro, T. S. *et al.* (2015) 'Dynamic wet etching of silicon through isopropanol alcohol evaporation', *Micromachines*, 6(10), pp. 1534–1545. doi: 10.3390/mi6101437.

Moody, A. (2002) 'Rapid diagnostic tests for malaria parasites', *CLINICAL MICROBIOLOGY REVIEWS*, 5, pp. 66–78. doi: 10.1128/CMR.15.1.66–78.2002.

Moon, S. and Keles, H. (2009) 'Integrating microfluidics and lensless imaging for point-of-care testing', *Biosensors and ...*, 24, pp. 3208–3214. doi: 10.1016/j.bios.2009.03.037.

Mudanyali, O., Bishara, W. and Ozcan, A. (2011) 'Lensfree super-resolution holographic microscopy using wetting films on a chip', *Optics Express*, 19(18), p. 17378. doi: 10.1364/OE.19.017378.

Mukherjee, D. P., Ray, N. and Acton, S. T. (2004) 'Level set analysis for leukocyte detection and

- tracking', *IEEE Transactions on Image Processing*, 13(4), pp. 562–572. doi: 10.1109/TIP.2003.819858.
- Murthy, S. K. *et al.* (2004) 'Effect of flow and surface conditions on human lymphocyte isolation using microfluidic chambers', *Langmuir*, 20(26), pp. 11649–11655. doi: 10.1021/la048047b.
- Nagrath, S. *et al.* (2007) 'Isolation of rare circulating tumour cells in cancer patients by microchip technology', *Nature*, 450(20), pp. 1235–1241. doi: 10.1038/nature06385.
- Nakamura, S., Pearton, S. and Fasol, G. (1999) *The Blue laser Diode The Complete Story, Cold-Adapted Organisms: Ecology, Physiology, Enzymology and Molecular Biology*. Springer-Verlag Berlin Heidelberg 1997, 2000. doi: 10.1007/978-3-662-06431-3.
- Navruz, I. *et al.* (2013) 'Smart-phone based computational microscopy using multi-frame contact imaging on a fiber-optic array', *Lab on a Chip*, 13(20), pp. 4015–4023. doi: 10.1039/c3lc50589h.
- Nedzved, a., Ablameyko, S. and Pitas, I. (2000) 'Morphological segmentation of histology cell images', *Proceedings 15th International Conference on Pattern Recognition. ICPR-2000*, 1, pp. 1–5. doi: 10.1109/ICPR.2000.905385.
- Newman, R. (1955) 'Visible light from a silicon p-n junction', *Physical Review*, 100(2), pp. 700–703. doi: 10.1103/PhysRev.100.700.
- Nielsen, F. and Yamashita, N. (1995) 'CLAIR VOYANCE : A Fast And Robust Precision Mosaicing System for Gigapixel Images'.
- O'Brien, W. A. *et al.* (1997) 'Changes in plasma HIV RNA levels and CD4+ lymphocyte counts predict both response to antiretroviral therapy and therapeutic failure', *Annals of Internal Medicine*, 126(12), pp. 939–945. doi: 10.7326/0003-4819-126-12-199706150-00002.
- Oh, K. W. *et al.* (2012) 'Design of pressure-driven microfluidic networks using electric circuit analogy', *Lab on a Chip*, 12, pp. 515–545. doi: 10.1039/c2lc20799k.
- Okoye, A. and Picker, L. (2013) 'CD4+T cell depletion in HIV infection: mechanisms of immunological failure', *Immunol Rev.*, 254(1), pp. 54–64. doi: 10.1111/imr.12066.CD4.
- Orth, A. *et al.* (2018) 'A dual-mode mobile phone microscope using the onboard camera flash and ambient light', *Scientific Reports*. Springer US, 8(1), pp. 1–8. doi: 10.1038/s41598-018-21543-2.
- Orth, A. and Crozier, K. (2012) 'Microscopy with microlens arrays: high throughput, high resolution and light-field imaging', *Optics Express*, 20(12), p. 13522. doi: 10.1364/OE.20.013522.
- Orth, A. and Crozier, K. (2013) 'Gigapixel fluorescence microscopy with a water immersion microlens array', *Optics Express*, 21(2), p. 2361. doi: 10.1364/OE.21.002361.
- Orth, A. and Crozier, K. B. (2014) 'High throughput multichannel fluorescence microscopy with microlens arrays', *Optics Express*, 22(15), p. 18101. doi: 10.1364/OE.22.018101.
- Ozcan, A. and Demirci, U. (2007) 'Ultra wide-field lens-free monitoring of cells on-chip', *Lab on a Chip*, 8(1), pp. 98–106. doi: 10.1039/b713695a.

- Pan, L. *et al.* (2018) ‘Super-Resolution Microscopy Reveals the Native Ultrastructure of the Erythrocyte Cytoskeleton’, *Cell Reports*, 22(5), pp. 1151–1158. doi: 10.1016/j.celrep.2017.12.107.
- Pankov, J. I. (1971) *Optical Processes in Semiconductors*. Englewood Cliffs, New Jersey: Prentice-Hall, Inc.
- Pedrotti, F. L. and Pedrotti, L. S. (1993) ‘Matrix method in paraxial optics’, in *Introduction to optics, 2nd edition*, pp. 62–86.
- Peli, E. (1990) ‘Contrast in complex images’, *Journal of the Optical Society of America A*, 7(10), p. 2032. doi: 10.1364/JOSAA.7.002032.
- Piel, F. B. *et al.* (2013) ‘Global epidemiology of Sickle haemoglobin in neonates: A contemporary geostatistical model-based map and population estimates’, *The Lancet*. Elsevier Ltd, 381(9861), pp. 142–151. doi: 10.1016/S0140-6736(12)61229-X.
- Pirnstill, C. W. and Coté, G. L. (2015) ‘Malaria Diagnosis Using a Mobile Phone Polarized Microscope’, *Scientific Reports*. Nature Publishing Group, 5, pp. 1–13. doi: 10.1038/srep13368.
- Pollak, J. J., Hourri-Yafin, A. and Salpeter, S. J. (2017) ‘Computer Vision Malaria Diagnostic Systems—Progress and Prospects’, *Frontiers in Public Health*, 5(August), pp. 1–5. doi: 10.3389/fpubh.2017.00219.
- Polysciences Inc. (2008) *Technical Data Sheet: The Benefits of Neutraavidin over Streptavidin and Avidin*, Polysciences, Inc.
- Ponampalam, R., Fook Chong, S. M. C. and Tan, S. C. (2012) ‘Comparison of Full Blood Count Parameters Using Capillary and Venous Samples in Patients Presenting to the Emergency Department’, *ISRN Emergency Medicine*, 2012, pp. 1–6. doi: 10.5402/2012/508649.
- Popovic, Z. D., Sprague, R. A. and Neville Connell, G. A. (1988) ‘Technique for monolithic fabrication of microlens arrays’, *Applied Optics*, 27(7), p. 1281. doi: 10.1364/AO.27.001281.
- Powars, D. R. *et al.* (2005) ‘Outcome of sickle cell anemia: A 4-decade observational study of 1056 patients’, *Medicine*, 84(6), pp. 363–376. doi: 10.1097/01.md.0000189089.45003.52.
- Prinyakupt, J. and Pluempitiwiriawej, C. (2015) ‘Segmentation of white blood cells and comparison of cell morphology by linear and naïve Bayes classifiers’, *BioMedical Engineering Online*. BioMed Central, 14, pp. 1–19. doi: 10.1186/s12938-015-0037-1.
- Pust, P., Schmidt, P. J. and Schnick, W. (2015) ‘A revolution in lighting’, *Nature Materials*. Nature Publishing Group, 14(5), pp. 454–458. doi: 10.1038/nmat4270.
- Rankov, V. *et al.* (2005) ‘An Algorithm for image stitching and blending’, in *Three-Dimensional and Multidimensional Microscopy: Image Acquisition and Processing XII*, pp. 190–199. doi: 10.1117/12.590536.
- Ranucci, M. *et al.* (2014) ‘Blood viscosity during coagulation at different shear rates’, *Physiological Reports*, 2(7), pp. 1–7. doi: 10.14814/phy2.12065.

- Rossi, A. F. and Khan, D. (2004) 'Point of care testing: Improving pediatric outcomes', *Clinical Biochemistry*, 37(6 SPEC. ISS.), pp. 456–461. doi: 10.1016/j.clinbiochem.2004.04.004.
- Ruberto, C. Di *et al.* (2000) 'Segmentation of Blood Images Using Morphological Operators Gradient', *IEEE*, pp. 397–400.
- Di Ruberto, C. *et al.* (2002) 'Analysis of infected blood cell images using morphological operators', *Image and Vision Computing*, 20(2), pp. 133–146. doi: 10.1016/S0262-8856(01)00092-0.
- S. Satyanarayana, K. Sagili, S. S. Chadha, M. P. (2014) 'Use of rapid point-of-care tests by primary health care providers in India: findings from a community-based survey', *Public Health Action*, 1(4), pp. 249–251. doi: 10.5588/pha.14.0061.
- Santos, a and Solorzano, C. O. De (1997) 'Evaluation of autofocus functions in molecular cytogenetic analysis', *Journal of microscopy*, 188(Pt 3), pp. 264–72. doi: 10.1046/j.1365-2818.1997.2630819.x.
- Sanz, M. *et al.* (2017) 'Compact, cost-effective and field-portable microscope prototype based on MISHSELF microscopy', *Scientific Reports*. Nature Publishing Group, 7(February), pp. 1–12. doi: 10.1038/srep43291.
- Sarioglu, A. F. *et al.* (2015) 'A microfluidic device for label-free, physical capture of circulating tumor cell clusters', *Nature Methods*. Nature Publishing Group, 12(7), pp. 685–691. doi: 10.1038/nmeth.3404.
- Saucedo-Zeni, N. *et al.* (2012) 'A novel method for the in vivo isolation of circulating tumor cells from peripheral blood of cancer patients using a functionalized and structured medical wire', *International Journal of Oncology*, 41, pp. 1241–1250. doi: 10.3892/ijo.2012.1557.
- Schaefer, S. S., Boehm, S. A. S. A. and Chau, K. J. K. J. (2012) 'Automated, portable, low-cost bright-field and fluorescence microscope with autofocus and autoscanning capabilities.', *Applied Optics*, 51(14), pp. 2581–2588. doi: 10.1364/AO.51.002581.
- Schonbrun, E., Steinvurzel, P. E. and Crozier, K. B. (2011) 'A microfluidic fluorescence measurement system using an astigmatic diffractive microlens array', *Optics express*, 19(2), pp. 1385–94. doi: 10.1364/OE.19.001385.
- Shabtai, M. *et al.* (1993) 'Analysis of peripheral blood lymphocyte cell surface density of functional and activation associated markers in young and old hemodialysis patients', *Journal of Urology*, 150(5 I), pp. 1369–1374. doi: 10.1016/S0022-5347(17)35782-8.
- Siegel, R., Miller, K. D. and Ahmedin, J. (2017) 'Cancer Statistics', *Ca Cancer Journal*, 67(1), pp. 7–30. doi: 10.3322/caac.21387.
- Siiman, O. and Burshteyn, A. (2000) 'Cell surface receptor-antibody association constants and enumeration of receptor sites for monoclonal antibodies', *Cytometry*, 40(4), pp. 316–326. doi: 10.1002/1097-0320(20000801)40:4<316::AID-CYTO7>3.0.CO;2-C.

- Simone, G. *et al.* (2012) ‘Cell rolling and adhesion on surfaces in shear flow. A model for an antibody-based microfluidic screening system’, *Microelectronic Engineering*. Elsevier B.V., 98, pp. 668–671. doi: 10.1016/j.mee.2012.07.008.
- Sin, A. *et al.* (2005) ‘Enrichment using antibody-coated microfluidic chambers in shear flow: Model mixtures of human lymphocytes’, *Biotechnology and Bioengineering*, 91(7), pp. 816–826. doi: 10.1002/bit.20556.
- Sinzinger, S. (2003) *Microoptics*. WILEY-VCH GmbH & Co. KGaA, Weinheim.
- Skandarajah, A. *et al.* (2014) ‘Quantitative imaging with a mobile phone microscope’, *PLoS ONE*, 9(5). doi: 10.1371/journal.pone.0096906.
- Society, A. (2016) ‘State of Sickle Cell Disease’.
- Sousa-Figueiredo, J. *et al.* (2010) ‘Investigating portable fluorescent microscopy (CyScope(R)) as an alternative rapid diagnostic test for malaria in children and women of child-bearing age’, *Malaria Journal*, 9(1), p. 245. Available at: <http://www.malariajournal.com/content/9/1/245>.
- Squires, T. M. and Quake, S. R. (2005) ‘Microfluidics: Fluid physics at the nanoliter scale.pdf’, *REVIEWS OF MODERN PHYSICS*, 77(July), pp. 977–1026.
- Su, T. W. *et al.* (2010) ‘Compact and light-weight automated semen analysis platform using lensfree on-chip microscopy’, *Analytical Chemistry*, 82(19), pp. 8307–8312. doi: 10.1021/ac101845q.
- Sun, Y., Duthaler, S. and Nelson, B. J. (2004) ‘Autofocusing in computer microscopy: Selecting the optimal focus algorithm’, *Microscopy Research and Technique*, 65(3), pp. 139–149. doi: 10.1002/jemt.20118.
- Takaishi, S. *et al.* (2009) ‘Identification of gastric cancer stem cells using the cell surface marker CD44’, *Stem Cells*, 27(5), pp. 1006–1020. doi: 10.1002/stem.30.
- Tan, S. T. *et al.* (2012) ‘Advances in the LED materials and architectures for energy-saving solid-state lighting toward lighting revolution’, *IEEE Photonics Journal*, 4(2), pp. 613–619. doi: 10.1109/JPHOT.2012.2191276.
- Tang, Y. *et al.* (2014) ‘Microfluidic device with integrated microfilter of conical-shaped holes for high efficiency and high purity capture of circulating tumor cells’, *Scientific Reports*, 4, pp. 1–7. doi: 10.1038/srep06052.
- Tangpukdee, N. *et al.* (2009) ‘Malaria diagnosis: A brief review’, *Korean Journal of Parasitology*, 47(2), pp. 93–102. doi: 10.3347/kjp.2009.47.2.93.
- Tanida, J. *et al.* (2001) ‘Thin observation module by bound optics (TOMBO): concept and experimental verification’, *Applied Optics*, 40(11), p. 1806. doi: 10.1364/AO.40.001806.
- The World Bank (2017) *Tracking universal health coverage: 2017 global monitoring report*. Available at: <http://documents.worldbank.org/curated/en/640121513095868125/Tracking-universal-health->

coverage-2017-global-monitoring-report.

Therapy, S. A. and Infection, P. H. I. V (2013) ‘Short-Course Antiretroviral Therapy in Primary HIV Infection’, *New England Journal of Medicine*, 368(3), pp. 207–217. doi: 10.1056/NEJMoa1110039.

Thermo Fisher Scientific (2006) *Crosslinking Reagents Technical handbook*.

Thermo Fisher Scientific (2018) *Human CD45 Biotinylated Antibody*.

Thiele, S. *et al.* (2016) ‘Design, simulation and 3D printing of complex micro-optics for imaging’, *International Conference on Optical MEMS and Nanophotonics*, 2016–Sept(c), pp. 30–31. doi: 10.1109/OMN.2016.7565887.

Thiele, S. *et al.* (2017) ‘3D-printed eagle eye: Compound microlens system for foveated imaging’, *Science Advances*, 3(2), pp. 1–6. doi: 10.1126/sciadv.1602655.

Torney, D. C., Saxman, K. and Hammer, D. (2015) ‘The reaction-limited kinetics of membrane-to-surface adhesion and detachment’, *Proceedings of the Royal Society of London. Series B, Biological Sciences*, 234(1274), pp. 55–83.

Tran, P. T. and Chang, F. (2001) ‘Transmitted light fluorescent microscopy revisited’, *Biological Bulletin*, 201, pp. 235–236.

Tripathi, A. and Chronis, N. (2011) ‘A doublet microlens array for imaging micron-sized objects’, *J Micromech Microeng.*, 21(10). doi: 10.1088/0960-1317/21/10/105024.

Tsai, J. C., Chen, M. F. and Yang, H. (2008) ‘Design and fabrication of high numerical aperture and low aberration bi-convex micro lens array’, *DTIP of MEMS and MOEMS - Symposium on Design, Test, Integration and Packaging of MEMS/MOEMS*, (April), pp. 174–176. doi: 10.1109/DTIP.2008.4752978.

U.S. Food and Drug Administration (2002) *General Principles of Software Validation; Final Guidance for Industry and FDA Staff*.

UNAIDS (2018) *2017 Global Hiv Statistics*.

Usdin, M., Guillermin, M. and Calmy, A. (2010) ‘Patient Needs and Point-of-Care Requirements for HIV Load Testing in Resource-Limited Settings’, *The Journal of Infectious Diseases*, 201(s1), pp. S73–S77. doi: 10.1086/650384.

Vaidya, N. and Solgaard, O. (2018) ‘3D printed optics with nanometer scale surface roughness’, *Microsystems & Nanoengineering*. Springer US, 4(1), p. 18. doi: 10.1038/s41378-018-0015-4.

Vardiman, J. W. *et al.* (2009) ‘The 2008 revision of the World Health Organization (WHO) classification of myeloid neoplasms and acute leukemia: Rationale and important changes’, *Blood*, 114(5), pp. 937–951. doi: 10.1182/blood-2009-03-209262.

Varjo, S., Hannuksela, J. and Silven, O. (2012) ‘Direct Imaging With Printed Microlens Arrays’, *2012 21st International Conference on Pattern Recognition (Icpr 2012)*, (March 2015), pp. 1355–1358. Available

at:

http://ieeexplore.ieee.org/ielx5/6425799/6460043/06460391.pdf?tp=&arnumber=6460391&isnumber=6460043%5Cnhttp://ieeexplore.ieee.org/xpls/abs_all.jsp?arnumber=6460391&tag=1.

Vincent, L. (1993) 'Morphological Grayscale Reconstruction in Image Analysis: Applications and Efficient Algorithms', *IEEE Transactions on Image Processing*, 2(2), pp. 176–201. doi: 10.1109/83.217222.

Virgini, V. *et al.* (2015) 'Check-up examination: Recommendations in adults', *Swiss Medical Weekly*, 145(January), pp. 1–11. doi: 10.4414/smw.2015.14075.

Voldman, J. (2006) 'Electrical Forces for Microscale Cell Manipulation', *Annual Review of Biomedical Engineering*, 8(1), pp. 425–454. doi: 10.1146/annurev.bioeng.8.061505.095739.

Walzik, M. P. *et al.* (2014) 'A portable low-cost long-term live-cell imaging platform for biomedical research and education', *Biosensors and Bioelectronics*. Elsevier, 64, pp. 639–649. doi: 10.1016/j.bios.2014.09.061.

Wang, J. *et al.* (2011) 'Selection of phage-displayed peptides on live adherent cells in microfluidic channels', *Proceedings of the National Academy of Sciences*, 108(17), pp. 6909–6914. doi: 10.1073/pnas.1014753108.

Wang, M. *et al.* (2014) 'Characterization of Two Human CD4+ Lymphocyte Preparations for Quantitative Flow Cytometry', *Clinical Proteomics*, 11(1), p. 43. doi: 10.1186/1559-0275-11-43.

Watkins, N. N. *et al.* (2013) 'Microfluidic CD4+ and CD8+ T lymphocyte counters for point-of-care HIV diagnostics using whole blood', *Science Translational Medicine*, 5(214). doi: 10.1126/scitranslmed.3006870.

Weinstein, R. S. *et al.* (2004) 'An array microscope for ultrarapid virtual slide processing and telepathology. Design, fabrication, and validation study', *Human Pathology*, 35(11), pp. 1303–1314. doi: 10.1016/j.humpath.2004.09.002.

Weinstein, R. S. *et al.* (2009) 'Overview of telepathology, virtual microscopy, and whole slide imaging: prospects for the future', *Human Pathology*. Elsevier Inc., 40(8), pp. 1057–1069. doi: 10.1016/j.humpath.2009.04.006.

Wheless, L. L. *et al.* (1994) 'Classification of red blood cells as normal, sickle, or other abnormal, using a single image analysis feature.', *Cytometry*, 17(2), pp. 159–166. doi: 10.1002/cyto.990170208.

WHO (2012) 'Malaria Rapid Diagnostic Test Performance', 4.

WHO (2015a) 'Global technical strategy for malaria 2016-2030', *World Health Organization*, pp. 1–35. doi: ISBN: 978 92 4 156499 1.

WHO (2015b) *GUIDELINES: GUIDELINE ON WHEN TO START ANTIRETROVIRAL THERAPY AND ON PRE-EXPOSURE PROPHYLAXIS FOR HIV*.

WHO (2016) *GLOBAL HEALTH SECTOR STRATEGY ON HIV 2016–2021 TOWARDS ENDING AIDS*.

WHO (2018) *Cancer key facts*. Available at: <http://www.who.int/news-room/factsheets/detail/cancer>.

WHO Global Malaria Programme (2017) *World Malaria Report 2017*.

Willmott, C. (2010) 'Point-of-care testing', *Surgery*, 28(4), pp. 159–160. doi: 10.1016/j.mpsur.2010.01.019.

Wu, G. and Zaman, M. H. (2012) 'Low-cost tools for diagnosing and monitoring HIV infection in low-resource settings', *Bulletin of the World Health Organization*, 90(12), pp. 914–920. doi: 10.2471/BLT.12.102780.

Wu, M., Whitesides, G. M. and Quality, B. (1997) 'Design, fabrication and testing of microlens arrays for sensors and microsystems', *Pure and Applied Optics: Journal of the European Optical Society*, 6, p. 617.

Wu, T.-H. *et al.* (2012) 'Pulsed laser triggered high speed microfluidic fluorescence activated cell sorter', *Lab Chip*, 12(7), pp. 1378–1383. doi: 10.1038/jid.2014.371.

Wyatt Shields Iv, C., Reyes, C. D. and López, G. P. (2015) 'Microfluidic cell sorting: A review of the advances in the separation of cells from debulking to rare cell isolation', *Lab on a Chip*. Royal Society of Chemistry, 15(5), pp. 1230–1249. doi: 10.1039/c4lc01246a.

Xu, K. *et al.* (2014) 'Silicon Avalanche Based Light Emitting Diodes and Their Potential Integration into CMOS and RF Integrated Circuit Technology', *Advances in Optical Communication*, p. 224. doi: 10.5772/58968.

Xu, L. *et al.* (2015) 'Optimization and evaluation of a novel size based circulating tumor cell isolation system', *PLoS ONE*, 10(9), pp. 1–23. doi: 10.1371/journal.pone.0138032.

Yang, D. *et al.* (2017) 'A portable image-based cytometer for rapid malaria detection and quantification', *PLoS ONE*, 12(6), pp. 1–18. doi: 10.1371/journal.pone.0179161.

Yousang Yoon *et al.* (2014) 'Separation and capture of circulating tumor cells from whole blood using a bypass integrated microfluidic trap array', *Conference proceedings: ... Annual International Conference of the IEEE Engineering in Medicine and Biology Society. IEEE Engineering in Medicine and Biology Society. Annual Conference*, 2014, pp. 4431–4434. doi: 10.1109/EMBC.2014.6944607.

Yousuff, C. M. *et al.* (2017) 'Microfluidic platform for cell isolation and manipulation based on cell properties', *Micromachines*, 8(1). doi: 10.3390/mi8010015.

Zaorsky, N. *et al.* (2016) 'Causes of death among cancer patients', *Annals of Oncology*, (November 2016), p. mdw604. doi: 10.1093/annonc/mdw604.

Zhang, Z. L. *et al.* (2005) 'In situ bio-functionalization and cell adhesion in microfluidic devices',

Microelectronic Engineering, 78–79(1–4), pp. 556–562. doi: 10.1016/j.mee.2004.12.071.

Zheng, G. *et al.* (2011) ‘Subpixel resolving optofluidic microscope based on super resolution algorithm’, *Proceedings - International Symposium on Biomedical Imaging*, pp. 1362–1365. doi: 10.1109/ISBI.2011.5872653.

Zheng, G. *et al.* (2011) ‘The ePetri dish, an on-chip cell imaging platform based on subpixel perspective sweeping microscopy (SPSM)’, *Proceedings of the National Academy of Sciences*, 108(41), pp. 16889–16894. doi: 10.1073/pnas.1110681108.

Zheng, S. *et al.* (2007) ‘Membrane microfilter device for selective capture, electrolysis and genomic analysis of human circulating tumor cells’, *Journal of Chromatography A*, 1162(2 SPEC. ISS.), pp. 154–161. doi: 10.1016/j.chroma.2007.05.064.

Zheng, S. *et al.* (2011) ‘3D microfilter device for viable circulating tumor cell (CTC) enrichment from blood’, *Biomedical Microdevices*, 13(1), pp. 203–213. doi: 10.1007/s10544-010-9485-3.

Zheng, Y. *et al.* (2009) ‘Automatic Correction of Intensity Nonuniformity from Sparseness of Gradient Distribution in Medical Images’, *Med Image Comput Comput Assist Interv.*, 12(1), pp. 852–859. doi: 10.1002/bmb.20244.DNA.

Zhou, E. H., Lim, C. T. and Quek, S. T. (2005) ‘Finite element simulation of the micropipette aspiration of a living cell undergoing large viscoelastic deformation’, *Mechanics of Advanced Materials and Structures*, 12(6), pp. 501–512. doi: 10.1080/15376490500259335.

Zhu, H. *et al.* (2011) ‘Wide-field fluorescent microscopy on a cell-phone’, *Proceedings of the Annual International Conference of the IEEE Engineering in Medicine and Biology Society, EMBS*, pp. 6801–6804. doi: 10.1109/IEMBS.2011.6091677.

Zhu, H. *et al.* (2012) ‘Optofluidics Fluorescent Imaging Cytometry on a Cell Phone’, *Analytical Chemistry*, 83(17), pp. 6641–6647. doi: 10.1021/ac201587a.Optofluidic.

Zhu, H., Sencan, I., *et al.* (2013) ‘Cost-effective and rapid blood analysis on a cell-phone’, *Lab on a Chip*, 13(7), pp. 1282–1288. doi: 10.1039/c3lc41408f.

Zhu, H., Isikman, S., *et al.* (2013) ‘Optical Imaging Techniques for Point-of-care Diagnostics’, *Lab Chip*, 31(1), pp. 51–67. doi: 0.1039/c2lc40864c.

Publications

Georgia Korompili, Georgios Kanakaris, Christos Ampatis, Nikos Chronis, **A portable, optical scanning microsystem for large field of view, high resolution imaging of biological specimens**, Sensors and Actuators A: Physical, Volume 279, 15 August 2018, p.p. 367-375

Georgia Korompili, Georgios Kanakaris, Christos Ampatis, Nikos Chronis, **A Portable, Optical Scanning System for Large Field of View, High Resolution Imaging of Biological Specimens**, proceeding at the “Eurosensors 2017” Conference, Paris, France, 3–6 September 2017.

Georgia Korompili, **A Ball Lens/LED micro-optical chip for imaging reflective surfaces**, Lecture in 7th International Conference "Micro&Nano 2018" , Aristotle University of Thessaloniki, 5- 7 November 2018

Georgia Korompili, Konstantinos Misiakos, Nikos Chronis, **An optoelectronic chip with integrated excitation and collection optics for lab-on-chip, imaging applications**, Sensors and Actuators A: Physical, peer review process.

Georgia Korompili*, Katerina Skorda*, Nikos Chronis, *coauthors, **A thin microfluidic chip for white blood cells isolation: studying the factors that affect cell capturing in microfluidic chambers with antibody functionalized walls**, under submission process.